EXPERIMENTAL AND NUMERICAL INVESTIGATION OF THE EFFECT OF
A VEGETATION ARRAY TO THE FLOW RESISTANCE AND
CHARACTERISTICS

A THESIS SUBMITTED TO
THE GRADUATE SCHOOL OF NATURAL AND APPLIED SCIENCES
OF
MIDDLE EAST TECHNICAL UNIVERSITY

BY

EMRE HASPOLAT

IN PARTIAL FULFILLMENT OF THE REQUIREMENTS
FOR
THE DEGREE OF DOCTOR OF PHILOSOPHY
IN
CIVIL ENGINEERING

DECEMBER 2022

Approval of the thesis:

EXPERIMENTAL AND NUMERICAL INVESTIGATION OF THE EFFECT OF A VEGETATION ARRAY TO THE FLOW RESISTANCE AND CHARACTERISTICS

submitted by **EMRE HASPOLAT** in partial fulfillment of the requirements for the degree of **Doctor of Philosophy in Civil Engineering, Middle East Technical University** by,

Prof. Dr. Halil Kalıpçılar
Dean, Graduate School of **Natural and Applied Sciences**   _____

Prof. Dr. Erdem Canbay
Head of the Department, **Civil Engineering**   _____

Prof. Dr. Mete Köken
Supervisor, **Civil Engineering, METU**   _____

Examining Committee Members:

Prof. Dr. Ayşe Burcu Altan Sakarya
Civil Engineering, METU   _____

Prof. Dr. Mete Köken
Civil Engineering, METU   _____

Assoc. Prof. Dr. Kerem Taştan
Civil Engineering, Gazi University   _____

Assoc. Prof. Dr. Ali Ercan
Civil Engineering, METU   _____

Assist. Prof. Dr. Önder Koçyiğit
Civil Engineering, Gazi University   _____

Date: 20.12.2022

I hereby declare that all information in this document has been obtained and presented in accordance with academic rules and ethical conduct. I also declare that, as required by these rules and conduct, I have fully cited and referenced all material and results that are not original to this work.

Name Last name : Emre Haspolat

Signature :

ABSTRACT

EXPERIMENTAL AND NUMERICAL INVESTIGATION OF THE EFFECT OF A VEGETATION ARRAY TO THE FLOW RESISTANCE AND CHARACTERISTICS

Haspolat, Emre
Doctor of Philosophy, Civil Engineering
Supervisor : Prof. Dr. Mete Köken

December 2022, 208 pages

Vegetation canopies play a crucial role in aquatic living and ecology which makes them an essential part of rivers and waterways. In the present study, flow resistance due to submerged and emergent vegetation arrays having various densities was investigated experimentally and numerically under different hydraulic scenarios. A novel experimental setup having a drag plate was developed to measure drag forces acting on emergent and submerged vegetation arrays imitated by a group of rigid smooth cylinders in a staggered pattern. In the literature, studies were mostly conducted with large vegetation density, small stem diameter, and under low stem Reynolds numbers. On the other hand, the present study was performed with relatively lower vegetation densities, large stem diameter, and under high stem Reynolds numbers to enhance current knowledge about the flow resistance due to the vegetation arrays. In this context, the effect of vegetation density, flow conditions, and submergence ratio on the total flow resistance parameters and drag coefficient were evaluated systematically, and some empirical equations were proposed to estimate these resistance parameters. Furthermore, some of the

experimental cases were investigated by a numerical study based on detached eddy simulation. The numerical analyses provided to evaluate bed shear stresses on the drag plate so that equations were derived to calculate the contribution of bed friction to the total flow resistance. It was observed that there was a strong consistency between the experimentally and numerically found drag coefficients. Finally, flow characteristics and structures in the vegetation arrays were examined by numerical analyses.

ÖZ

BİTKİ DİZİLERİNİN AKIM DİRENCİNE VE AKIM KARAKTERİSTİKLERİNE OLAN ETKİSİNİN DENEYSEL VE SAYISAL OLARAK İNCELENMESİ

Haspolat, Emre
Doktora, İnşaat Mühendisliği
Tez Yöneticisi: Prof. Dr. Mete Köken

Aralık 2022, 208 sayfa

Bitki kanopilerinin sudaki yaşam ve ekoloji üzerinde oynadığı önemli rol, onları nehirlerin ve su yollarının vazgeçilmez bir parçası yapmaktadır. Bu çalışmada, farklı hidrolik koşullar altında, çeşitli yoğunluklara sahip batık ve batık olmayan bitki dizileri kaynaklı akım direnci deneysel ve sayısal olarak incelenmiştir. Şaşırtmalı dağılıma sahip bir grup rijit pürüzsüz silindirlerle taklit edilen batık ve batık olmayan bitki dizileri üzerindeki sürükleme kuvvetini ölçebilmek için sürükleme plakasına sahip özgün bir deney düzeneği geliştirilmiştir. Literatürde, çalışmalar çoğunlukla yüksek bitki yoğunluğu, küçük gövde çapı ve düşük bitki Reynolds sayısı altında icra edilmiştir. Diğer yandan, bitki dizileri kaynaklı akım direnci hakkındaki mevcut bilgileri artırmak amacıyla bu çalışma göreceli düşük bitki yoğunluğu, geniş gövde çapı ve yüksek bitki Reynolds sayıları altında gerçekleştirilmiştir. Bu bağlamda, bitki yoğunluğunun, akım durumlarının ve batıklık oranlarının toplam akım direnç parametreleri ve sürükleme katsayısı üzerindeki etkisi sistematik olarak değerlendirilmiş ve bu direnç parametrelerini tahmin etmek için deneysel denklemler önerilmiştir. Ayrıca, bazı deneysel durumlar detached eddy simülasyonuna dayanan sayısal çalışmayla da incelenmiştir. Sayısal analizler sürükleme plakası üzerindeki

vii

yatak kayma gerilmelerinin değerlendirilmesini sağlamış ve böylece yatak sürtünmesinin toplam akım direncine olan katkısını hesaplayacak denklemler türetilmiştir. Deneysel ve sayısal olarak bulunan sürükleme katsayıları arasında güçlü bir tutarlılık olduğu görülmüştür. Son olarak, bitki dizilerindeki akım özellikleri ve yapıları sayısal analizler vasıtasıyla incelenmiştir.

Anahtar Kelimeler: Açık kanal hidroliği, Batık ve batık olmayan bitki dizileri, Akım direnci ve özellikleri, Sürükleme katsayısı, Hesaplamalı Akışkanlar Dinamiği

To Humanity and Human Welfare

ACKNOWLEDGMENTS

Last but not least, I am grateful to my mother and my wife. I could not find any words to express your never-ending support. You are the sunshine that enlightens my way whenever I am lost in the darkness.

TABLE OF CONTENTS

LIST OF TABLES

TABLES

LIST OF FIGURES

FIGURES

xxii

LIST OF ABBREVIATIONS

ABBREVIATIONS

ADV   : Acoustic Doppler Velocimetry

AR   : Aspect Ratio

CFD   : Computational Fluid Dynamics

CNC   : Computer Numerical Control

CV   : Control Volume

DES   : Detached Eddy Simulation

FORTRAN   : Formula Translation

L   : Laminar

LDA   : Laser Doppler Anemometer

LDV   : Laser Doppler Velocimetry

LES   : Large Eddy Simulation

METU   : Middle East Technical University

RANS   : Reynolds-averaged Navier-Stokes

RMS   : Root Mean Square

SA   : Spalart-Allmaras

SB   : Sucker and Brauer's Function

SGS   : Subgrid-scale

T   : Fully Turbulent

TKE   : Turbulent Kinetic Energy

TrBL   : Transition in Boundary Layers

TrSL   : Transition in Shear Layer

TRUBA   : Turkish National e-Science e-Infrastructure

TrW   : Transition in Wake

TUBITAK   : The Scientific and Technological Research Council of Türkiye

LIST OF SYMBOLS

SYMBOLS

a	: Frontal area of stem per canopy volume	$[\text{m}^{-1}]$
A	: Flow area	$[\text{m}^2]$
B	: Channel width	$[\text{m}]$
B_d	: Width of drag plate	$[\text{m}]$
C_D	: Drag coefficient	$[-]$
C_{Db}	: Drag coefficient based on bulk velocity	$[-]$
C_{Dc}	: Drag coefficient based on constricted cross section velocity	$[-]$
C_{Dp}	: Drag coefficient based on pore velocity	$[-]$
C_{Dref}	: Drag coefficient based on reference velocity	$[-]$
C_{Ds}	: Drag coefficient based on average stem layer velocity	$[-]$
C_p	: Pressure coefficient	$[-]$
C_{pb}	: Base pressure coefficient	$[-]$
C_{D-f}	: Drag coefficient due to friction drag	$[-]$
C_{D-p}	: Drag coefficient due to pressure drag	$[-]$
C_{D-SB}	: Drag coefficient of isolated cylinder based on Sucker and Brauer's formula	$[-]$
d	: Turbulence length scale	$[\text{m}]$
d_{min}	: Distance to the nearest wall	$[\text{m}]$

D	: Stem diameter	[m]
D_h	: Hydraulic diameter	[m]
f	: Darcy-Weisbach friction factor	[-]
f_b	: Bed friction factor	[-]
Fr	: Froude number	[-]
F_B	: Bed shear force	[N]
F_D	: Drag force due to vegetation	[N]
F_S	: Shear force at interface layer	[N]
F_T	: Total drag force on drag plate	[N]
g	: Gravity acceleration	$[m/s^2]$
h^*	: Submergence ratio	[-]
h_f	: Head loss	[m]
h_v	: Height of vegetation stem	[m]
H	: Flow depth	[m]
k	: Turbulent kinetic energy	$[m^2/s^2]$
k_s	: Equivalent roughness height	[m]
L	: Length of control volume	[m]
L_c	: Canopy drag length scale	[m]
L_d	: Length of drag plate	[m]
M	: Number of stem in control volume	[-]
n	: Manning's roughness coefficient	$[s/m^{1/3}]$

Q	: Discharge	[m³/s]
R^2	: Coefficient of determination	[-]
Re_d	: Stem Reynolds number	[-]
Re_{db}	: Stem Reynolds number based on bulk velocity	[-]
Re_{dc}	: Stem Reynolds number based on constricted cross section velocity	[-]
Re_{dp}	: Stem Reynolds number based on pore velocity	[-]
Re_{ds}	: Stem Reynolds number based on stem layer velocity	[-]
Re_H	: Channel Reynolds number	[-]
R_h	: Hydraulic radius	[m]
s	: Center to center distance between vegetation stems	[m]
S	: Slope of channel	[-]
$\tilde{S}$	: Magnitude of vorticity	[s⁻¹]
S_f	: Friction (energy) slope	[-]
S_{fb}	: Energy slope corresponding to bed resistance	[-]
S_{fv}	: Energy slope corresponding to vegetation resistance	[-]
u	: Mean velocity	[m/s]
U_*	: Shear velocity	[m/s]
U_b	: Bulk velocity	[m/s]
U_c	: Constricted cross section velocity	[m/s]
U_p	: Pore velocity	[m/s]

U_{ref}	: Reference velocity	[m/s]
U_s	: Average stem layer velocity	[m/s]
U_{sl}	: Average surface layer velocity	[m/s]
t	: Time	[s]
X_D	: Initial adjustment length	[m]
γ	: Specific weight of water	[N/m^3]
θ_s	: Separation angle	[-]
κ	: von Karman constant	[-]
λ	: Areal vegetation density	[-]
μ	: Dynamic viscosity of water	[Pa.s]
ν	: Kinematic viscosity of water	[m^2/s]
ρ	: Density of water	[kg/m^3]
τ_b	: Bed shear stress	[Pa]
ψ	: Staggered pattern effect	[-]
ω_y	: Angular velocity in y direction	[rad/s]
ω_z	: Angular velocity in z direction	[rad/s]

CHAPTER 1

INTRODUCTION

A vegetated aquatic flow has been one of the main interests of not only hydraulic engineers but also ecologists from the past to now. From an ecological point of view, vegetation in rivers or coastal areas is crucial for aquatic creatures. Vegetation creates a shelter and habitat for aquatic living, so it supports biodiversity in rivers (Inoue & Nakano, 1998; Wilcock et al., 1999). Furthermore, aquatic canopies enhance water quality through oxygen production. Some vegetation types also play an essential role in ecology and improve water purification by filtering contaminants and pollutants (Liu et al., 2008) and removing elements such as nitrogen (Shin et al., 2004), phosphorous (Skłodowski et al., 2014) and even heavy metals (e.g., mercury and lead) (Windham et al., 2003). In addition, vegetation reduces bank erosion and increases bank stability (Pollen & Simon, 2005; Liu et al., 2008).

On the other hand, from a hydraulic perspective, the existence of vegetation in rivers or floodplains is still debatable due to its drawbacks and advantages. While it was considered throughout history that vegetation increases the flood risk due to its contribution to the total flow resistance (Nepf, 2012), many studies (e.g., Liu et al., 2008; Kothyari et al., 2009; Cheng & Nguyen, 2011) mentioned that vegetation can help flood attenuation in floodplains and control sediment transport in rivers. Moreover, the canopies in coastal regions (e.g., seagrasses, mangroves) protect coastal sides and communities by wave attenuation and damping wave energy (Fonseca & Cahalan, 1992; Quartel et al., 2007). Vegetation introduces an additional drag to flow which reduces the bed shear stress (Thompson et al., 2004), thereby altering sediment transport (Hendriks et al., 2008; Kothyari et al., 2009), deposition

1

and resuspension capacity of the river (Gacia & Duarte, 2001). Therefore, it can be stated that vegetation indirectly affects channel morphology and bathymetry (Bennett et al., 2008; Luhar et al., 2008). The shear stress acting on a bed particle responsible for sediment transport (Thompson et al., 2004) is the difference between the total flow resistance and the canopy drag (Kothyari et al., 2009). Thus, it is essential to accurately estimate the vegetation resistance (i.e., form drag) in canopy flows to obtain the bed shear stress, thus calculating the sediment transport rate. Moreover, canopies significantly modify the hydrodynamics of rivers (Ghisalberti & Nepf, 2009; Etminan et al., 2017) so that the mean velocity, turbulence intensity, and diffusion in vegetated aquatic flow are considerably different from those of bare channels (Liu et al., 2008). For instance, turbulence intensity in the stem wakes is enhanced by the transformation of mean kinetic energy to turbulent kinetic energy (TKE) in canopy flows (Ben Meftah & Mossa, 2013). Besides all these, the vegetation is also used for stream restoration and recreation and adds aesthetic properties (i.e., landscapes) to waterways (Ishikawa et al., 2000, 2003; Simon et al., 2004; Liu et al., 2008; Nikora et al., 2008). All these ecological and hydraulic benefits make vegetation an essential part of natural rivers and waterways. Therefore, it is important to understand the effect of vegetation on river hydraulics and hydrodynamics. As stated previously, a significant impact of vegetation on river hydraulics is the flow resistance responsible for modifying many mechanisms such as sediment or pollutant transport, flow conveyance, and flood attenuation. Thus, the flow resistance due to vegetation in rivers and waterways has been one of the main concerns of hydraulic engineers for many years.

Most of the studies in the literature (e.g., Tanino & Nepf, 2008a; Stoesser et al., 2010; Kim & Stoesser, 2011; Etminan et al., 2017; van Rooijen et al., 2018) mainly focus on the drag of vegetation with small stem diameter for flows having low velocities (i.e., low stem Reynolds number, Re_d). However, only a few studies investigate the drag coefficient and resistance of vegetation arrays with large stem diameters similar to riparian vegetation or trees in the floodplain under actual flow conditions having

high velocities (e.g., flood conditions). Therefore, to extend current knowledge and fill the gap in the literature, the present study aims to investigate flow resistance due to emergent and submerged rigid vegetation arrays both experimentally and numerically. Furthermore, the effect of vegetation density and submergence ratio on the flow characteristics within the vegetation array are examined in detail.

The objectives of the present study are given as follows:

• A novel experimental setup will be developed to directly measure total forces acting on a drag plate having emergent and submerged vegetation array in different densities under various flow conditions.

• The effect of flow conditions and vegetation characteristics (e.g., areal vegetation density) on the total flow resistance will be investigated experimentally for both emergent and submerged vegetation arrays by considering Manning's roughness coefficient and Darcy-Weisbach friction factor.

• The bed shear stresses will be evaluated by conducting a numerical study for specific emergent and submerged vegetation cases. Furthermore, a formula will be derived to estimate the contribution of bed shear stresses to total flow resistance in a channel having a smooth bed with emergent and submerged vegetation array. Therefore, the actual drag forces acting on vegetation stems will be obtained by extracting the bed friction force from the total force on the drag plate.

• The temporally and spatially averaged drag coefficients of emergent and submerged vegetation arrays with different densities will be determined experimentally and numerically under several hydraulic scenarios. Moreover, the effect of vegetation density, stem Reynolds number and submergence ratio on the drag coefficient will be investigated systematically. The results of the present study will be compared with previous studies in the literature and discussed comprehensively.

• Flow characteristics and structures within an emergent and submerged vegetation arrays will be examined using numerical analyses.

The present study was organized to have eight chapters, and the content of each chapter is briefly explained as follows:

Chapter 1 introduces the importance of vegetation in waterways and its effects on open channel hydraulics. After that, the objectives of the present study are presented. The thesis outline is given in this chapter as well.

Chapter 2 presents relevant and important studies from the literature. Their approaches to the problem, findings and results of these studies are mentioned briefly.

Chapter 3 explains the physics behind the drag force and drag-modifying mechanisms in canopies. Later, these mechanisms will be mentioned to clarify the results of experimental and numerical analyses.

Chapter 4 starts with a dimensional analysis where the important dimensionless parameters related to the vegetation drag are derived. Afterward, properties and the working principle of the novel experimental setup are introduced in detail. The present experimental setup is compared with those in the literature, and its prominent features are mentioned. Finally, an experimental methodology that includes procedures to be followed during experiments is described as well.

Chapter 5 begins with a description of the numerical method used in the present study. Thereafter, seven different cases investigated in numerical analyses are introduced. Detailed information about meshing strategies and domains is also mentioned in this chapter.

Chapter 6 shows the results of experimental and numerical analyses. A comprehensive discussion of these results is made. Moreover, the results of the present study are compared with those of similar studies in the literature. Several relations are proposed to evaluate the total flow resistance parameters (i.e., Manning's roughness coefficient and Darcy-Weisbach friction factor), the bed shear stresses and the spatially averaged drag coefficient of vegetation arrays having

different densities under various flow conditions. Also, these relations' performance in estimating measured parameters is investigated.

Chapter 7 presents the flow characteristics and flow structures within an emergent and submerged vegetation arrays using visualization techniques in numerical analyses. The effect of vegetation density and submergence ratio on the flow characteristics is investigated.

Chapter 8 summarizes the conclusions and gives recommendations for future studies.

CHAPTER 2

LITERATURE REVIEW

For the present study, many studies, researches and projects in the literature were examined in detail, and important studies related to the flow resistance due to the canopy drag are mentioned in the present section for emergent and submerged vegetation arrays, respectively. The first subsection begins with experimental studies and ends up with numerical research. In all of these studies, vegetation stems were reproduced by rigid circular cylinders having a uniform diameter as in the present study.

2.1   Important Studies about the Flow Resistance and Characteristics in Emergent Vegetation Array

Ishikawa et al. (2000) carried out an experimental study to examine the effect of riparian tree density on the drag force exerted by the flow. In their experiments, the drag force on a single cylinder located in a staggered cylinder array was measured directly using strain gauges. The measurement mechanism was mounted on top of the channel to measure only drag force without bed friction. The location of the cylinder was altered systematically during tests, so a spatially averaged drag coefficient of the array, C_D, was obtained. It was reported that any relationship could not be established between C_D and Re_d, and C_D significantly varies with the density of trees, λ. It was found that the drag coefficient increases with the density of trees. Moreover, it was stated that the coefficient of velocity, U_b/U_*, where U_b is the bulk velocity and U_* is the shear velocity, has a stronger correlation with roughness

concentration, aH, where a is the frontal area of stem per canopy volume and H is the flow depth, than the density of trees, and the following equations were derived by performing regression analyses:

$$\frac{U_b}{U_*} = 1.25(aH)^{-0.47} \text{ with R}^2\text{=0.98.} \tag{2.1}$$

$$\frac{U_b}{U_*} = 0.26\lambda^{-0.53} \text{ with R}^2\text{=0.90.} \tag{2.2}$$

Liu et al. (2008) examined the variation of flow characteristics such as velocity and turbulence intensity along the rigid emergent vegetation array having various configurations (i.e., both linear and staggered patterns) and densities using laser Doppler velocimetry (LDV) in experiments. Generally, longitudinal velocity profiles revealed that the velocity distribution is constant along the depth, and there is a slight increase in the velocity near the free surface. It was also noted that the flow velocities at upstream of the cylinder and free stream zone are substantially higher than those just downstream. While the velocities do not change considerably in a vegetation array having low density, velocities in higher densities can be changed depending on the measurement location. Likewise, it was stated that the magnitude of turbulence intensities varies with a location such that the largest turbulence intensities occur just downstream of the cylinder, whereas lower turbulence intensities were observed at the free stream region. Moreover, it was mentioned that the turbulence intensity is nearly constant along the flow depth. It was also revealed that there was no considerable effect of bed roughness on the turbulent intensity and velocity profiles in the vegetation array except just downstream of the cylinder.

An experimental study was performed by Tanino and Nepf (2008a) to investigate the effect of vegetation density and stem Reynolds number on the drag of vegetation array where rigid cylinders were randomly distributed. In this study, the drag force was obtained indirectly using a free surface gradient in the force balance equation. However, it was stated that free surface displacement was very small at low Re_{dp}

(i.e., stem Reynolds number based on pore velocity, U_p) and small vegetation densities which caused significant uncertainties and even negative drag coefficient predictions. The temporally and spatially averaged drag coefficient, C_D, was found to decrease as Re_{dp} increased for all tested vegetation densities. Moreover, contrary to the study of Nepf (1999), C_D increases with increasing vegetation density. It was also noted that these results are only valid for the tested values of vegetation density and Re_{dp} (i.e., $O(30) \leq Re_{dp} \leq O(700)$ and $\lambda \leq 0.35$).

An experimental study was performed by Kothyari et al. (2009) to directly obtain the drag coefficient of an emergent single rigid stem using a load cell in a relatively short vegetation array (i.e., the array length is 1.80 m) having a staggered pattern. The drag coefficient values were found to be higher than those of other studies in the literature. According to Cheng and Nguyen (2011), this is due to the fact that the vegetation array is not long enough to allow fully developed flow, especially for low vegetation densities. In addition, Kothyari et al. (2009) found that while the drag coefficient considerably increases with increasing vegetation density, the effect of stem Reynolds number on the drag coefficient is insignificant. It was also stated that there is no effect of Froude number (i.e., Fr) on the drag coefficient in subcritical flow, whereas the drag coefficient decreases as Froude number increases in supercritical flow. Finally, the following relation was proposed:

$$C_D = 1.8\psi Re_{dp}^{-3/50}[1+0.45\ln(1+100\lambda)](0.8+0.2Fr-0.15Fr^2) \tag{2.3}$$

where ψ represents the staggered pattern effect on C_D (e.g., $\psi=0.8$ for regular square staggering pattern, $\psi=1$ for triangular staggering stem pattern).

Cheng and Nguyen (2011) conducted an experimental study and proposed a new length scale called the vegetation-related hydraulic radius, r_v, by considering the size and density of the vegetation and channel geometry to be used in stem Reynolds number, Re_v, calculation. The drag coefficient of the vegetation array having a staggered stem pattern was calculated indirectly using the force balance equation.

Although bed and sidewalls are made of smooth material, the bed and sidewall correction procedure proposed by Vanoni and Brooks (1957) was applied to obtain actual drag coefficients. Moreover, additional data groups were gathered from several studies to be used in the analysis, and an equation given below was proposed:

$$C_{Dv} = \frac{50}{Re_V^{0.43}} + 0.7 \left[1 - e^{-\frac{Re_V}{15000}} \right] \tag{2.4}$$

which is valid for $52 < Re_v < 5.6 \times 10^5$. It was shown that the drag coefficient decreases as the stem Reynolds number increases and does not depend on the vegetation density. Furthermore, it was stated that Equation (2.4) successfully consolidates the experimental data groups with a broad range of vegetation density.

van Rooijen et al. (2018) performed an experimental study that covers various vegetation densities and hydrodynamic conditions to accurately predict the drag coefficient of vegetation stem. In experiments, the drag force acting on a single rigid vegetation stem placed in an emergent vegetation array was directly measured using a load cell. The results of this study demonstrated that the drag coefficients based on both bulk velocity and pore velocity (i.e., C_{Db} and C_{Dp}) become nearly constant after a high stem Reynolds number (i.e., $Re_d > 1000$). However, it was stated that these drag coefficients are scattered and considerably deviate from those of isolated cylinders described with White's (1991) equation:

$$C_D = 1 + 10 Re_d^{-2/3} \tag{2.5}$$

On the other hand, it was noted that if constricted cross-section velocity, U_c, is used as the reference velocity, the calculated drag coefficients are consistent with the isolated cylinder's drag coefficients, and data scatter was reduced as recommended by Etminan et al. (2017). As a consequence, for the given stem Reynolds number, it was mentioned that the drag coefficient of canopies can be well predicted with Equation (2.5) provided that the use of constricted cross-section velocity.

D'Ippolito et al. (2019) studied flow resistance due to rigid emergent vegetation arrays by conducting experiments with several vegetation densities under various flow conditions. The vegetation stems were distributed in linear (i.e., in-line) arrangement. A drag force acting on a group of cylinders was measured using load cells. In addition to direct measurement, the drag forces were indirectly calculated using the momentum equation. It was stated that the drag coefficient increases with an increase in vegetation density; however, there was no considerable effect of stem Reynolds number on the drag coefficient for the given flow conditions (i.e., $Re_d \geq 2000$). Although there was a large discrepancy between the drag coefficients found by direct and indirect measurements, it was claimed that drag forces computed using the momentum equation were comparable with those of direct measurement. In addition, one of the experimental runs was numerically modeled using Reynolds-averaged Navier-Stokes equations (RANS), and it was observed that there was an agreement between the experiment and numerical analysis considering water level profiles along the vegetation array.

Stoesser et al. (2010) carried out a numerical study using large eddy simulations (LES) to investigate the flow resistance and characteristics of emergent vegetation arrays having staggered rigid cylinder distribution. Three different vegetation densities (i.e., λ=0.016, 0.063 and 0.251) and two stem Reynolds numbers based on the bulk velocity (i.e., Re_{db}=500 and 1340) were used in simulations. One of the experimental runs from the study of Liu et al. (2008) was selected as a case to verify the LES model. There was a good agreement between the data of Liu et al. (2008) and the result of LES. It was also demonstrated that the contribution of bed shear stresses to total resistance decreases as the vegetation density or stem Reynolds number increases. Furthermore, it was stated that the drag coefficient increases as the vegetation density increases, and it is a function of stem Reynolds number for lower Re_{db}. These drag coefficients were also found to be consistent with those of Tanino and Nepf (2008a). Finally, visualization of turbulence structures

11

demonstrates that the effect of vegetation density on flow and turbulence is more prominent than stem Reynolds number.

Kim and Stoesser (2011) conducted a numerical study using RANS with a vegetation closure model and low-resolution LES to investigate vegetation resistance at various densities and stem Reynolds numbers. It was stated that a priori knowledge of the bulk drag coefficient supplied to RANS is important and considerably affects the results of the RANS model. On the other hand, the low-resolution LES method does not need any input to compute total resistance or vegetation drag and is computationally cheaper than the high-resolution LES. It was stated that the proposed LES method predicts the bulk drag coefficients satisfactorily. Furthermore, while the flow characteristics (i.e., velocity distribution, recirculation zones, secondary flows) can be reasonably estimated in low and moderate vegetation densities with low-resolution LES, there are still uncertainties for vegetation with high densities. Moreover, it was demonstrated that the vegetation density has a more considerable impact on the bed friction contribution than the stem Reynolds number. The bed friction contribution exponentially reduces with an increase in vegetation density.

Etminan et al. (2017) performed a numerical analysis (based on LES) to investigate the drag forces on emergent vegetation array with various densities (i.e., $0.016 \leq \lambda \leq 0.25$) in a staggered pattern under four different stem Reynolds numbers (i.e., Re_{dp}=200, 500, 1000 and 1340). The time-averaged streamwise velocity and turbulence intensity profiles in the numerical analysis were compared with those of Liu et al.'s (2008) study. It was seen that there was a perfect agreement between measured profiles, so the numerical model was validated satisfactorily. A variation of the drag coefficient with vegetation density and stem Reynolds number was examined using the bulk velocity and pore velocity as the reference velocities. It was stated that while the drag coefficients slightly decrease as the stem Reynolds number increase, the vegetation density has a significant effect on the drag coefficient which

increases with an increase in canopy density. However, it was noted that the drag coefficient data were scattered and did not collapse on a single cylinder curve (i.e., White's (1991) equation) using either U_b or U_p. It was also observed that delayed separation and sheltering effects, which reduce the canopy drag, are evident for only the sparsest canopy (i.e., $\lambda=0.016$). On the other hand, drag coefficients of other vegetation densities were found to be significantly larger than that of a single cylinder for the given stem Reynolds numbers. This was explained by the fact that the blockage effect governs the drag mechanism in higher vegetation densities and increases the drag coefficient as the canopy density increases. These drag-modifying mechanisms will be explained in Chapter 3 in detail. To improve the estimation of the drag coefficient in canopy flow, the constricted cross-section velocity, U_c, was proposed to be used as the reference velocity. It was also stated that the drag coefficients based on this velocity (i.e., C_{Dc}) were gathered on White's (1991) equation for the given canopy densities, and data scatter was significantly reduced using U_c as the reference velocity. In addition, it was reported that White's (1991) equation successfully predicts the bulk drag coefficient of vegetation array having random stem distribution if U_c is used as the reference velocity.

Finally, Table 2.1 summarizes some of the important parameters of the above-mentioned studies.

Table 2.1 The range of important parameters used in the previous studies

Study	λ	D (cm)	Re_{db}/Re_{dp}
Ishikawa et al. (2000)	0.00314-0.0322	0.4/0.64	887-4541
Liu et al. (2008)	0.0061-0.016	0.635	1432-2011
Tanino and Nepf (2008a)	0.091-0.35	0.64	25-685
Kothyari et al. (2009)	0.0022-0.0885	1	1264-7200
Cheng and Nguyen (2011)	0.0043-0.1189	0.32/0.66/0.83	154-1199
van Rooijen et al. (2018)	0.05-0.10	0.64	320-1408
D'Ippolito et al. (2019)	0.0031-0.0436	0.8-1.0	131-962
Stoesser et al. (2010)	0.0157/0.0628/0.2513	-	500/1340
Kim and Stoesser (2011)	0.016-0.25	-	500/1340
Etminan et al. (2017)	0.016-0.25		200-1340

2.2 Important Studies about the Flow Resistance and Characteristics in Submerged Vegetation Array

Dunn et al. (1996) performed an experimental study to examine spatially averaged longitudinal velocity profiles, turbulence intensity, Reynolds stresses and drag coefficient of rigid and flexible vegetation arrays with a staggered pattern. Acoustic Doppler velocimetry (ADV) was used in experiments to obtain Reynolds stresses and velocities, and the following momentum equation was used to calculate the drag coefficient:

$$C_D' = \frac{gS - \frac{\partial}{\partial y}(\overline{u'v_h'})}{a/2\bar{u}_h^2} \tag{2.6}$$

where C_D' is the horizontally averaged local drag coefficient (i.e., vary in the vertical direction), g is the gravitational acceleration, S is bed slope, $(\overline{u'v_h'})$ is horizontally averaged Reynolds stress, and $\bar{u}_h$ is horizontally and time-averaged streamwise

velocity. Thus, the bulk drag coefficient of submerged vegetation, $\overline{C_D}$, can be found using the following equation:

$$\overline{C_D} = \frac{\int_0^{h_v} C_D' u_h^2 \, \partial y}{\int_0^{h_v} u_h^2 \, \partial y} \tag{2.7}$$

where h_v is the height of the vegetation stem. It was stated that while the velocity profiles are considerably affected by the vegetation density in canopies having rigid stems, the velocity profiles in flexible stem arrays are rather influenced by the flexibility of the stem and stem Reynolds number. Moreover, it was observed from measurements that while Reynolds stresses and turbulence become maximum near the top of the submerged vegetation array, they substantially decrease within the canopy. It was also noted that the drag coefficient data of the canopy having rigid cylinders was scattered so that any relationship between the drag coefficient and other parameters can not be established. Furthermore, the mean value of the bulk drag coefficient was found to be 1.13 for the rigid submerged canopy; however, for canopy having flexible stems, it was mentioned that this bulk drag coefficient significantly reduces due to the deflection of flexible stems.

Stone and Shen (2002) investigated the flow resistance in submerged vegetation arrays having different densities under various hydraulic conditions by conducting experiments. Analytical formulas were developed to obtain the average stem layer velocity, u_s, and average surface layer velocity, u_{sl}, in submerged canopies. The drag coefficient included in these analytical formulas was obtained from emergent vegetation experiments using the constricted cross-section velocity and was found to be 1.05. Later, analytical expression was compared with experimental data from the present study and past studies in the literature to verify the analytical relationship. It was shown by a comparison that there is a strong consistency between measured and computed average stem layer velocities. Finally, the following equation was proposed to predict average stem layer velocity:

$$\frac{u_s}{U_b} = \sqrt{h^*} \left[\frac{1 - \sqrt{\frac{4\lambda}{\pi}}}{1 - h^* \sqrt{\frac{4\lambda}{\pi}}} \right]$$
(2.8)

where h^* is the submergence ratio (i.e., h_v/H).

Huthoff et al. (2007) developed an analytical model based on a two-layer approach to describe depth-averaged flow velocity for flow in a submerged vegetation array. It was stated that the velocity data from the study of Meijer and van Velzen (1999) was used to calibrate some parameters in analytical expression. The following analytical formulas were proposed for average velocities in stem (i.e., resistance) and surface layers, respectively:

$$\frac{U_r}{U_{r0}} = \sqrt{\frac{H}{h_v}} \text{ for } H \geq h_v$$
(2.9)

$$\frac{U_s}{U_{r0}} = \left(\frac{H - h_v}{s} \right)^{\frac{2}{3}\left(1 - \left(\frac{H}{h_v}\right)^{-5}\right)}$$
(2.10)

where U_r and U_{r0} are depth-averaged flow velocities in the resistance layer for submerged and emergent resistance elements, U_s is the depth average flow velocity in the surface layer, and s is the distance between vegetation stems. Furthermore, the performance of these analytical formulas was evaluated by comparison of computed and measured dimensionless velocities (i.e., U_r/U_{r0} and U_s/U_{r0}). It was seen that there is a perfect agreement between computed and measured velocity scales.

Yang and Choi (2010) performed a study to develop mean velocity relationships for the stem and surface layer for flows in submerged canopies using a two-layer approach. It was assumed that the velocity distribution in the stem layer is uniform along the water depth. Moreover, the mean velocity (i.e., layer-averaged velocity) in the stem layer, u_s, is derived using simple force balance equilibrium by neglecting the bottom shear and given as follows:

$$u_s = \sqrt{\frac{2gHS}{aC_Dh_v}} \tag{2.11}$$

On the other hand, the mean velocity for the surface layer, u_{sl}, was derived by assuming a logarithmic velocity distribution in the surface layer as recommended by previous studies (e.g., Nepf and Vivoni, 2000). Thus, the following relation was proposed:

$$u_{sl} = \frac{C_u u_*}{\kappa} \cdot \left[\frac{H}{(H-h_v)} \ln\left(\frac{H}{h_v}\right) - 1 \right] + u_s \tag{2.12}$$

where C_u is the coefficient, $C_u=1$ for a≤5 m^{-1} and $C_u=2$ for a>5 m^{-1}, U_* is the shear velocity at the interface between the stem and surface layer, $U_* = \sqrt{g(H-h_v)S}$. Equations (2.11) and (2.12) were compared with those of Stone and Shen (2002) and Huthoff et al. (2007) using data sets from previous experimental studies. It was shown that the performance of the proposed equations in the prediction of layer-averaged velocities (i.e., Equations (2.11) and (2.12)) is better than those of Stone and Shen (2002) and Huthoff et al. (2007).

Liu and Zeng (2017) collected data from several studies in the literature to analyze the effect of Froude number, stem Reynolds number, vegetation density and submergence ratio on the drag coefficient for rigid submerged vegetation in subcritical open channel flow. It was stated that an obvious relation could not be established between Froude number and the drag coefficient up to a certain Froude number (i.e., 0<Fr<0.28). However, the drag coefficient becomes independent from Froude number and is almost constant for given vegetation densities in larger Froude numbers (i.e., 0.28<Fr<0.48). In addition, it was demonstrated that the drag coefficient exponentially decreases as stem Reynolds number increases under a fixed vegetation density and submergence ratio. An effect of vegetation density on the drag coefficient was examined by keeping the submergence ratio constant, and it was reported that the drag coefficient logarithmically decreases with an increase in

vegetation density (valid for $0.012 < \lambda < 0.12$). Finally, it was noted that there is a logarithmic rising in the drag coefficient with an increase in the submergence ratio.

CHAPTER 3

PHYSICAL BACKGROUND

3.1   Drag Mechanism of Single Smooth Circular Cylinder

The present study focuses only on smooth circular cylinders (i.e., rigid vegetation stem), so the words 'smooth circular' is removed and not used in this part for brevity. Moreover, in the present part, cylinders are considered infinitely long rather than finite length. However, it should be noted that there are several discrepancies between the finite length and infinitely long cylinders in terms of flow characteristics and drag. For instance, there is a free end at the top of a finite-length cylinder where flow separation occurs in addition to two separations from sides. The shear layer separated from the free end affects those separated from the sides of the cylinder. As a result of this interference, a three-dimensional flow structure is created and the drag of the cylinder can differ (Luo et al., 1996).

There are two types of drag forces acting on the cylinder; friction (viscous) and pressure (form) drag. While pressure drag results from pressure distribution on the front and rear sides of the cylinder, friction drag is generated by viscous friction on the surface of the cylinder (Zdravkovich, 1997). The sum of these components forms the total drag, so the drag coefficient of total drag can be expressed as follows:

$$C_D = C_{D-f} + C_{D-p} \tag{3.1}$$

where C_{D-f} and C_{D-p} are drag coefficients due to the friction and pressure drag, respectively. Moreover, the cylinder's drag depends on the flow state that was classified according to cylinder Reynolds number (i.e., Re_d) as given in Table 3.1.

19

Table 3.1 State of flow and corresponding Re_d ranges (Zdravkovich, 1997)

State of Flow	Reynolds Range
Laminar (L)	$0 < Re_d < 200$
Transition in Wake (TrW)	$200 < Re_d < 400$
Transition in Shear Layer (TrSL)	$400 < Re_d < 200000$
Transition in Boundary Layers (TrBL)	$200000 < Re_d <$ unspecified
Fully Turbulent (T)	unspecified $< Re_d < \infty$

Each state of flow is represented by several flow regimes, and one can investigate the study of Zdravkovich (1997) to find further information about these regimes. According to Table 3.1, it can be stated that experiments and numerical analyses were performed at TrSL flow state in the present study.

The variation of drag coefficients based on friction and pressure drag is given Figure 3.1.
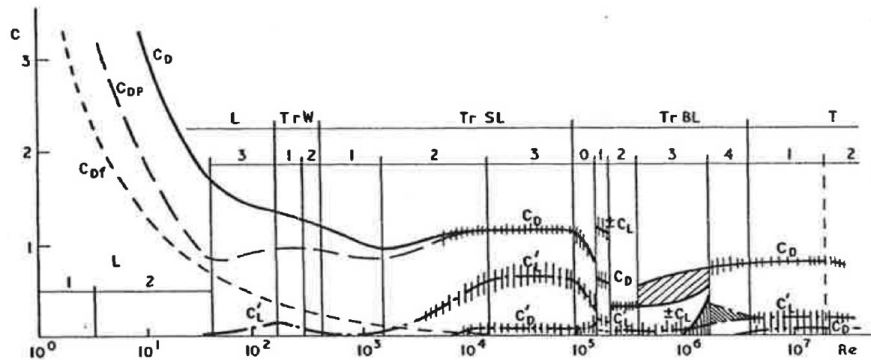
Figure 3.1. Variation of friction and pressure drag coefficients with state of flow

Note: Reprinted from *Flow around circular cylinders vol1: Fundamentals* (p. 17), by Author M. M. Zdravkovich, 1997, Oxford University Press. Copyright 1997 by M. M. Zdravkovich.

It is clearly observed from Figure 3.1 that the friction drag diminishes as cylinder Reynolds number increases in TrSL flow state so that the pressure drag dominates

the total drag. Also, Achenbach (1968) stated that friction drag is responsible for a very small portion of the total drag (i.e., 1-2%) and the rest of which is formed by pressure drag in subcritical flow regime (i.e., $Re_d < 2 \times 10^5$). Hence, it can be stated that the friction drag on the cylinders is negligible, so form drag dominates the total drag in the present study.

To better understand the pressure drag mechanism, one can consider a free stream flow around an infinite-length cylinder as given in Figure 3.2. Fluid particles that impact the cylinder create a stagnation point A, where the velocity of the fluid is zero, and maximum pressure occurs. The closest fluid particles to the cylinder surface in the boundary layer which travel along the cylinder surface from point A to B, where a favorable pressure gradient occurs (i.e., $dp/dx < 0$), undergo friction (viscous) losses. When the particle passes point B, where the maximum fluid velocity is formed, an adverse pressure gradient (i.e., $dp/dx > 0$) starts to develop at the rear side of the cylinder surface. The fluid particles in the boundary layer do not have sufficient kinetic energy to overcome the adverse pressure gradient and thus stop by decelerating at point S which is somewhere between points B and C (i.e., the base of the cylinder). Afterward, these fluid particles move in a reverse direction and begin to curl so that wake vortices are generated.
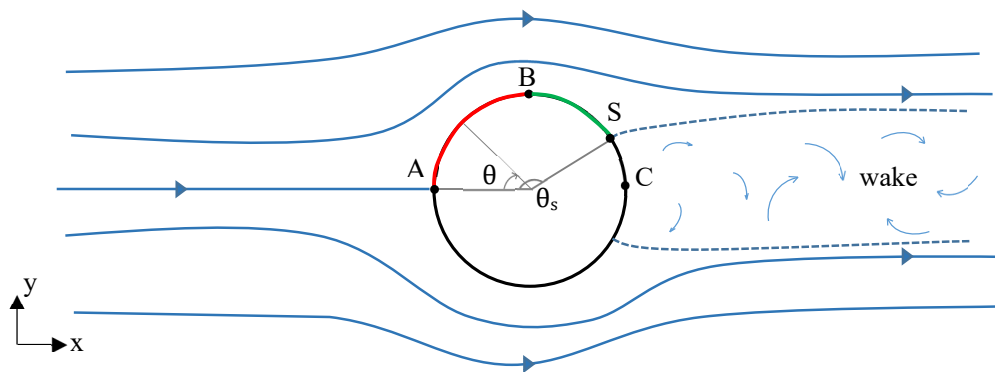
Figure 3.2. Flow around cylinder and formation of wake, inspired by Hoerner (1965) and Žukauskas (1972)

It was stated that while the point of separation (i.e., point S) can be predicted by theoretical analysis in laminar boundary layer flows, it can not be found in turbulent boundary layer flow (Hoerner, 1965). The separation location on the cylinder is defined by an angle between the stagnation point A and separation point S called the separation angle, θ_s (i.e., time-averaged separation angle). The pressure further downstream of the separation point is stable and constant as shown in Figure 3.3 (Žukauskas, 1972). If pressures along the front and rear sides of the cylinder are integrated with surface area, the resultant pressure drag force can be found. However, if the integration process is performed for curve four valid for inviscid potential flow in Figure 3.3, the resultant drag force becomes zero because of symmetrical pressure distribution. This phenomenon is called d'Alembert's paradox. Furthermore, there is a dead region called a wake between separated boundary layers which proceed to develop downstream as free shear layers. Large flow structures are generated within the wake and dissipated along the wake, and this process is dependent on the state of flow (Zdravkovich, 1997). Moreover, the turbulence in the main flow does not affect the drag coefficient in the subcritical regime (Žukauskas, 1972).
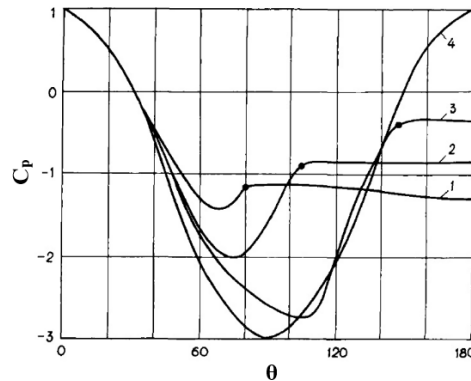
Figure 3.3. Variation of pressure coefficient (C_p) around the single cylinder for different Re_d shown by 1-3

Note: Reprinted from 'Heat Transfer from Tubes in Crossflow' by Author A. Žukauskas, 1972, *Advances in Heat Transfer, 8,* 93-160, Copyright by Elsevier

3.2   Physical Background of Flow and Drag in Cylinder Array

The drag and wake characteristics of a single cylinder have been widely investigated in the literature (e.g., Petryk, 1969; Zdravkovich, 1997). Wieselsberger (1922), Hoerner (1965), Schlichting (1979) and White (1991) presented diagrams based on experiments that reveal the relation between drag coefficient and cylinder Reynolds number. However, these well-known drag coefficient graphs are valid for infinitely long single cylinder and thus do not represent the cylinder array's drag. On the other hand, the drag and wake characteristics of a cylinder located in an array differ from those of a single cylinder. Žukauskas (1972) stated that only the flow around the first row of the cylinder array is similar to that of a single cylinder in the subcritical regime; however, the flow is considerably changing as it moves inside the array. Also, there are three different flow regimes that depend on Re_d for cylinders in an array: laminar flow regime (i.e., $Re_d < 10^3$), subcritical flow regime (i.e., $5 \times 10^2 < Re_d < 2 \times 10^5$), and critical flow regime (i.e., $Re_d > 2 \times 10^5$) (Žukauskas, 1972).

In the present section, the main hydrodynamic mechanisms (i.e., delayed separation, sheltering and blockage effect) that are responsible for the discrepancy between the drag coefficient of the cylinder array and that of a single cylinder are explained briefly. The diameter of cylinders, flow condition and distance between cylinders are important factors determining which mechanism will prevail as depicted in Figure 3.4. Herein, U_∞, U_l, U_w, s_x and s_y are average incoming flow velocity, increased gap velocity (due to the contraction in flow area), velocity in the wake (decreased due to the sheltering effect), streamwise and spanwise cylinder spacings, respectively (Gijón Mancheño et al., 2021).

23
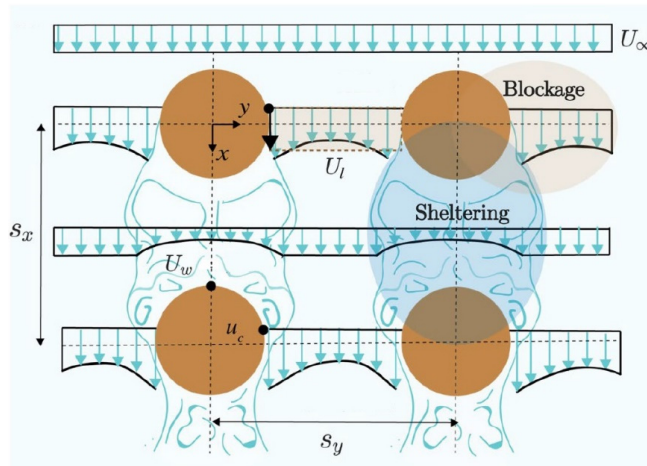
Figure 3.4. Illustration of sheltering and blockage effect (Gijón Mancheño et al., 2021)

Note: Adapted from 'Predictive model of bulk drag coefficient for a nature-based structure exposed to currents' by Authors A. Gijón Mancheño, W. Jansen, J. C. Winterwerp and W. S. J. Uijttewaal, 2021, *Scientific Reports*, 11, 3517, Copyright by Springer Nature

3.2.1 Delayed Separation

The location of the separation point can affect the drag of cylinders by altering the width of the wake region on which the pressure drag depends. A wider wake means a lower pressure recovery on the rear surface of the single cylinder (Afgan et al., 2011). Thus, the maximum pressure drag coefficient develops with the largest width of the wake region in the subcritical flow regime (Žukauskas, 1972). In other words, a delay in the separation of the boundary layer can lead to a decrease in pressure drag. This mechanism is also responsible for the drastic decrease in the drag coefficient called 'drag crisis' where separation points move to further downstream. Separation can also delay with time and Re_d (Jiang, 2020) as shown in Figure 3.3

where black circles represent the point of separation. Herein, the transition from laminar to turbulent boundary layer is responsible for the delay of the separation point (Žukauskas, 1972).

In the cylinder array, the separation point of the downstream cylinder can be delayed by the turbulence in the wake created by the upstream cylinder (Nepf, 1999). Thus, in a cylinder array, the separation point of the rear cylinder may move further downstream compared to that of a single cylinder so that the average drag coefficient of the cylinder array can decrease. Furthermore, there is an accelerated flow between adjacent cylinders due to blockage which maintains the positive velocity of near cylinder fluid particles further in the adverse pressure gradient region so that separation points are delayed (Etminan et al., 2017).

3.2.2   Sheltering Effect

Nepf (1999) presented a figure (i.e., Figure 3.5) to demonstrate the effect of upstream cylinder wake which depends on the longitudinal (L/d) and transverse (T/d) distance between the cylinders on the drag coefficient of the downstream cylinder.
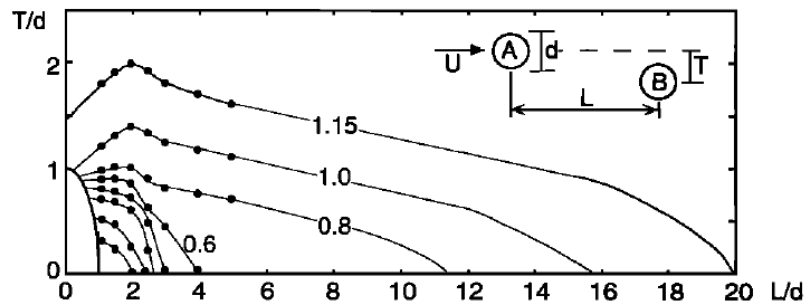
Figure 3.5. Drag coefficient contours of downstream cylinder B (Nepf, 1999)

Note: Reprinted from 'Drag, turbulence, and diffusion in flow through emergent vegetation' by Author H. M. Nepf, 1999, *Water Resources Research*, (35-2), 479-489, Copyright by American Geophysical Union

As can be seen from Figure 3.5, the wake of the upstream cylinder diminishes the drag coefficient of the downstream cylinder based on the upstream velocity. It can also be stated that the effect of the upstream cylinder wake is enhanced as the longitudinal and transverse distance between the cylinders decrease. Nepf (1999) attributed this effect, called 'sheltering effect' (or 'shielding effect'), to the wake characteristic which reduces an impingement velocity acting on the downstream cylinder and thus cylinder drag. In other words, sheltering is generated when the velocity approaching the downstream cylinders is lower than the average velocity in a cylinder array (i.e., velocity deficit) due to the effect of the upstream cylinder (Etminan et al., 2017). Moreover, Luo et al. (1996) stated that the downstream cylinder can be experienced a thrust instead of drag at very small longitudinal spacings. Based on the wake interference model developed by Nepf (1999), it was stated that the bulk drag coefficient of a staggered array decreases more quickly than that of a random array as array density increases. This is because the sheltering effect is more prominent in the staggered array where the cylinders are aligned (i.e., T/d=0) periodically. Thus, it can be said that the sheltering effect considerably depends on the distribution of vegetation stems in the canopy (Etminan et al., 2017).

3.2.3   Blockage Effect

An influence of solid boundaries (i.e., walls) on a flow around and downstream of the bluff bodies such as cylinders is called blockage effect (Petryk, 1969). Zdravkovich (2003) stated that the blockage effect causes a set of variations in the flow around the cylinder as follows: Firstly, the presence of a cylinder decreases the flow area locally leading to an increase in velocity around the cylinder. Secondly, wall boundaries restrict the widening of the wake (i.e., wake blockage), and the pressure in the wake is further reduced due to increased flow velocity outside the wake. The discrepancy between cylinders' drag that is present in flow with or without boundaries is explained by the effect of the latter one. Moreover,

Zdravkovich (2003) stated that the rise of the local velocity around the cylinder due to the blockage results in a decrease in pressure coefficient, C_p. The strength of the blockage effect is quantified by a non-dimensionless term, blockage ratio, which is the ratio of cylinder diameter to channel width (i.e., d/B). Zdravkovich (2003) also demonstrated that a larger blockage ratio ceases the widening of wake in a shorter streamwise range (see figure 23.29 in the study of Zdravkovich (2003)) and causes the lower base pressure coefficient (i.e., C_{pb}), thus increasing C_D directly (see figures 23.15 and 23.16 in the study of Zdravkovich (2003)). In addition to the blockage ratio, the blockage effect also depends on Reynolds number, shape and position of the bluff body in the test section. Based on the position of the cylinder, solid boundaries create symmetric or asymmetric blockage where the influence of a closer wall prevails (Zdravkovich, 2003).

To account for the blockage effect on the drag of the cylinder and represent the increased local velocities better, Ramamurthy and Lee (1973) proposed to replace the bulk velocity (i.e., free stream velocity) with some other reference velocities such as jet velocity, U_j, and mean gap velocity (i.e., constricted cross-section velocity, U_c), U_l, which can be acquired using the continuity equation. It was observed that while the drag coefficient based on bulk velocity, C_{Db}, has a parabolic relation with the blockage ratio, the drag coefficients based on jet velocity and mean gap velocity, C_{Dj} and C_{Dl}, are independent (i.e., constant) of the blockage ratio (see figure 7a in the study of Ramamurthy and Lee (1973)). It was also concluded in the study of Ramamurthy and Lee (1973) that the blockage effect of wall boundaries on the drag force of a single cylinder is similar to the blockage effect of adjacent cylinders on each other's drag force in the cylinder array. Furthermore, blockage and turbulence generation are improved as the spanwise distance between cylinders reduces in the array (Gijón Mancheño et al., 2021).

CHAPTER 4

EXPERIMENTAL SETUP AND METHODOLOGY

In the present section, firstly, dimensional analysis was performed to reveal which parameters affect the drag of the vegetation array. Also, dimensionless parameters having a relation with vegetation drag were obtained. Secondly, the design stages of each member in the experimental setup were mentioned in detail. After that, several steps and strategies followed to construct the experimental setup were stated. Finally, an experimental methodology was explained.

4.1   Dimensional Background of Canopy Flows

Dimensional analysis is a key procedure to determine important physical parameters that can affect relevant hydraulic phenomena. From the past to the present, many researchers have conducted their experiments under the guidance of dimensional analysis. Furthermore, it minimizes time and effort in experimentation by reducing the number of relevant variables. In the following dimensional analysis procedure, some of the vegetation characteristics (e.g., flexural rigidity, leaf area, surface roughness) are not included, because they are not in the scope of the present study. The present study focuses on the flow resistance of smooth rigid cylindrical stems with a uniform diameter (i.e., without any branch or leaves) that mimic the rigid vegetation or trees in the channel and floodplain. Flow resistance generally depends on bed friction and vegetation drag in vegetated channels. While bed friction is usually neglected compared to canopy drag in most practical cases (Stone & Shen, 2002), bed friction can form a significant portion of the total resistance in sparsely

vegetated channels (Huthoff et al., 2007). However, the present study is interested in the flow resistance due to vegetation drag rather than the bed friction, so experiments were performed on a smooth bed to minimize the bed drag. Therefore, the bed and stem surface roughness heights are not changed in experiments, so they are not taken into account in the dimensional analysis. In canopy flows, the main parameters that influence the stem drag can be summarized as follows:

$$f_1 \, (C_D, U_b, H, g, S, D, h_v, s, \rho, \mu, \psi) = 0 \tag{4.1}$$

where C_D is the drag coefficient, U_b is the average bulk velocity (i.e., Q/A), H is the flow depth, g is the gravitational acceleration, S is the channel slope, D is the stem diameter, h_v is the stem height, s is center to center spacing between two adjacent stems, ρ is the density of water, μ is the dynamic viscosity of water, and ψ is the dimensionless coefficient that defines the type of staggering pattern (e.g., regular triangular or regular square staggering pattern) (Kothyari et al., 2009). In this functional relation, only the drag coefficient is the dependent variable, so the rest of the other parameters are defined as independent parameters. Liu et al. (2021) stated that turbulence produced by vegetation dominates the total turbulence inside the canopy. In emergent vegetation flows, this turbulence is mainly generated within stem wakes under sufficient stem Reynolds number. Also, it was stated that the integral length scale of turbulence is defined as min$\{D, s_n\}$ where s_n is the surface to surface distance of two neighbor stems (Tanino & Nepf, 2008b). In the present study, the stem diameter is always less than spacing s_n so that the stem diameter can be considered as turbulence length scale. In other words, the length scale which governs the turbulence in the canopies is the stem diameter for the present study. Therefore, the stem diameter is selected as the characteristic length for canopy flows in the present study. Consequently, among independent variables, ρ, U_b and D are selected as repeating variables representing the fluid, flow and geometrical properties, respectively.

If Buckingham Pi Theorem is performed for the aforementioned functional relationship by considering that C_D, S and ψ are dimensionless variables, the following relation will be obtained.

$$C_D = f_2 \left(\frac{H}{D}, \frac{gD}{U_b{}^2}, S, \frac{h_v}{D}, \frac{s}{D}, \frac{\mu}{\rho U_b D}, \psi \right) \tag{4.2}$$

In the present study, ψ can be eliminated from this functional relationship, because only one staggered pattern (i.e., equiangular triangle pattern) was used. Moreover, if further mathematical operations are performed, the final form of the relationship can be achieved as follows:

$$C_D = f_3 \left(\frac{U_b}{\sqrt{gH}}, S, h^*, \lambda, \frac{\rho U_b D}{\mu} \right) \tag{4.3}$$

which means that the drag coefficient is in relation to Froude number, channel slope, submergence ratio h^* (i.e., $h^* = h_v/H$), areal stem density λ (i.e., $\lambda = \frac{\pi D^2}{s^2 \sqrt{3}}$) and stem Reynolds number (i.e., $Re_d = \frac{\rho U_b D}{\mu}$), respectively. This general relation is valid for the submerged canopy flows. On the other hand, in emergent vegetation flows, the stem height should be replaced by flow depth, so the submergence ratio becomes a unit, and it can be removed from the functional relation.

4.2   Design of the Experimental Setup

The design stages of the experimental setup are explained in this part. One of the available open channel setups was renewed and modernized in METU Hydraulics Laboratory for the present study. Experiments were decided to be conducted in a tilting flume to create different hydraulic scenarios by changing the slope of the flume and discharge ratios. Discharges were measured by a V-notch weir placed at the end of the side channel in the previous experimental setup. Also, it was known from past experiences that electromagnetic flowmeters have higher accuracy than

weirs or portable ultrasonic flowmeters. Thus, a new electromagnetic flowmeter having $\pm 0.5\%$ accuracy was decided to be used in experiments.

The tilting flume having a large slope capacity (i.e., $0<S<0.05$) is 12 m in length, 1 m in width and 0.45 m in height. The sidewalls of the flume were made of plexiglass which makes the observations possible. To minimize the effect of bed shear stresses on the flow resistance, plexiglass material that provides a smooth boundary was selected to cover of the channel base. Moreover, plexiglass is not only water resistant but also user-friendly material which makes it preferable to other materials such as wood, steel and concrete. A wired mesh fence and floating raft were planned to be placed to eliminate excess energy and fluctuations of water in the head tank.

The position of vegetation stems is generally random along the river in nature and have been idealized by linear (i.e., aligned or in-line) or staggered pattern in most of the laboratory studies which investigate the flow resistance (e.g., Ishikawa et al., 2000; Stone & Shen, 2002; Kothyari et al., 2009; Mulahasan & Stoesser, 2017; van Rooijen et al., 2018 and D'Ippolito et al., 2019). However, it was stated that pattern distribution is effective on the flow resistance, and staggered pattern generates more resistance than the linear pattern (Li & Shen, 1973; Schoneboom et al., 2011) where the sheltering effect on vegetation stems is more pronounced (Etminan et al., 2017; Liu et al., 2020). On the other hand, it was observed that the spatially averaged drag coefficients of vegetation arrays having random distribution or staggered pattern are close to each other (Cheng & Nguyen, 2011; Kim & Stoesser, 2011). Thus, a staggered pattern can be used as a practical and rational approach to representing the actual flow resistance of vegetation in nature. Some staggered pattern types have been used in experimental studies such as regular square (Stone & Shen, 2002; Liu et al., 2008; Cheng & Nguyen, 2011) or triangular (Kothyari et al., 2009) depending on the spacing between stems as shown in Figure 4.1. Furthermore, two different arrangements commonly used in engineering applications are aligned and regular

equilateral triangle (Zdravkovich, 1987). Hence, in the present study, the triangular (equilateral) staggered pattern was selected to be used in experiments.
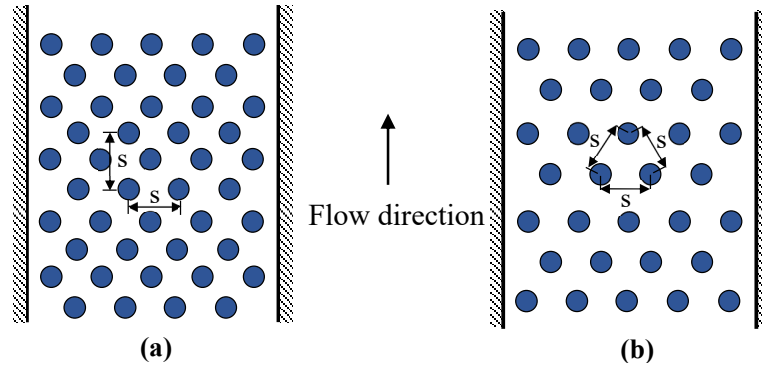
Figure 4.1. a) Staggered regular square pattern b) Staggered regular triangular pattern

In nature, there are two types of vegetation in terms of stiffness flexible and rigid. While some plants may include leaves or branches, others may be composed of only the main trunk. The diameter (i.e., size) of the main trunk can also be varied with the height of the plant. All these vegetation characteristics play a crucial role in the determination of flow resistance. For instance, Fathi-Maghadam and Kouwen (1997) stated that there is a linear relation between the drag force and square of mean velocity as was in the drag force equation for rigid emergent stems. On the other hand, for flexible emergent plants, it was found that the flexibility of the stem leads to a linear relationship between the drag force and velocity which results in a decrease in the drag coefficient with increasing velocity. Similar conclusions were drawn in the study of Armanini et al. (2005), and it was also mentioned that the effect of foliage on total flow resistance is significant.

Most of the previous laboratory studies usually used rigid vegetation stem with a small diameter to imitate aquatic vegetation canopy. For instance, Nepf (1999), Ghisalberti and Nepf (2006), Tanino and Nepf (2008a), Liu et al. (2008) and van Rooijen et al. (2018) preferred to use 0.0064 m diameter, corresponding to the stem

diameter of cordgrass (van Rooijen et al., 2018), in their experiments. However, vegetation stem with larger diameter can also be encountered in nature. Herein, trees usually encountered in the floodplain of rivers can be given as an example. Moreover, Armanini et al. (2005) used a plant named Salix Alba with an average diameter between 0.015 and 0.02 m is commonly available in watercourses in their experiments. Hence, considering its practical applicability and availability in the markets, it was decided to use rigid plastic smooth pipes having a uniform outer diameter of 0.0208 m to mimic vegetation stems in the present study. Moreover, the heights of vegetation stems were selected as 35 cm and 5 cm for emergent and submerged vegetation cases, respectively.

After selecting stem diameter, stem height and array pattern, previous studies were investigated comprehensively to determine another vegetation characteristic, areal vegetation density λ. In the literature, unlike lower vegetation density, denser vegetation cases have been usually studied by researchers (e.g., Tanino & Nepf, 2008a; Kim & Stoesser, 2011; van Rooijen et al., 2018, Wang et al., 2019). Zhang et al. (2021) stated that comparatively few studies focus on flow resistance in sparsely vegetated areas with stem-type and woody vegetation. Moreover, Kothyari et al. (2009) stated that the floodplains of Sandai River in Japan include vegetation having a density of less than 0.05 (i.e., $\lambda \leq 0.05$). Thus, four relatively sparse vegetation densities, λ=0.00436, 0.00981, 0.01744 and 0.03921, were decided to be used in the present study. These areal densities were obtained by changing of center to center distance between cylinders (s=30, 20, 15 and 10 cm) as shown in Figure 4.1b.

Many experimental studies have been performed in the literature to measure flow resistance due to vegetation drag. As mentioned in Chapter 2, there are two ways to measure the drag force in experimental studies called indirect and direct methods. Most of the studies used energy slope or free surface gradient of uniform or non-uniform flows to calculate the drag coefficient indirectly using the force balance

equation (e.g., Nepf, 1999; Stone & Shen, 2002; Tanino & Nepf, 2008a; Cheng & Nguyen, 2011; Mulahasan & Stoesser, 2017; Zhang et al., 2018). On the other hand, relatively few studies (e.g., Fathi-Maghadam & Kouwen, 1997; Ishikawa et al., 2000; Armanini et al., 2005; Callaghan et al., 2007; Kothyari et al., 2009; Schoneboom et al., 2011; van Rooijen et al., 2018) determined drag coefficient by measuring the drag force directly due to the requirement of more complex mechanisms and equipment such as load cells, strain gauges or force sensors. Furthermore, van Rooijen et al. (2018) stated that the accuracy (in percent) in the measurement of free surface gradient decreases for the low flow cases, and it causes a significant discrepancy (i.e., 22%) between the results of direct and indirect methods. Therefore, direct measurement methods provide more precise results using high device performance in these cases and are recommended. All of the studies mentioned above using the direct method measured the drag force acting only on a single stem. However, Schoneboom et al. (2011) stated that the average drag force acting on a vegetation array can not be represented by the drag measurement of the single stem which can diverge from average drag up to 23% in a staggered pattern. Although few studies (e.g., D'Ippolito et al., 2019) have a mechanism that can measure the drag force on emergent vegetation array directly, their mechanism is not applicable to be used in submerged vegetation cases due to their way of design. However, in nature, the flow conditions of rivers can show a discrepancy from season to season, and the variation in flow conditions causes a change in flow depths. In addition, the heights of some plants can increase along with the onset of a growing season. These flow and vegetation conditions determine whether the plant will be submerged. In other words, emergent and submerged vegetation conditions are frequently encountered in rivers. In the result of a comprehensive literature review, it was seen that there is only one study able to measure drag forces acting on both submerged and emergent vegetation array was carried out by Tinoco and Cowen (2013).

A novel drag plate mechanism able to measure drag forces directly for both emergent and submerged rigid vegetation arrays was developed to satisfy all these aforementioned design requirements. At the beginning of the design, a car-type drag plate having four roller bearings at each side was designed. However, it was seen from preliminary tests that there was a significant friction larger than expected between roller bearings and smooth plexiglass roadway, so this design was canceled out. After many trial and error procedures, it was seen that there is the only way to eliminate friction, and this can be achieved by breaking contact with the drag plate with the ground. Herein, a solution was developed inspired by the simple pendulum's motion. Thus, it was decided to hang the drag plate with fish lines having a too small thickness (≈ 0.5 mm) not to affect the flow above it. Furthermore, the dimensions of the drag plate were determined as 0.905 m in length and 0.95 m in width, so it includes a sufficient number of vegetation stems to represent the spatially averaged drag coefficient of all canopy at various densities. Contrary to vegetation patches in short length, a larger part of the channel (i.e., the last 7 meters) was allocated for placement of the vegetation array. The drag plate's location was determined so that the plate's back edge coincides approximately with the middle (i.e., center) of the vegetation array to obtain fully developed flow on and around the drag plate. Moreover, a 0.5 cm gap was left between the drag plate and side plates having a 2 cm width to prevent friction as shown in Figure 4.2.
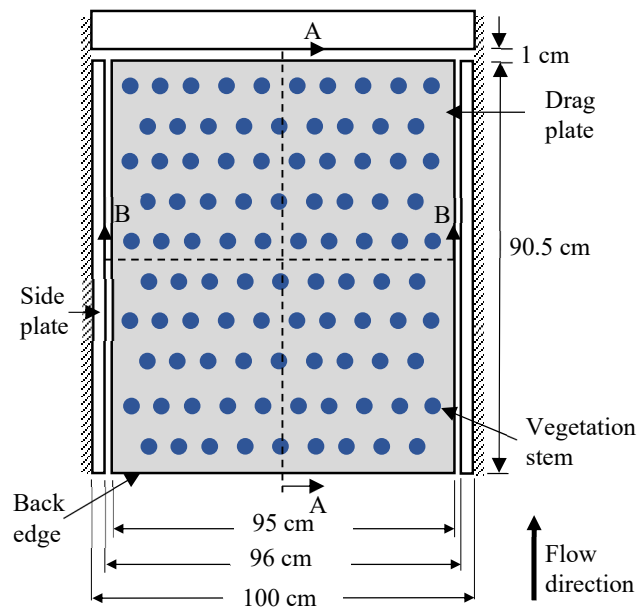
Figure 4.2. Plan view of the drag plate

Before placement of the drag plate, four roller bearings with a 2 cm outer diameter corresponding to corners were fitted horizontally on slats using nut bolts as shown in Figure 4.3a which depicts the relevant mechanism. Moreover, four feet made of plexiglass were placed under the drag plate in a way that they come into contact with corresponding roller bearings from their inner side as demonstrated in Figures 4.3b and 4.3c corresponding to sections A-A and B-B in the previous figure, respectively. While these bearings and feet prevent lateral movement or rotation of the drag plate in the horizontal plane, they allow the motion of the plate only in the flow direction. Also, in the preliminary experiments, it was observed that the weight of the drag plate having a 2 cm thickness was not heavy enough to stay submerged. Thus, it was decided to place four small steel plates having a 0.5 cm thickness uniformly under the drag plate.
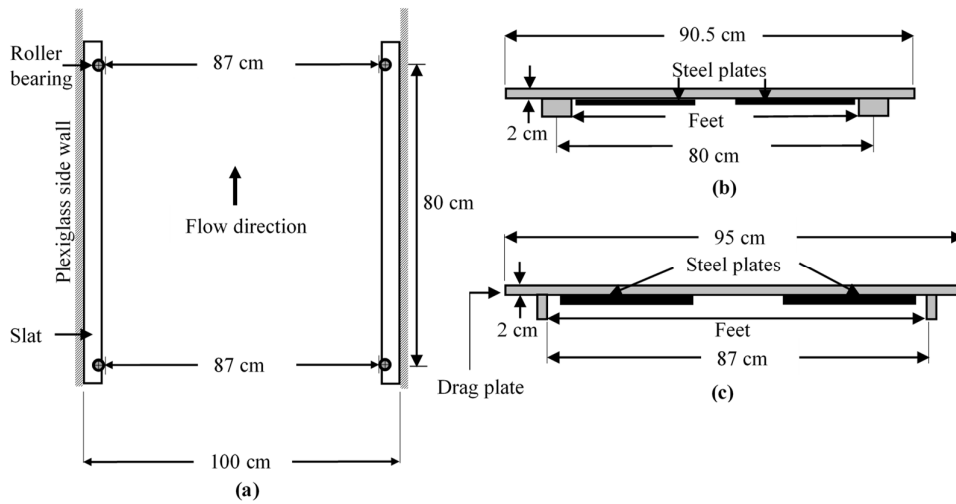
Figure 4.3. a) Mechanism underneath the drag plate b) Longitudinal (A-A) section of the drag plate c) Transverse (B-B) section of the drag plate

Moreover, 2D drawings of pulleys from different perspectives were prepared to be used in CNC machine for production. Finally, the drag plate was hung from its corners to two steel bars which can rotate through their axis to adjust the level of the back and front edges of the drag plate as demonstrated in Figure 4.4.
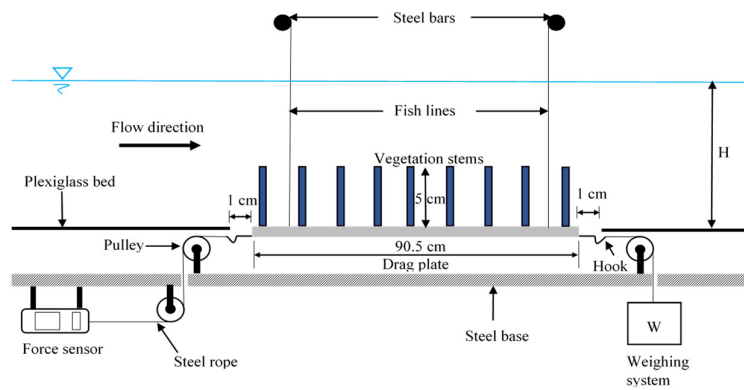
Figure 4.4. Side view of the drag plate and rope-pulley mechanism

4.3   Construction of the Experimental Setup

In this subsection, the construction steps of the new experimental setup are explained in detail. As mentioned in the previous subsection, discharges had been measured using a V-notch weir placed end of the side channel in the previous experimental setup, and there was no flow measurement instrument on the pipeline. Therefore, a new electromagnetic flowmeter was mounted on a long straight pipeline with nearly 30 cm diameter to get more accurate measurements as recommended in the installation manual. Some parts of an old experimental setup were removed to start construction. The base of the channel made of steel was painted with a dye having an antirust feature. The condition of the side plexiglass walls seems reasonable, so they did not undergo any repair. Before starting construction, the tilting flume was horizontally adjusted using a screw jack. Afterward, L-shaped foots made of plexiglass were put on both sides of the channel using a total station device to accurately increase the bed level of the channel by 8 cm above the steel base. According to pre-inspection, an 8 cm vertical distance between the steel base and the new bed level is sufficient to place a rope-pulley system. It was decided to use plexiglass plates as the base material to provide a smooth flow boundary. Furthermore, longitudinal and transverse guidelines were plotted on these plexiglass plates, and the intersection of guidelines which represents the center of each vegetation stem was marked with a waterproof marker. Plexiglass plates have 1 cm thickness and were strengthened by supportive slats placed beneath these plates to carry water weight without bending. Later, these plates were placed using screws and silicon onto L-shaped feet along the channel except around the drag plate part. While the construction of the channel was proceeding, vegetation stems imitated by rigid plastic pipes with an outer diameter of 2.08 cm were prepared. For each vegetation condition (i.e., emergent and submerged), 769 pieces of the pipe segment corresponding to the number of vegetation stem in the densest case of vegetation (i.e., λ=0.03921) were prepared. Afterward, ordered steel pulleys were installed on

39

the mid-width of the steel base by adjusting their heights and positions. With these adjustments, it was prevented that steel ropes make any angle in horizontal and vertical directions, so the force on the drag plate can be directly transferred to the force sensor. As mentioned before, small steel plates were placed under the drag plate to avoid floating off it. However, it was seen in preliminary tests that these steel plates lead to the bending of drag plate in longitudinal and transverse directions. Therefore, the drag plate was re-constructed by adding an extra plexiglass plate on an existing one to prevent bending by increasing the moment of inertia. Finally, rigid plastic pipe segments (i.e., vegetation stems) were glued to the plexiglass base tightly using silicon in a way that they do not sway with the flow action as shown in Figure 4.5.

Figure 4.5. Placement of rigid vegetation stems for emergent and submerged cases

Moreover, Figure 4.6 demonstrates the final form of the experimental setup in detail.
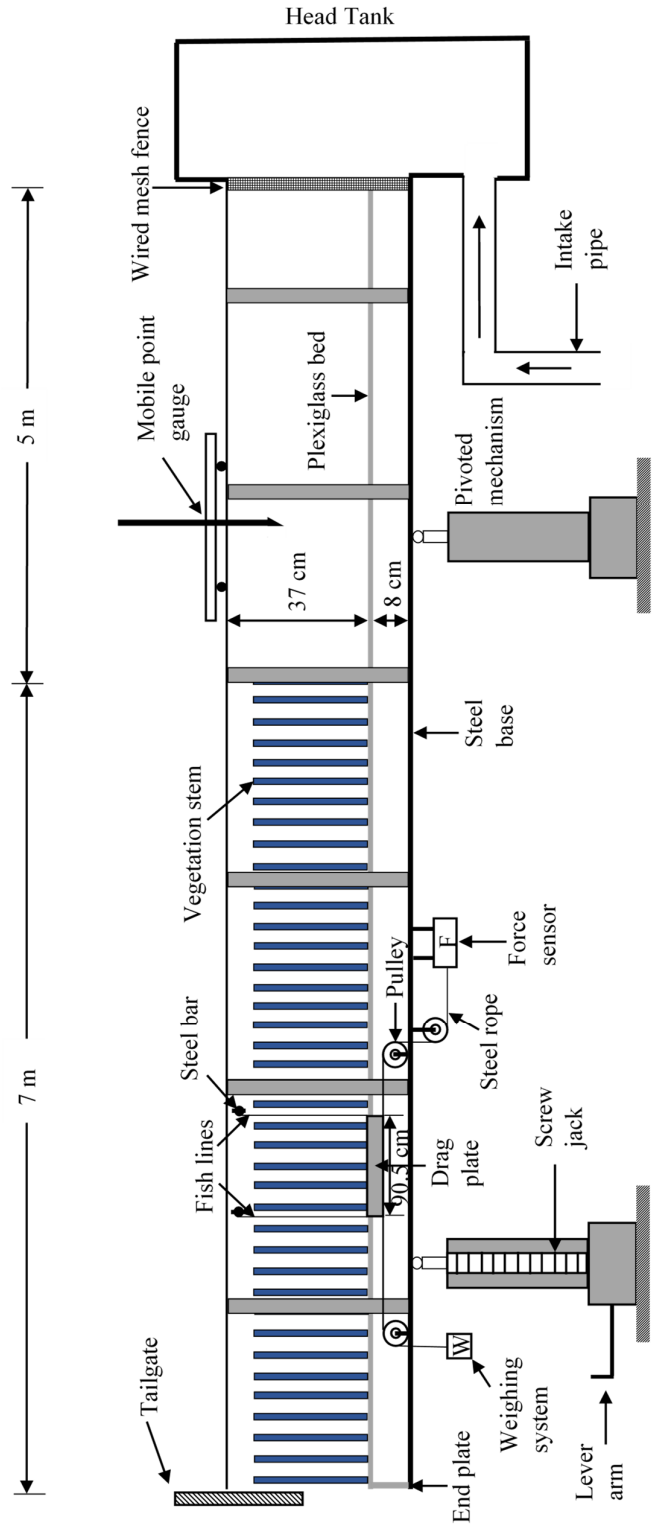
Figure 4.6. Final form of the experimental setup

41

4.4   Experimental Methodology

Before starting the experiment, the tilting flume's slope is adjusted to a pre-determined value (i.e., S=0.0025, 0.005 and 0.01). Also, an inspection is performed to check the flume and drag plate mechanism conditions. After that, the pump, which supplies water from the sump to the upper reservoir, is activated. When the upper reservoir is filled, it starts to discharge excess water to prevent overtopping. Thus, experiments are conducted under constant water head. Firstly, a tailgate is closed and the flume is filled with water having a very low discharge. Then, a valve is closed to stop the filling process. Meanwhile, a calibration process of the drag plate is performed with known weights using a weighing system. Some weights are left on the weighing system to create pre-tension in steel cables, which prevents buckling. Later, the force sensor is reset, so it is ready to measure the forces acting on the drag plate. The force on the drag plate was measured with PCE-DFG N 200 force sensor with 0.1% accuracy and 0.1 N resolution. Experiments started with the lowest discharge, and the discharge is increased by nearly 10 lt/s for each step. In some experiments, the tailgate was totally opened to provide lower depths and higher velocities. The tailgate is partly closed to obtain higher depths and lower mean velocities or increase the submergence. Each experiment set includes 5 or 6 different discharge values. Some illustrations from runs are demonstrated in Figure 4.7 for vegetation densities λ=0.03924 and λ=0.00436, respectively.
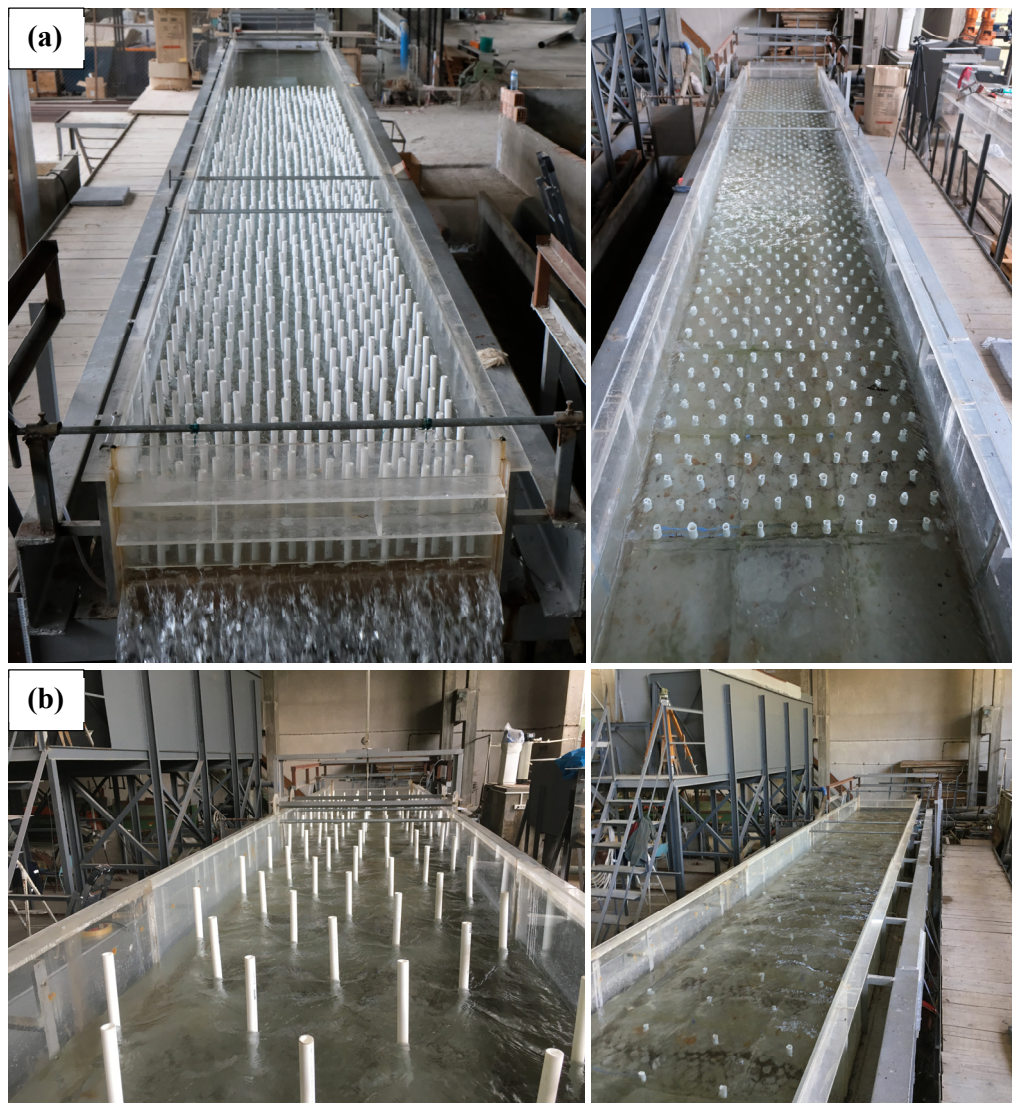
Figure 4.7. Illustrations from some of the experiment runs in emergent and submerged condition for a) λ=0.03924, b) λ=0.00436

The force and discharge values are noted when the steady state condition is reached. Furthermore, water depths are measured throughout the center of the flume using a mobile point gauge having ± 1 mm accuracy at stations placed with a meter interval.

Above the drag plate; however, flow depths are measured at three stations having a 30 cm interval, and an average of these depths are used in computations and analyses. Due to the interaction of flow and vegetation stems, flow depths change along the flume in some cases (e.g., lower depths, steeper slopes and sparser stem distribution); however, uniform flow condition was almost obtained above the drag plate in most of the experiments. Manometer readings are also taken at every meter of the flume. During the experiments, the drag plate's straightness and elevation are checked from the back and front edges to ensure that it does not protrude above the actual bed level. Also, it was seen that the back and forward movement of the drag plate under hydrodynamic forces is very restricted due to the pre-tension of steel rope so that it does not contact the rear and front plates during the experiment. Once the experiment is finished, the remaining water is discharged by opening drainage holes, and maintenance of the drag plate mechanism is carried out.

CHAPTER 5

NUMERICAL STUDY

In the present section, a detailed description of a numerical model used in the numerical analyses is given. After that, information and illustrations about numerical cases (e.g., computational domain, mesh generation) are provided for emergent and submerged vegetation conditions, respectively.

5.1   Description of the Numerical Model

A numerical part was performed using detached eddy simulation (DES) in the present study. DES has become one of the most prominent techniques between several hybrid Reynolds-averaged Navier-Stokes (RANS) and large eddy simulation (LES) methods in recent years (Chang et al., 2007). Some of the numerical studies used the LES method to evaluate drag forces and to investigate flow characteristics in emergent cylinder arrays (e.g., Stoesser et al., 2010; Kim & Stoesser, 2011; Etminan et al., 2017) in relatively low Re_d numbers (i.e., $500 < Re_d < 1340$) with various areal vegetation densities. However, it was stated that using LES without a wall function (i.e., well resolved) is computationally too expensive to simulate the flows at high Reynolds numbers (Constantinescu et al., 2011; Koken & Constantinescu, 2011). At this point, DES can be considered a better alternative and applicable at high Reynolds numbers (Constantinescu & Squires, 2004). While DES activates RANS mode where the one-equation Spalart-Allmaras (SA) model is used in regions close to the solid boundaries (i.e., in thin attached boundary layers), it runs

in LES mode using Smagorinsky-type subgrid-scale (SGS) model away from solid walls (Spalart, 2000a; Chang et al., 2007).

In DES, a fully implicit fractional-step method is utilized in the integration of Navier-Stokes equations for incompressible and three-dimensional flow (Chang et al., 2007). Moreover, a blend of fifth-order accurate upwind biased and second-order central schemes are used for the discretization of convective terms in the momentum equation to decrease the numerical dissipation level away from solid walls.

A transport equation solved by SA RANS model for the modified eddy viscosity $\tilde{v}$, to generate turbulent eddy viscosity v_t is given below (Koken & Constantinescu, 2011):

$$\frac{\partial \tilde{v}}{\partial t} + u^j \frac{\partial \tilde{v}}{\partial \xi^j} = C_{b1}\tilde{S}\tilde{v} + \frac{1}{\sigma}[\nabla \times ((v + \tilde{v})\nabla\tilde{v}) + C_{b2}(\nabla\tilde{v})^2] - C_{w1}f_w \left(\frac{\tilde{v}}{d}\right)^2 \qquad (5.1)$$

where t is the time, v is the molecular viscosity, u^j is the contravariant resolved velocity, ξ^j is the curvilinear coordinate in the j direction, C_{b1}, C_{b2} and σ are the model constants, d is the turbulence length scale and can be found as (Spalart, 2000b):

$$d = d_{min} + 0.03k_s \qquad (5.2)$$

where d_{min} and k_s are the distance to the nearest wall and equivalent roughness height, respectively. Also, $\tilde{v}$ and k_s should be set to zero for smooth boundaries (Chang et al., 2017).

Another model constant C_{w1} is defined as:

$$C_{w1} = \frac{C_{b1}}{\kappa^2} + \frac{(1+C_{b2})}{\sigma} \qquad (5.3)$$

where κ is von Karman constant. Also, $\tilde{S}$ is the magnitude of vorticity and given as follows:

$$\tilde{S} \equiv S_r + \left(\frac{\tilde{v}}{(\kappa d)^2}\right)f_{v2} \qquad (5.4)$$

where $f_{v2} = 1 - \frac{\tilde{v}}{(v+\tilde{v}f_{v1})}$ and S_r is the strain rate.

The turbulent eddy viscosity v_t is computed from;

$$v_t = \tilde{v}f_{v1} \tag{5.5}$$

The functions (f_{v1} and f_w) shown in the above equations are stated below:

$$f_{v1} = \frac{\chi^3}{\chi^3 + C_{v1}^3} \text{ and } f_w = g_f \left[\frac{1 + C_{w3}^6}{g_f^6 + C_{w3}^6} \right]^{\frac{1}{6}} \tag{5.6}$$

where $\chi = \frac{\tilde{v}}{v} + 0.5\frac{k_s}{d}$, $g_f = r + C_{w2}(r^6 - r)$, $r \equiv \frac{\tilde{v}}{\tilde{S}\kappa^2 d^2}$,and C_{v1}, C_{w2}, C_{w3} are the model constants.

The numerical values of the all model constants are given Table 5.1.

Table 5.1 The model constants and their value used in the transport equation

The model constant	Value
C_{b1}	0.135
C_{b2}	0.622
C_{v1}	7.1
C_{w2}	0.3
C_{w3}	2.0
σ	0.67
κ	0.41

To formulate the SA type of DES, the turbulence length scale, d, in the destruction term of the transport equation for modified eddy viscosity is changed with another length scale, d_{DES} that is defined as (Koken & Constantinescu, 2011; Chang et al., 2017):

$$d_{DES} = \min (d, C_{DES}\Delta) \tag{5.7}$$

where Δ is local grid spacing and $\Delta \equiv \max(\Delta x, \Delta y, \Delta z)$ (Constantinescu & Squires, 2004).

In the previous relation, C_{DES} is a model parameter that controls the transition from RANS mode to LES mode (Koken & Constantinescu, 2021). An optimal value of C_{DES} was found to be 0.65 in the study of Constantinescu and Squires (2004).

The numerical model used in the present study was validated many times by comparing the results with experimental data adopted from several experimental studies. For instance, Chang et al. (2017) investigated the effect of main geometrical parameters on flow and turbulence structures formed by circular patch having emergent cylinders and the distribution of drag forces acting on these cylinders. The longitudinal streamwise velocity profile and root mean square (i.e., RMS) of the lateral velocity fluctuations along the centerline of the circular patch were compared with those of Zong and Nepf (2011) and Chen et al. (2012). It was stated that there is a good agreement between the DES model's result and the aforementioned experimental studies. In addition, Koken and Constantinescu (2021) performed a numerical study using the DES model to examine the flow structures inside and around the rectangular emergent vegetation patch near the channel sidewall. The results of the numerical model were compared with those of White and Nepf (2007) by considering dimensionless spanwise profiles of streamwise velocity and Reynolds stresses at half of the flow depth to validate the numerical model. It was noted that although there are some discrepancies between arrays of numerical and experimental studies, there is a consistency between the results. Therefore, it can be stated that the numerical model can be used to validate the novel experimental setup results in the present study.

5.2   Dimensional and Physical Properties of Computational Domains in the Numerical Analysis

This section presents information about the computational domains of emergent and submerged vegetation cases separately. Several meshing strategies were tried for each case to find the most effective solution and to reduce computational costs. However, when the number of stems in different cases is considered, it is known from previous experiences that even a high-performance single computer (i.e., workstations) can not solve this type of computation domain in less than nearly two months. Thus, it was decided to use TRUBA resources that were included in TUBITAK ULAKBIM High Performance and Grid Computing Center. However, sometimes, there may be a long queue in the TRUBA platform due to the demand of other users, especially in a single partition (i.e., partition for codes based on single-core) where some of the steps in the post-process were performed in the present study, which may also postpone the finish time of all procedures. Luckily, the DES code can be executed with a parallel-computing option (valid for nodes in x and y directions) which reduces the total time required to complete the analysis. Therefore, 64 cores were utilized to execute the DES code for each simulation case. TRUBA platform provides limited spacing for each user to store the program and solution outputs. Thus, it was decided to generate domains such that the total cell amount is not greater than 28-30 million in each case to restrict computation time and size of output files. One of the commercial mesh generator programs was used to generate meshes for each case. An expansion ratio, defined as the ratio of edges of adjacent cells (i.e., the ratio of larger edge to smaller one) in a given direction, was always maintained below 1.3 considering the mesh quality of the domain as recommended by Franke et al. (2007). The grid distribution was performed using hyperbolic tangent, tanh, function. Moreover, Thomas-Middlecoff interior control functions were applied to required regions to improve grid quality. The flow depth 'H' is selected as the length scale so that geometrical parameters of the experimental setup

49

(i.e., diameter and spacing of stems, channel width and length of the vegetation array) are normalized with H in the mesh generator program. The width and length of the straight channel are 7.33H and 74H, respectively. In simulations, a pressure gradient was applied in the flow direction to maintain the flow with a certain velocity. The vegetation array is placed after 8H from the inlet to ensure that an approaching flow is fully developed as in the studies of Koken and Constantinescu (2009) and Koken and Constantinescu (2021). The diameter of the plant stem and length of the vegetation array are 0.153H and 51.28H, respectively. Experiments conducted in the mildest slope (i.e., S=0.0025) are selected to be simulated in the numerical analysis where the channel bed is horizontal. The cylinders that are placed over the drag plate are shown in green color in the following figures. Moreover, the bulk velocity, U_b (i.e., mean velocity), is used as the velocity scale in every simulation. In each simulation, the shear (i.e., friction) velocity, U_*, is calculated by assuming U_*/U_b=0.04 as in the previous studies (e.g., Constantinescu & Squires, 2004; Koken & Constantinescu, 2009; Koken & Constantinescu, 2011). All solid surfaces (i.e., channel bed, side walls and cylinder surfaces) are designed as smooth boundaries where no-slip boundary condition was imposed. Similar to the previous studies (e.g., Etminan et al., 2017), a rigid lid assumption was also applied to the free surface where vertical velocity is zero. Furthermore, at the outlet section, a convective boundary condition was imposed which provides the coherent structures to leave the domain in a time-accurate way without generating unrealistic oscillations (Koken & Constantinescu, 2008). On the other hand, a precursor RANS simulation was performed in a straight and unobstructed channel (i.e., H in height, 10H in length and 7.326H in width) with periodic boundary conditions in the flow direction to provide the velocity fields having resolved turbulent fluctuations that are used at inflow section of the DES similar to previous studies in the literature (Kirkil & Constantinescu, 2009; Chang et al. 2017, 2020). This standard procedure decreases the computational domain length and ensures that the inflow is turbulent and fully developed (Rodi et al., 2013; Chang et al., 2020). The time step used in each

simulation was $0.025H/U_b$. Totally, the DES code ran for nearly 124000 core hours to solve computational domains of seven cases according to TRUBA platform output. 17000 iterations were performed in each numerical solution. To check whether the solution reached a statistically steady state condition, another simulation, except for 7 cases, was run with nearly 50% more iterations for one of the cases. It was seen from the comparison of these two cases that the difference between spatially averaged drag coefficients of vegetation array situated on the drag plate is found to be less than 1%. Therefore, it can be stated that all solutions are in a statistically steady state condition.

5.2.1   Emergent Vegetation Cases

As stated previously, each numerical scenario originated from some of the experimental cases conducted in the laboratory and is presented in Table 5.2. Three different cases having the same depth were selected to be simulated in numerical analyses to investigate the bed shear stresses, the drag forces and flow characteristics.

Table 5.2 Main flow characteristics for each emergent vegetation case

Case	λ	s (cm)	Experimental Data		Numerical Application		
			H (m)	U_b (m/s)	H (m)	U_b (m/s)	Re_{db}
E10	0.03924	10	0.1365	0.296	0.1365	0.296	6157
E20	0.00981	20	0.133	0.522	0.1365	0.522	10865
E30	0.00436	30	0.1365	0.588	0.1365	0.588	12230

Herein, the name of the cases was given such that letter and number represent the vegetation condition (i.e., emergent) and spacing between vegetation stems (in cm), respectively.

5.2.1.1 Case E10

In the present case, the geometrical properties of the channel are presented in Figure 5.1, where the origin of the Cartesian coordinate system and domain is demonstrated with a legend at the lower right. The streamwise, spanwise and vertical directions are represented by the x, y and z-axis, respectively.
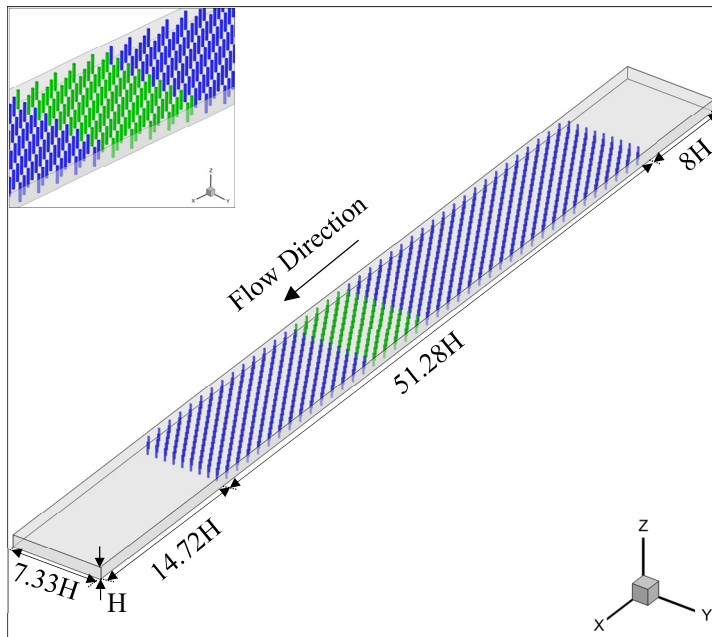
Figure 5.1. Dimensions of the channel in 3D view for Case E10

Other geometrical features of the domain related to vegetation characteristics (i.e., diameter, spacing between stems) are illustrated in Figure 5.2 with the top and longitudinal view of the channel part corresponding to the drag plate region.
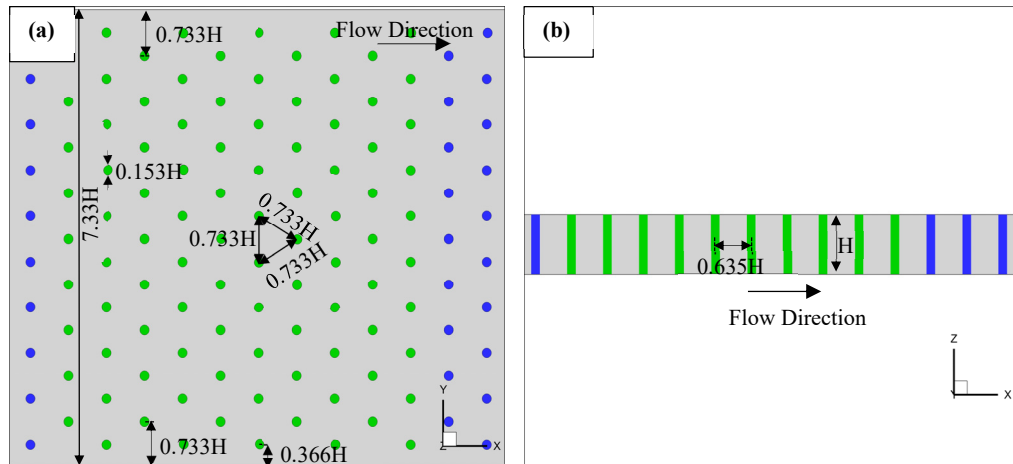
Figure 5.2. Dimensions related with vegetation characteristics for Case E10 in a) top view and b) side view

There are 857153 and 24857437 cells (i.e., 2688x320x30 grid points in x, y and z direction) in 2D (i.e., horizontal mesh) and 3D computational domains, respectively. The mesh was refined inside the vegetation array compared to regions without vegetation (i.e., inflow and outflow sections). In mesh generation, a rectangular pattern around the single stem surrounded by red lines as shown in Figure 5.3a was constructed and used as a sample to create all vegetation domains. The meshing strategy followed on and around the single stem and the vegetation array is demonstrated in Figure 5.3 with 2D and 3D views.
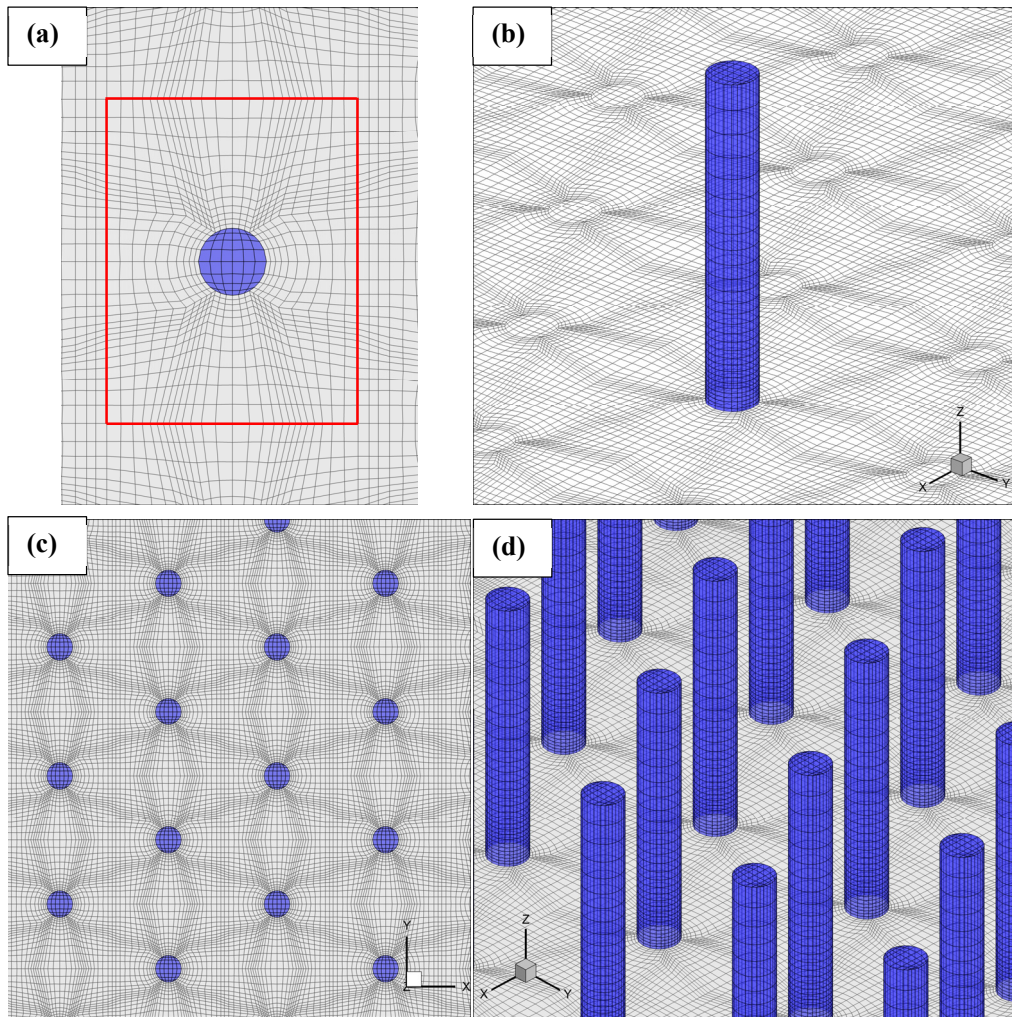
Figure 5.3. Mesh pattern on and around the single stem with a) 2D view,
b) 3D view and the vegetation array c) 2D and d) 3D view

The simulation was performed with $Re_{db}=6157$, larger than the critical cylinder Reynolds number ($Re_d \approx 120$), which is a threshold value for the formation of vortex shedding in the wakes of the cylinders situated at and closer to the front of the array (Koken & Constantinescu, 2021). Also, the channel Reynolds number based on the bulk velocity and flow depth, $Re_H=U_bH/\nu$, is $Re_H=40404$.

5.2.1.2 Case E20

The dimensions of the channel and arrangement of vegetation stems are given in Figure 5.4. As mentioned earlier, the numerical cases of emergent vegetation are selected from the experimental runs with the same flow depth so that the dimensions of the channel are the same as each other in all cases.
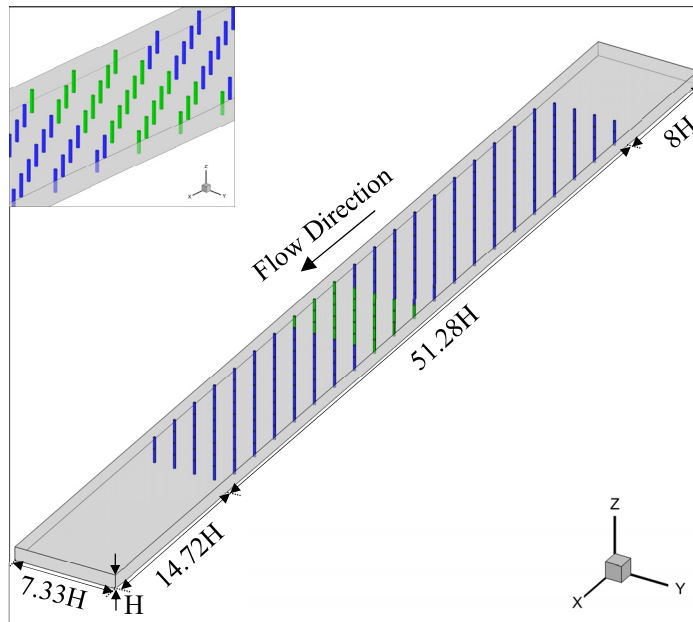
Figure 5.4. Dimensions of the channel in 3D view for Case E20

Vegetation characteristics in and around the drag plate region are depicted in Figure 5.5 similar to the previous case.
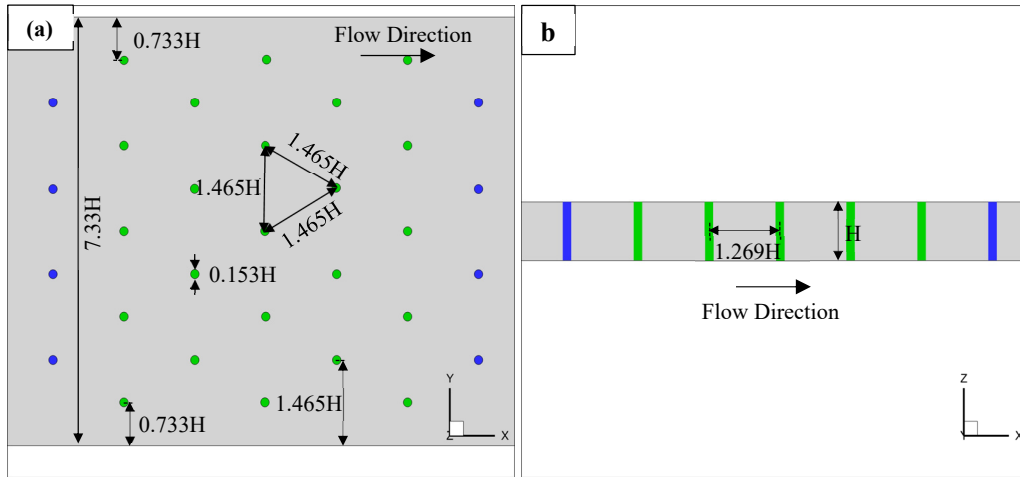
Figure 5.5. Dimensions related with vegetation characteristics for Case E20 in a) top view and b) side view

The 2D and 3D domains of the E20 case include 836737 and 25938847 hexahedron cells (i.e., 2624x320x32 grid points in x, y and z directions), respectively. Although the number of stems in the E20 case is lower than that of E10 case, the number of cells in both cases is close to each other. This is due to the fact that an average expansion ratio was used in the E20 case is less than that in the E10 case to refine grids, thus improving the mesh quality further. Furthermore, numerical runs were carried out with stem and channel Reynolds numbers corresponding to Re_{db}=10865 and Re_H=71253, respectively.

Similar to the previous case, a rectangular pattern that encloses the single stem with red lines, as shown in Figure 5.6a, was produced and used to generate meshes in the vegetation array. The pattern of mesh on and around the single stem and the vegetation array is revealed in Figure 5.6, respectively, with 2D and 3D views.
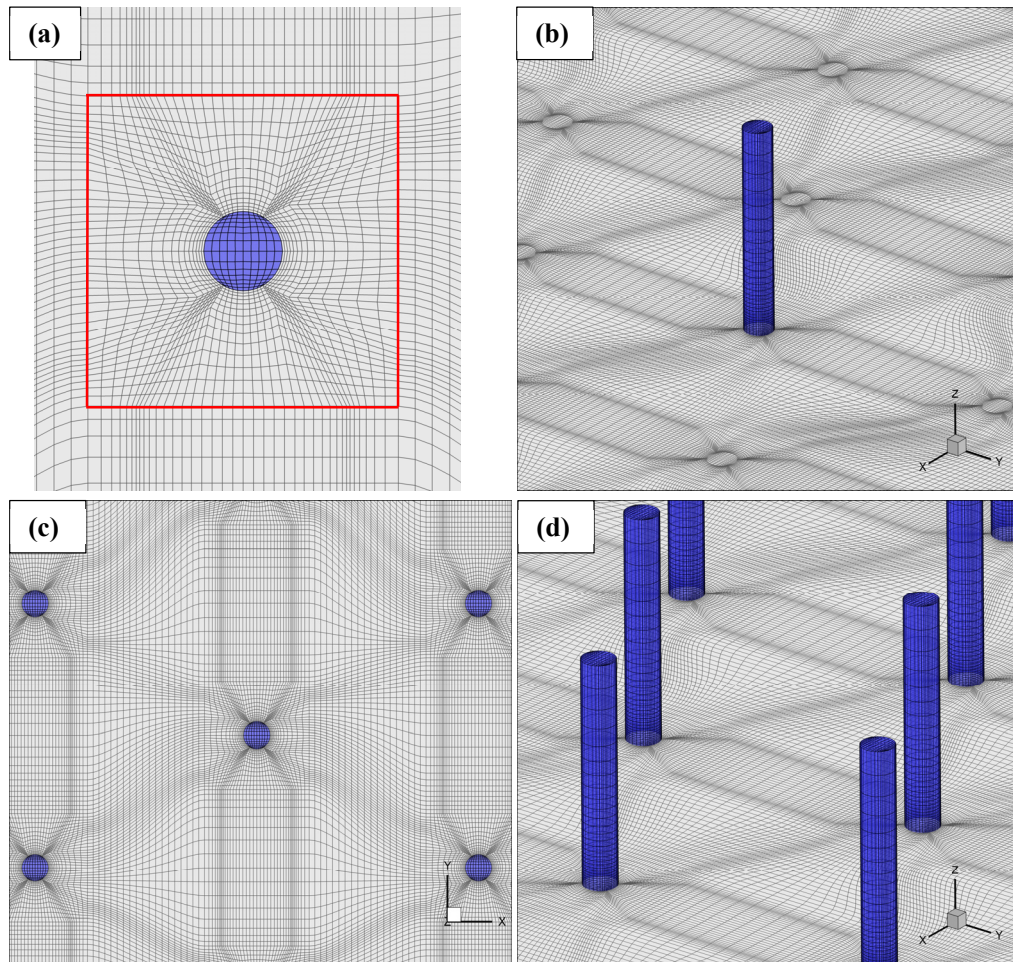
Figure 5.6. Mesh pattern on and around the single stem with a) 2D view,
b) 3D view and vegetation array with c) 2D and d) 3D view

5.2.1.3   Case E30

The dimensional properties of the channel and distribution of vegetation stems are demonstrated in Figure 5.7 for the present case which has a sparser stem distribution than others. As can be seen from Figure 5.7, the same geometrical properties of the channel with the former cases are maintained except for the stem distribution.
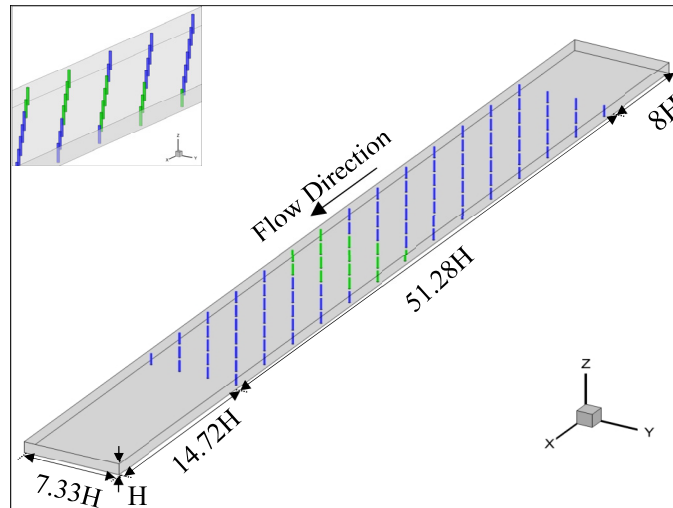
Figure 5.7. Dimensions of the channel in 3D view for Case E30

The distribution of vegetation stems is uniform along the channel. Therefore, the spatial properties of the vegetation stem on the drag plate which represent those of the whole channel are presented in Figure 5.8 with top and longitudinal views, respectively. Simulations were performed with stem and channel Reynolds numbers corresponding to $Re_{db}=12230$ and $Re_{H}=80262$, respectively.
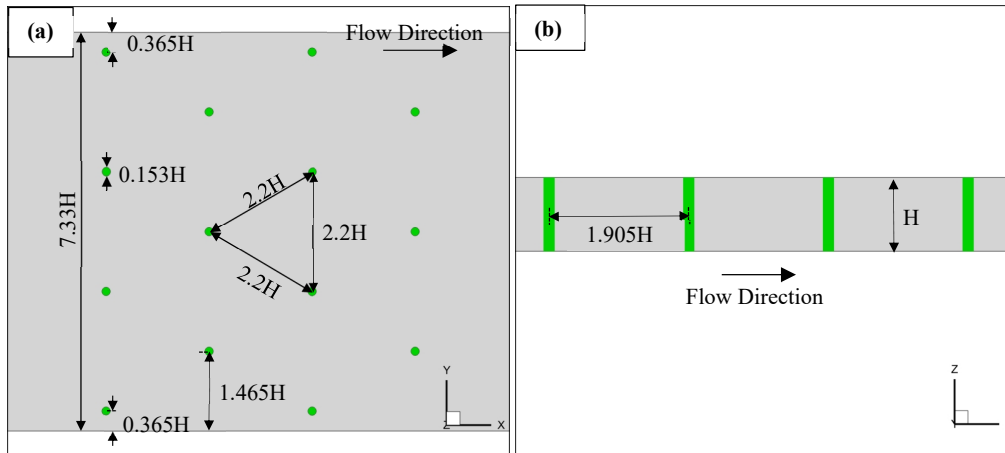
Figure 5.8. Dimensions related with vegetation characteristics for Case E30 in a) top view and b) side view

The computational domain of the E30 case has 938817 and 27225693 cells (i.e., 2944x320x30 grid points in x, y and z directions) in 2D and 3D, respectively. As stated in the previous subsection, a lower stem number gives a chance to obtain finer mesh that enhances the mesh quality further by reducing the average expansion ratio. A rectangular grid pattern around the single cylinder shown in Figure 5.9a was generated as a sample unit to construct meshes in the vegetation array. Mesh patterns on and around the single and grouped vegetation stems are demonstrated by 2D and 3D views in Figure 5.9.
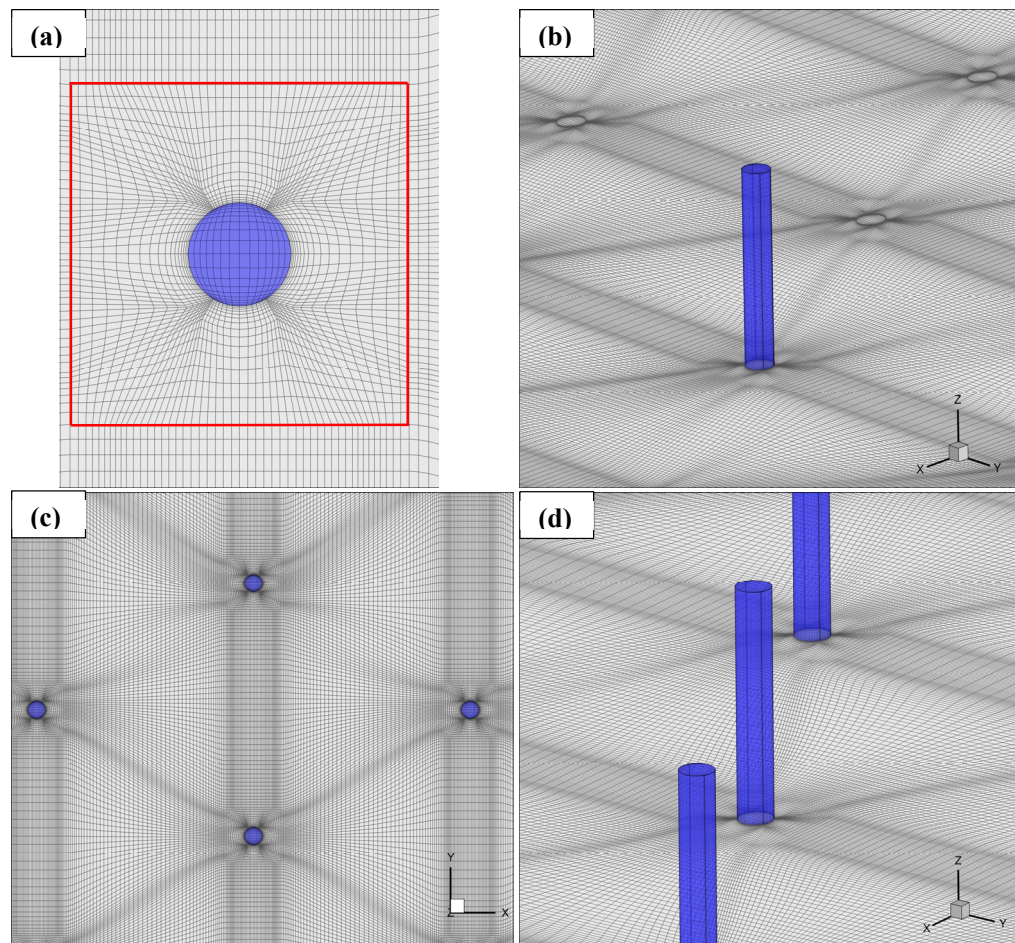
Figure 5.9. Mesh pattern on and around the single vegetation with a) 2D view b) 3D view and vegetation array with c) 2D and d) 3D view

5.2.2   Submerged Vegetation Cases

The submergence ratio, $h^*=h_v/H$, is one of the important parameters that determines which vegetation condition (i.e., submerged or emergent) prevails in the canopy flow. Due to the velocity difference between the surface and stem layers, there is a significant difference in flow characteristics between the emergent and submerged vegetation conditions, that is, the formation of the horizontal shear layer just above the submerged vegetation array. As the height of the vegetation increases, the shear layer characteristics change for the given flow conditions, and the shear layer is totally diminished when the vegetation height is equal to the flow depth (i.e., emergent vegetation condition). Therefore, three numerical scenarios were prepared to investigate the effect of the submergence ratio on the flow resistance and flow characteristics by keeping other flow parameters (e.g., flow depth, stem Reynolds number) and vegetation characteristics (e.g., vegetation density, stem diameter) the same. Contrary to emergent vegetation cases, unfortunately, the submerged vegetation cases simulated in numerical analyses could not be selected from experimental runs, because there are no experimental cases with common vegetation density and stem Reynolds number. Instead, submerged conditions of the E10 case having three different submergence ratios (i.e., $h^*=0.25$, 0.50 and 0.75) were considered to reveal discrepancies in the flow resistance and flow characteristics between submerged and emergent vegetation conditions.

The horizontal (i.e., 2D in the x-y plane) grid pattern of the E10 case was used to construct 3D computational domains in submerged cases. Thus, dimensions related to the vegetation array (e.g., spacing, diameter) and mesh pattern around vegetation stems were not shown with additional figures in the following subsections (see Figures 5.2 and 5.3 for relevant information). Contrary to emergent domains, each submerged domain was divided into two regions in the vertical direction. Thus, in addition to the inside of the array in the x-y plane, finer grid spaces (in the z-direction) were also used in critical regions such as around the top of the vegetation

stems where the shear layer develops. Numerical analyses of submerged vegetation cases were conducted in the same stem and channel Reynolds number with those of the E10 case, $Re_{db}=6157$ and $Re_{H}=40404$. Furthermore, the letter and number in the name of the simulated cases were given in a way that they correspond to vegetation condition and submergence ratio (in percent) (e.g., S25, S50 and S75).

5.2.2.1   Case S25

The geometrical properties of the channel and vegetation stem are demonstrated in Figure 5.10. As mentioned earlier, Figure 5.10a is identical to Figure 5.1 (i.e., corresponding to Case E10) except for the height of vegetation stems.
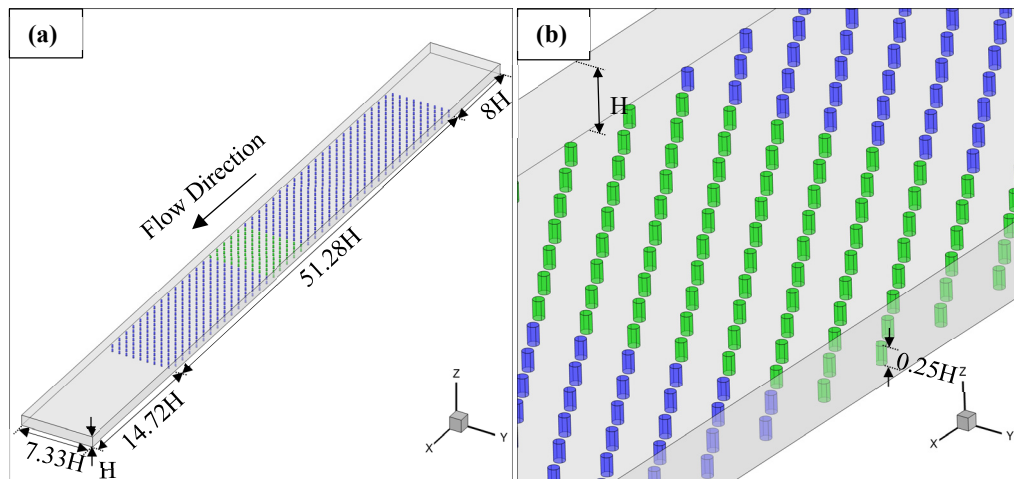
Figure 5.10. a) Dimensions of the channel b) height of the vegetation stems in 3D for Case S25

The computational domain of Case S25 includes 24857437 cells (i.e., 2688x320x30 grid points in x, y and z directions) in 3D. Vertical nodes were distributed in such a way that there are 16 and 14 nodes in the stem and surface layer, respectively. A vertical grid distribution of the domain and the stem is demonstrated in Figure 5.11.
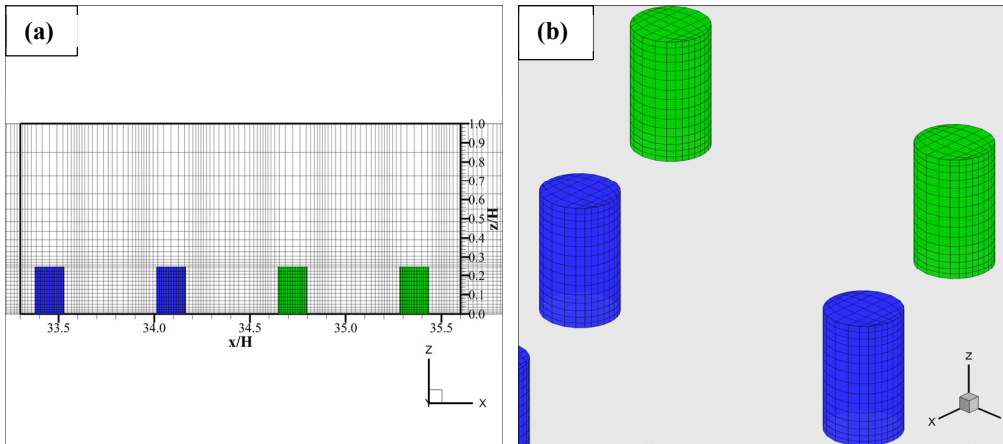
Figure 5.11. Vertical grid distribution on a) x-z plane b) vegetation stem for
Case S25

5.2.2.2   Case S50

Figure 5.12 reveals the characteristic dimensions of the channel and height of the
vegetation stem.
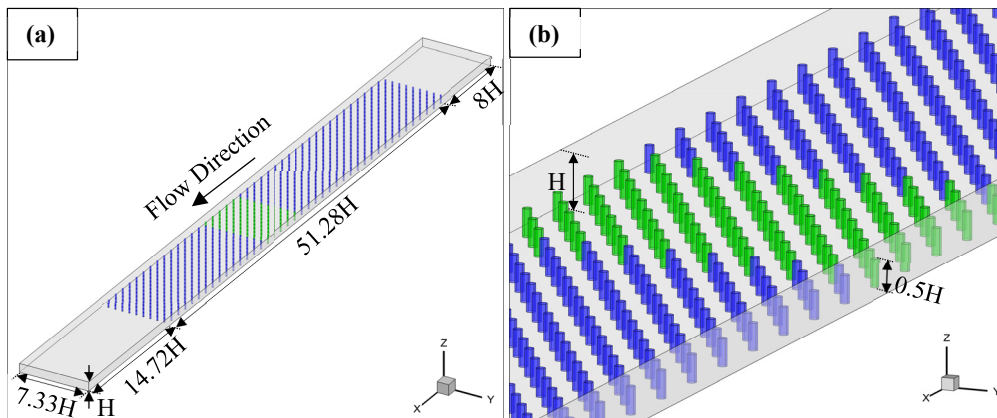
Figure 5.12. a) Dimensions of the channel b) height of the vegetation stems in 3D
for Case S50

There are 24857437 cells (i.e., 2688x320x30 grid points in x, y and z directions) in the 3D computational domain. The stem and surface layer contains 19 and 11 nodes in the vertical direction, respectively. Figure 5.13 demonstrates the vertical mesh arrangement in the longitudinal section of the domain (i.e., x-z plane) and on vegetation stems.
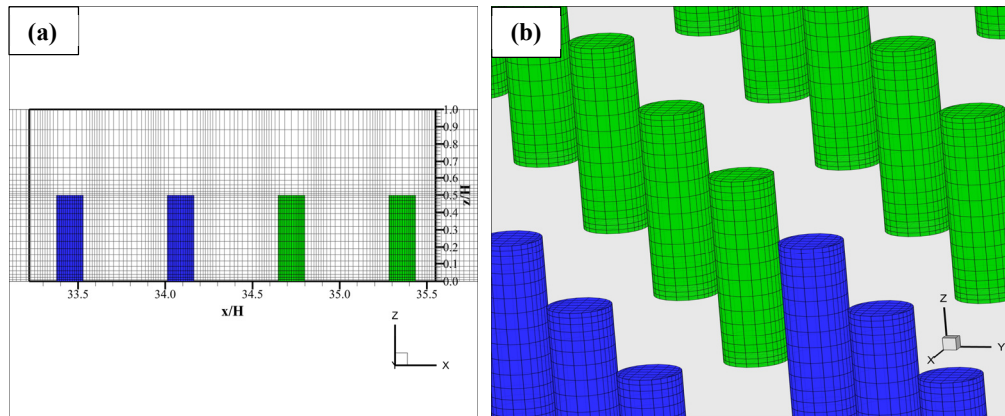
Figure 5.13. Vertical grid distribution on a) x-z plane b) vegetation stem for Case S50

5.2.2.3   Case S75

The characteristic lengths of the channel and height of the vegetation stem are shown in Figure 5.14.
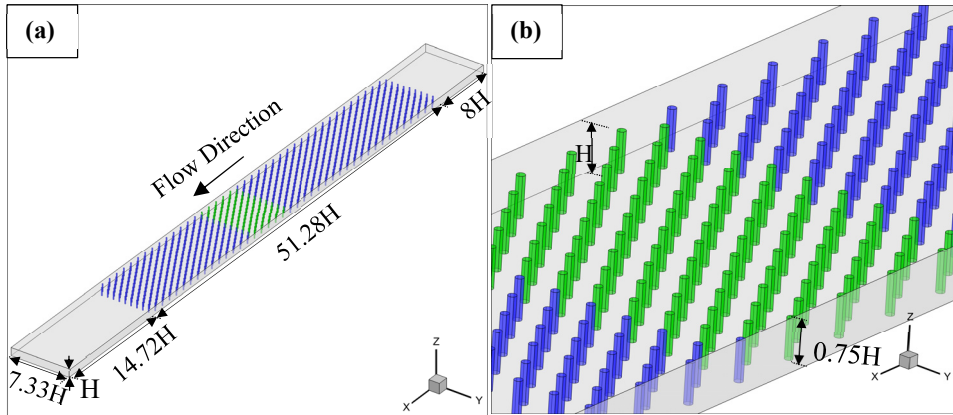
Figure 5.14. a) Dimensions of the channel b) height of the vegetation stems in 3D
for Case S75

The computational flow domain of the S75 case has 26571743 cells (i.e.,
2688x320x32 grid points in x, y and z directions). Since the height of the stem is
larger than those in other previous cases, the stem layer includes most of the vertical
nodes (i.e., 23 nodes). The vertical mesh pattern in the x-z plane of the domain and
on vegetation stems are depicted in Figure 5.15.
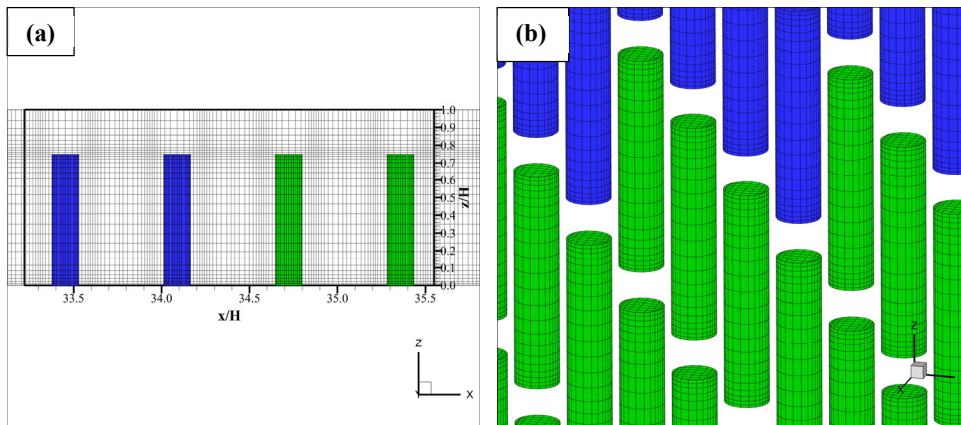
Figure 5.15. Vertical grid distribution on a) x-z plane b) vegetation stems for
Case S75

CHAPTER 6

ANALYSES AND DISCUSSION OF THE RESULTS

6.1   Emergent Vegetation Cases

6.1.1   Experimental Analysis and Results of the Emergent Vegetation Conditions

In this part, firstly, the effect of emergent vegetation on the total flow resistance was examined using two resistance parameters commonly used in literature; Manning's roughness 'n' and Darcy-Weisbach friction factor 'f', respectively. Secondly, the contribution of bed friction to total flow resistance will be evaluated in detail. Finally, the drag coefficient of emergent vegetation having four different densities will be investigated under various hydraulic scenarios.

6.1.1.1   Effect of Emergent Vegetation on Manning's Roughness Coefficient

Consider a steady flow in a channel having a smooth bed and sidewalls with emergent rigid vegetation. If the force balance equation is applied to control volume (CV) having length L (m) and width B (m) as shown in Figure 6.1, the following equilibrium can be obtained:

$$\gamma A_1 L S_f (1 - \lambda h^*) = \frac{1}{2} M C_D \rho U_{ref}^2 A_2 + \frac{f_b}{8} \rho U_{ref}^2 B L (1 - \lambda) \tag{6.1}$$

where γ is the specific weight of water (N/m^3), A_1=B.H is cross-sectional area of flow (m^2), H is the flow depth (m), S_f is energy slope, $\lambda = \frac{M\frac{\pi D^2}{4}}{B.L}$ is dimensionless areal vegetation density, $h^* = \frac{h_v}{H}$ is the submergence ratio where h_v is the vegetation height (m) and h^*=1 for emergent vegetation, M is the number of stem in control volume, C_D is the bulk drag coefficient of vegetation array, ρ is the density of water (kg/m^3), A_2=D.H is projection area of vegetation stem perpendicular to flow direction (m^2) where D is the stem diameter (m), U_{ref} is the reference velocity (m/s) and f_b is bed friction factor, respectively.
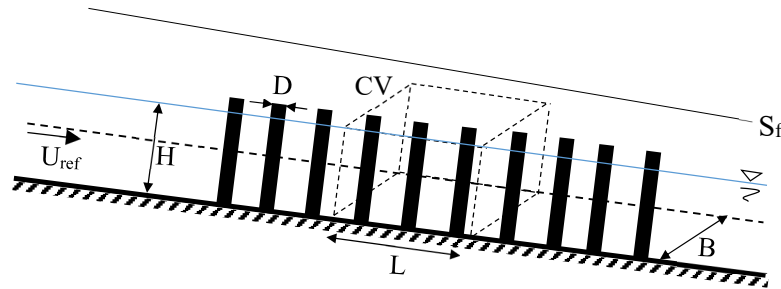
Figure 6.1. Application of force balance equation using control volume in emergent vegetation array

As mentioned in Chapter 4, the drag plate measures the total flow resistance due to vegetation drag and bed friction. Although plexiglass bed material can be considered smooth, the present study includes low vegetation densities (i.e., λ=0.00436, 0.00981), where the bed resistance can not be neglected (Cheng & Nguyen, 2011). Even though pore velocity, U_p=Q/(A_1(1-λ)), represents the actual approach velocity in a channel with emergent vegetation better than a bulk velocity, U_b, the bulk velocity can also be used for studies having low-density vegetation as in the present study ($U_p \approx U_b$) (Cheng & Nguyen, 2011). Therefore, for the emergent vegetation part in the present study, the bulk flow velocity, U_b=Q/A_1, is used as characteristic velocity (i.e., reference velocity) to calculate total resistance parameters as in the

previous studies (e.g., Wu et al., 1999; Ishikawa et al., 2000; Lee et al., 2004). For most of the data in the present study, the aspect ratio is larger than five (i.e., B/H>5); therefore, the effect of sidewalls is insignificant and not included in Equation (6.1) (Cheng, 2011). In most of the previous studies, areal vegetation density is selected to represent the density of emergent vegetation (e.g., Kothyari et al., 2009; Sonnenwald et al., 2019) in the drag coefficient relations. However, Manning's roughness is also dependent on flow depth unlike C_D. Therefore, a robust dimensionless parameter that includes both the effect of vegetation density and flow depth must be used in the functional relation of Manning's coefficient. The dimensionless parameter ah_v, called the roughness concentration (Wooding et al., 1973), has the properties mentioned above and was therefore selected as a parameter to be used in the following functional relations. Herein, ah_v is the frontal area of stem per unit bed area, and 'a' is the frontal area of stem per canopy volume (Nepf, 2012). In canopy flows, most of the flow resistance is originated from form drag represented by frontal area of vegetation stems. Thus, it can be stated that roughness concentration can be considered as a measure of the form drag and, therefore, the flow resistance in a physical manner. Here, a is defined as follows:

$$a = \frac{D.h_v}{\left(\frac{B.L.h_v}{M}\right)} = \frac{M.D}{B.L} = \frac{\lambda}{\left(\frac{\pi D}{4}\right)} \tag{6.2}$$

where $h_v = H$ for emergent vegetation.

Ishikawa et al. (2000) also stated that total flow resistance is correlated with aH better than λ. This functional relationship can also be obtained if Manning's equation,

$$U_b = \frac{1}{n} R_h^{2/3} \sqrt{S_f} \tag{6.3}$$

is substituted into Equation (6.1), where R_h is the hydraulic radius, Equation (6.4) will be obtained,

$$n = \sqrt{\left(\frac{R_h^{\frac{1}{3}}}{2g}\right)\left(\frac{C_D(aR_h)}{(1-\lambda)} + \frac{f_b R_h}{4H}\right)} \tag{6.4}$$

For wide channels ($R_h \approx H$), Equation (6.4) becomes:

$$n = \sqrt{\left(\frac{H^{\frac{1}{3}}}{2g}\right)\left(\frac{C_D(aH)}{(1-\lambda)} + \frac{f_b}{4}\right)} \tag{6.5}$$

and it means n=f_1 (λ, aR_h (or aH), R_h (or H), C_D, f_b). In the present study, single vegetation diameter size and single staggered pattern were used in experiments, so the drag coefficient of emergent vegetation array can be defined as C_D=f_2 (Re_{db}, λ), similar to previous studies (e.g., Kothyari et al., 2009) where Re_{db} is the stem (vegetation) Reynolds number based on the bulk velocity, $Re_{db} = \frac{U_b D}{\nu}$ and ν is the kinematic viscosity of water (m^2/s). In functional relationship f_1, the first three parameters can be easily calculated; however, determining the drag coefficient is not easy, especially in the field, so it is usually obtained in laboratory conditions. Although many relationships between C_D and Re_{db} have been developed in the literature, most of these studies are usually valid for low stem Reynolds numbers (e.g., Tanino & Nepf, 2008a) or have a limited Re_{db} range which is not the actual condition found in nature most of the time, especially during flood conditions. Liu et al. (2020) collected a large number of data from several studies conducted in the literature, and it was shown that only a very few of these data have large stem Reynolds numbers (see Figure 2 in their study).

van Rooijen et al. (2018) stated that the drag coefficient of emergent vegetation array becomes constant at high stem Reynolds numbers (i.e., Re_{db}>1000). Thus, it can be said that C_D is only a function of λ for high stem Reynolds numbers as in the case of the present study (i.e., Re_{db}>2500), and it can be omitted from the functional relation of C_D. Furthermore, vegetation stems were distributed rather sparsely in the present study (i.e., λ is very small, (($1-\lambda$) $\approx$1)) so that ($1-\lambda$) term can also be eliminated from

Equations (6.4) and (6.5). Furthermore, there is no need to keep λ in the functional relation, because Equation (6.2) demonstrates that the roughness concentration of stems is already a function of areal vegetation density (i.e., a= f_3 (λ)). Unfortunately, bed shear stresses in vegetated channels can not be determined by applying typical methods valid for bare channels, because total flow resistance includes not only the bed shear stress but also the vegetation drag (Yang et al., 2015). In the literature, there are some studies that estimate bed shear stress in emergent vegetated channels having smooth beds (e.g., Yang et al., 2015; Etminan et al., 2018). However, partitioning the total flow resistance into bed shear and vegetation drag is not in the scope of this subsection. Instead, total flow resistance coefficients (e.g., Manning's roughness, Darcy-Weisbach friction factor) represent the combined effect of the vegetation and bed resistance in simple forms. The present subsection rather aims to propose practical relations between total flow resistance coefficients and flow conditions and vegetation characteristics in channels having a smooth bed. Thus, the final relation becomes n=f_4 (H (or R_h), aR_h (or aH)), and the effects of these parameters on n are investigated below, respectively. In addition, in the present study, left hand side of Equation (6.1) is equal to the total force (acting on drag plate) measured by force sensor, so energy slope (S_f), which is the only unknown parameter at left hand side of Equation (6.1), can be calculated easily. Later, Manning's roughness coefficient is obtained by using this energy slope in Manning's equation (i.e., Equation (6.3)).

Figure 6.2 shows a change in Manning's roughness coefficient with flow depth for various vegetation densities. Manning's roughness coefficient increases as the flow depth increase similar to previous studies (e.g., James et al., 2004; Zhang et al., 2021) as a result of resistance on the water body acting along water depth in emergent vegetation (Zhang et al., 2021). The relation between n and flow depth can be approximated with linear best-fit lines for each density, and it was seen that each best-fit line is a good estimator of n (i.e., all R^2>0.8). It can also be stated that

Manning's roughness is strongly dependent on areal vegetation density and increases as density increases.
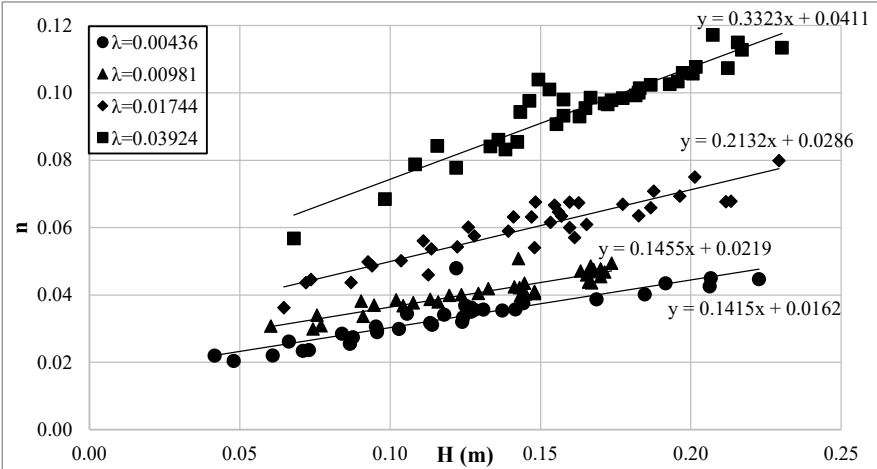
Figure 6.2. Variation of Manning's roughness with flow depth for different vegetation densities

In addition to flow depth, as stated in the former relation f_4, Manning's roughness also depends on aH. To examine the relation between n and aH, the data of the present study and similar studies in the literature (i.e., Cheng & Nguyen, 2011; Zhang et al., 2018) were given in Figure 6.3 with their best-fit functions (i.e., solid lines in Figure 6.3).
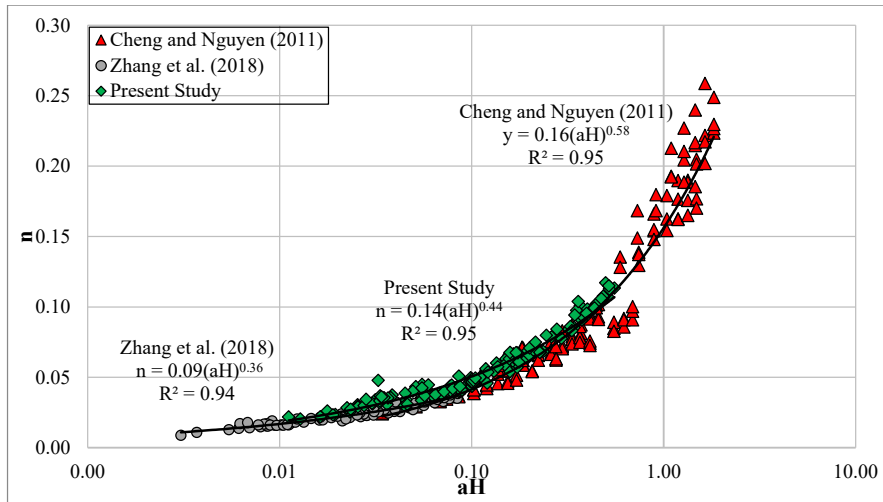
Figure 6.3. The effect of aH on Manning's roughness in different studies

It is clearly observed that most of the data of all studies overlap each other and exhibit similar trends as aH increases. These studies were performed with an experimental setup having a smooth bed and sidewalls, and a staggered pattern was used in the distribution of stems. The range of important parameters of these studies is given in Table 6.1.

Table 6.1 The range of important parameters in the relevant studies

Study	λ	D (cm)	Re_{db}	n
Cheng and Nguyen (2011)	0.0043-0.1189	0.32/0.66/0.83	154-1199	0.024-0.259
Zhang et al. (2018)	0.0020	0.3	271-2072	0.009-0.038
Present Study	0.0044-0.0392	2.08	2678-17333	0.020-0.1170

The best-fit functions of all studies were found in terms of power function and the corresponding coefficient of determination (R^2) of each study is well enough to represent data sets properly as indicated in Figure 6.3. For lower aH values, the

71

present study slightly overestimates other studies; however, the power function of the present study and that of Cheng and Nguyen (2011) converge with each other as aH increases. On the other hand, if Table 6.1 is considered, it can be seen that stem Reynolds numbers (Re_{db}) of other studies are relatively low compared to those of the present study. Similar to the study of van Rooijen et al. (2018), White (1991) shows for the isolated cylinders that C_D is a function of Re_{db} for values that are lower than 1000 (i.e., $Re_{db}<1000$) and reaches a fairly constant value when stem Reynolds number is between 10^3 and 10^5. Thus, it can be stated that there is a combined effect of aH and Re_{db} on Manning's roughness for the other two studies given in Figure 6.3. To eliminate the indirect effect of Re_{db} on n, data groups having a lower Re_{db} than 1000 were removed and presented in Figure 6.4 where a change in n was shown with respect to aR_h. It should be noted that the data group of Zhang et al. (2018) was excluded due to its very low and limited density.
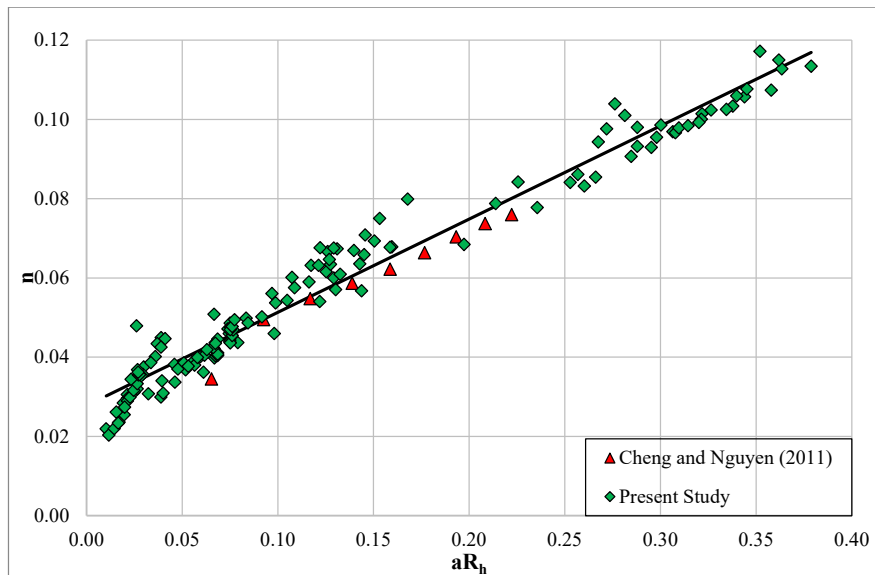
Figure 6.4. The relation of Manning's roughness with aR_h for data set $Re_{db}>1000$

Figure 6.4 demonstrates that data groups have better agreement with each other and very similar trends when the effect of Re_{db} on Manning's roughness coefficient is eliminated.

Now, the best fit function (i.e., the solid line in Figure 6.4) belonging to both data groups can be represented by linear relation having high R^2 as given below:

$$n=0.24(aR_h)+0.028 \text{ with } R^2=0.97 \tag{6.6}$$

which is valid for $0.01 \leq aR_h \leq 0.379$ and $0.00436 \leq \lambda \leq 0.03924$. Equation (6.6) indicates that aR_h represents the roughness well as aH.

Figure 6.5a was presented to show the performance of Equation (6.6) by comparing the measured and computed Manning's roughness coefficients of both studies. Most of the data remain between $\pm 15\%$ error lines and collapse onto the perfect agreement line which means that Manning's roughness can be estimated satisfactorily using Equation (6.6). In addition to that, Figure 6.5b demonstrates in detail the percentage of data at each percent error band.
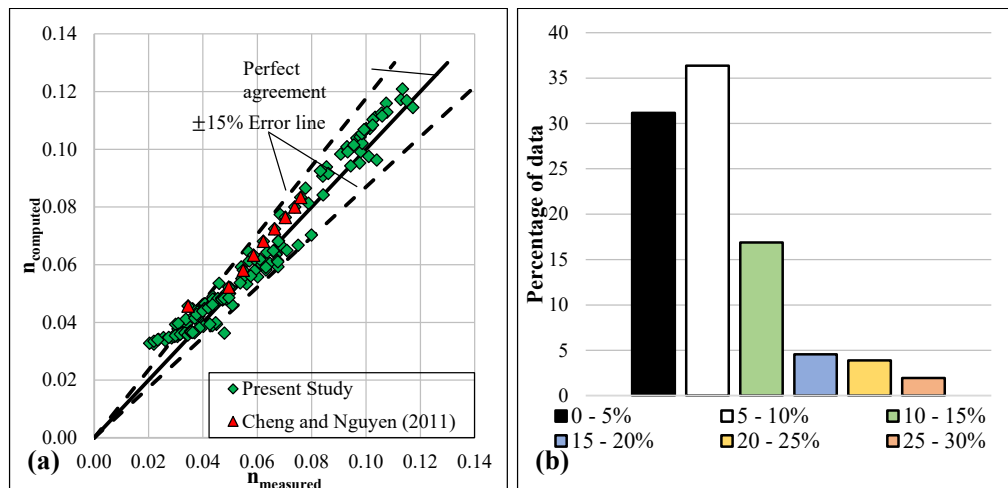
Figure 6.5. a) Comparison of $n_{measured}$ with $n_{computed}$ using Equation (6.6)

b) Histogram of error percentages

Some studies in the literature can calculate the total resistance of the channel by combining resistance sources. For instance, Cowan (1956) proposed an equation based on the linear addition of Manning's roughness coefficients belonged different resistance sources as follows:

$$n_T = (n_b + n_1 + n_2 + n_3 + n_4)m \tag{6.7}$$

where n_T is the total Manning's roughness coefficient of a channel, n_b defines the base value of n valid for smooth, straight and bare channels, n_1 is the correction factor for the surface irregularities effects, n_2 is the roughness value for the variation of channel cross section in shape and size, n_3 is roughness value for obstructions on the channel, n_4 defines Manning roughness of vegetation and m is a correction factor for sinuosity (meandering) of the channel (Cowan, 1956; Arcement & Schneider, 1989; Green, 2005). Herein, Equation (6.6) provides a valuable output, a combination of base and vegetation resistance coefficient (i.e., $n_b + n_4$), to be used in the calculation total resistance of the channel.

6.1.1.2   Effect of Emergent Vegetation on Darcy-Weisbach Friction Factor

The well-known head loss equation of Darcy-Weisbach is principally proposed for pipe flow (Chow, 1959) and given as:

$$h_f = f\frac{L_p}{d}\frac{U_b^2}{2g} \tag{6.8}$$

where h_f is head loss through length of pipe, L_p, and d_p is the pipe diameter. If Darcy-Weisbach equation is rewritten for the friction factor in open channel flows,

$$f = \frac{8gR_hS_f}{U_b^2} = 8\left(\frac{U_*}{U_b}\right)^2 \tag{6.9}$$

where hydraulic diameter $D_h = 4R_h$, $S_f = h_f/L$ and $U_* = \sqrt{gR_hS_f}$ is friction (shear) velocity. Also, if Equation (6.1) is combined with Equation (6.9), Equation (6.10) is obtained as given below:

$$\frac{U_b}{U_*} = \sqrt{\frac{8}{f}} = \sqrt{\frac{8H(1-\lambda)}{4C_D(aR_h)H + f_b R_h(1-\lambda)}} \tag{6.10}$$

and if the necessary simplification in Equation (6.10) is made by considering wide channels,

$$\frac{U_b}{U_*} = \sqrt{\frac{8}{4C_D(aH) + f_b}} \tag{6.11}$$

where U_b/U_* is called coefficient of velocity (Ishikawa et al., 2000) and the function of $U_b/U_* = f_5$ (C_D, aR_h (or aH), f_b). Similar statements and conditions described in the previous subsection are still valid here, so C_D and f_b can be removed from functional relation. Basically, there are two types of formulas that predict friction factor in open channels based on properties of roughness, logarithmic or power law type, as follows (Stewart et al., 2019):

$$\frac{U_b}{U_*} = \sqrt{\frac{8}{f}} = a_1 \ln\left(\frac{R_h}{k}\right) + a_2 \quad \text{or} \quad \frac{U_b}{U_*} = \sqrt{\frac{8}{f}} = a_1 \left(\frac{R_h}{k}\right)^{a_2} \tag{6.12}$$

where k is the roughness length scale, a_1 and a_2 are constants. Thus, by making an analogy with Equation (6.12), a power law type of relations is constructed in the present study. To examine the functional relationship of U_b/U_* with aR_h, Figure 6.7 is plotted using additional data groups of Cheng and Nguyen (2011) and Zhang et al. (2018).
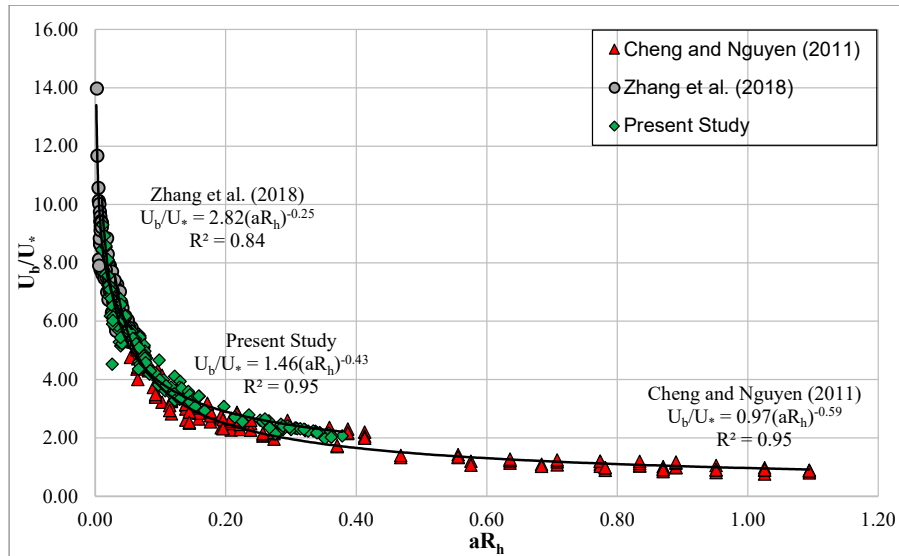
Figure 6.6. Variation of coefficient of velocity U_b/U_* with aR_h

It can be stated that data groups of each study exhibit similar trends which are represented by power functions (i.e., solid lines in Figure 6.6) in the best manner. Furthermore, for lower values of aR_h, all data groups and their power functions coincide with each other; however, the present study starts to overestimate the study of Cheng and Nguyen (2011) as aR_h increases. In the present study, stem Reynolds numbers are large enough which means that C_D does not change significantly with Re_{db} as stated in the previous subsection, so C_D only depends on λ. Thus, the data group with low Re_{db} values in other studies, $Re_{db} < 1000$, was removed to more clearly investigate the effect of aR_h on U_b/U_*. Moreover, the data group of Zhang et al. (2018) is eliminated due to its limited range, and Ishikawa et al.'s (2000) relation was included in Figure 6.7 where all of the data has stem Reynolds number larger than 1000. Unlike the present study, the best fit function and friction velocity in Ishikawa et al.'s study (2000) were given in terms of flow depth rather than the hydraulic radius (i.e., aH and $U_* = \sqrt{gHS_f}$). However, it is known that the hydraulic radius and flow depth are close parameters in wide channels, and most of the data ($\approx 93\%$) in the present study satisfy $B/H > 5$ condition, which is usually recommended

76

as the limit of wide channel criteria where the sidewall effects are relatively negligible (e.g., Auel et al., 2014; Cheng, 2011; Rousar et al., 2016).
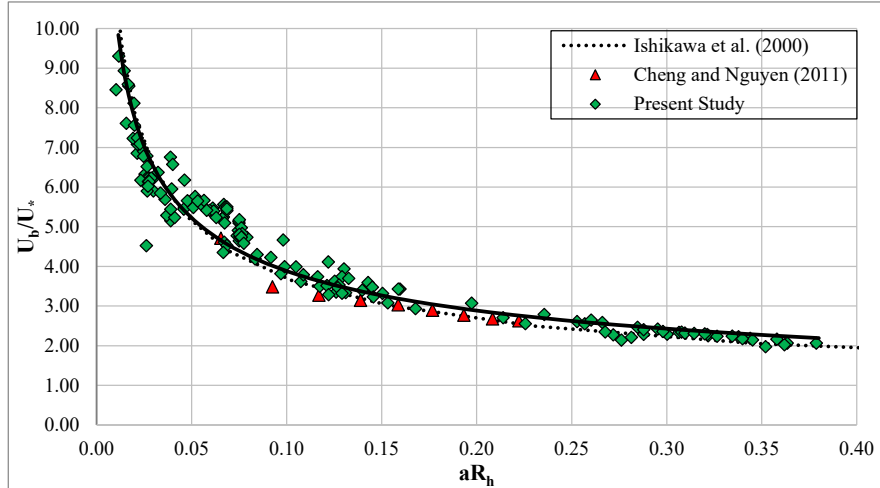
Figure 6.7. Variation of coefficient of velocity U_b/U_* with aR_h for data set $Re_{db}>1000$

It is clearly seen that when the data group having an effect of Re_{db} on itself is eliminated, the study of Cheng and Nguyen (2011) and the present study converge and get closer to each other as shown in Figure 6.7. The best-fit function (i.e., the solid line in Figure 6.7) formed by the usage of both data groups is given below:

$$\frac{U_b}{U_*} = 1.45(aR_h)^{-0.43} \text{ with R}^2\text{=0.95.} \tag{6.13}$$

The performance of Equation (6.13) was investigated in Figure 6.8a. As can be seen from this figure, almost all of the data including the study of Cheng and Nguyen (2011) stays between $\pm15\%$ error lines. The histogram in Figure 6.8b shows the percent distribution of data at each percent error band. Therefore, it can be stated that the friction factor in vegetated channels can be estimated effectively using Equation (6.13).
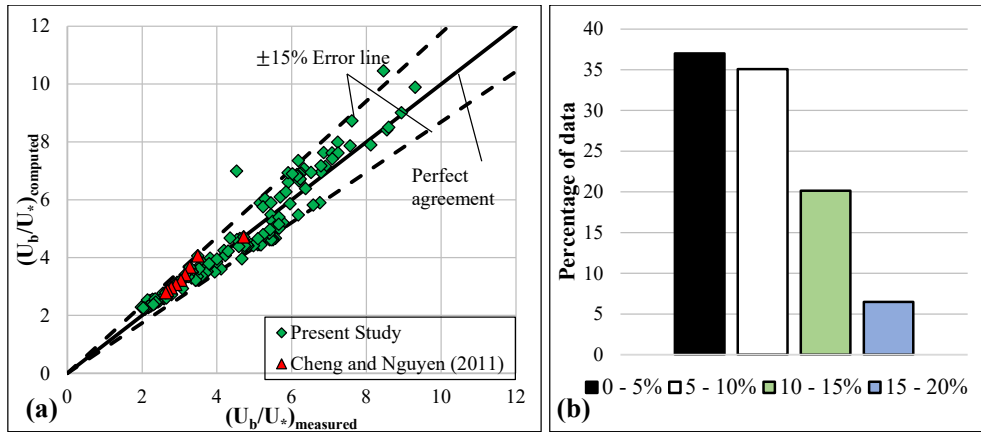
Figure 6.8. a) Comparison of $(U_b/U_*)_{measured}$ with $(U_b/U_*)_{computed}$ using Equation (6.13) and   b) Histogram of error percentages

On the other hand, Ishikawa et al. (2000) found a relation between U_b/U_* and aH as given below:

$$\frac{U_b}{U_*} = 1.25(aH)^{-0.47} \text{ with } R^2=0.98. \tag{6.14}$$

As can be seen above, Equations (6.13) and (6.14) have similar power, close coefficients and high R^2 which reveals that dimensionless roughness concentration aR_h (for wide channels aH) is a good descriptor parameter for the friction factor as well.

Although Ishikawa et al.'s study (2000) was carried out on a rough sand bed having a 1.8 mm mean diameter, best-fit functions are in close agreement with each other which means that vegetative drag is responsible for most of the resistance in emergent vegetated channels rather than bed roughness. In other words, Ishikawa et al.'s (2000) relation slightly remains below the present study which demonstrates that bed roughness increases flow resistance a little compared to vegetation resistance. However, it should also be considered that the contribution of bed resistance to total flow resistance may increase in channels having a larger roughness size. It is also important to state that the previous and present subsections may not

78

directly reflect the actual flow resistance which is encountered in nature, because there are some additional drag (resistance) sources in natural channels such as bed roughness, bed forms and foliage of stems which increase the resistance coefficients.

6.1.1.3   Determination of Bed Friction in Emergent Vegetation Array

As mentioned in Chapter 4, the drag plate measures not only drag forces acting on the vegetation stem but also bed drag on the smooth plate. In other words, the drag coefficient obtained from the drag plate measurements is a lumped parameter that theoretically includes both vegetation drag and bed friction. Actually, the bed friction is very low compared to the vegetation drag, so the bed drag is usually neglected in some of the previous studies having higher vegetation densities (e.g., Sonnenwald et al., 2019). However, James et al. (2004) stated that the effect of bed shear on the total resistance can be significant for low vegetation densities as in the present study. Investigation of the bed shear stresses is also helpful in making inferences about sediment erosion and deposition in canopy flows. The existence and density of vegetation considerably modify the bed shear stress distribution (Etminan et al., 2018). Therefore, several analyses were performed to investigate the contribution of the bed friction on the overall resistance in this section.

There are several ways to eliminate the bed drag from the total drag experimentally in flows having emergent vegetation. For instance, if the drag measurement mechanism is mounted on the top of the channel as in some of the experimental studies (e.g., Ishikawa et al., 2000; Kothyari et al., 2009; D'Ippolito et al., 2019), only forces acting on the vegetation stems are measured. However, as stated in Chapter 4, these types of mechanisms are not eligible to measure the drag force on submerged vegetation. Thompson et al. (2004) used hot-film anemometry to measure boundary shear stresses directly in their experiments. Cheng and Nguyen (2011) carried out sidewall and bed shear correction by following the procedure proposed by Vanoni and Brooks (1957) in emergent vegetation analyses. Yang et al. (2015)

proposed a new model supported by experimental measurements to predict the bed shear stresses in an emergent vegetated channel having a smooth bed. Tanino and Nepf (2008a) estimated the bed shear stress contribution using a formula derived to calculate the drag coefficient of a single isolated cylinder. However, it was known that the drag coefficient of the cylinder placed in an array is different from that of a single cylinder. Thus, this type of approximation is not representative of the actual bed shear stresses most of the time. In addition to experimental ways, there is another option to determine the bed drag in vegetation flows. Computational fluid dynamics (CFD) is a powerful tool to investigate flow resistance and structures in hydraulics. There are some studies in the literature where the bed resistance was determined in vegetation flows using RANS and LES models (e.g., Stoesser et al., 2010; Kim & Stoesser, 2011). Moreover, Etminan et al. (2018) revised the model proposed by Yang et al. (2015) and demonstrated that this model is also valid for sparse canopies (i.e., λ=0.016) using the LES model. In the present study, the bed shear stresses were evaluated by performing the DES model with three cases in emergent vegetation flow conditions.

The DES model was executed for three different emergent cases (i.e., E10, E20 and E30) including the lowest and highest vegetation densities to derive a general relation that is valid for the given flow conditions and vegetation characteristics in the present study. Firstly, the form drag acting on each vegetation stem in the drag plate was evaluated. Afterward, the total bed shear force was obtained by integrating dimensionless temporally-averaged bed shear stresses in the streamwise direction, $\frac{\tau_b}{\rho U_b^2}$, over the drag plate. The dimensionless bed shear stresses are calculated by $\tau_b = \mu \left(\frac{\partial u}{dz} \right)_{z=0}$, where u is the temporally-averaged mean velocity in a streamwise direction and $\mu = \frac{1}{Re_{db}}$ in the dimensionless background, considering that the first point off the wall is situated inside the viscous sublayer. Moreover, spatial variations of the magnitude of dimensionless temporally-averaged bed shear stress on the drag

plate, $\mu \left| \dfrac{\partial u_m}{dz} \right|_{z=0}$ where u_m is the temporally-averaged mean velocity magnitude, are demonstrated in Figure 6.9 for each case.

Flow Direction
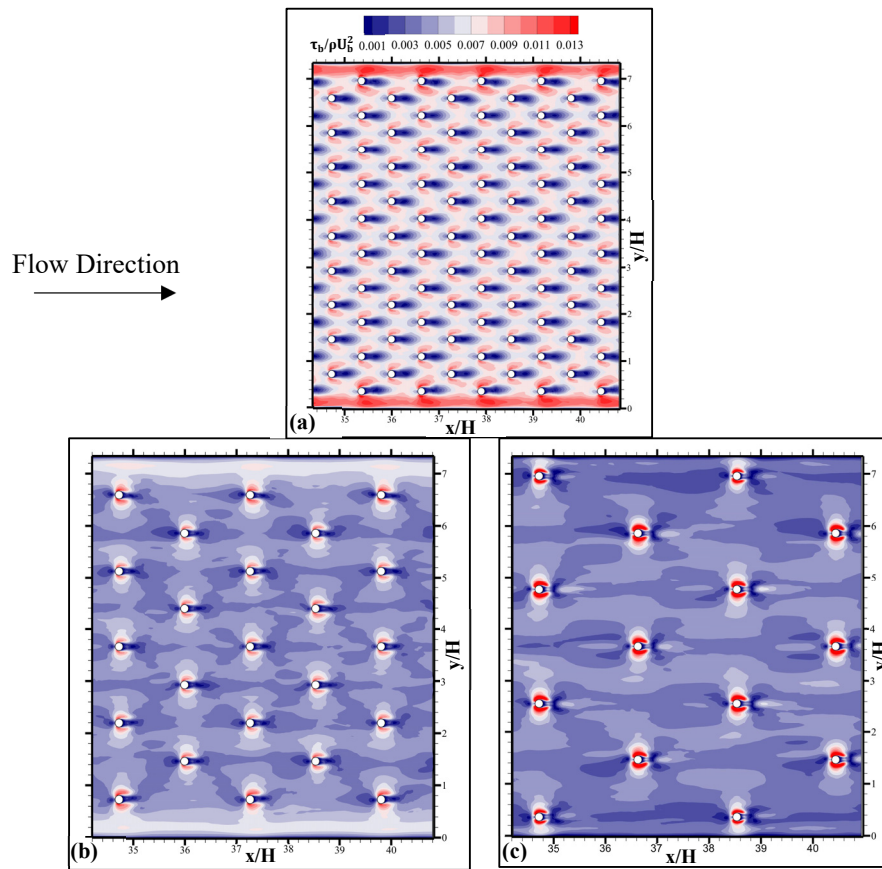
Figure 6.9. Spatial variation of non-dimensional bed shear stress on the drag plate for cases a) E10, b) E20 and c) E30

In Figure 6.9, stem Reynolds numbers vary for each case and increase as the vegetation density decreases (i.e., from low to high densities, Re_{db}=12230, 10865 and 6157). The lower shear stresses (shown by dark blue) are obtained just upstream of each vegetation stem. However, it was observed that these regions are contracted and diminished as the canopy density increases. Moreover, at another region, immediately downstream of stems, the lower bed shear stresses are existed due to

81

the recirculation in the wake region where the lower velocities develop. These regions (i.e., just upstream and downstream of the stems) are favorable for sediment deposition. Furthermore, there are some regions on the sides of stems (shown by dark red) where the bed shear stresses become larger with the local contraction of streamlines (Etminan et al., 2018). The sediment will be entrained at these regions in the case of a loose bed. It is also noted from Figure 6.9 that larger shear stresses dominate the drag plate region as the vegetation density increases. This is because the streamwise velocity is increased due to the flow acceleration between neighbor stems; thereby, larger shear stresses develop with the decrease in stem spacing.

The contribution of the bed shear stress (i.e., bed shear force), F_B, to the total drag, $F_T = F_B + F_D$, is shown in Figure 6.10 where three different groups of data with their power fit functions are presented.
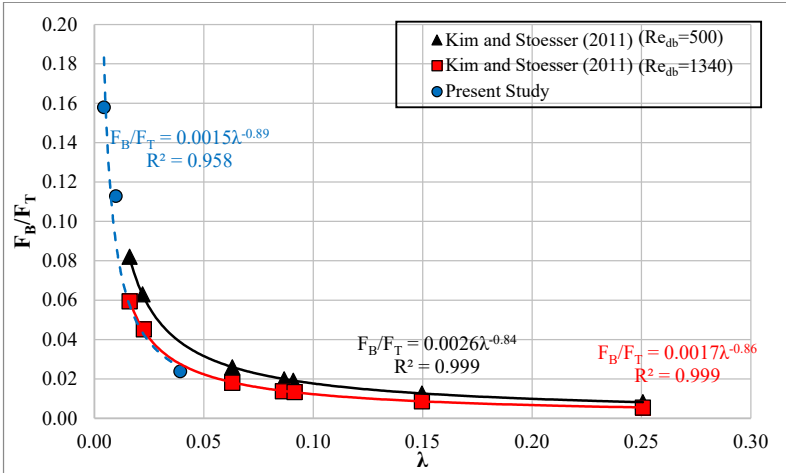
Figure 6.10. Variation of the bed drag with vegetation density in different stem Reynolds numbers

Each data group and its corresponding power fit functions to them were represented by different colors and markers to reflect the effect of Re_{db} on the bed friction contribution more clearly. Two of them (i.e., red and black ones in Figure 6.10) were gathered from the numerical study of Kim and Stoesser (2011) where analyses of

each group were performed with a single stem Reynolds number value (i.e., $Re_{db}=500$ and $Re_{db}=1340$). On the other hand, the data group of the present study consists of data having different stem Reynolds numbers (i.e., $Re_{db}=6157$, 10865 and 12230). It was noted that each data group is well represented with power functions having a high coefficient of determination, R^2, value. According to data groups of Kim and Stoesser (2011), it was seen that while the bed friction considerably depends on the vegetation density (especially for $\lambda<0.075$), variation of the stem Reynolds number does not affect the bed friction significantly for the given vegetation densities. Similarly, if the coefficients and powers of the fit functions (for $Re_{db}=500$ and $Re_{db}=1340$) are investigated, it is seen that they reduce slightly as the stem Reynolds number increases. The power fit function derived for the present study is also compatible with this reducing trend. Furthermore, it is seen from Figure 6.10 that although stem Reynolds numbers are significantly different, there is a strong consistency (nearly overlapping each other) between the power fit functions of the present study and the study of Kim and Stoesser (2011) for $Re_{db} \geq 1340$. This consistency can be supported by the study of Etminan et al. (2018) where non-dimensional spatially-averaged friction velocity, $\frac{\langle U_* \rangle}{U_p}$ (i.e., $\langle U_* \rangle = \langle \sqrt{\frac{|\tau_b|}{\rho}} \rangle$), converges a constant value after $Re_{dp}>1000$ for $0.016 \leq \lambda \leq 0.25$ (see Figure 7a in their study). This convergence means that the effect of stem Reynolds number on the bed friction almost vanishes for $Re_{dp}>1000$. Although the vegetation density ranges of studies (i.e., the present study and Etminan et al. (2018)) are different, it seems that the effect of the stem Reynolds number on the bed friction diminishes substantially also for sparser vegetation densities. Thus, from these points of view, it can be stated that data with larger stem Reynolds numbers (i.e., $Re_{db} \geq 1340$) can be defined as a single group, thereby, can be represented by a single power fit function. Consequently, if both data groups having larger stem Reynolds numbers are combined as single data set, the following power fit function is obtained:

$$\frac{F_B}{F_T} = 0.0017\lambda^{-0.863} \text{ with R}^2 = 0.992 \tag{6.15}$$

which is valid for $0.00436 \leq \lambda \leq 0.25$ and $Re_{db} \geq 1340$. Both data group and corresponding power fit function are revealed in Figure 6.11.
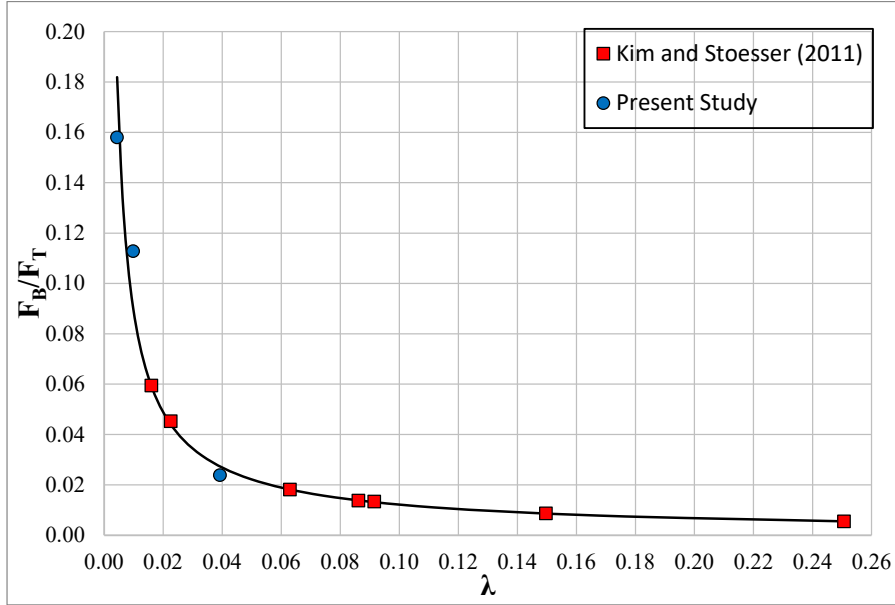
Figure 6.11. Variation of the bed drag with vegetation density for $Re_{db} \geq 1340$

According to Figure 6.11, it can be stated that the bed friction contribution can not be ignored for the vegetation densities $\lambda \leq 0.016$ in the emergent vegetation canopies having a large stem Reynolds number (i.e., $Re_{db} \geq 1340$). Of course, these results are only valid for channels having smooth beds. Otherwise, if the roughness condition of the bed is different from the present one, the contribution of bed shear will be more pronounced based on the roughness condition (i.e., relative roughness) so that its effect will be important at even higher vegetation densities (i.e., $\lambda \geq 0.016$).

6.1.1.4   Determination of the Drag Coefficients in Emergent Vegetation Array

In the present section, the effect of vegetation density and stem Reynolds number on the drag coefficient of emergent vegetation array were evaluated using experimental results. A force balance equation, Equation (6.1), can also be written in another form by considering a steady and uniform flow in emergent vegetation as follows:

$$\gamma A L_d S_f (1 - \lambda) = F_T = F_D + F_B \tag{6.16}$$

where A is the flow area (i.e., A=B_dH where B_d is the width of the drag plate), L_d is the length of the drag plate, S_f is the total energy slope and includes both the stem drag and the bed friction. As stated before, the sidewall effect is not considered in the force balance equation (i.e., Equation (6.16)). All experimental data for the emergent vegetation conditions have a large stem Reynolds number (i.e., Re_{db}>1340), so the bed friction acting on the drag plate can be eliminated using Equation (6.15). Thus, Equation (6.16) can be rewritten as Equation (6.17) given below;

$$\gamma A L_d S_{fv} (1 - \lambda) = F_D = \frac{1}{2} M \rho C_{Dref} U_{ref}^2 A_2 \tag{6.17}$$

where S_{fv} is the energy slope corresponding to vegetation resistance (i.e., S_{fv}= $S_f(F_D/F_T)$), M is the number of vegetation stem on the drag plate, C_{Dref} is the spatially averaged drag coefficient based on reference velocity. In some of the previous studies (e.g., Kothyari et al., 2009; Etminan et al., 2017; van Rooijen et al., 2018), different velocity scales than the bulk velocity U_b were used to represent the flow resistance such as pore velocity, U_p, or constricted cross-section velocity, U_c. In addition to these velocity scales, Etminan et al. (2017) propose to use separation velocity which represents the drag of vegetation array well; however, this velocity can not be practically obtained since it requires determination of the base pressure

coefficient, C_{pb}. The description of the U_p and U_c are given below (Stone & Shen, 2002; Etminan et al., 2017; van Rooijen et al., 2018);

$$U_p = \frac{U_b}{(1-\lambda)} \text{ and } U_c = \frac{U_b}{\left(1 - \sqrt{\frac{4\lambda}{\left(\frac{s_l}{s_s}\right)\pi}}\right)} \tag{6.18}$$

where s_l and s_s are the lateral spacing between two neighboring stems at the same streamwise location and longitudinal distance between two rows of array stems, respectively. The effect of using different velocity scales (i.e., U_b, U_p and U_c) on the variation of drag coefficient was analyzed and discussed below.

Firstly, a variation of the spatially averaged drag coefficient based on U_b, C_{Db}, with stem Reynolds number (Re_{db}) is demonstrated in Figure 6.12 for all of the vegetation densities.
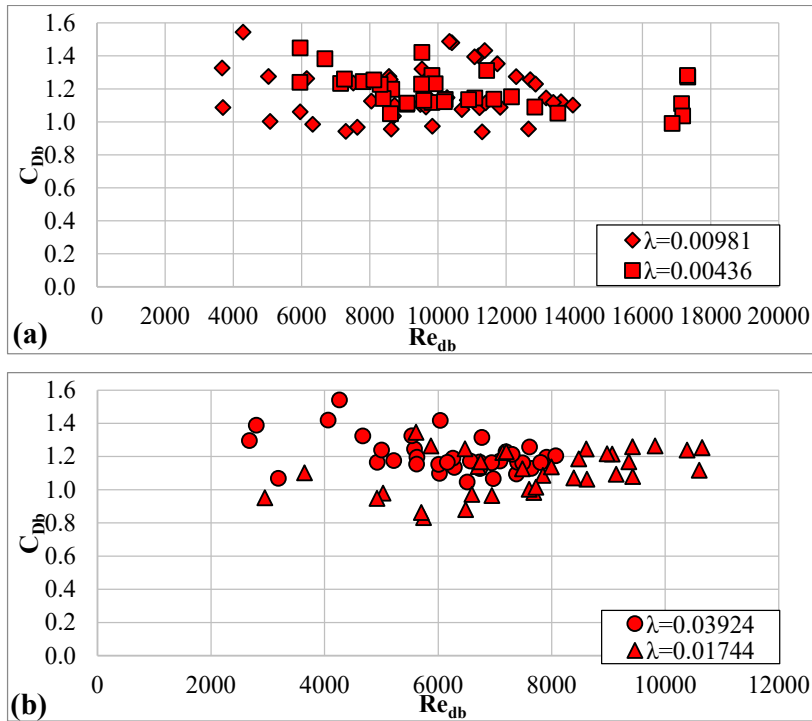
Figure 6.12. Variation of C_{Db} with Re_{db} for a) $\lambda=0.00436$ and $\lambda=0.00981$, b) $\lambda=0.01744$ and $\lambda=0.03924$

86

Figure 6.12 indicates that most data are distributed between $1.0 \leq C_{Db} \leq 1.4$, and the spatially averaged drag coefficient is independent of stem Reynolds number for the tested vegetation densities and stem Reynolds number ranges. Unfortunately, the data distribution is scattered such that any other relation between C_{Db} and Re_{db} is not established. Similar figures (i.e., similar to Figure 6.12) were not plotted for the other velocity scales (i.e., U_p and U_c) to not fall into repetition. Instead, these results will be presented in common graphs.

As mentioned in Chapter 2, White (1991) proposes a well-known equation that demonstrates a relationship between the drag coefficient of an isolated cylinder with cylinder Reynolds number for unconfined flow is given below:

$$C_D = 1 + 10Re_d^{-2/3} \tag{6.19}$$

which is valid for $1 < Re_d < 10^5$. This equation is also quite consistent with Wieselsberger's (1922) data up to $Re_d = 250000$ where a drag crisis occurs (White, 1991). All data groups together with Equation (6.19) are plotted in a common graph (i.e., Figure 6.13) to see the effect of vegetation density on the C_{Db} more clearly.
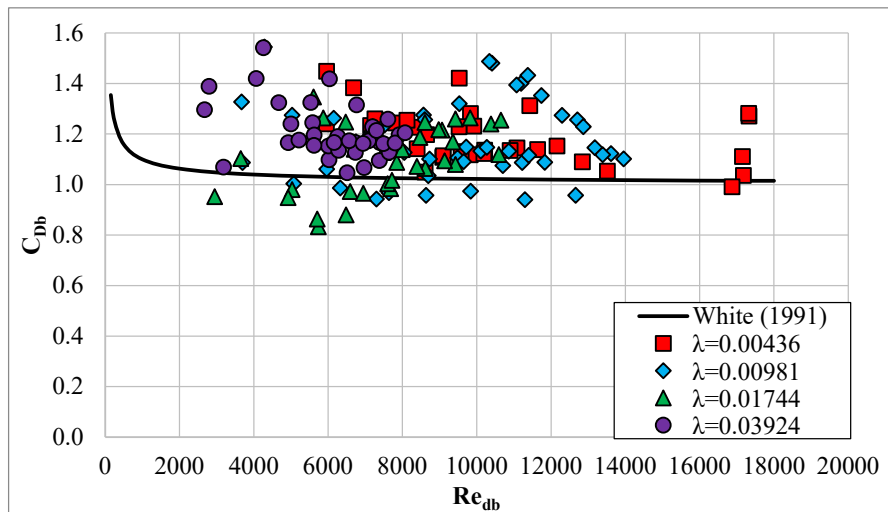
Figure 6.13. Variation of C_{Db} with Re_{db} for all emergent vegetation cases and for an isolated cylinder

If the distribution of the vegetation stems is considered in this study (i.e., staggered pattern), it can be stated that each vegetation stem placed on the drag plate undergoes a sheltering effect which should decrease the drag coefficient of vegetation stems. On the contrary, Figure 6.13 reveals that most data remain above White's (1991) equation. This is due to the fact that the blockage effect dominates each canopy increasing the local velocity values around the cylinders compared to an isolated cylinder and hence overcoming the sheltering effect. Thus, the spatially averaged drag coefficient of each vegetation array becomes larger than that of a single cylinder. On the other hand, all data groups nearly overlapped each other which means that the vegetation density does not have a significant impact on C_{Db} for the tested values of stem Reynolds numbers and vegetation densities.

As stated earlier, many studies (e.g., Tanino & Nepf, 2008a; Kothyari et al., 2009; Cheng & Nguyen, 2011) proposed and used pore velocity by considering the presence of vegetation stems in the flow domain. Thus, Figure 6.14 was plotted to investigate the effect of vegetation density and stem Reynolds number on the spatially averaged drag coefficient based on pore velocity, C_{Dp}.
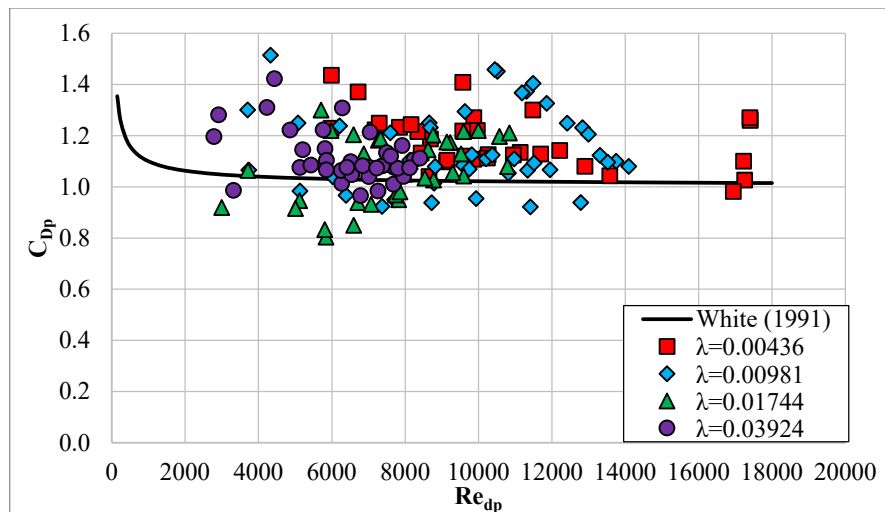
Figure 6.14. Variation of C_{Dp} with Re_{dp} for all emergent vegetation cases and for an isolated cylinder

From Figure 6.14, it was seen that the drag coefficient of vegetation groups having lower densities (i.e., λ=0.00436 and 0.00981) are not affected as much as those of higher densities (i.e., λ=0.01744 and 0.03924) due to the replacement of the bulk velocity with the pore velocity. It can be explained in a way that an increase in the velocity (i.e., the difference between U_b and U_p) due to the presence of vegetation is directly proportional to the vegetation density as shown in Equation (6.18). Thus, the spatially averaged drag coefficient of vegetation groups with larger densities reduces further than those with lower densities. In addition, White's (1991) function is not affected by the velocity replacement, because this function is proposed only for the single cylinder (i.e., λ=0). It was also seen that stem Reynolds number does not have an influence on C_{Dp} in each vegetation density similar to the study of van Rooijen et al. (2018) and single cylinder case (i.e., White's (1991) equation) for the tested Reynolds number intervals. While the studies of Tanino and Nepf (2008a) and Kothyari et al. (2009) show that the drag coefficients based on pore velocity increase with the increase of vegetation density, Nepf (1999) stated that the drag coefficient of an emergent canopy reduces as the vegetation density increases ($0.006 \leq \lambda \leq 0.053$). Contrary to these studies, Figure 6.14 demonstrates that most C_{Dp} values of vegetation groups having different densities coincide with each other, so there were no such trends for the given vegetation densities in high stem Reynolds numbers.

The results mentioned above show that the sheltering and delayed separation mechanisms are not effective enough to reduce the average drag coefficient of the canopies. Herein, the blockage effect is the dominant mechanism that modifies the canopy drag, because most of the drag coefficients are larger than that of an isolated cylinder.

Finally, a similar analysis was performed by changing the reference velocity with constricted cross-section velocity in Figure 6.15 which demonstrates the drag coefficient variation with vegetation density and stem Reynolds number.
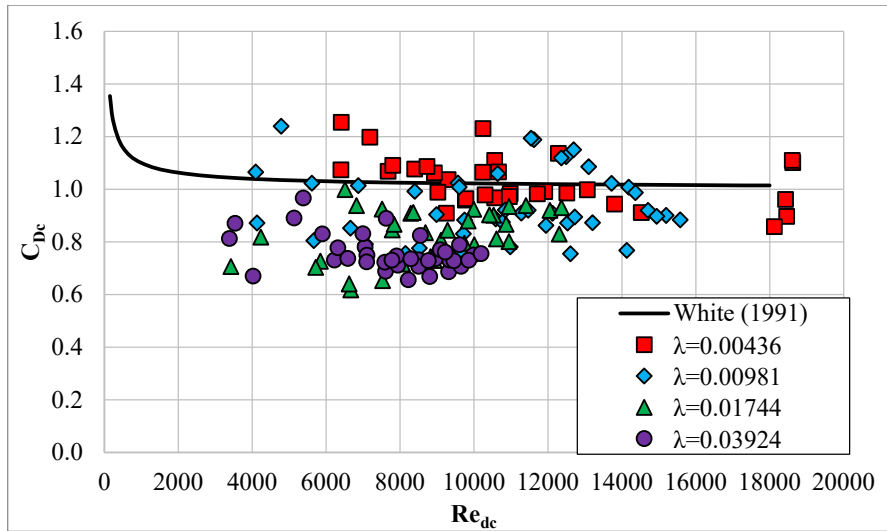
Figure 6.15. Variation of C_{Dc} with Re_{dc} for all emergent vegetation cases and for an isolated cylinder

Figure 6.15 reveals that, compared to Figures 6.13 and 6.14, all data groups considerably shift downward and towards the right-hand side in the vertical and horizontal axes, respectively. As stated previously, the increase in the velocity (i.e., $U_b<U_p<U_c$) decreases the array averaged drag coefficient and causes a higher stem Reynolds number. It was also observed that the drag coefficient of vegetation groups with higher densities (i.e., λ=0.01744 and 0.03924) are affected more than those with lower densities, because an increase in the velocity is directly proportional to the vegetation density.

Unlike the studies of Etminan et al. (2017) and van Rooijen et al. (2018), the use of constricted cross-section velocity does not diminish the scatter of the data in the present study significantly. The main reason is that the present study includes relatively lower vegetation densities (i.e., 0.00436≤λ≤ 0.03924) than the studies mentioned above. It was seen that the use of U_c in the calculation of the drag coefficient is more successful in reducing the scatter of the data at higher vegetation densities than lower ones. In fact, Etminan et al. (2017) proposed the use of U_c as the

reference velocity in Equation (6.19) to calculate the drag coefficient for emergent vegetation (see Figure 9b in their study). This recommendation was also supported by the experimental study of van Rooijen et al. (2018). Contrary to the studies of Etminan et al. (2017) and van Rooijen et al. (2018), the drag coefficient of vegetation groups having higher densities does not collapse on the function of White (1991) in the present study. On the other hand, it was also noted that the data of vegetation groups having lower densities (i.e., λ=0.00436 and 0.00981) are generally gathered onto the White (1991) curve in the present study. Thus, it can be stated that the spatially averaged drag coefficient C_{Dc} (i.e., based on U_c) of emergent vegetation canopy having a density lower than $\approx$0.01 (i.e., $\lambda \leq \approx$0.01) can be estimated roughly using White's (1991) equation for staggered emergent vegetation array at high stem Reynolds numbers.

As mentioned earlier, researchers have not agreed on a single velocity scale that represents the flow velocity and governs the drag force in emergent vegetation. On the one hand, some previous studies simply used the bulk velocity U_b (e.g., Wu et al., 1999; Ishikawa et al., 2000; Lee et al. 2004). On the other hand, most of the researchers preferred to use the pore velocity U_p (e.g., Tanino & Nepf, 2008a; Kothyari et al., 2009; Cheng & Nguyen, 2011) or the constricted cross-section velocity U_c (Stone & Shen, 2002; Etminan et al., 2017; van Rooijen et al., 2018) by considering the presence of emergent vegetation. Moreover, it was observed from some of the studies (e.g., Liu et al., 2008) that the longitudinal velocity profile does not vary significantly along the depth, and the actual velocity can be approximated by the pore velocity (Cheng & Nguyen, 2011). In addition to these velocity scales, the depth-averaged velocity obtained by measuring velocities in vegetation array has also been used in some experimental studies (e.g., Liu et al., 2008). However, it is evident that the selection of the reference velocity significantly influences the calculated drag coefficient values as can be seen from the comparison of Figures 6.13, 6.14 and 6.15. It is considered that the use of the bulk velocity as the velocity scale is not representative of densely vegetated channels, as the presence of

vegetation stems is ignored which can lead to misleading results in the assessment of the drag coefficients. However, it might be used as an approximate velocity in channels with low-density vegetation (Cheng & Nguyen, 2011). On the other hand, both the constricted cross-section velocity and pore velocity consider the presence of vegetation in the flow domain; however, they are not able to reduce the data scattering considerably in the present study. Thus, it can be stated that one of these velocity scales is not superior to the other for the relatively sparse emergent canopies in high stem Reynolds numbers. It should also be noted that as the vegetation density decreases, both velocity scales become closer. Etminan et al. (2017) also stated that the drag modification mechanisms (i.e., sheltering, delayed separation and blockage effects) are not important for low vegetation densities (i.e., $\lambda < 0.04$), so both velocity scales can effectively be used to calculate the canopy drag forces. Nevertheless, it was seen that Equation (6.19) does not represent the data of the present study properly, even if U_b and U_c were used as the reference velocities. Therefore, there is a requirement for equations that can estimate the drag coefficient much better.

In the literature, most of the experimental studies (e.g., Cheng & Nguyen, 2011; van Rooijen et al., 2018) were performed with relatively lower and limited stem Reynolds numbers (i.e., $Re_{dp} < 2000$). However, in nature, there are no limits to restrict the flow conditions, especially during floods. Thus, this experimental study was conducted in large stem Reynolds numbers to extend our knowledge about vegetation flow. To see the overall trend of the drag coefficient in the larger stem Reynolds number range, results of other studies having different stem Reynolds number intervals were gathered and presented together with the result of the present study using U_p and U_c as reference velocities in Figure 6.16. The experimental conditions of all studies are presented in Table 6.2. Moreover, in all these studies, a staggered pattern was used in the distribution of vegetation stems. Figure 6.16 also includes the equation of Sucker and Brauer (1975) which is more robust than White's (1991) equation and given as follows:

$$C_{D-SB} = \frac{6.8}{Re_d^{0.89}} + \frac{1.96}{Re_d^{0.5}} - \frac{1}{\frac{1}{4.10^{-4}Re_d} + \frac{Re_d}{1100}} + 1.18 \qquad (6.20)$$

where $C_{D\text{-}SB}$ is the drag coefficient of an isolated cylinder, and subscript 'SB' describes the Sucker and Brauer's (1975) function.
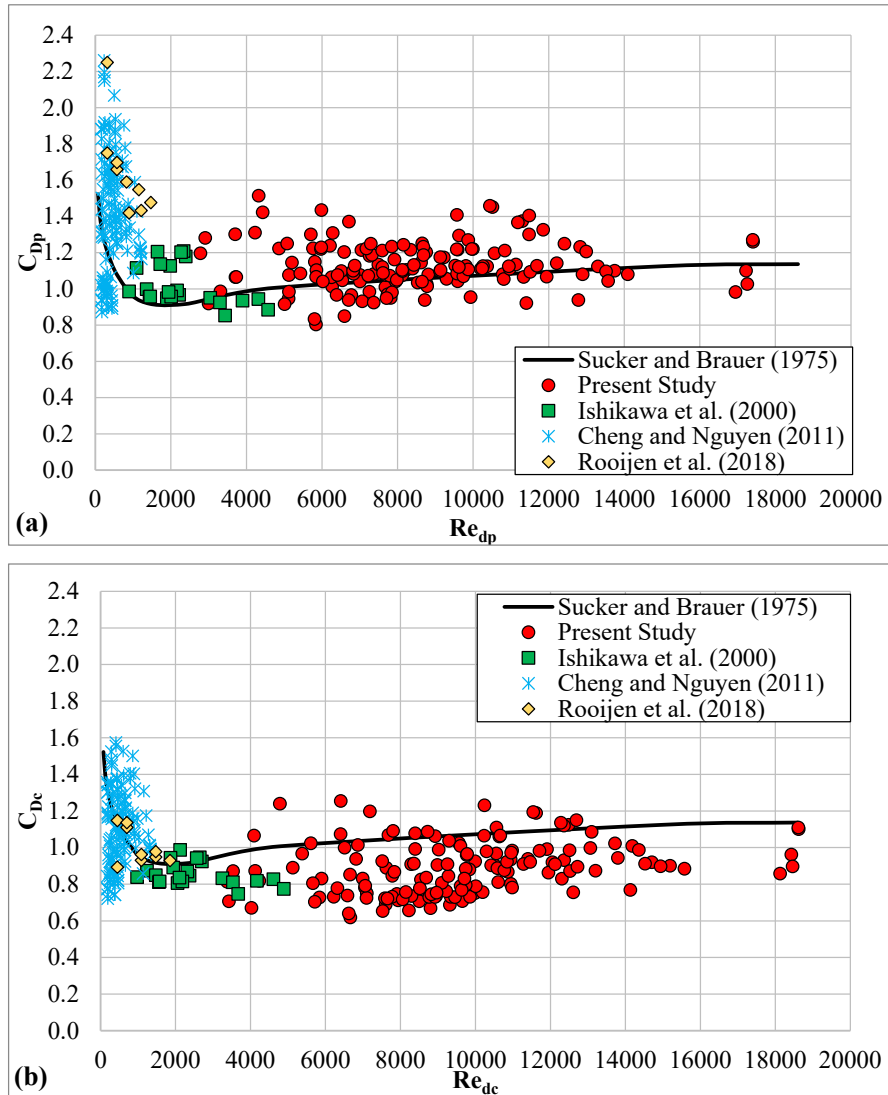
Figure 6.16. Variation of drag coefficients of the present study and similar studies in literature with stem Reynolds number based on a) pore velocity, b) constricted cross section velocity

Table 6.2 Experimental conditions of the present study and similar studies in the literature

Study	λ	D (cm)	Re_{dp}	Re_{dc}	Bed Condition
Ishikawa et al. (2000)	0.0081 - 0.0322	0.40 - 0.64	898 - 4577	974 - 4891	Rough
Cheng and Nguyen (2011)	0.0043 - 0.1189	0.32 - 0.83	163 - 1222	179 - 1347	Smooth
van Rooijen et al. (2018)	0.05 - 0.10	0.64	320 - 1472	448 - 1856	Smooth
Present Study	0.00436 - 0.03924	2.08	2787 - 17409	3381 - 18625	Smooth

As stated previously, Ishikawa et al. (2000) performed experiments on a bed covered with sand having a 1.8 mm mean diameter. Drag force on a single cylinder was measured directly by a mechanism having a strain gauge mounted on top of the channel, so the bed friction effect was eliminated and not included in the drag coefficient calculations. The drag force measurements were repeated for the same flow condition and vegetation array by changing the place of the cylinder in the array. Thus, a spatially-averaged drag coefficient was obtained for a given flow conditions and vegetation array. On the other hand, Cheng and Nguyen (2011) did not directly measure the drag forces, but the array averaged drag coefficients were found from the force balance equation with the use of energy slope. van Rooijen et al. (2018) also measured drag force directly on a single cylinder situated in a vegetation array; however, the location of the dowel was not changed which means that the measured drag coefficient does not represent the array averaged one. In all of these experimental studies, experiments were performed in a channel having smooth sidewalls, so sidewall resistance was also neglected for the present analyses. In the previous sections, it was indicated that the bed shear can be significant and contribute

to total resistance even if the bed is smooth. Thus, it was decided to apply the bed friction correction using Equation (6.15) only for the study of Cheng and Nguyen (2011), as the measured drag forces of other studies do not include bed friction.

As mentioned earlier, if stem Reynolds number intervals of previous studies are considered, the present study can be seen as a complementary study for the literature where the available data is restricted to low stem Reynolds numbers. Moreover, Figure 6.16 shows that the use of U_c in the drag coefficient calculation reduces the data scattering considerably for the studies of Cheng and Nguyen (2011) and van Rooijen et al. (2018). This is because these studies include rather large vegetation densities where the use of U_c decreases the data scattering more satisfactorily. Figure 6.16 also demonstrates that data from the given studies approximately follow Sucker and Brauer's (1975) curve. While this curve has a good performance in the estimation of drag coefficients based on pore velocity (i.e., Figure 6.16a), the same curve slightly overestimates the drag coefficients based on constricted cross-section velocity (i.e., Figure 6.16b). This is due to the fact that this equation is developed for only the drag of single cylinders. Therefore, it needs to be modified in a way that it should also consider the effect of vegetation density on the drag coefficient. Equations (6.21) and (6.22) based on Sucker and Brauer's (1975) formula were derived to consider the vegetation density using a statistical analysis program, and the results are given below:

$$C_{Dp} = C_{D-SB} \cdot (1 + 0.2 \, \lambda^{0.5}) \tag{6.21}$$

which is based on U_p and valid for $0.0043 \leq \lambda \leq 0.03924$ and $163 \leq Re_{dp} \leq 17409$.

$$C_{Dc} = C_{D-SB} \cdot (1 - 0.165 \, \lambda^{0.001}) \tag{6.22}$$

which is based on U_c and valid for $0.0043 \leq \lambda \leq 0.03924$ and $179 \leq Re_{dc} \leq 18625$.

In the derivation of these equations, in addition to the data of the present study, the data of the studies of Ishikawa et al. (2000) and Cheng and Nguyen (2011) were also

used by considering the vegetation density range of the present study. Moreover, it should be noted that Equations (6.21) and (6.22) are valid for the estimation of the drag coefficients not only for an emergent vegetation array but also for a single stem.

In Figure 6.16, the effect of vegetation density on the drag coefficients was not mentioned in detail. Thus, Figures 6.17-6.20 were plotted to compare Equations (6.21), (6.22) and White's (1991) equation with data used in the derivation of Equations (6.21) and (6.22). These figures are classified according to vegetation densities, and data groups having similar vegetation densities were demonstrated in the same graph using C_{Dp} and C_{Dc} as the stem drag coefficients, respectively. Moreover, the vegetation densities of the present study were used to plot revised Sucker-Brauer's (1975) curves (using Equations (6.21) and (6.22)) in Figures 6.17-6.20.

Figure 6.17 shows the comparison of data groups having the lowest vegetation densities with the relevant equations.
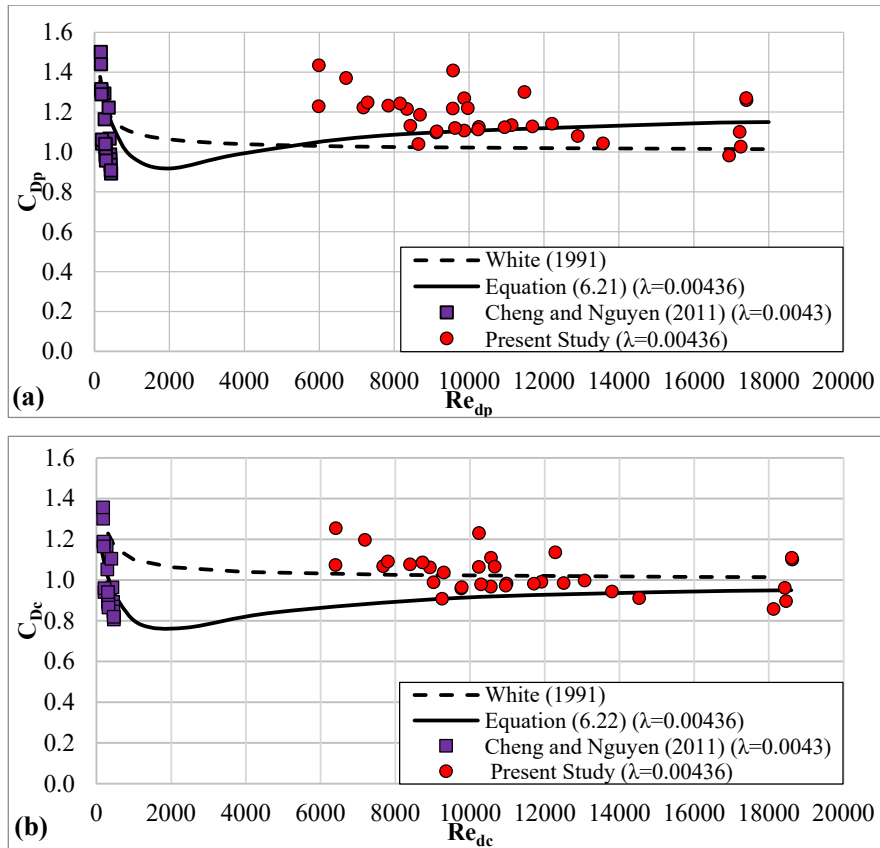
Figure 6.17. Comparison of data groups having lowest vegetation density with
White's (1991) equation, a) Equation (6.21) and b) Equation (6.22)

It was seen that although the drag coefficient of the data group having lower stem Reynolds numbers (i.e., $Re_{dp}<500$ and $Re_{dc}<500$) varies with the stem Reynolds number significantly, Equations (6.21) and (6.22) show consistency with this data group. For the present study's data group having larger stem Reynolds numbers (i.e., $Re_{dp}>6000$ and $Re_{dc}>6000$), it can be stated that while there is an agreement between Equation (6.21) and this data group, Equation (6.22) generally underestimates the drag coefficient values. On the other hand, except for the range of $Re_{dc}>6000$, White's (1991) equation has a poor predictive ability for the given vegetation densities and the stem Reynolds numbers.

Figure 6.18 indicates that although experimental data is quite scattered, Equations (6.21) and (6.22) can averagely represent the variation of the drag coefficients of both data groups.
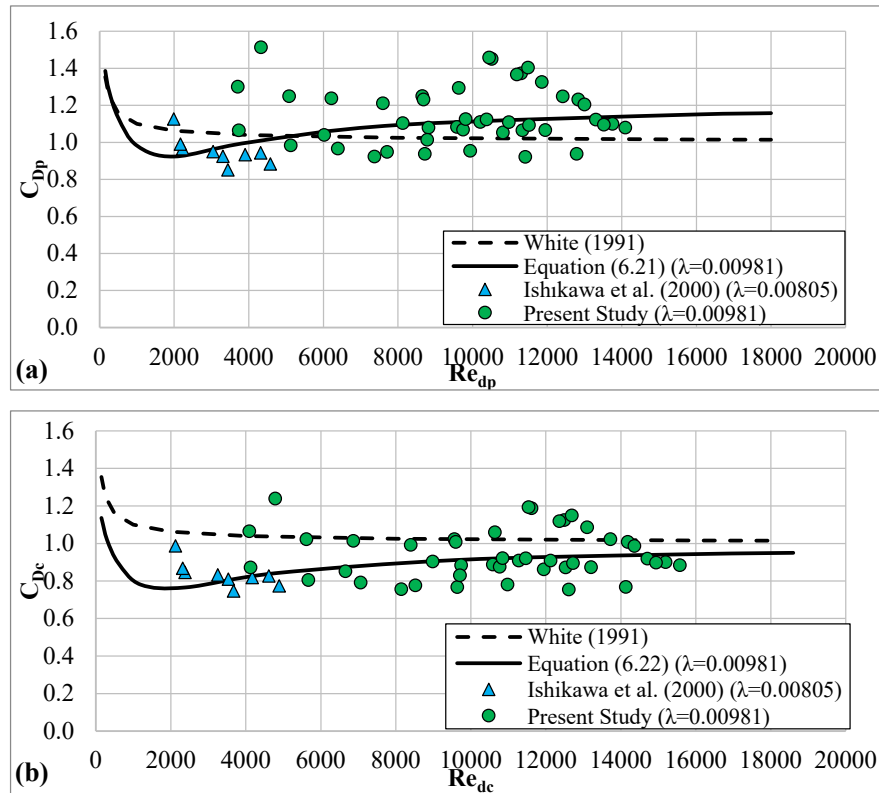
Figure 6.18. Comparison of data groups having relatively low vegetation density with White's (1991) equation, a) Equation (6.21) and b) Equation (6.22)

However, it was also seen from Figure 6.18 that White's (1991) equation considerably deviates from the general trend of data groups, and it estimates the drag coefficient as either less or larger than the experimental results.

Figure 6.19 presents a comparison of four data groups having different stem Reynolds number intervals with Equations (6.21), (6.22) and White's (1991) equation.
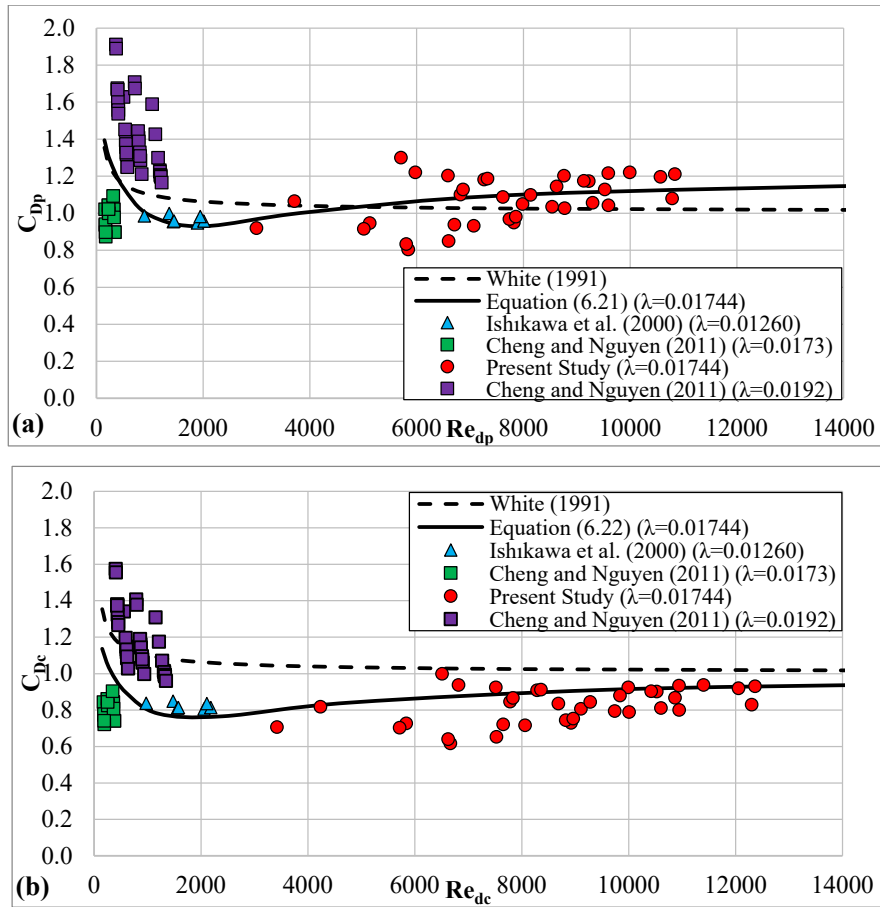
Figure 6.19. Comparison of data groups having relatively high vegetation density with White's (1991) equation, a) Equation (6.21) and b) Equation (6.22)

According to the main trend of data groups in Figure 6.19, it can be stated that the drag coefficient sharply decreases and then increases slightly as the stem Reynolds number increases. Equations (6.21) and (6.22) successfully follow this trend. On the other hand, while White's (1991) equation can roughly represent the main trend of data groups in Figure 6.19a, it substantially overestimates the drag coefficients given in Figure 6.19b.

Figure 6.20 was plotted to investigate a consistency between data groups having the highest vegetation densities and Equations (6.21) - (6.22) and White's (1991) equation.
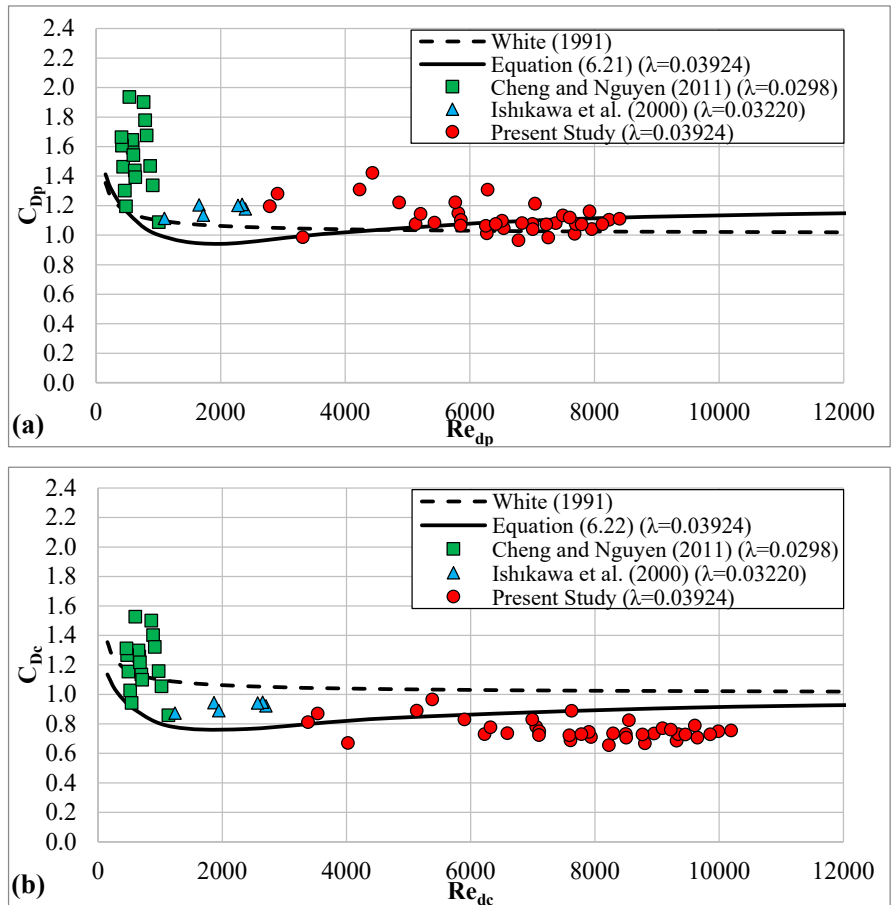
Figure 6.20. Comparison of data groups having highest vegetation density with White's (1991) equation, a) Equation (6.21) and b) Equation (6.22)

It was seen from Figure 6.20 that Equations (6.21) and (6.22) underestimate the drag coefficients of data groups having $Re_{dp}<2500$ and $Re_{dc}<3000$, respectively. For larger stem Reynolds numbers, Equation (6.21) is in good agreement with the data group, whereas Equation (6.22) mostly overestimates the drag coefficients compared

100

to the given data. Moreover, similar to the previous cases, White's (1991) equation considerably deviates from the data distribution.

In summary, while some of the previous studies (e.g., Etminan et al., 2017; van Rooijen et al., 2018) state that White's (1991) equation is quite successful in estimating the drag coefficient of vegetation arrays when U_c is used as the reference velocity, the present study shows that White's (1991) equation is not successful in predicting the drag coefficient of vegetation arrays with the use of neither U_p nor U_c as the reference velocities for the given vegetation densities and stem Reynolds number intervals.

The performance of Equations (6.21) and (6.22) in the prediction of drag coefficients were demonstrated in Figure 6.21 using a data group of the present study.
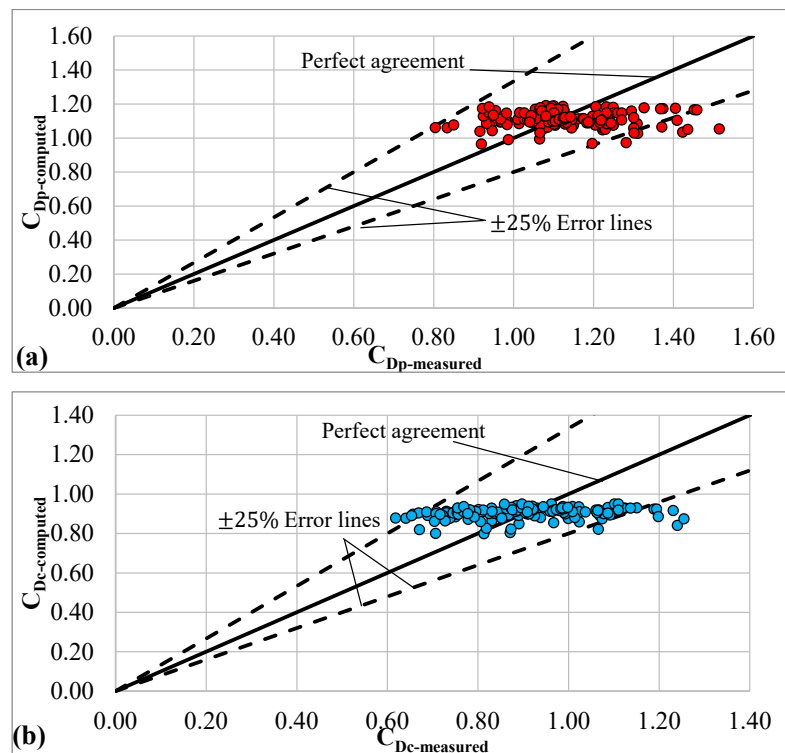
Figure 6.21. Comparison of measured data of the present study with computed ones using a) Equation (6.21) and b) Equation (6.22)

101

Although the data of the present study is scattered and can not be represented by a function easily as demonstrated in Figures 6.17-6.20, Figure 6.21 indicates that almost all of the data remains between $\pm 25\%$ error lines. Thus, it can be stated that the averaged drag coefficient of rigid emergent canopies can be estimated approximately using Equations (6.21) and (6.22) instead of White's (1991) equation for the given vegetation characteristics and flow conditions.

6.1.2 Numerical Analysis and Results of the Emergent Vegetation Conditions

In this section, the drag coefficient of emergent vegetation cases having three different densities was examined by numerical analyses in detail. Each numerical analysis was run for 17000 iterations with a Δt of $0.025H/U_b$ to ensure that the numerical results reached to statistically steady state condition. For post-processing, a macro was developed to evaluate the drag force acting on each member. This macro reads the pressure at each grid point placed on the vegetation stem and calculates the partial drag force in a streamwise direction by integrating pressure on each mesh surface. Later, these partial drag forces were combined into the total drag force of the stem member using Fortran code. As a result, the drag force in the flow direction for each vegetation stem was evaluated. Furthermore, to check the integration process of the macro, the drag force on a random stem sample in the densest vegetation case was calculated by hand. It was seen that both results were very close (i.e., 0.26% deviation) to each other, so it was sure that the macro and the Fortran code executed properly. It is not possible to give the drag coefficients of each vegetation stem in figures because of the large number of vegetation stems (e.g., 769 members in one of the cases). Thus, the drag coefficient results will be given as an arithmetic means of each vegetation row (i.e., spanwise averaged drag coefficient) as shown in Figure 6.22.
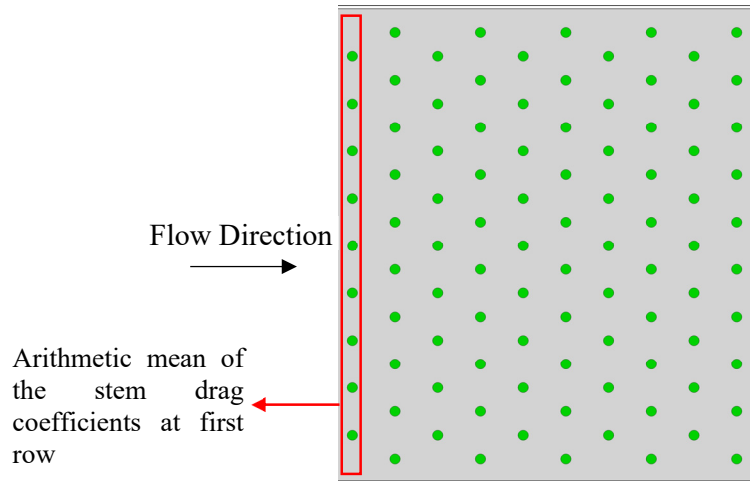
Figure 6.22. Illustration of the spanwise averaged drag coefficient process from top view

For the densest emergent vegetation case, E10, a variation of the drag coefficient of each stem row with longitudinal distance is demonstrated in Figure 6.23. Here, the longitudinal distance is defined as the dimensionless horizontal distance between the channel entrance and the center of the vegetation stem. As can be seen from Figure 6.22, there are 9 and 10 stems at every two consecutive rows.
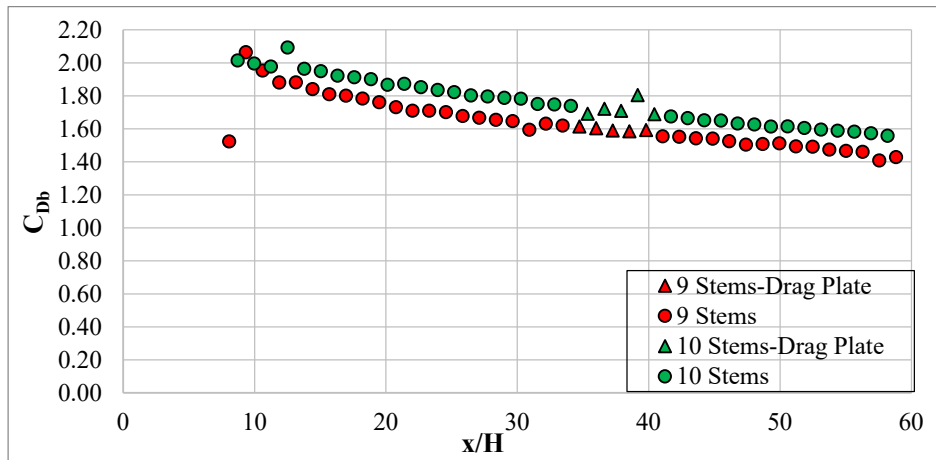
Figure 6.23. Variation of the spanwise averaged drag coefficients with longitudinal distance for the E10 case

103

In Figure 6.23, the spanwise averaged drag coefficients of rows having 9 and 10 vegetation stems are represented by red and green circles, respectively. Furthermore, the drag coefficient of rows placed on the drag plate is demonstrated with triangular markers. Figure 6.23 reveals that the row-averaged drag coefficients do not reach a constant value; instead, they change with a decreasing trend till the end of the domain. There are two possible reasons for this: Firstly, the simulation does not reach a statistically steady state condition, so the number of iterations should be increased. Secondly, which seems more probable, it may be possible that the total length of the vegetation array is not long enough to reach fully developed flow conditions. Thus, to test the first option, the number of iterations was increased by nearly 50% for the same configuration to check whether the statistically steady state condition was reached. It was seen that there was not any change in the decreasing trend and the magnitude of the drag coefficients. The longitudinal velocity profiles at six different sections were investigated to evaluate the second possibility. The measurement stations of the velocity profiles are shown in Figure 6.24.
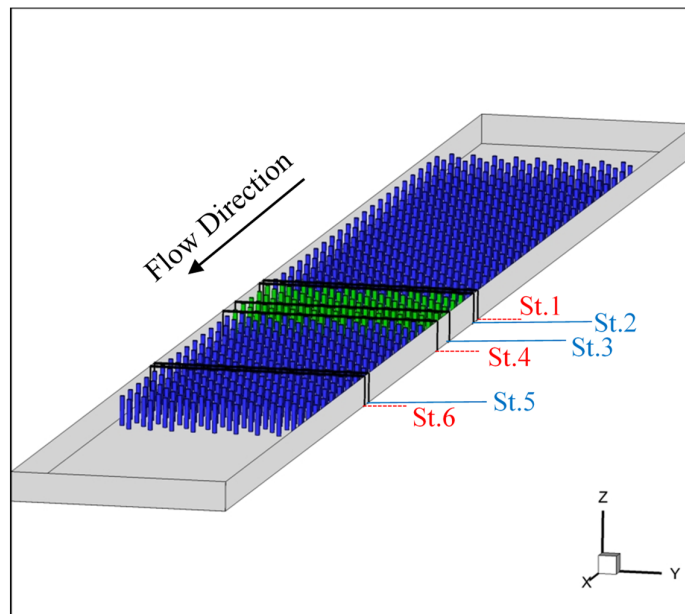
Figure 6.24. The measurement stations of the velocity profiles

In Figure 6.24, the measurement stations downstream of the rows having 9 and 10 stems are shown by blue color (i.e., stations 2,3 and 5) and red color (i.e., stations 1, 4 and 6), respectively. Figure 6.25 compares the velocity profiles of red and blue stations separately. These velocity profiles represent spanwise averaged streamwise velocities in the transverse section (i.e., in the y direction).
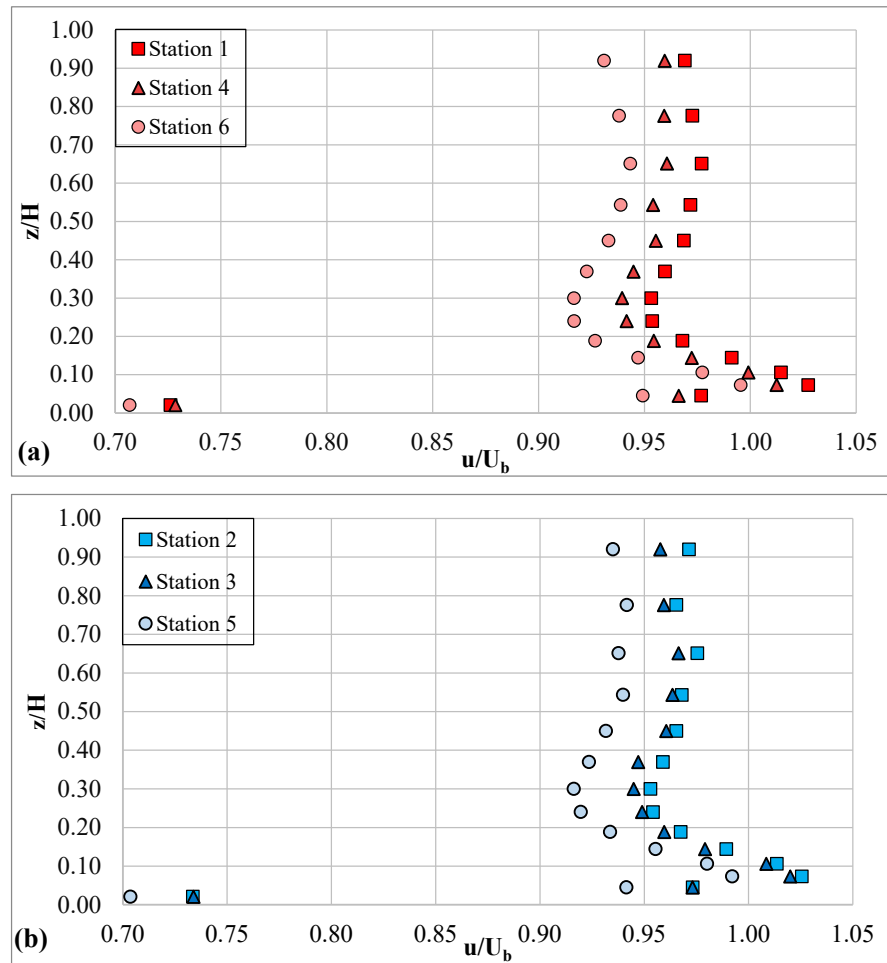
Figure 6.25. Comparison of the velocity profiles a) Red stations b) Blue stations

Figure 6.25 indicates that there are discrepancies between the velocity profiles which means that the velocity is not fully developed in the streamwise direction for the given flow conditions and vegetation array. Thus, it can be stated that this

configuration acts as a vegetation patch rather than a vegetation array. A longer vegetation array is required to obtain fully developed velocity profiles and, thus, the fully developed drag coefficients. However, it is not possible to elongate the vegetation array in the streamwise direction for now, because there is already a large amount of mesh in the domain.

The present numerical analysis suggests that the spatially averaged drag coefficient of vegetation members on the drag plate is C_{Db-num}=1.664. This result is significantly greater than the corresponding experimental result of the present study, C_{Db-exp}=1.166, and those of similar studies in the literature. Likewise, in the study of Kothyari et al. (2009), the drag coefficient of a cylinder placed in a relatively short array was close to the numerical analysis result of the present case at similar stem Reynolds number and vegetation density. This is due to the fact that the given vegetation array lengths are not long enough to obtain a fully developed flow as shown in Figure 6.25. Cheng and Nguyen (2011) also drew a similar conclusion for the study of Kothyari et al. (2009). In addition to these, it seems from Figure 6.23 that although there is no sheltering effect on the plant stems at the first row of the vegetation array, the spanwise averaged drag coefficient of them is considerably lower than others. This is because channeling starts after the first row of the vegetation array. Here, the presence of two neighbor vegetation stem situated at sequent rows creates a 'mini channel' between them where the streamwise velocities are considerably larger than the average streamwise velocity as shown in Figure 6.26. These higher velocities near the plant stem further decrease pressures in the wake, so the drag force of the corresponding stem is increased due to the larger pressure gradient. That phenomenon was mentioned in Chapter 3 as the blockage effect which is also responsible for having a larger spanwise averaged drag coefficient in the first row than that of an isolated (single) cylinder (i.e., $C_{D-isolated} \cong 1.0$).
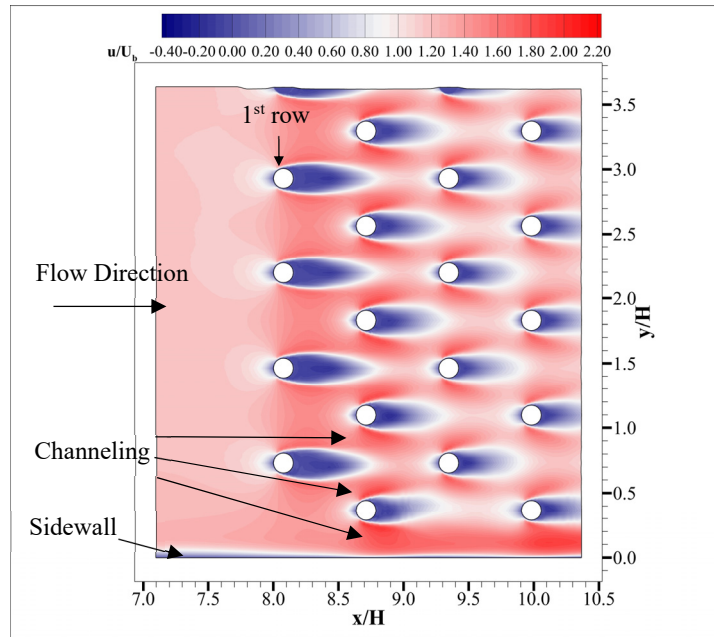
Figure 6.26. Velocity distribution between vegetation stems and channeling for the E10 case

It was also observed from Figure 6.23 that the spanwise averaged drag coefficient of rows with 10 stems is larger than that of rows with 9 stems. This can be explained in a way that two stems situated close to both sidewalls in the rear rows (i.e., rows with 10 plant stems) have larger drag coefficients than others. Figure 6.26 demonstrates that the channeling near the sidewalls is stronger than the inner ones, which increases the blockage effect and, thus the drag coefficient of these two plant stems.

As mentioned in Chapter 5, an additional numerical case was performed to investigate whether the numerical solutions are grid independent, and the E10 case was selected to be used in this grid independency study. Although the number of grid points in the coarser mesh is nearly 19% lower than that of the finer mesh (i.e., the number of grid points are 25804800 and 20992000 for finer and coarser meshes, respectively), there is no difference between the spatially averaged drag coefficients

for these two cases (i.e., deviation 0.66%). Thus, it can be stated that solutions are independent of the grid.

For another case, E20, a variation of the drag coefficient with longitudinal distance is revealed in Figure 6.27. As can be remembered from Chapter 5, this vegetation array includes rows with 4 and 5 stems, respectively.
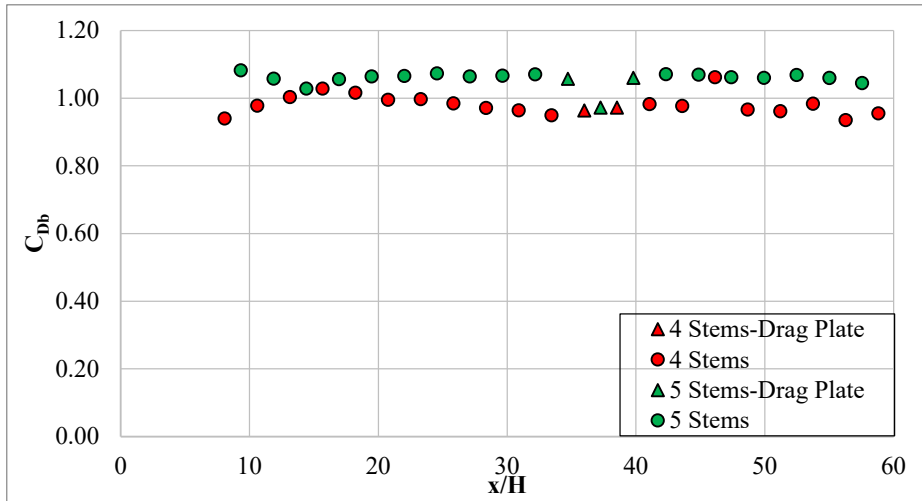
Figure 6.27. Variation of the spanwise averaged drag coefficients with longitudinal distance for the E20 case

Figure 6.27 depicts that the spanwise averaged drag coefficient of rows with 5 plant stems is slightly larger than that of rows with 4 plant stems. Similar to the previous case, this slight difference is due to the fact that a stronger channeling occurs near the sidewalls, which reduces the pressures in the wake much more, thus increasing the drag force of relevant plant stems. On the other hand, having a nearly constant drag coefficient distribution in Figure 6.27, it can be stated that the flow in the vegetated array was fully developed for the given flow and vegetation conditions. Moreover, the velocity profiles were investigated at various sections, and it was observed that fully developed flow occurs in the vegetation array (the velocity profiles are not presented here). The spatially averaged drag coefficient of stems

situated at the drag plate was found as C_{Db-num}=1.026 from the present numerical analysis. On the other hand, the drag coefficient of the corresponding experimental case was calculated as C_{Db-exp}=1.132. There is a reasonable agreement (i.e., a slight discrepancy ≈10%) between the results of the experimental study and the numerical analysis, which proves that the novel experimental setup measures the drag forces of emergent stems with quite good accuracy. This little discrepancy may be attributed to this possible reason: The free surface effects (e.g., a slight wave action) were neglected in the numerical analysis (i.e., rigid lid assumption). Additionally, the value of the spatially averaged drag coefficient demonstrates that the drag modifying mechanisms such as sheltering and blockage effects are not significant in the present case for the given flow conditions. Thus, the spatially averaged drag coefficient of the vegetation array is similar to that of an isolated cylinder for the given vegetation density, λ=0.00981.

Finally, Figure 6.28 presents the variation of the drag coefficient along the vegetation array for the lowest vegetation density case, E30. This vegetation array includes rows with 4 and 3 stems, respectively. As in the previous case, Figure 6.28 demonstrates that the spanwise averaged drag coefficients are constant which means that the fully developed flow conditions were reached in the vegetation array.
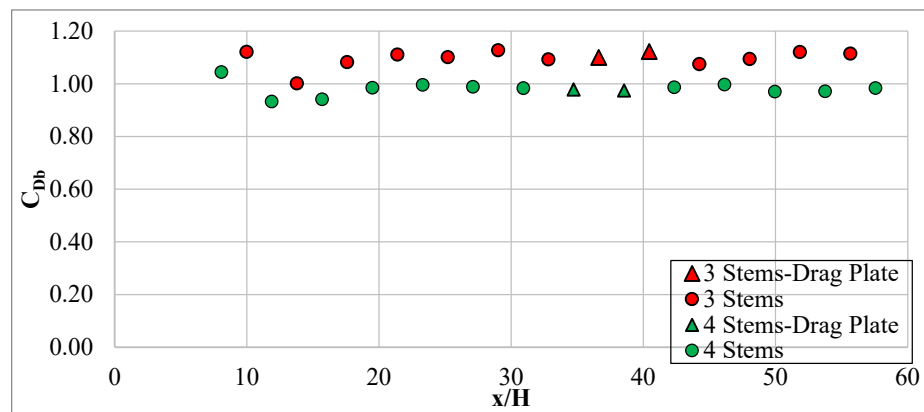
Figure 6.28. Variation of the spanwise averaged drag coefficients with longitudinal distance for the E30 case

Contrary to former cases, it was observed that the spanwise averaged drag coefficient of rows having a higher number of stems is less than that of rows having a lower number of stems. This condition can be explained as follows: This time, Figure 6.29 shows that a stronger channeling which occurred at the inner sections (e.g., (2) and (3)) rather than near the sidewalls (e.g., (1)) creates larger velocities near the plant stems at these regions. Thus, the wake pressure of stems situated inner sections is lower than that of stems near the sidewalls due to larger velocity at the outside of the wake. Of course, lower pressure in the wake results in higher stem drag force and drag coefficient.
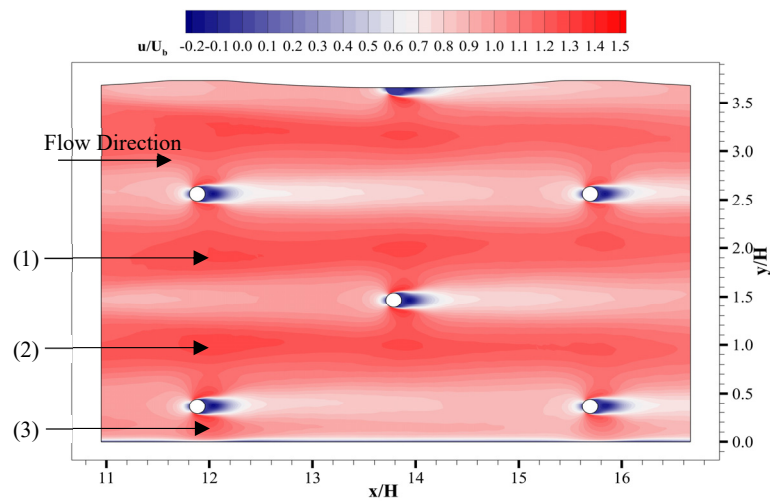
Figure 6.29. Velocity distribution between vegetation stems and channeling for the E30 case

The spatially averaged drag coefficient of stems on the drag plate was found as $C_{Db\text{-}num}=1.034$ and $C_{Db\text{-}exp}=1.152$ from the numerical analysis and experiments, respectively. As in the previous case, there is an agreement (i.e., a little discrepancy $\approx 11\%$) between numerical and experimental results for this vegetation density as well. Moreover, these averaged drag coefficients reveal that the drag modifying mechanisms are not effective so much in the emergent vegetation array having a density less than 0.01 for the given flow conditions. Thus, the spatially averaged drag

110

coefficients of these emergent cases are similar to that of an isolated cylinder for the given flow conditions.

Finally, the effect of vegetation density on the pressure coefficients of stems, c_p, was investigated. Herein, the pressure coefficients were calculated using Equation (6.23) as given below:

$$c_p = 1 - \frac{p_{\theta=0} - p}{0.5 \rho U_b^2} \tag{6.23}$$

where $p_{\theta=0}$ is the pressure at the stagnation point, p is the pressure at any measurement point, and θ is the angle between the stagnation point (i.e., $\theta=0$) and the pressure measurement point on the stem (see Figure 3.2 in Chapter 3 for illustration). Figure 6.30 reveals the variation of pressure coefficient with θ for various vegetation densities. The pressure measurements were taken from a stem located in the mid-width of the drag plate for each vegetation density. Moreover, c_p curve of a single cylinder taken from the study of Etminan et al. (2017) was also included for completeness. Although stem Reynolds numbers are different for each case (e.g., Re_{db}=1340, 12230, 10865 and 6157 for single cylinder and cases E30, E20 and E10, respectively), it was seen from the study of Etminan et al. (2017) that the effect of the stem Reynolds number on the pressure coefficients nearly vanishes after Re_{db}>1000 (see Figure 6b in their study). Thus, it can be said that Figure 6.30 merely shows the effect of canopy density on the pressure coefficient.
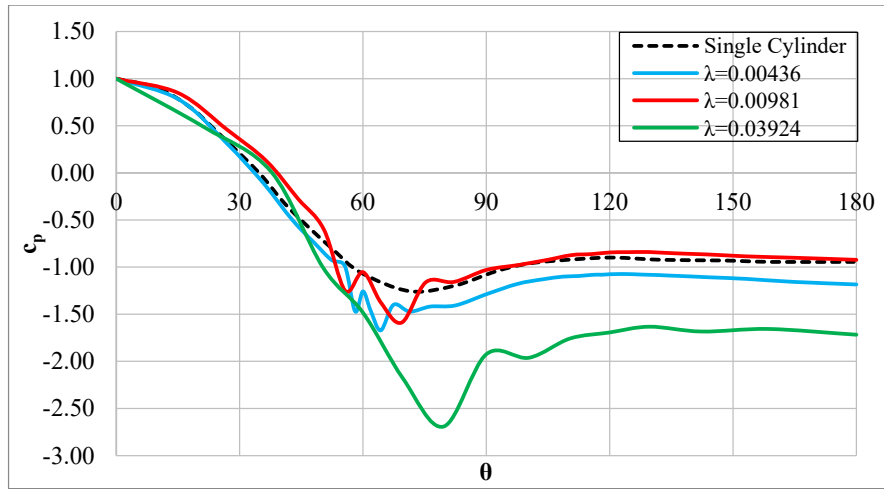
Figure 6.30. Pressure coefficient distribution on stems for various vegetation densities

The velocities between the plant stem in the same streamwise position increase as the vegetation density increases, which further decreases the pressure inside the wake. In other words, a larger blockage ratio leads to a lower pressure coefficient. As expected, the vegetation array with the largest canopy density, case E10, has the lowest pressure coefficient distribution due to a larger blockage effect, so its pressure coefficient curve remains under the curve of other cases. Figure 6.30 also demonstrates that the pressure coefficient of the stem in case E30 is lower than that of case E20. The reason for this may be that sheltering effect diminishes as the streamwise distance between stems increases (as the vegetation density decreases), so the mid-dense vegetation array (i.e., case E20) has lower impact velocities, which results in a larger pressure coefficient. This explanation was also supported by the study of Etminan et al. (2017) which stated that sheltering effect becomes more pronounced in relatively sparse canopies as the vegetation density increases. Furthermore, it was observed that the pressure coefficient distribution of the mid-dense vegetation array is very similar to that of a single cylinder, because the sheltering and blockage effects cancel each other out. Thus, the pressure coefficient

distribution of the mid-dense vegetation array becomes very close to that of a single cylinder. In summary, in the present study, it was found that while the pressure coefficient distribution of the stems in the vegetation arrays with lower densities (i.e., cases E20 and E30) is similar to that of the isolated cylinder, the pressure coefficients considerably decrease for stems in the array with the highest vegetation density (i.e., the E10 case).

6.2   Submerged Vegetation Cases

6.2.1   Experimental Analysis and Results of the Submerged Vegetation Conditions

Similar to the emergent vegetation case, in the first subsection, the effect of submerged vegetation on the total flow resistance will be investigated using Manning's roughness coefficient and Darcy-Weisbach friction factor, respectively. Later, the bed shear stresses and their contribution to the total drag will be examined for cases having various submergence ratios. At the end of this subsection, the average drag coefficient of the submerged vegetation array will be evaluated for four different vegetation densities.

6.2.1.1   Effect of Submerged Vegetation on Manning's Roughness Coefficient

In the previous subsection (i.e., subsection 6.1.1.1.), the force balance equation, Equation (6.1), was derived for the emergent vegetation flow. Now, for similar flow conditions, if the force equilibrium between gravitational and resistive forces (e.g., vegetation and bed drag) is written for the control volume in the submerged vegetation array using average stem layer velocity, U_s (m/s), as the reference velocity, Equation (6.24) can be obtained as follows:

$$\gamma A_1 L S_f (1 - \lambda h^*) = \frac{1}{2} M C_D \rho U_s^2 A_2 + \frac{f_b}{8} \rho U_s^2 B L (1 - \lambda) \tag{6.24}$$

where U_s represents the average velocity in the submerged vegetation layer. Herein, Stone and Shen (2002) proposed a simplified relationship between U_s and U_b as follows:

$$\frac{U_s}{U_b} \approx \sqrt{h^*} \tag{6.25}$$

If Equation (6.25) and Manning's equation are substituted into Equation (6.24), the following relation can be obtained:

$$n = \sqrt{\left(\frac{R_h^{\frac{1}{3}}}{2g}\right)\left(\frac{C_D(aR_h)h^*}{(H-\lambda h_v)} + \frac{f_b R_h(1-\lambda)h^*}{4(H-\lambda h_v)}\right)} \tag{6.26}$$

For wide channels ($R_h \approx H$), Equation (6.26) becomes:

$$n = \sqrt{\left(\frac{H^{\frac{1}{3}}}{2g}\right)\left(\frac{C_D(aH)h^*}{(H-\lambda h_v)} + \frac{f_b H(1-\lambda)h^*}{4(H-\lambda h_v)}\right)} \tag{6.27}$$

where $C_D = f_6(Re_{db}, \lambda, h^*)$. Equation (6.26) shows that $n = f_7(C_D, aR_h$ (or aH), h^*, $f_b)$, and the effect of these parameters on Manning's roughness coefficient will be investigated individually.

In the study of van Rooijen et al. (2018), drag coefficients based on the bulk velocity are nearly constant where stem Reynolds number is larger than 1000, $Re_{db} > 1000$, for a given submergence ratio and areal vegetation density (see Figure 6A in their study). Like the discussion of the emergent vegetation part in the present study, stem Reynolds numbers of submerged vegetation cases are also large enough so that the effect of the stem Reynolds number on the drag coefficient can be negligible. Moreover, areal stem density and submergence ratio are already defined in the functional relation of Manning's roughness, so the final relation is obtained by discarding C_D as $n = f_8(aR_h$ (or aH), h^*, $f_b)$. Since the experiments were performed on only single (smooth) bed material as mentioned in the previous part, f_b can also be eliminated from the functional relation for the present study.

Although the submerged vegetation height is largely variable in canopy flows, shallow submergence (i.e., $H/h_v \leq 5$) is usually encountered in aquatic systems due to limited light penetration (Ghisalberti & Nepf, 2009; Nepf, 2012). Therefore, the submergence ratio in the present study is also limited by considering this recommended threshold (i.e., $h^* > 0.2$). Figure 6.31 reveals the relation between Manning's roughness coefficient and submergence ratio for different vegetation densities. In this figure, trend lines having the same color with their data set were also plotted to show the relation more clearly.
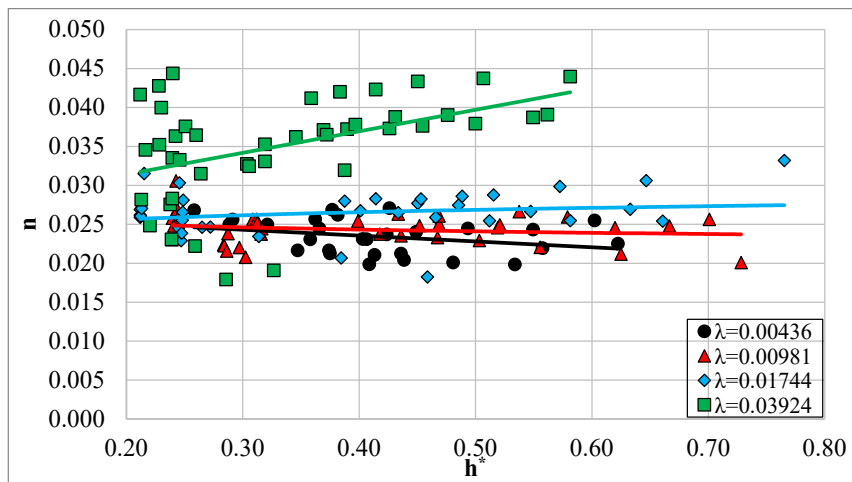
Figure 6.31. Variation of Manning's roughness with submergence ratio for different vegetation densities

As seen from Figure 6.31, trend lines are almost constant, except for the highest density case, which means that there is no significant effect of the submergence ratio on the total flow resistance for these three vegetation densities. Nepf (2012) proposes a threshold roughness concentration value for submerged vegetation, $ah_v \approx 0.1$, which determines whether the canopy is sparse or dense. It was also stated that the resistance of the canopy is small compared to the bed resistance in sparse canopies, and bed roughness is enhanced with the contribution of vegetation, where the velocity profile can be represented by a turbulent boundary-layer profile. In other

words, flow behavior in sparse canopies is similar to those having rough boundary characteristics. According to this description, vegetation groups having an areal density of λ=0.00436, 0.00981 and 0.01744 can be classified as sparse canopies in the present subsection. Yen (2002) reported that Manning's roughness coefficient is nearly constant and does not depend on relative roughness for fully developed turbulent flow over the rough boundary. Thus, this statement clarifies the constant trend of Manning roughness coefficients in Figure 6.31. However, in the present study, even for sparse densities of submerged vegetation, Manning's roughness coefficient approximately reaches a value of 0.025. This is a value much larger than the typical value of 0.01 for smooth plexiglass (Chow, 1959). On the other hand, Manning's roughness coefficient can further increase as the submergence ratio increases for the dense vegetation case, λ=0.03924, similar to the findings of Wu et al. (1999) and Wilson and Horritt (2002).

The relation between aR_h and Manning's roughness is demonstrated in Figure 6.32 for different submergence ratios. Trend lines (i.e., linear best fits) having the same color with the data group were also plotted to show the relation more clearly. Each color represents different submergence ratio groups within an interval of 0.1.
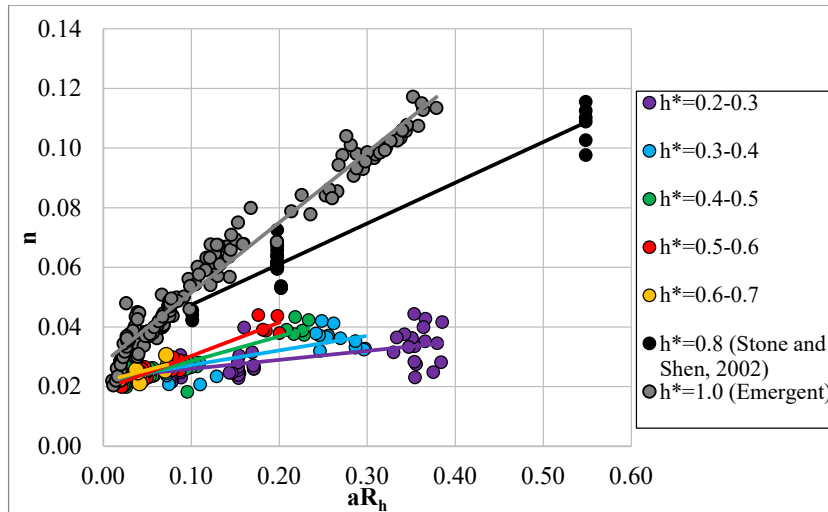
Figure 6.32. Variation of Manning roughness with aR_h for different submergence ratios

As can be seen from this figure, Manning's roughness increases as aR_h parameter increase for each h^* value. Also, the slope of trend lines, which shows the increasing rate of n, increases as the submergence ratio increase. Unfortunately, there are only two submergence ratio data above $h^*=0.7$ (i.e., $h^*>0.7$), so these points were not added to the graph. Herein, the literature was investigated extensively to find data groups having a submergence ratio larger than 0.7 (i.e., $h^*>0.7$). Most of the studies were eliminated due to their discrepancy in experimental setup and flow conditions (e.g., rough wall boundaries, flexible stems and $h^*<0.7$). Finally, the study of Stone and Shen (2002) was found to be compatible with the criteria mentioned above and thus added to Figure 6.32. It was seen that the data of Stone and Shen (2002) (i.e., $h^*=0.8$) was distributed between the zone of $0.7<h^*<1.0$, and the slope of the best-fit line of this data group is matched with an increasing slope trend.

To make a more comprehensive analysis and enhance the range of related parameters (e.g., aR_h, h^* or ah_v), in the present study, data groups of three additional studies; Dunn et al. (1996), Stone and Shen (2002) and Cheng (2011), having a similar experimental setup and conditions (e.g., smooth bed and sidewalls, staggered

pattern) were gathered from literature, and thus a larger data set was obtained. The range of important parameters of these studies are presented in Table 6.3.

Table 6.3 The range of important parameters in the relevant studies

Study	λ	D (cm)	Re_{db}	h^*	n
Dunn et al. (1996)	0.0014-0.0120	0.635	1891-5421	0.300 - 0.720	0.025 - 0.056
Stone and Shen (2002)	0.0055-0.0610	0.32/0.635/1.3	126-5405	0.395 - 0.821	0.027 - 0.139
Cheng (2011)	0.0043-0.1189	0.32/0.66 /0.83	459-2130	0.500 - 0.769	0.036 - 0.139
Present Study	0.0044-0.0392	2.08	2641-16653	0.212 - 0.765	0.018 - 0.044

It was seen that aR_h and submergence ratios are the main parameters that affect the bulk flow resistance from Equation (6.26) and Figure 6.32. Thus, a multiple non-linear regression analysis was performed using these data sets. In that analysis, 247 data points having a stem Reynolds number larger than 1000 (i.e., Re_{db}>1000) were used to eliminate the indirect effect of Re_{db} on n, and the following equation was obtained:

$$n = 0.129(aR_h)^{0.355}(h^*)^{0.724} \text{ with } R^2=0.867. \tag{6.28}$$

Figure 6.33 was also presented to demonstrate the performance of Equation (6.28) in the estimation of n. Figure 6.33a shows that most data points remain between ±20% error bands. Also, the percentages of data corresponding to the relevant error band were presented in Figure 6.33b in detail. Thus, it can be concluded that Equation (6.28) shows good performance so that it can be used to predict Manning's

roughness coefficient in submerged canopies for the given flow condition and vegetation characteristics.
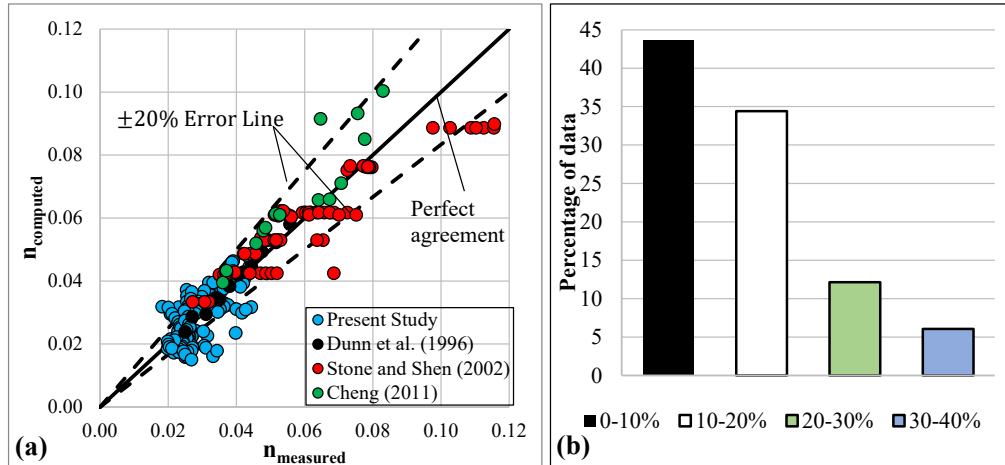
Figure 6.33. a) Comparison of $n_{measured}$ with $n_{computed}$ using Equation (6.28)

b) Histogram of error percentages

In addition to the relation presented above, an alternative relation can be proposed to estimate the bulk flow resistance using roughness concentration, ah_v, instead of aR_h as follows:

$$n = 0.101(ah_v)^{0.294}(h^*)^{0.416} \text{ with } R^2 = 0.848. \tag{6.29}$$

A statistical performance analysis was also conducted for Equation (6.29) and presented in Figure 6.34.
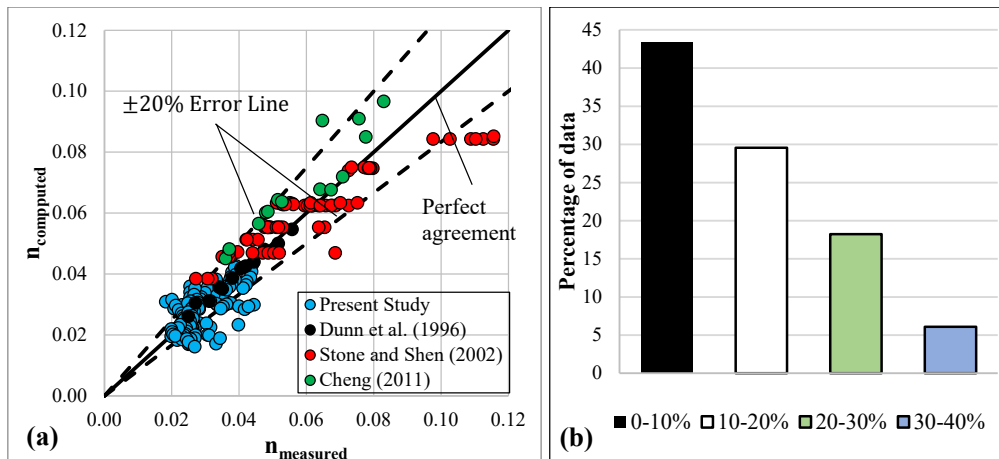
Figure 6.34. a) Comparison of $n_{measured}$ with $n_{computed}$ using Equation (6.29)

b) Histogram of error percentages

Figure 6.34 and the corresponding R^2 value shows that there was not any significant improvement in the estimation of Manning's roughness coefficient when the roughness concentration was used instead of aR_h, and they exhibit a similar prediction performance. Besides to general performance of Equations (6.28) and (6.29), it was observed that almost all data points belonging to the study of Dunn et al. (1996) lie very close to the perfect agreement line in Figures 6.33a and 6.34a. Therefore, it can be said that these equations are quite successful in estimating Manning's roughness coefficient for the data of Dunn et al. (1996).

6.2.1.2   Effect of Submerged Vegetation on Darcy-Weisbach Friction Factor

Flow resistance due to submerged vegetation can also be defined with Darcy-Weisbach friction factor as shown in the emergent vegetation case. To determine independent parameters that can affect the friction factor in the submerged cases, a mathematical process similar to that in emergent vegetation case can be followed.

If Equations (6.9) and (6.25) are substituted into Equation (6.24), Equation (6.30) can be obtained as follows:

$$\frac{U_b}{U_*} = \sqrt{\frac{8}{f}} = \sqrt{\frac{8(H-\lambda h_v)}{4C_D h^* a h_v R_h + f_b R_h h^*(1-\lambda)}} \tag{6.30}$$

As can be seen from Equation (6.30), the coefficient of velocity can be defined by a dimensionless relationship, U_b/U_*=f_9(C_D, h^*, ah_v (or aR_h), f_b, λ). If similar statements about C_D, f_b and λ are considered as in the previous section (e.g., Re_{db}>1000, single bed roughness (smooth)), the coefficient of velocity can be expressed simply as U_b/U_*=f_{10}(h^*, ah_v (or aR_h)). Herein, a statistical analysis can be performed to explicitly see the relation between the coefficient of velocity and these independent dimensionless parameters.

Multivariate non-linear regression analysis is carried out using data from the present and aforementioned three similar studies (Dunn et al., 1996; Stone & Shen, 2002; Cheng, 2011). Firstly, the statistical relation between aR_h, h^* and the coefficient of velocity was examined, and the following power relation was found:

$$\frac{U_b}{U_*} = 2.567(aR_h)^{-0.249}(h^*)^{-0.501} \text{ with } R^2\text{=}0.784. \tag{6.31}$$

The performance of Equation (6.31) was assessed in Figure 6.35a which shows that most of the data remain within $\pm$20% error band. Furthermore, Figure 6.35b demonstrates the error bands and corresponding data percentages in detail. Herein, it was observed that nearly half of the data was included in 0-10% error bands. Therefore, it can be said that the prediction accuracy and performance of Equation (6.31) is good enough to be used to calculate the coefficient of velocity (or friction factor).
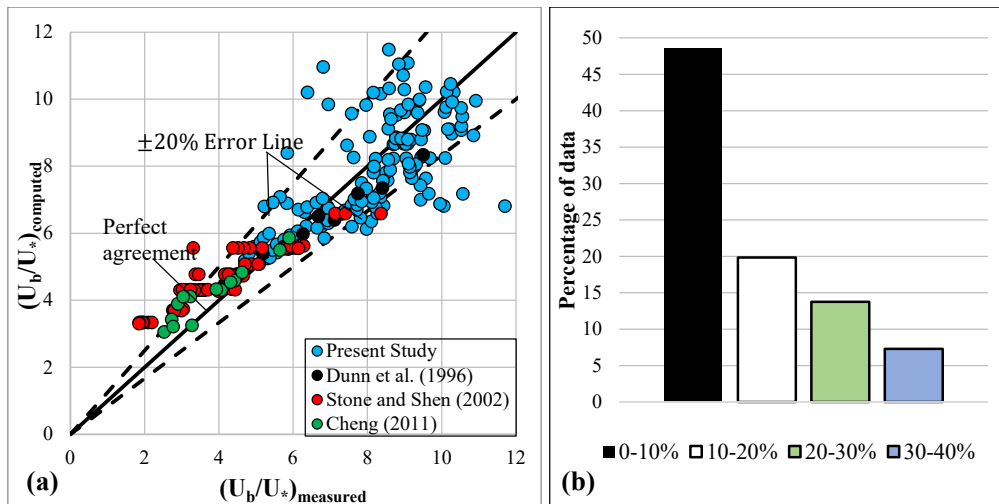
Figure 6.35. a) Comparison of $(U_b/U_*)_{measured}$ with $(U_b/U_*)_{computed}$ using Equation (6.31) b) Histogram of error percentages

Alternative to Equation (6.31), Equation (6.32) is also proposed using roughness concentration, ah_v, instead of aR_h and given below:

$$\frac{U_b}{U_*} = 2.994(ah_v)^{-0.222}(h^*)^{-0.261} \text{ with } R^2=0.80.$$ (6.32)

The performance of Equation (6.32) was examined in Figure 6.36. Similar to Figure 6.35, data are mostly distributed within $\pm$ 20% error bands, and $\pm$10% error bands include almost half of the data.
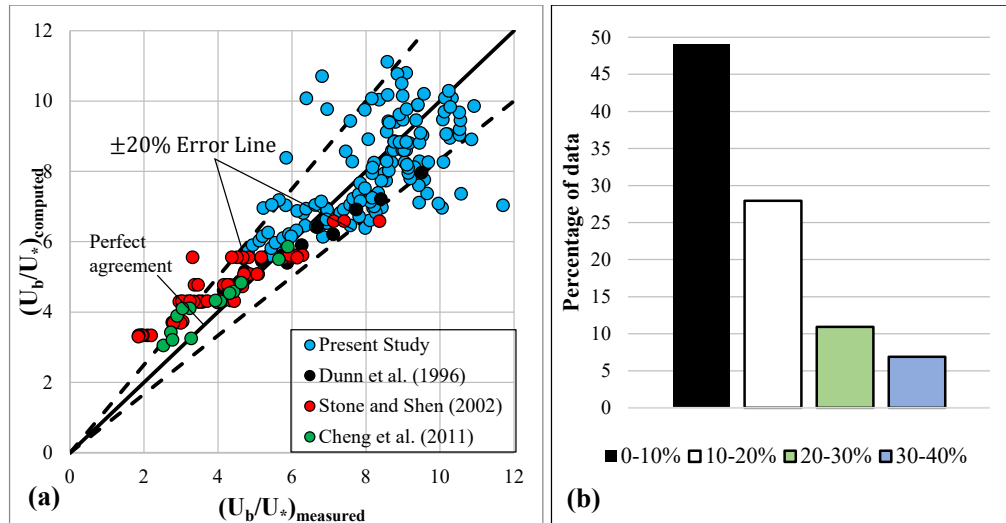
Figure 6.36. a) Comparison of $(U_b/U_*)_{measured}$ with $(U_b/U_*)_{computed}$ using Equation (6.32) b) Histogram of error percentages

As a result, either Equation (6.31) or (6.32) can be used as practical tools to calculate the bulk flow resistance represented by friction factor in submerged rigid vegetation flows for the given vegetation and flow conditions.

6.2.1.3   Determination of Bed Friction in Submerged Vegetation Array

In the present section, three submerged cases (i.e., S25, S50 and S75) with different submergence ratios (i.e., h^*=0.25, 0.50 and 0.75) and single vegetation density (λ=0.03924) are studied numerically under single stem Reynolds number (Re_{db}=6157) to investigate the effect of submergence ratio on the bed shear stresses. A spatial distribution of the dimensionless temporally averaged bed shear stresses on the drag plate region is revealed in Figure 6.37 for each submerged case.
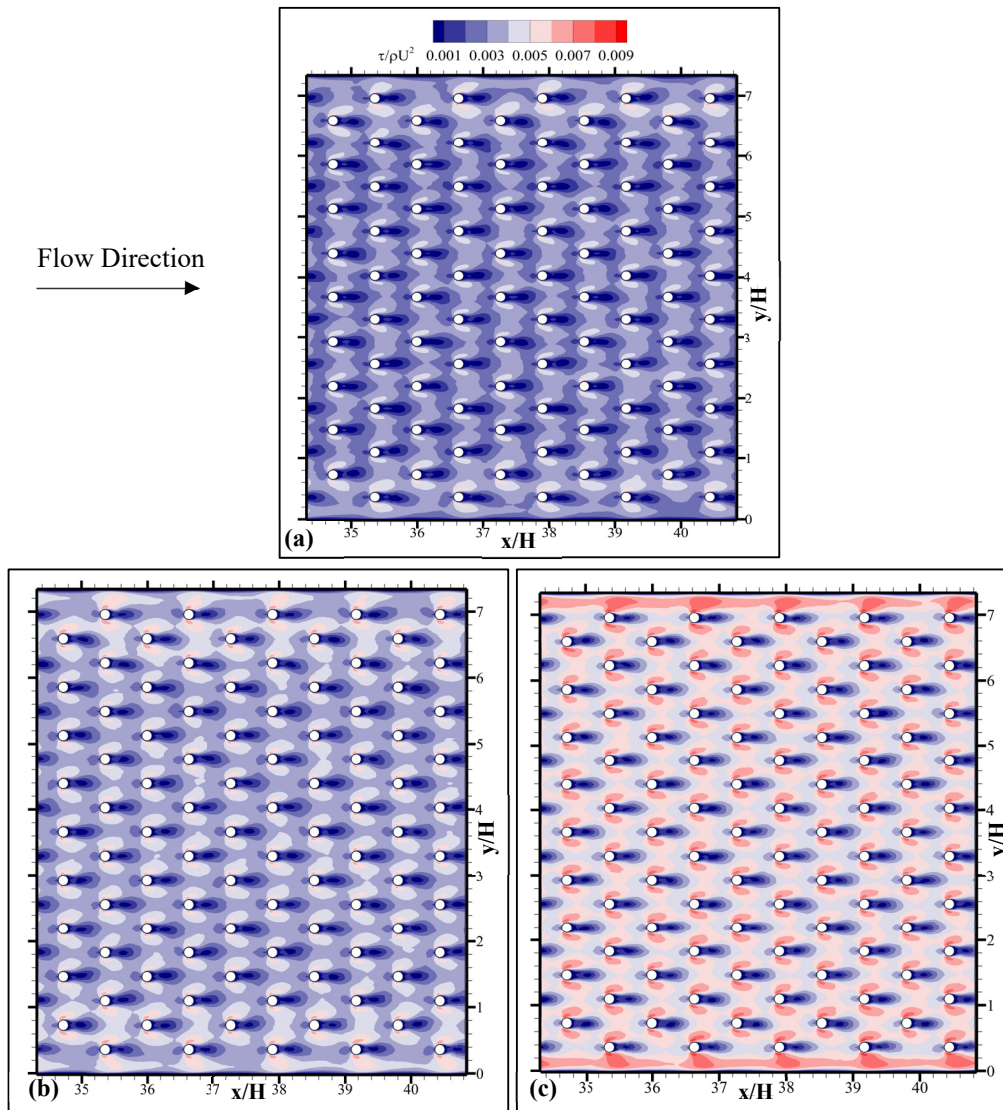
Figure 6.37. Spatial variation of bed shear stresses for cases a) S25, b) S50 and c) S75

Figure 6.37 demonstrates that the bed shear stresses are enhanced as the submergence ratio increases. This is due to the fact that the velocity distribution and velocity profiles are modified as the submergence ratio changes. A larger amount of flow is enforced to pass through the stem layer for greater submergence ratio values

124

(i.e., the flow area is increasing) so that the average velocity and near-bed velocities in the stem layer, therefore the bed shear stresses increase. Similar to emergent cases, Figure 6.37 indicates that the lower bed shear stresses occur in the wake region of each cylinder. It was also seen that the bed shear stress near each side of the cylinder increases due to the contraction in the flow area (i.e., due to the presence of the cylinder). In addition, Sumner et al. (2004) stated that the aspect ratio (AR) of the cylinder (i.e., $AR=h_v/D$) affects the wake structures. In the present section, the aspect ratios of stems are AR=1.62, 3.28 and 4.92, respectively. Thus, it can be stated that the difference in the wake structures may also be responsible for the variation of the bed shear stresses in these cases. The wake and coherent structures will be investigated in Chapter 7. Moreover, larger bed shear stress values were observed near the sidewalls, since the sidewalls are continuous solid boundaries that create a greater blockage effect than the porous ones.

The ratio of the bed shear force to the total resistance force is demonstrated in Figure 6.38 for the densest vegetation case (i.e., $\lambda=0.03924$) under stem Reynolds number $Re_{db}=6157$. It is possible to evaluate the contribution of the bed shear force on the total resistance force using Figure 6.38.
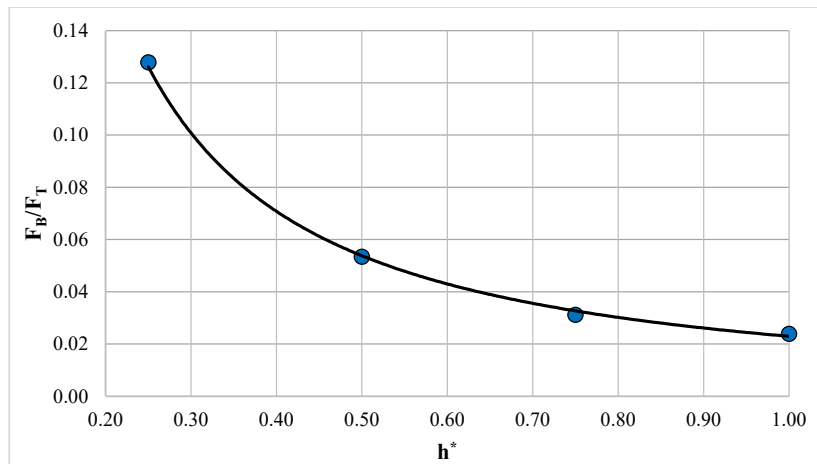
Figure 6.38. Variation in the contribution of bed drag with submergence ratio for $\lambda=0.03924$

The emergent vegetation case is the threshold condition (i.e., $h^*=1$) for the submerged vegetation cases; therefore, it was also considered in Figure 6.38 for completeness. Similar to the emergent vegetation condition, the power fit function was found as the best-fit function for the submerged vegetation case and is given as follows:

$$\frac{F_B}{F_T} = 0.0229(h^*)^{-1.23} \text{ with } R^2=0.998 \tag{6.33}$$

which is valid for $\lambda=0.03924$ and $Re_{db}=6157$.

The contribution of the bed shear force on the total resistance increases approximately from 2% to 13% as the submergence ratio decreases up to 0.25. Unfortunately, there is no study in the literature so far where the effect of the submergence ratio on the bed friction contribution is discussed quantitatively. Thus, Figure 6.38 is the only guide to estimate the contribution of bed friction in various submergence ratios for the present study. Consequently, one can simply evaluate the bed friction contribution and make a correction to find the actual vegetation drag using Equations (6.15) and (6.33), respectively. Of course, Equation (6.33) is valid for the given λ and Re_{db} ranges, so additional runs are necessary to check whether Equation (6.33) is still valid beyond its range.

6.2.1.4   Determination of the Drag Coefficients in Submerged Vegetation Array

In the present section, the effect of stem Reynolds number, vegetation density and the submergence ratio on the drag coefficient was investigated using experimental results. Consider steady and uniform flow in a channel with a submerged canopy as shown in Figure 6.39.

126
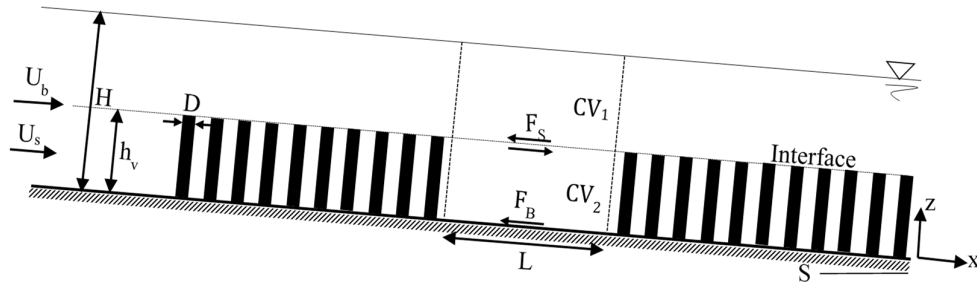
Figure 6.39. A steady uniform flow in submerged canopy

If the force balance equation is written for the first control volume, CV$_1$, Equation (6.34) is obtained as given below:

$$\gamma(H - h_v)BLS_f = F_S \tag{6.34}$$

where γ is the specific weight of water, H is the flow depth, h_v is the vegetation height, B is the channel width, L is the length of the control volume, S is the channel slope, and F_S is the shear force at the interface layer. Similarly, the following equation, Equation (6.35), can be derived if the force balance equation is applied for the second control volume, CV$_2$:

$$\gamma h_v BLS_f(1 - \lambda) + F_S = \gamma HBLS_f(1 - \lambda h^*) = F_B + F_D = F_B + \frac{1}{2}M\rho C_{Ds}U_s^2 A_s \tag{6.35}$$

where F_B is the bed friction force, F_D is the drag force acting vegetation stems, M is the number of vegetation stems in CV$_2$, C_{Ds} is the actual drag coefficient based on U_s, and A_s is the projected stem area (i.e., $A_s = Dh_v$). Herein, U_s, average stem layer velocity, is used instead of the average bulk velocity U_b (i.e., $U_b = Q/(HB)$), because U_s represents the average impact velocity acting on the stem and responsible for the drag force. Thus, the stem layer velocity U_s must be known to obtain C_{Ds} using Equation (6.35). The following part will explain the determination of actual velocity in detail.

As mentioned in Chapter 2, there are several studies to determine average velocity in submerged canopies having a single stem height, h_v. While some of these studies

127

evaluate the submerged canopy flow as a single layer (e.g., Cheng, 2015), most of the studies (e.g., Klopstra et al., 1997; Stone & Shen, 2002; Defina & Bixio, 2005; Huthoff et al., 2007; Yang & Choi, 2010) consider the submerged canopy flow as two layers as shown in Figure 6.40.
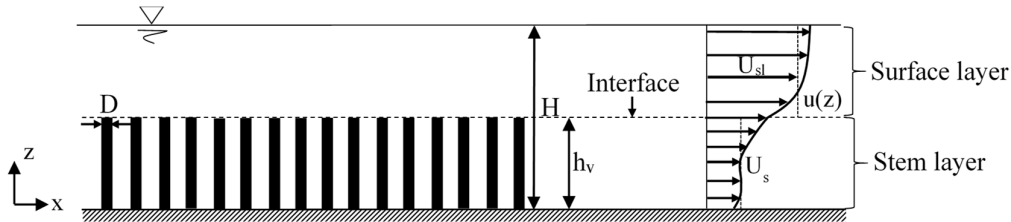
Figure 6.40. Illustration of the two-layer approach for submerged vegetation flow

As mentioned previously, it is necessary to obtain the average stem layer velocity to calculate the actual drag coefficient of submerged vegetation in the experiments. Single-layer models are not capable of finding the average stem layer velocity. On the other hand, while some of the two-layer models (e.g., Stone & Shen, 2002; Huthoff et al., 2007; Yang & Choi, 2010) provide only the average stem layer velocity U_s, a few studies (e.g., Klopstra et al., 1997; Defina & Bixio, 2005) suggest a vertical velocity distribution in the stem layer. Also, most of the two-layer models (e.g., Klopstra et al., 1997; Defina & Bixio, 2005; Yang & Choi, 2010) propose a logarithmic velocity distribution for the surface layer. In the literature, some experimental studies (e.g., Nepf & Vivoni, 2000) reveal that the velocity profile at the surface layer follows a logarithmic profile. In the scope of the present study, the performance of some two-layer models was evaluated by comparing them with the numerical analysis results of the present study. Firstly, the study of Stone and Shen (2002) was assessed. In this study, an analytical formula (i.e., Equation (10) in their study) was derived to estimate average stem layer velocity using both the drag coefficient, C_D and the energy slope due to the vegetation drag, S_{fv}. It was mentioned that there is a close agreement between the measured average stem layer velocity and the calculated one, if C_D is taken as 1.05 which was determined experimentally.

Furthermore, there is an only one parameter, which was determined using experimental data, in their analytical formula. Finally, Equation (6.36) was proposed and given below:

$$\frac{U_s}{U_b} = \sqrt{h^*} \left[\frac{1 - \sqrt{\frac{4\lambda}{\pi}}}{1 - h^* \sqrt{\frac{4\lambda}{\pi}}} \right] \tag{6.36}$$

To investigate the performance of Equation (6.36) in the estimation of average stem layer velocity, error rates were calculated for each numerical case. Error-values (in %) evaluated by considering the numerical results as actual values of the stem layer velocity were found as 17.9%, 1.8% and 0.36% for S25, S50 and S75 cases, respectively. It was seen that Equation (6.36) is quite successful in finding U_s for cases with a larger submergence ratio (i.e., h^*=0.50 and 0.75). However, it was also observed that a large error rate was found for one case in the determination of U_s (i.e., h^*=0.25). The reason for this is explained as follows: Although Stone and Shen (2002) stated that the formulation is developed analytically and, thus slightly based on experimental data, it was seen that the submergence ratio range used in their experiments (i.e., $0.35 < h^* < 1.0$) does not include the submergence ratio of the numerical analysis S25 (i.e., h^*=0.25) in the current study. Therefore, Equation (6.36) was not used to determine U_s values for the experimental study.

Secondly, Yang and Choi (2010) proposed Equation (6.37) derived from the force balance equilibrium by neglecting the bed friction as follows:

$$U_s = \sqrt{\frac{2gHS}{aC_{Ds}h_v}} \tag{6.37}$$

where a is the roughness concentration, C_{Ds} is the actual stem drag coefficient. In the evaluation of average stem layer velocity, Yang and Choi (2010) used the stem drag coefficient C_{Ds} =1.13 which was recommended by the study of Dunn et al. (1996). Huthoff et al. (2007) also give a similar expression for calculation of average stem layer velocity. The corresponding error rates in determining U_s were found as 25%,

24% and 19.5% for S25, S50 and S75 cases, respectively. Therefore, it was concluded that Equation (6.37) can not also be applied due to these error rates.

Finally, an analytical model proposed by Klopstra et al. (1997) was evaluated. In this study, a physically based analytical equation was developed to determine the longitudinal velocity profile for the stem layer and surface layer separately. Steps in the derivation of the velocity profile are explained below. Firstly, consider the momentum equation (i.e., Equation (6.38)) which is valid for uniform and steady flow:

$$\frac{\partial \tau(z)}{\partial z} = F_D(z) - \rho g S \tag{6.38}$$

where τ is the turbulent shear stress, and $F_D(z)$ is the stem drag force and described as:

$$F_D(z) = \frac{1}{2} \rho a D C_{Ds} u(z)^2 \tag{6.39}$$

The turbulent shear stress was defined using the Boussinesq concept as follows:

$$\tau(z) = \varepsilon \frac{\partial u(z)}{dz} = \rho \nu_t \frac{\partial u(z)}{dz} \tag{6.40}$$

where ε and ν are turbulent viscosity and eddy viscosity, respectively. Herein, eddy viscosity was assumed as the production of a velocity scale $u(z)$ and characteristic turbulent length scale α. Thus, Equation (6.40) becomes;

$$\tau(z) = \rho \alpha u(z) \frac{\partial u(z)}{dz} \tag{6.41}$$

If Equation (6.41) is substituted into Equation (6.38), Equation (6.42) is derived as follows:

$$u(z) \frac{\partial^2 u(z)}{dz^2} + \left(\frac{\partial u(z)}{dz}\right)^2 = \frac{a D C_{Ds} u(z)^2}{2\alpha} - \frac{g S}{\alpha} \tag{6.42}$$

If Equation (6.42) is solved analytically, a following stem layer velocity profile is obtained:

$$u(z) = \sqrt{C_1 e^{-\sqrt{2A}z} + C_2 e^{\sqrt{2A}z} + u_{s0}^2} \qquad (6.43)$$

where $A = \frac{aDC_{Ds}}{2\alpha}$ and $u_{s0} = \sqrt{\frac{2gS}{C_{Ds}aD}}$. Here, u_{s0} is defined as characteristic constant

flow velocity. It was also assumed that at the bottom of the channel, the bed shear stress is neglected and the flow velocity is equal to u_{s0}. The integration constants C_1 and C_2 in Equation (6.43) can be calculated using proper boundary conditions. On the other hand, a logarithmic velocity profile was applied to determine the velocity distribution in the surface layer. However, this part aims to find only the proper model to describe U_s by comparing the results of the numerical analyses with proposed equations. Thus, a description and derivation of the surface layer velocity profile are not supplied at this point. For further information, one can investigate the study of Klopstra et al. (1997). Now, there are two unknown variables which are α and C_{Ds}. Herein, the characteristic length scale, α, was selected in such a way that the analytical velocity profile and measured flow velocities are in good agreement. In other words, α is a calibration parameter obtained by comparison of the analytical velocity profile formula with the measured flow velocities from experiments, and the following relation was derived:

$$\alpha = 0.0793 h_v \ln\left(\frac{H}{h_v}\right) - 0.0009 \text{ for } \alpha > 0.001 \qquad (6.44)$$

It was noted that α is the only empirical model parameter in this analytical study. In the calculation of the velocity profile, Klopstra et al. (1997) used a single drag coefficient as $C_{Ds}=1.40$ obtained from experiments of emergent cylinders. Additionally, Meijer and van Velzen (1999) conducted an extensive set of experiments in a large channel (i.e., prototype-scale) to improve the estimation of calibration parameter and verify the model proposed by Klopstra et al. (1997). In addition to their experiments, the result of some of the previous studies in the literature was also used in this calibration process. This time, the calibration process was made by adjusting the α value to match calculated and measured discharges.

Similar to the study of Klopstra et al. (1997), in the study of Meijer and van Velzen (1999), some experiments in emergent vegetation conditions (with rigid steel cylinders) were carried out to determine the drag coefficient to be used in the investigation of the performance of the analytical formula. Finally, the following relation was proposed:

$$\alpha = 0.0144\sqrt{Hh_v} \tag{6.45}$$

which is valid for an extensive range of flow and field conditions.

Now, the aforementioned analytical method will be evaluated using the results of numerical analyses before using it in the present experimental study. Figure 6.41 compares the numerical analyses' results with the analytical velocity profile function. Herein, Equation (6.45) was used to obtain α values for each case. As in the studies of Klopstra et al. (1997) and Meijer and van Velzen (1999), the drag coefficient value was taken from the corresponding emergent vegetation numerical analysis (i.e., C_{Db}=1.66) to be used in the velocity profile calculations.
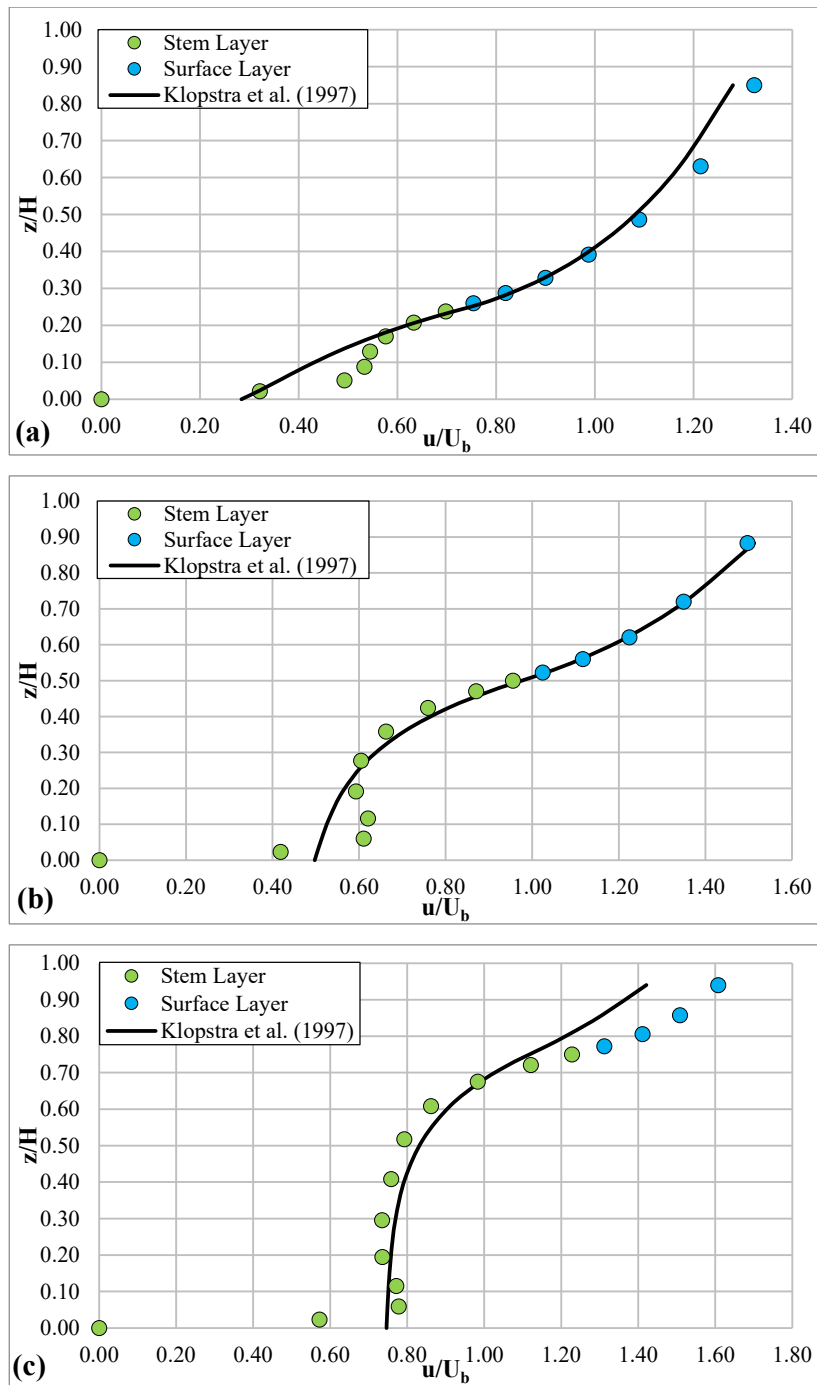
Figure 6.41. Comparison of the analytical velocity profiles with the numerical

cases a) S25, b) S50 and c) S75

133

In Figure 6.41, the velocity values of the numerical analyses were shown with green and blue colors for the stem layer and surface layer, respectively. From Figure 6.41, it was seen that while the analytical formula underestimates the velocities close to bed (i.e., z/H<0.20), velocities at larger depths (i.e., z/H>0.20) were predicted in a quite good accuracy for cases S25 and S50. On the other hand, the analytical formula shows good consistency with the stem layer velocity distribution of the numerical analysis for the S75 case. Herein, it should be noted that one can not expect the overfitting of analytical expression with the measured velocity data, because Equation (6.45) already represents the best fit function (see Figure 3 in the study of Meijer and van Velzen (1999)). Moreover, even in the study of Meijer and van Velzen (1999), the experimentally measured velocity data was distributed close to the analytical formula and did not perfectly fit. In addition to that, Equation (6.43) is too complex to take its integration, so a numerical approximation (e.g., trapezoidal rule) was used to calculate the average stem layer velocity. According to calculations, error rates in the prediction of U_s were found as 6.5%, 2.1% and 5.1% for S25, S50 and S75 cases, respectively. It was seen that the analytical method proposed by Klopstra et al. (1997) gives the best results among other models. Thus, this method was preferred in calculating averaged stem layer velocity in the experimental results part of submerged vegetation.

Figure 6.42 demonstrates the effect of stem Reynolds number based on the stem layer velocity, Re_{ds}, and vegetation density on the drag coefficient of submerged stems, C_{Ds}.
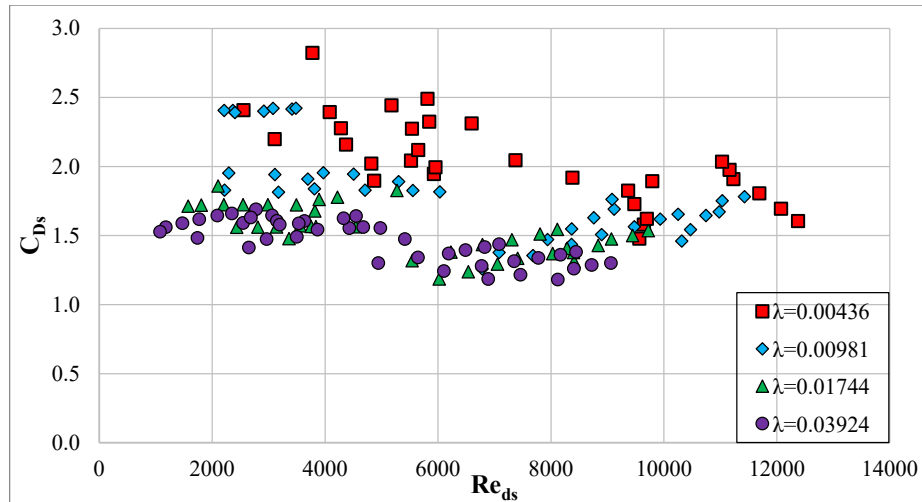
Figure 6.42. Variation of C_{Ds} with Re_{ds} for various vegetation density

It was seen from Figure 6.42 that there is not any clear effect of Re_{ds} on C_{Ds} for the given vegetation densities and $Re_{ds}<6000$. Up to this stem Reynolds number, the drag coefficients are almost constant and do not vary with Re_{ds} for each vegetation density. On the other hand, for $Re_{ds}>6000$, it was seen that all drag coefficients shift downward as a whole; nevertheless, a constancy of the drag coefficient is still maintained for the given vegetation densities. Thus, it is evident that another parameter is responsible for the decrease in the drag coefficients as a whole for $Re_{ds}>6000$. When data groups were investigated in detail, it was seen that data was distributed in a way that the first data group (i.e., $Re_{ds}<6000$) has lower submergence ratios (i.e., $h^*<0.4$) mostly. In contrast, another data group (i.e., $Re_{ds}>6000$) almost completely composes of data having higher submergence ratios (i.e., $h^*>0.4$). Thus, the submergence ratio should be kept constant to see the effect of stem Reynolds number on the drag coefficient more evidently.

Figures 6.43 and 6.44 examine the variation of drag coefficients with stem Reynolds number and vegetation density for different submergence ratio intervals. The submergence ratio intervals corresponding to each subfigure are $0.2<h^*<0.3$, $0.3<h^*<0.4$, $0.4<h^*<0.5$, $0.5<h^*<0.6$ and $0.6<h^*<0.7$, respectively.
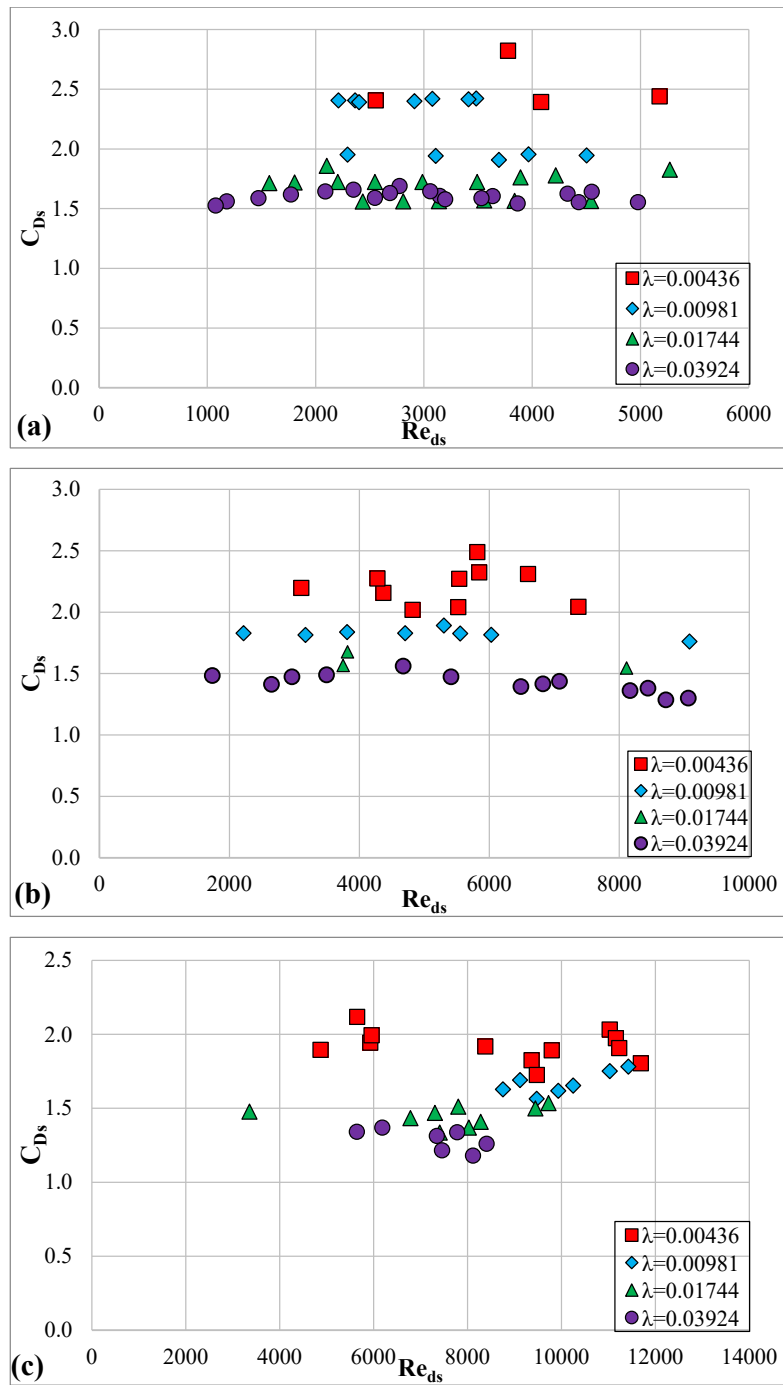
Figure 6.43. Variation of C_{Ds} with Re_{ds} for different submergence ratios

a) $0.2 < h^* < 0.3$, b) $0.3 < h^* < 0.4$, c) $0.4 < h^* < 0.5$
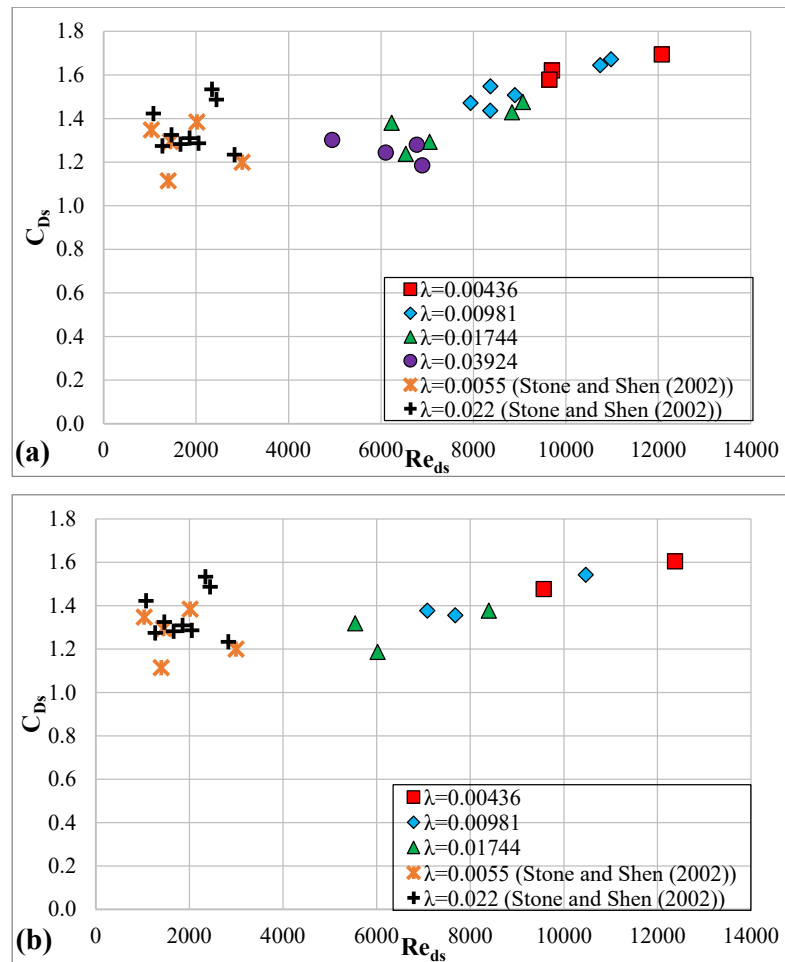
Figure 6.44. Variation of C_{Ds} with Re_{ds} for different submergence ratios
a) $0.5 < h^* < 0.6$ and b) $0.6 < h^* < 0.7$

In Figures 6.43a-6.43c, it was seen that the drag coefficient of data groups having different vegetation density almost stay constant as stem Reynolds number increases, which means that there is no considerable effect of stem Reynolds number on the drag coefficient for the given flow condition and vegetation characteristics. However, there is no available data in the present study to show the relation between Re_{ds} and C_{Ds} for the submergence ratios $0.5 < h^* < 0.6$ and $0.6 < h^* < 0.7$ and stem Reynolds number range $Re_{ds} < 5000$. Therefore, additional data were obtained from

the study of Stone and Shen (2002) for submergence ratio h^*=0.6 and stem Reynolds number Re_{ds}<5000. These additional data groups were selected in a way that their stem Reynolds numbers are comparatively large (i.e., Re_{ds}>1000), and their vegetation density is compatible with those of the present study. Now, it can be stated from Figures 6.44a-6.44b that the drag coefficients of submerged stems are nearly independent of stem Reynolds number for Re_{ds}<3500 and given the submergence ratio. It may also be stated that the drag coefficients increase with stem Reynolds number for Re_{ds}>5000 except for the highest vegetation density group. However, it should be noted that a number of data for the given vegetation densities are not enough to draw an exact conclusion. Therefore, additional experiments should be conducted to see the overall trend in these flow conditions (i.e., Re_{ds}>5000). Furthermore, similar to the conclusion of the study of Liu and Zeng (2017), Figures 6.43 and 6.44 demonstrate that the drag coefficients increase as the vegetation density decreases.

Figure 6.45 demonstrates the effect of the submergence ratio on the drag coefficients for the given vegetation densities. Moreover, the trendlines in the same color with their data group were plotted to show the relation more clearly.
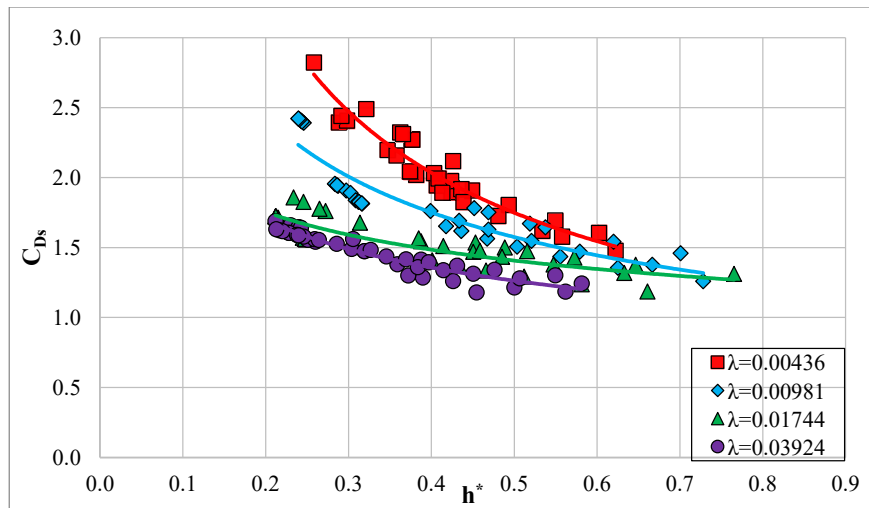
Figure 6.45. Variation of C_{Ds} with h^* for different vegetation densities

In Figure 6.45, it is clearly seen that the drag coefficient of submerged vegetation exponentially decreases as the submergence ratio increases for each vegetation density. It was noted that the decreasing rate of drag coefficient reduces with an increase in the vegetation density. Moreover, it was observed that the trendlines approach a constant drag coefficient level which means that the effect of the submergence ratio on the drag coefficient diminishes as the submergence ratio increases. Similar to Figures 6.43 and 6.44, Figure 6.45 also reveals that the drag coefficient of submerged vegetation increases as the vegetation density decreases. Furthermore, Equation (6.46) was derived by performing multivariate non-linear regression analysis with the use of the present study's data and given as follows:

$$C_{Ds} = 0.453(h^*)^{-0.397}\lambda^{-0.211} \text{ with } R^2 = 0.84 \tag{6.46}$$

which is valid for $1078 \leq Re_{ds} \leq 12376$, $0.00436 \leq \lambda \leq 0.03924$ and $0.212 \leq h^* \leq 0.765$. As discussed previously, there is no considerable effect of the stem Reynolds number on the drag coefficients for the tested range, so Re_{ds} was not included in the derivation of Equation (6.46). In addition to Figure 6.45, Equation (6.46) also proposes that the drag coefficient of the submerged stem reduces as the submergence ratio and vegetation density increase. The performance of Equation (6.46) in estimating the drag coefficient was demonstrated in Figure 6.46.
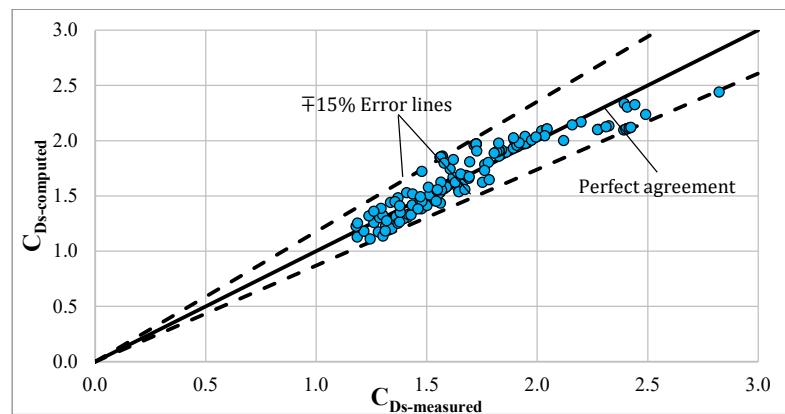
Figure 6.46. Comparison of the drag coefficients of measured data and computed ones using Equation (6.46)

Figure 6.46 demonstrates that all the data remain between $\mp 15\%$ error lines, and most of the data collapse onto the perfect agreement line. Thus, it can be stated that Equation (6.46) estimates the spatially averaged drag coefficient of submerged vegetation array effectively for the given vegetation characteristics and flow conditions.

To compare and discuss the results and inferences from the present study, the raw data of Stone and Shen's (2002) study was also re-analyzed. As previously mentioned, Stone and Shen (2002) performed an experimental study with rigid submerged and emergent vegetation to develop a formula for evaluating average stem layer velocity. The raw data for this study was found from the study of Stone (1997), and necessary parameters (i.e., U_s, S_{fv} and C_{Ds}) were calculated using equations in the study of Stone and Shen (2002). In the evaluation of S_{fv}, the bed friction correction procedure proposed by their study was followed. This procedure is based on the determination of the friction (energy) slope corresponding to bed resistance, S_{fb} (i.e., $S_f = S_{fv} + S_{fb}$), using the relative roughness of the bed and Reynolds number. After that, C_{Ds} can be found by applying the force balance equation similar to Equation (6.35). Figure 6.47 investigates the effect of the stem Reynolds number on the drag coefficient for the submergence ratios $h^*=0.4$, $h^*=0.6$ and $h^*=0.8$, respectively. The effect of the submergence ratio on the drag coefficient was eliminated by keeping it constant in each subfigure.
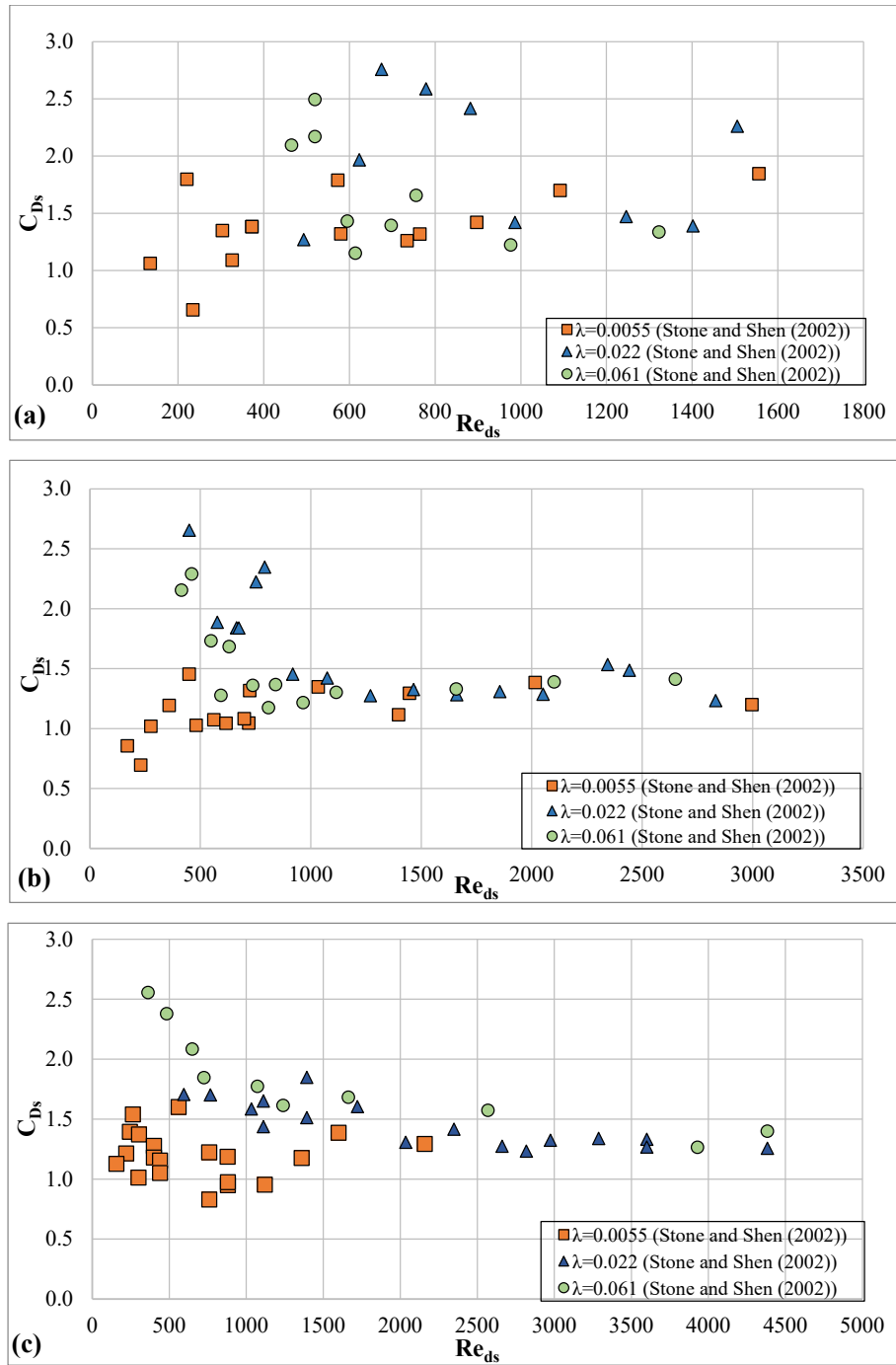
Figure 6.47. Variation of C_{Ds} with Re_{ds} for different submergence ratios in the study of Stone and Shen (2002) a) $h^*=0.4$, b) $h^*=0.6$, c) $h^*=0.8$

From Figures 6.47b-6.47c, it is clearly seen that there is an exponential decrease of the drag coefficients with the increase of stem Reynolds number for the vegetation densities $\lambda=0.022$ and $\lambda=0.061$. After a specific stem Reynolds number, the drag coefficients approach a constant value and become almost independent from the stem Reynolds number. On the other hand, it was also observed that the data group having vegetation density $\lambda=0.0055$ does not vary considerably with the stem Reynolds number for $h^*=0.6$. However, the drag coefficient does not have any clear relation with the stem Reynolds number for other submergence ratios of that vegetation density. Unfortunately, the data sets are too scattered and complicated to make any inferences about the effect of vegetation density on the drag coefficient from Figure 6.47. Similarly, the effect of the submergence ratio on the drag coefficient was investigated by similar figures (which are not presented here) in detail; however, any clear relation can not be established between the submergence ratio and the drag coefficient for the given flow conditions and vegetation characteristics.

Additional data based on submerged vegetation array were found from the study of Nguyen (2012). Herein, the average stem layer velocities were measured experimentally with a laser Doppler anemometer (LDA) and supplied by the author in a table. However, the raw data includes the bed shears, so equations proposed by the present study (i.e., Equations (6.15) and (6.33)) were applied before the drag coefficient calculations. After that, actual drag coefficients were found using the force balance equation. The effect of the vegetation density, stem Reynolds number and the submergence ratio on the drag coefficient were investigated in Figure 6.48 for similar vegetation densities to those of the present study.
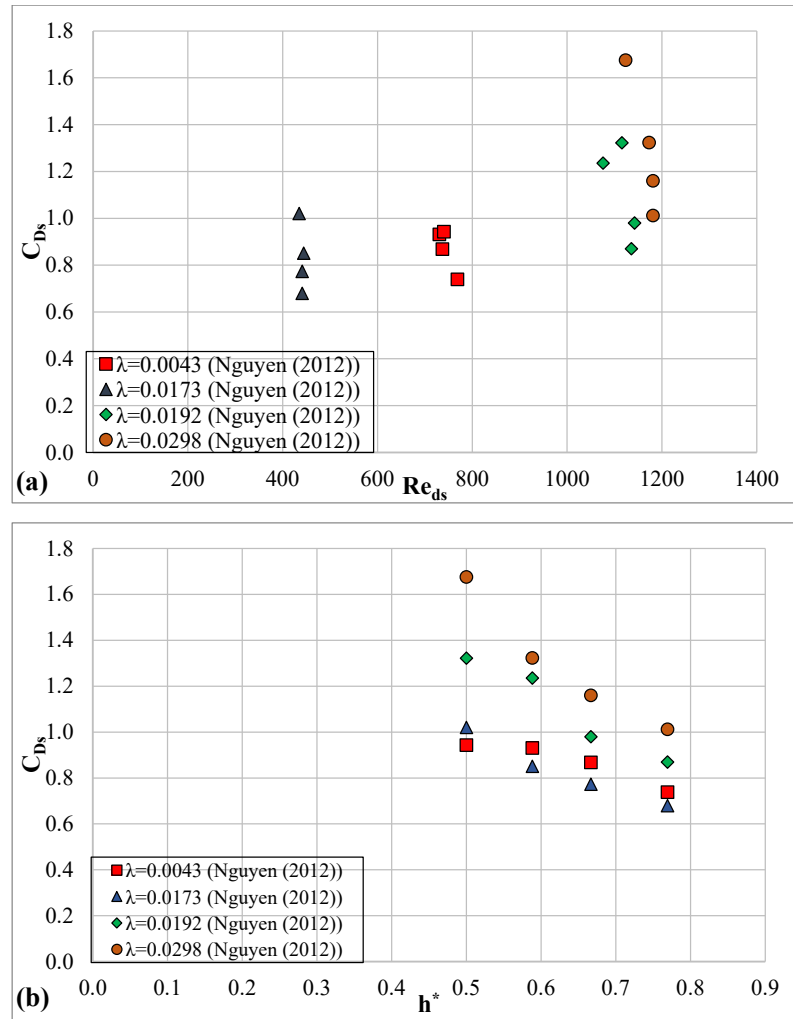
Figure 6.48. a) Variation of C_{Ds} with Re_{ds} for different vegetation densities and b) Variation of C_{Ds} with h^* for different vegetation densities in the study of Nguyen (2012)

From Figure 6.48a, it was seen that experiments were conducted in a way that the stem Reynolds number is almost constant for each vegetation density. Therefore, it is not possible to see the effect of the stem Reynolds number on the drag coefficients. On the other hand, similar to the conclusion of the present study, Figure 6.48b demonstrates that the drag coefficients of submerged vegetation decrease as the

submergence ratio increase for each vegetation density. However, contrary to the present study, it was also observed from Figure 6.48b that the drag coefficient of submerged stem increases with an increase of the vegetation density for lower stem Reynolds numbers (i.e., Re_{ds}<1200).

6.2.2 Numerical Analyses and Results of the Submerged Vegetation Conditions

In the present section, the drag coefficients of submerged vegetation having three different submergence ratios (i.e., h^*=0.25, 0.50 and 0.75) with single vegetation density (i.e., λ=0.03924) were investigated by performing numerical analyses. Similar to the emergent ones, each numerical analysis was executed for 17000 iterations. The same macro code was rearranged and used for submerged cases to calculate drag forces on each vegetation stem. Again, the drag coefficient results were given as spanwise-averaged also for this section. The results of submerged cases were introduced below from low to high submergence ratios, respectively.

For the S25 case (i.e., h^*=0.25), a variation of the drag coefficient with dimensionless streamwise distance was revealed in Figure 6.49. As mentioned in the emergent section, the vegetation array is distributed in a way that each sequent rows includes 9 and 10 stems, respectively.
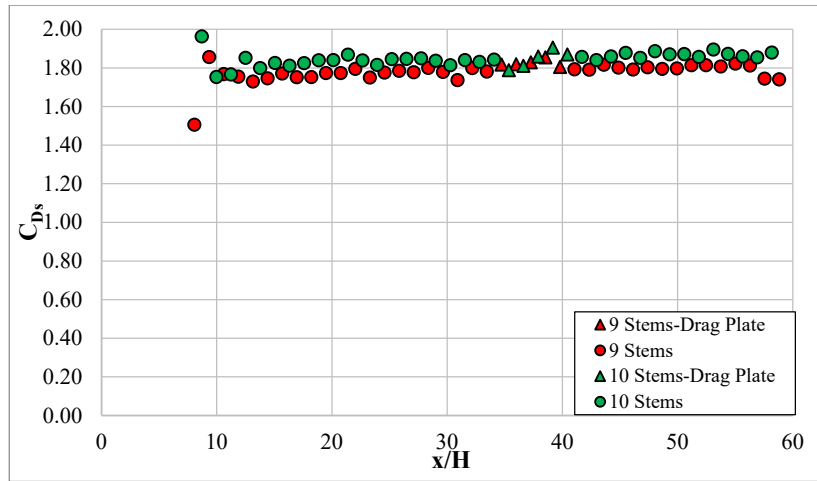
Figure 6.49. Variation of the spanwise averaged drag coefficients with streamwise distance for S25 case

Herein, the drag coefficient of each stem was calculated by considering the average stem layer velocity around the stem. On the contrary to the densest emergent case (i.e., λ=0.03924), it was seen from Figure 6.49 that the spanwise averaged drag coefficients of each row reach nearly a constant value at the beginning of the vegetation array (i.e., x/H≈12.5). Furthermore, a fully developed flow occurs before the drag plate, which was verified by an investigation of longitudinal velocity profiles at various sections. When the drag coefficients of each stem were investigated individually, it was observed that stems situated at the outermost of the sequent rows have larger drag coefficients than ones at the inner side. Moreover, it was noted that the discrepancy between spanwise averaged drag coefficients of sequent rows (i.e., 9 stems and 10 stems) reduced compared to the emergent vegetation case. The reason is that stronger channeling was developed between the outermost stems of sequent rows instead of near the sidewall, as shown in Figure 6.50.
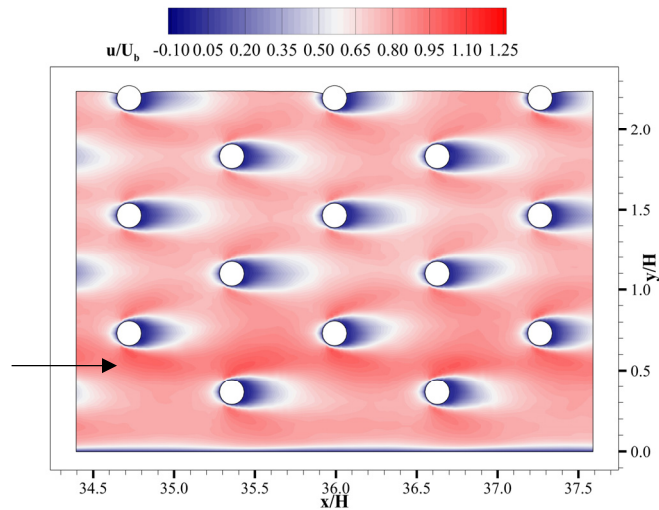
Figure 6.50. Streamwise velocity contours between stems for S25 case at z/H=0.25

Again, the spanwise averaged drag coefficient of the first row (i.e., row having 9 stems) is considerably lower than that of other rows, because the blockage effect becomes more pronounced after the first stem row. Furthermore, the spanwise averaged drag coefficient of the second row (i.e., the first green circle in Figure 6.49) is larger than the other rows' drag coefficients. This is because there is no stem in the direct front of the second row, so stems in the second row did not experience any sheltering effect. The averaged drag coefficient of stems at the drag plate was found as C_{Ds-num}= 1.84, which is nearly 10% larger than the emergent one. In addition to drag coefficients, according to velocity distribution in the channel, it was observed that 15% and 85% of the total discharge were conveyed by the stem layer and surface layer, respectively, from the beginning of the vegetation array.

The result of the second submerged case, S50 (i.e., h^*=0.50), was presented in Figure 6.51. Similar to the previous case, the spanwise averaged drag coefficient reaches a constant level after a small streamwise distance. According to the comparison of the longitudinal velocity profile at various sections, a fully developed flow was observed on the drag plate. It was also seen that the averaged drag coefficient of rows having

146

a different number of the stem becomes closer to each other compared to the S25 case.
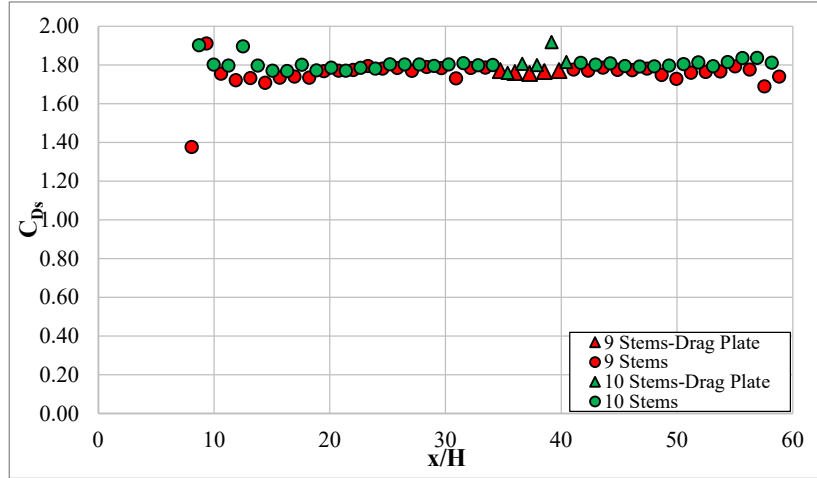
Figure 6.51. Variation of the spanwise averaged drag coefficients with streamwise distance for S50 case

It was also noted that the outermost stems in the successive rows had experienced higher velocities at their sides (i.e., stronger channeling), which reduced the wake pressure and increased drag forces. The spatially averaged drag coefficient of stems located at the drag plate was calculated as C_{Ds-num}= 1.79. Although the submergence ratio is considerably increased compared to the previous case, it was seen that the spatially averaged drag coefficient almost did not change at all. Furthermore, it was found from the calculations that 39% and 61% of the total flow discharge were conveyed by the stem layer and surface layer, respectively.

Finally, the distribution of spanwise averaged drag coefficients was revealed in Figure 6.52 for the S75 case (i.e., h^*=0.75). After a few rows of stems, the spanwise averaged drag coefficient of rows with a different number of stems overlaps each other and reaches a constant value. Longitudinal velocity profiles at various sections on the drag plate are consistent with each other, which reveals that a fully developed flow is present on the drag plate. Similar to the previous cases, the average drag

coefficient of the first row was substantially lower than other rows because of the lower blockage effect. Likewise, the outermost stems in each row have larger drag coefficients than those in the same row.
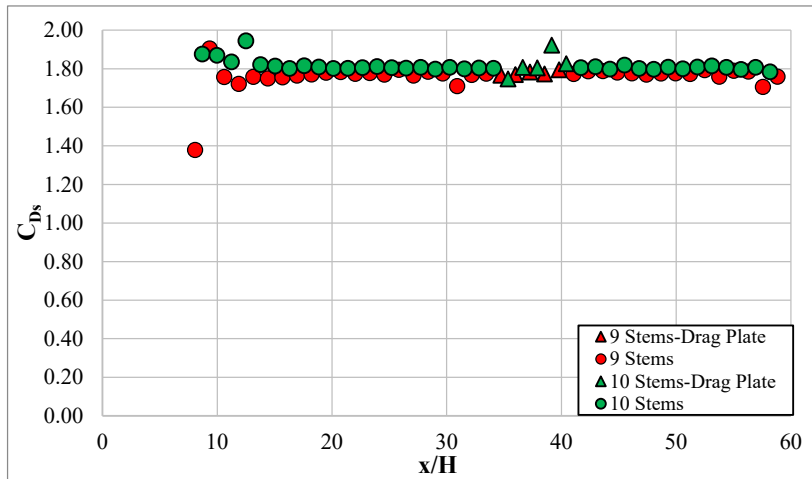
Figure 6.52. Variation of the spanwise averaged drag coefficients with streamwise distance for S75 case

According to the average velocity distribution in the layers, 68.5% and 31.5% of the total discharge were conveyed by the stem layer and surface layer, respectively. The spatially averaged drag coefficient of stems on the drag plate was found as $C_{Ds-num}=1.80$. Thus, contrary to experimental results, numerical analyses show that there is no significant effect of the submergence ratio on the spatially averaged drag coefficient of the vegetation array for the given flow and vegetation conditions. The reason for this may be that the average stem layer velocities were estimated by analytical relation instead of determined experimentally. Thus, any deviation in the determination of stem layer velocity may contribute to discrepancies between the results. In addition, Figure 6.53 shows the distribution of the pressure coefficient on the vegetation stem situated in the middle of the first stem row at the drag plate. Herein, a spatially averaged velocity around the stem was considered in the pressure coefficient calculations.
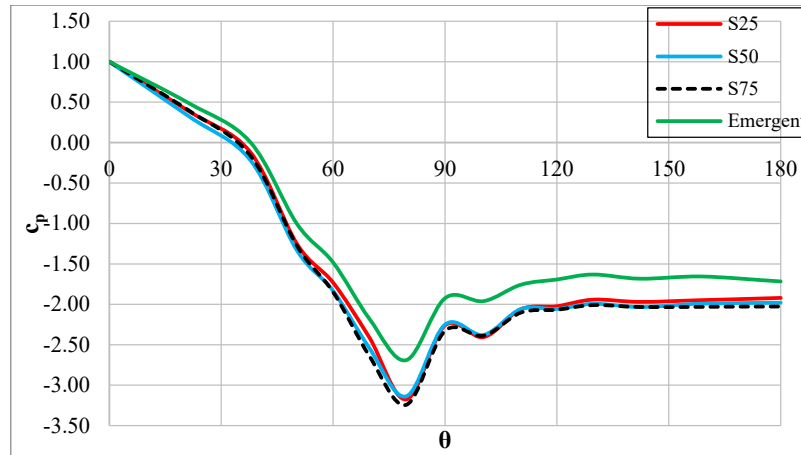
Figure 6.53. Pressure coefficient distribution on stem for various submergence ratios

Figure 6.53 demonstrates that the pressure coefficient of all submerged cases coincides with each other which explains the closeness between the spatially averaged drag coefficients. On the other hand, the pressure coefficient distribution of the emergent case remains above the submerged ones (i.e., lower pressure gradient), so a lower drag coefficient was obtained for the emergent case.

Finally, a comparison of the drag coefficient results from the numerical analyses (i.e., S25 and S50) and experiments was demonstrated in Figure 6.54. As previously mentioned, there is no experimental case matched exactly with numerical analyses' conditions in terms of flow conditions (i.e., stem Reynolds number) and submergence ratio for submerged vegetation arrays. Therefore, the results of numerical analyses were compared with those of experimental studies having similar flow conditions (i.e., for S25; $4054 \leq Re_{db} \leq 8307$, for S50; $6926 \leq Re_{db} \leq 8390$) and similar submergence ratios (i.e., for S25; $0.24 \leq h^* \leq 0.26$, for S50; $0.48 \leq h^* \leq 0.55$). Unfortunately, there is no experimental case data with a similar submergence ratio and flow condition to the S75 case, so a comparison for this case is not possible. The numerical analyses were performed with stem Reynolds number based on the bulk velocity (i.e., Re_{db}), so this Reynolds number was also used in comparisons for the

sake of consistency. Experimental results and the numerical result were represented by the blue and red circles in Figure 6.54, respectively.
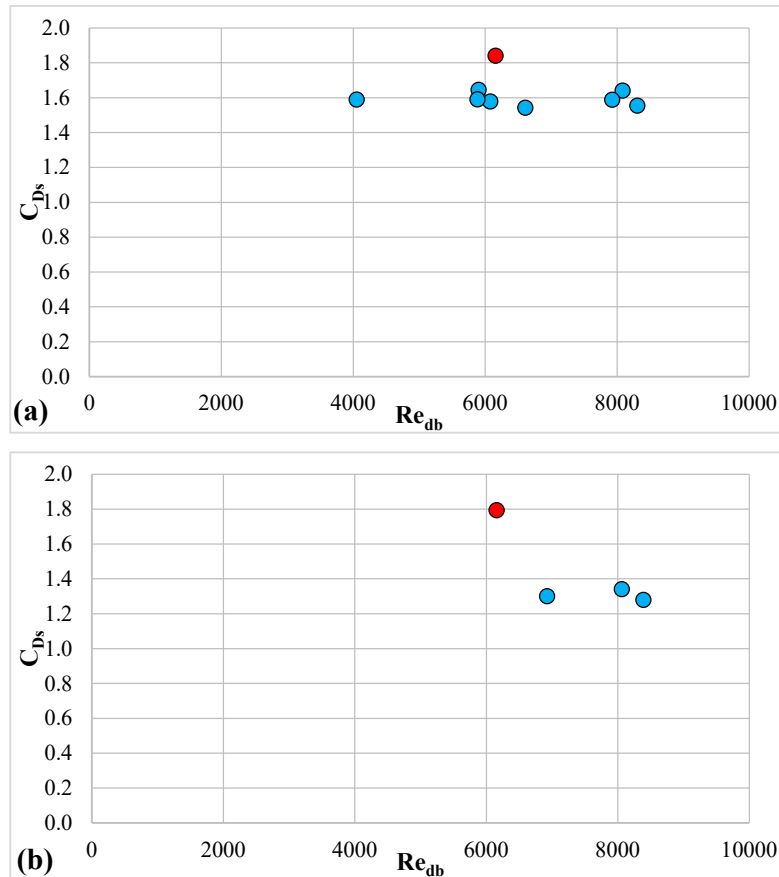
Figure 6.54. Comparison of the experimental results with a) S25 case b) S50 case

It was seen from Figure 6.54a that the drag coefficients of the experimental study and the S25 case are similar and consistent with each other. The average stem drag coefficient of the experimental data group was found as $C_{Ds}=1.59$. Similar to emergent cases, there is a slight discrepancy ($\approx13\%$) between the average drag coefficient of experimental data and the numerical case. On the other hand, Figure 6.54b reveals that the difference between the drag coefficient of the experimental group and the S50 case increased compared to the previous case. The average drag coefficient of experimental data is $C_{Ds}=1.31$. Herein, the deviation between the

150

experimental and numerical cases was found to be relatively high (i.e., $\approx 27\%$). The reason for these discrepancies may be that the stem layer velocities of the experimental cases were not accurately determined, because, as shown in Figure 6.41, deviations (i.e., 6.5%, 2.1% and 5.1% for S25, S50 and S75) were found between the average stem layer velocities of numerical results and those of analytical function. In addition, the difference between the drag coefficients can also be explained by a simple calculation. For instance, if the analytical function overestimated the actual average stem layer velocity by 7.5%, the deviations between the actual drag coefficients of experimental and numerical results will reduce to 1% and 14.8% for S25 and S50 cases, respectively. Of course, these deviations may also increase if the actual stem layer velocities are underestimated by the analytical function. Therefore, it is recommended that the velocity profiles should be taken in experiments using proper equipment without disturbing the flow (e.g., laser Doppler velocimetry).

CHAPTER 7

FLOW CHARACTERISTICS AND STRUCTURES INSIDE THE VEGETATION ARRAYS

7.1   Emergent Vegetation Array

In this subsection, flow characteristics and structures in three emergent cases (i.e., E10, E20 and E30) were investigated. As mentioned in Chapter 5, these cases were selected from experimental runs having the same flow depth but different stem Reynolds numbers and vegetation densities. Therefore, it is not possible to assess the effect of stem Reynolds number and the vegetation density on the flow characteristics separately. This means that one should carefully evaluate the following figures considering the effect of both parameters.

Figure 7.1 illustrates the flow around the emergent vegetation stem in the E30 case using 3D streamlines. It was seen that the flow velocity locally increases (shown by dark red) near the sides of the vegetation stem in the streamwise direction (i.e., x direction).
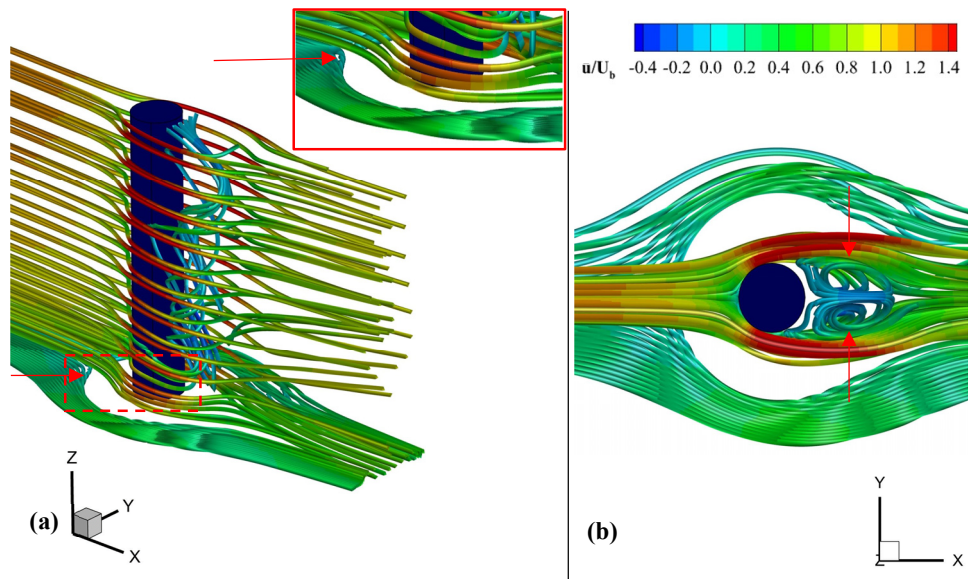
Figure 7.1. Flow around the emergent vegetation stem in the E30 case a) 3D view b) top view

Figure 7.1a reveals that a horseshoe vortex (i.e., spiral streamline demonstrated with a red arrow) is weakly formed at the base of the stem. In addition, a 3D wake structure developed behind the stem as shown in Figure 7.1b.

It is known that the drag forces acting on the vegetation stems are directly associated with the streamwise velocity. Therefore, it is essential to understand how streamwise velocity changes inside the array. A non-dimensional temporally averaged streamwise velocity distribution is presented in Figure 7.2 using velocity contours at the top of the drag plate for each case.
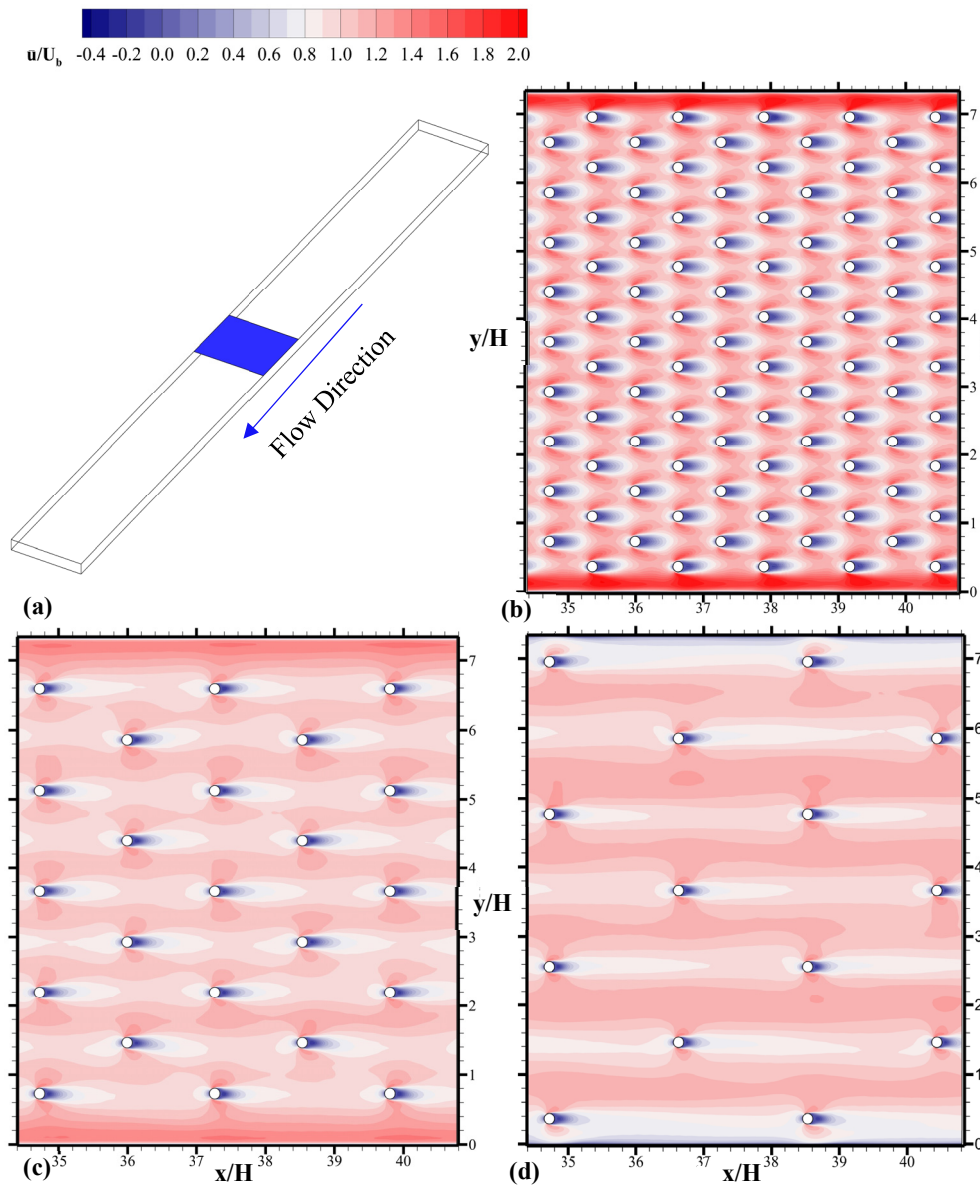
Figure 7.2. a) Place of the drag plate, and distribution of dimensionless temporally averaged streamwise velocity at top of the drag plate for b) E10, c) E20 and d) E30

Figure 7.2 demonstrates that higher velocities dominate the drag plate region in the E10 case compared to others for the given velocity scale. In addition, a strong

155

channeling, where streamwise velocities increase, was observed near the sidewalls in E10 and E20 cases. As mentioned in Chapter 6, higher streamwise velocities near the vegetation stem further reduce the wake pressure, so larger drag forces act on stems close to the sidewalls (i.e., blockage effect). Contrary to E10 and E20 cases, lower streamwise velocities develop nearby the sidewalls in the E30 case.

The depth-averaged ($0<z<H$) turbulent kinetic energy (TKE) profiles, $\bar{k}/U_b^2$, are presented in Figure 7.3 where the left and right sides show the whole channel (except entrance and exit regions) and the upstream part of the vegetation array, respectively. The TKE in each simulation is obtained using the formula given below:

$$k = \frac{1}{2}\left(\overline{u'u'} + \overline{v'v'} + \overline{w'w'}\right) \tag{7.1}$$

where terms in the parenthesis are Reynolds stresses. A vegetation stem transforms the mean kinetic energy into the TKE at the stem scale (Nepf, 1999). As can be seen from Figure 7.3, there are some local regions (shown in red color) where the TKE amplifies inside arrays. This amplification is generally due to the vortex shedding in the wake of vegetation stems (Koken & Constantinescu, 2021). Although the E10 case was simulated with the lowest stem Reynolds number among the three cases, the largest TKE generation was observed in that case. This means that vegetation density is the main parameter that governs the TKE amplification inside emergent arrays for the given flow conditions and vegetation characteristics. In addition, Figure 7.3a demonstrates that while the local regions behind the stem, where the TKE amplification occurs, generally have a symmetrical shape inside the array, the local regions close to the sidewalls are in non-symmetrical shape. The reason for this is that the streamwise velocities near the sidewalls of the channel are higher than those at the inner side (see Figure 7.2b). Thus, the outer side of these local regions elongates with an increased streamwise velocity which results in an asymmetrical shape.
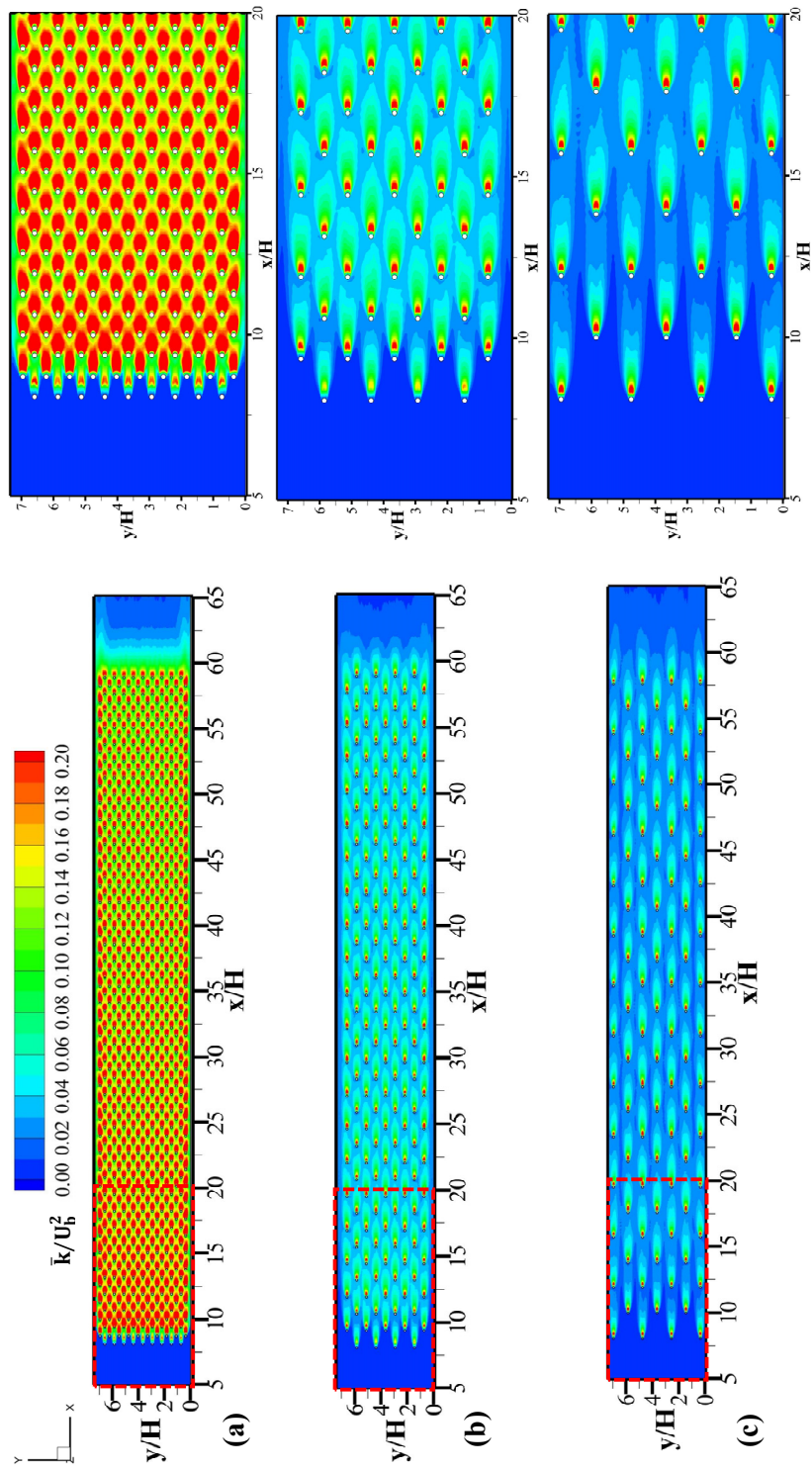
Figure 7.3. Depth averaged TKE profiles a) E10, b) E20 and c) E30

157

Figure 7.4 demonstrates the width averaged TKE variation (0<y<B), $\tilde{k}/U_b^2$, along the streamwise direction for emergent arrays. Although the TKE is amplified at the upstream part of the array in the E10 case (Figure 7.4a), it starts to diminish in the streamwise direction as shown in the downstream part of this array (i.e., 45<x/H<60). On the other hand, the TKE distribution behind the stems was not changed after a certain distance from the front edge of arrays along the streamwise direction in E20 and E30 cases. Figure 7.4 also reveals that the maximum TKE initially occurs nearby the free surface and then propagates toward the bed in the streamwise direction. Moreover, the TKE was almost uniformly distributed along the depth at the upstream part of the array in the E10 case; however, in other cases, the TKE distribution was not uniform over the depth such that the TKE reduced nearby the bed.
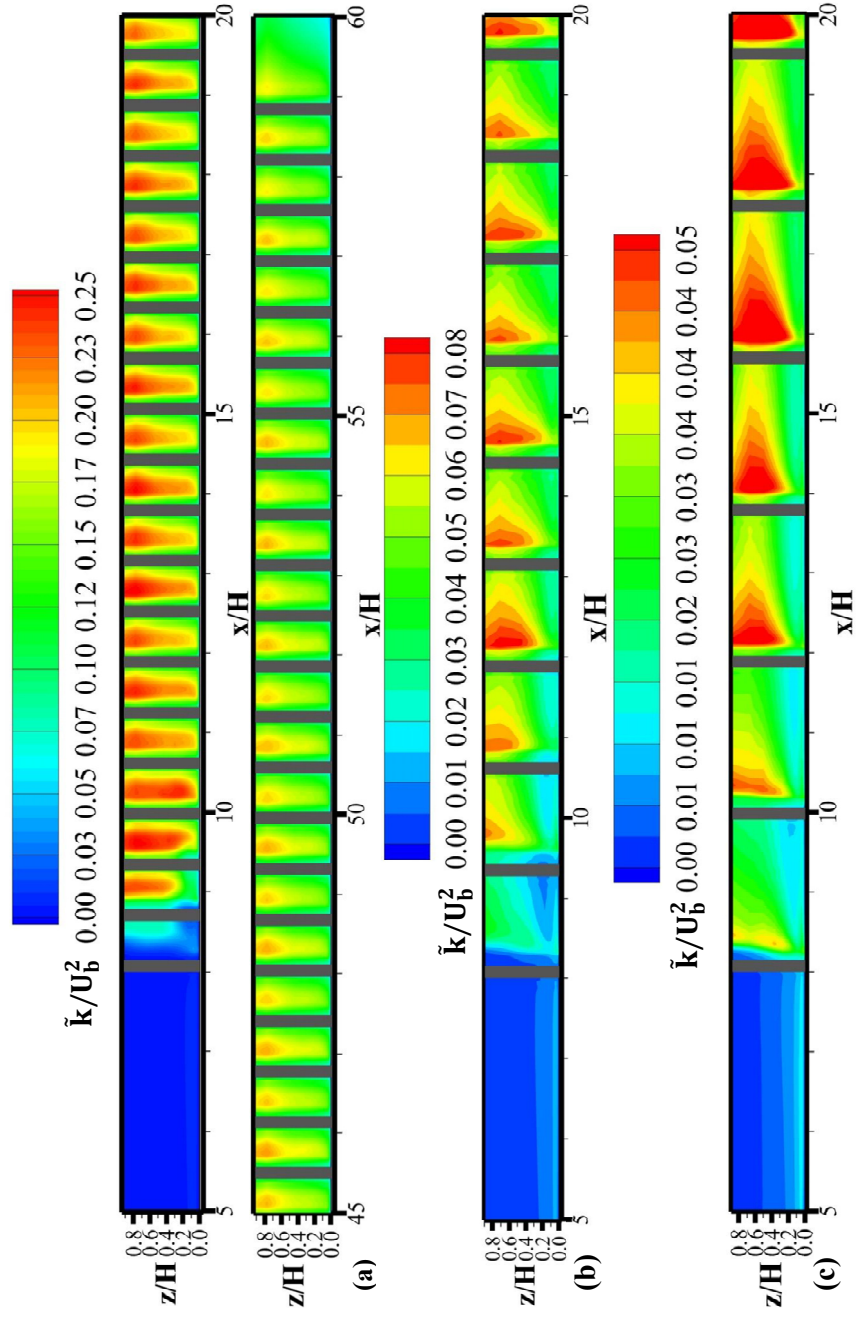
Figure 7.4. Width averaged TKE profiles a) E10, b) E20 and c) E30

159

Figure 7.5 reveals the variation of the cross-sectionally averaged TKE, $\overline{\tilde{k}}/U_b^2$ (i.e., depth and width averaged; 0<z<H and 0<y<B) inside the emergent arrays in the streamwise direction. The overbar '-' and tilde '~' on the TKE denote averaging over the vertical and spanwise directions, respectively. These TKE profiles were also window averaged in the flow direction to remove the local effect of vegetation stems.
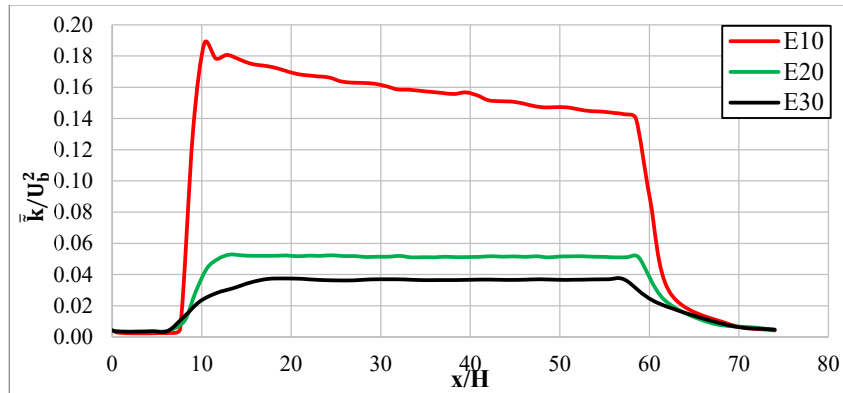
Figure 7.5. Variation of the cross-sectionally averaged TKE inside the emergent array in the streamwise direction

It was revealed in Figure 7.5 that the streamwise distance between the front of the array and the location where the maximum TKE is reached elongates as the vegetation density decreases. For E20 and E30 cases, it was observed from Figure 7.5 that the averaged TKE reaches its maximum value and stays constant along the array. However, in the densest vegetation case, E10, the averaged TKE monotonically decays after reaching its maximum value. This decay can be seen in Figure 7.3a where the local regions having high TKE are contracted in the streamwise direction. Moreover, the width-averaged TKE profile confirms this decay by showing that the local region with high TKE behind the stem slightly diminishes in the streamwise direction (see the downstream part of the array in Figure 7.4a). Interestingly, after a certain distance from the end of the array ($\approx$9H), the TKE profiles coincide with each other and then follow the common trendline till the end of the array.

Figure 7.6 shows depth averaged ($0<z<H$) vertical vorticity, $\overline{\omega_z}(H/U_b)$, distribution at the upstream part of each array.
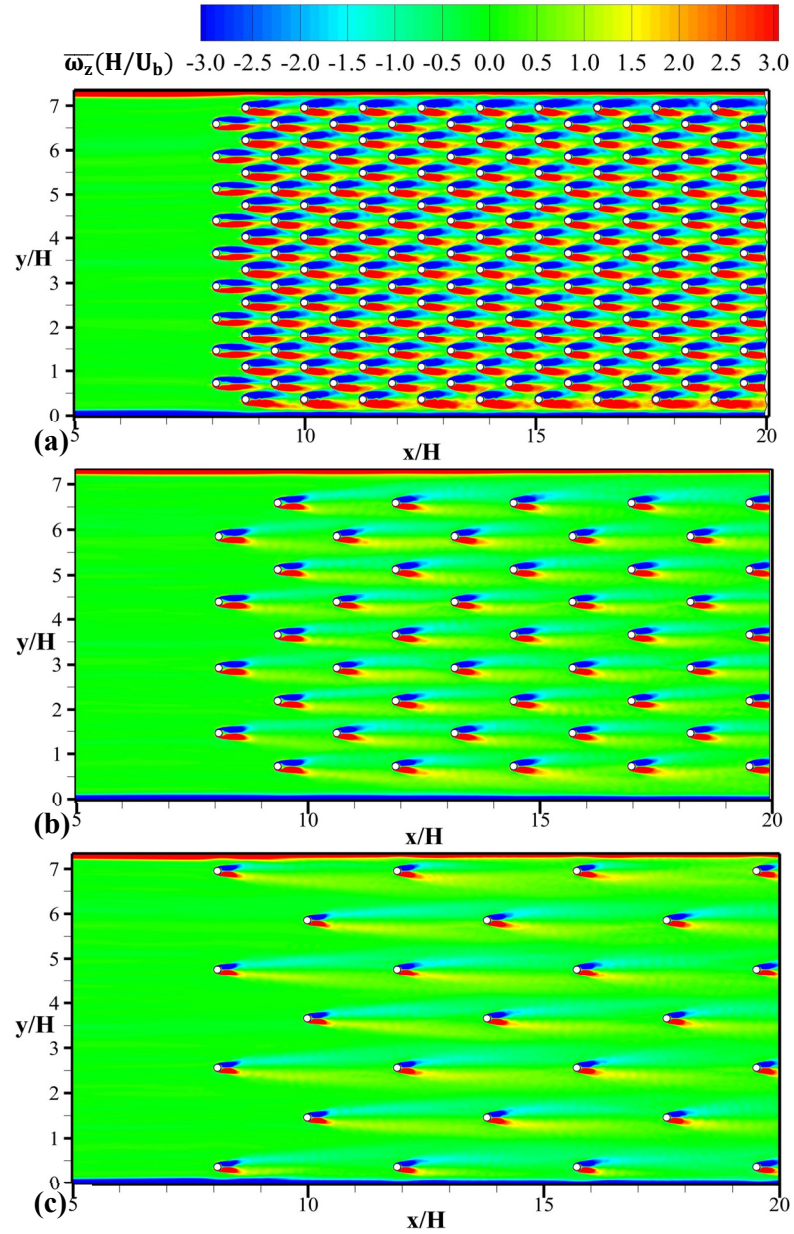
Figure 7.6. Depth averaged vertical vorticity distribution in close to the front of the array a) E10, b) E20 and c) E30

It was observed that the wake characteristics of the stems are slightly changed along the streamwise direction in E10 and E20 cases. Firstly, the wakes are long and straight at the beginning of the array. Later, their length decreases, and the wakes at both sides of the stem are no longer straight and start to make an angle with each other. Although the stem Reynolds number decreases as the array density increases, it was noted that the wake lengths also increase. Moreover, while the wakes of stems situated inner side of the array are usually in symmetrical shape in the E10 case, the wake shapes of stems located near the sidewalls are non-symmetrical. In fact, part of the wake near the sidewall is more extended than another, because larger streamwise velocities develop near the sidewall as shown in Figure 7.2a. On the other hand, in the E30 case, it was observed that there are no significant discrepancies between the wake of stems neither in streamwise nor spanwise directions. Furthermore, in the E10 case, it was noticed by comparison of the wake pattern of stems at different depths (figures are not given here) that the angle between wakes increases along the depth. However, there is no considerable change in the wake angles with depth for the E20 and E30 cases. It was also observed from the width averaged vorticity profiles of arrays, $\widetilde{\omega_y}(H/U_b)$, that maximum vorticity magnitude is observed almost at mid-depth of the array in the E10 case (figures are not given here). In the E20 and E30 cases, on the other hand, the vorticity magnitudes are amplified near the free surface.

Figure 7.7 shows the coherent structures developed inside the arrays using one of the prominent flow visualization techniques called the Q criterion. This criterion can be defined as the second invariant of the resolved velocity gradient tensor and reveals locations where strain in the flow is prevailed by rotation (Dubief & Delcayre, 2000; Rodi et al., 2013). The Q criterion has been successfully used in similar numerical studies (e.g., Chang et al., 2020; Koken & Constantinescu, 2021) to detect coherent structures.
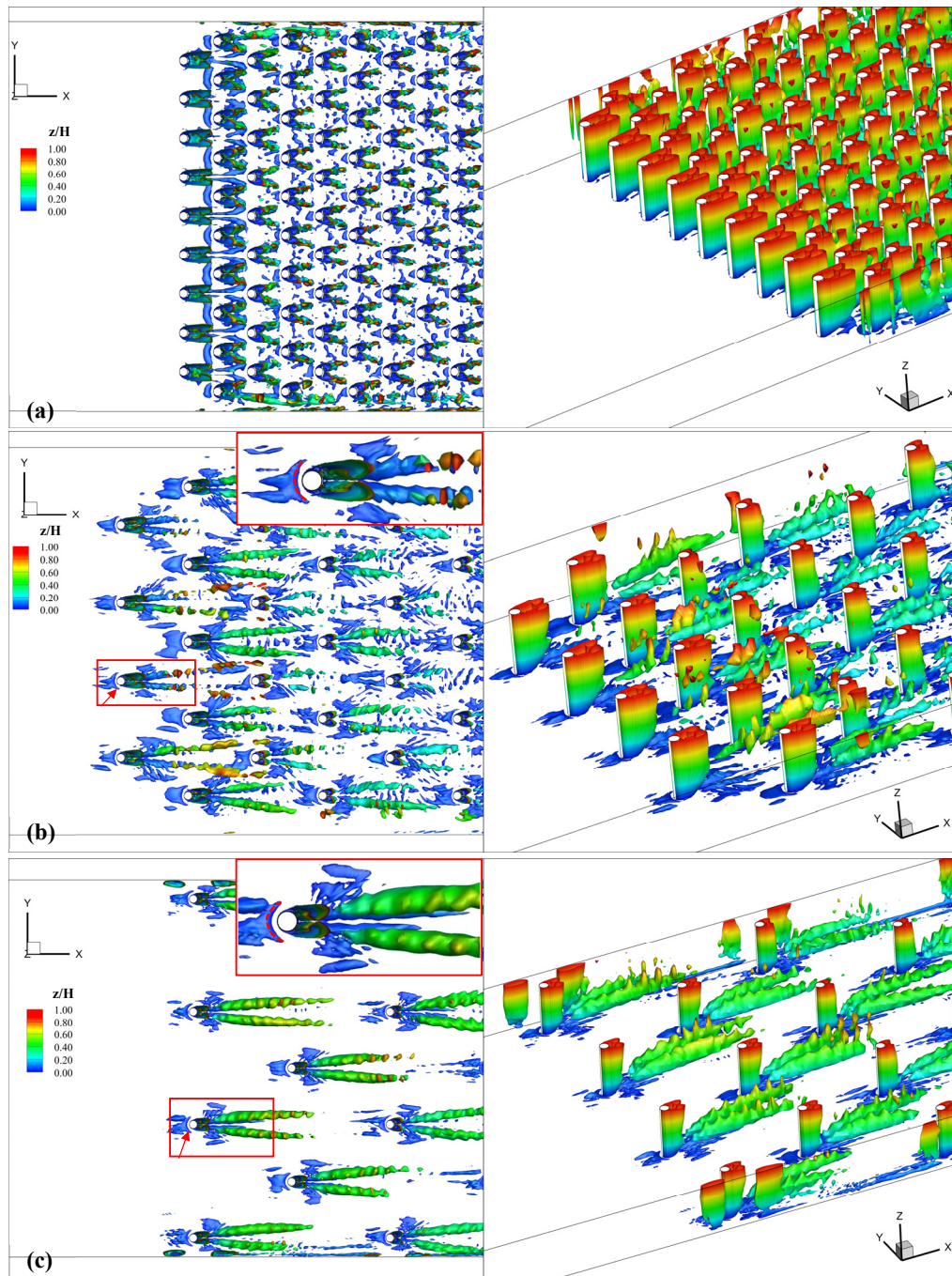
Figure 7.7. Mean-flow visualization inside the upstream part of the arrays with the Q criterion a) E10, b) E20 and c) E30

Figure 7.7 demonstrates that horseshoe vortices, indicated by red arrows and dashed lines, weakly develop on the front of stems situated upstream of the arrays for E20 and E30 cases. The horseshoe vortices can locally increase the bed shear stresses, so they are responsible for sediment entrainment in loose beds (Koken & Constantinescu, 2021). On the other hand, in case E10, it was observed that there is no horseshoe vortex formation inside the array. The reason for this is that sparser cases (i.e., E20 and E30) were simulated under higher stem Reynolds numbers (i.e., Re_{db}=10865, 12230 for E20 and E30 cases) compared to the E10 case (i.e., Re_{db}=6157). In other words, the flow velocity of the E10 case is not sufficiently large to generate coherent horseshoe vortices around the plant stems. In addition, Figure 7.7 reveals that while there is an interaction of wakes in the E10 case, the flow around the stems situated lower density arrays (i.e., E20 and E30) is similar to the flow around an isolated cylinder.

7.2   Submerged Vegetation Array

In Figure 7.8, a representative submerged vegetation stem at the front of the array in the S75 case was selected to reveal complex flow patterns around vegetation stems having a free end (i.e., top of the stem) using time-averaged streamlines. Firstly, an approaching flow moves over the top of the stem, and there is a separation at the leading edge. However, a recirculation zone was not observed at the top of the stem for the given vegetation stem and flow conditions. As can be seen in Figure 7.8, streamlines near the top and sides of the stem are contracted, so the local velocities at these regions are increased (i.e., represented by red color). In addition, two longitudinal recirculation regions shown by red arrows were observed behind the stem. The core of the first and second recirculation regions are located at $x/H \approx 8.225$, $z/H \approx 0.32$ and $x/H \approx 8.425$, $z/H \approx 0.66$, respectively. It was also observed that the number of the recirculation zones behind the stem and their core location vary with stem location and the submergence ratio, h_v.
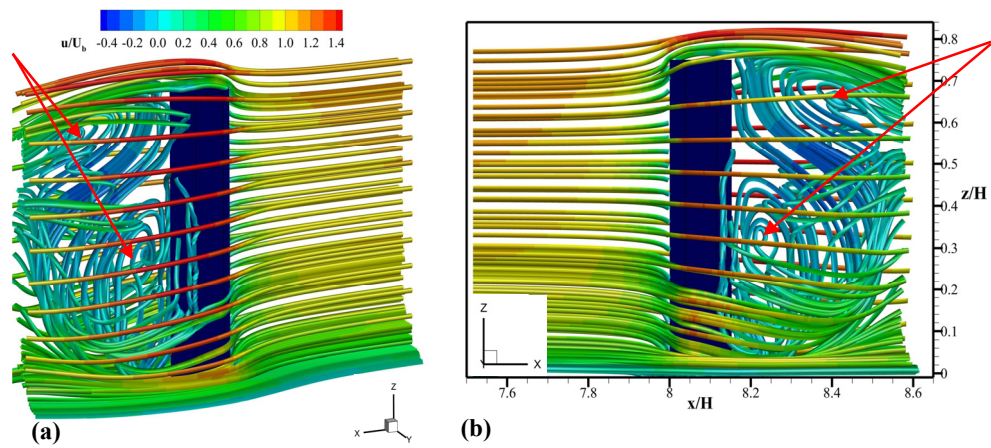
Figure 7.8. Flow around the submerged vegetation stem in S75 case a) 3D view
b) Longitudinal view

The effect of the submergence ratio on the spatial variation of temporally-averaged streamwise velocity is demonstrated in Figure 7.9. The drag plate region (shown in blue in Figure 7.9a), where fully developed flow occurs for each submerged case, was selected to represent the whole channel flow. Moreover, the streamwise velocity measurements were taken from the mid-height of the vegetation stem (i.e., $z=h_v/2$) for each case in Figure 7.9.
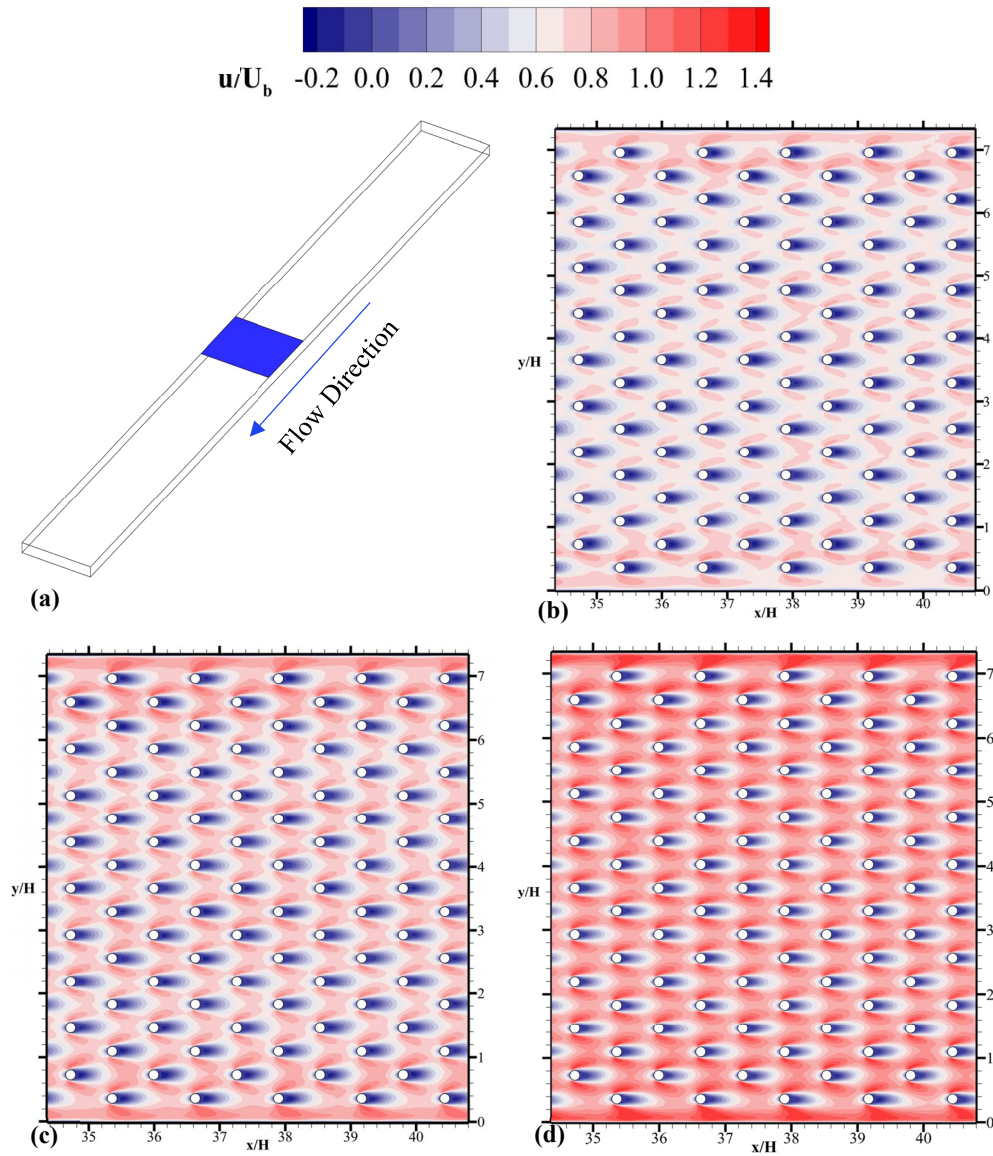
Figure 7.9. a) Place of the drag plate, and streamwise velocity contours at $0.5h_v$ height on the drag plate for b) S25, c) S50 and d) S75

It was observed that the streamwise velocity between the vegetation stems increases as the submergence ratio (or stem height) increases for the given stem Reynolds

number and vegetation density. A similar conclusion is valid for any depth along the stem layer (i.e., $0<z<h_v$).

Figure 7.10 shows the variation of vertical and spanwise-averaged streamwise velocity in the stem layer, $\overline{\overline{u}}_s/U_b$ ($0<z<h_v$), and surface layer, $\overline{\overline{u_{sl}}}/U_b$ ($h_v<z<H$) along the streamwise direction. Moreover, the mean streamwise velocity profiles in Figure 7.10 were also window averaged in the flow direction to remove the local effect of vegetation stems.
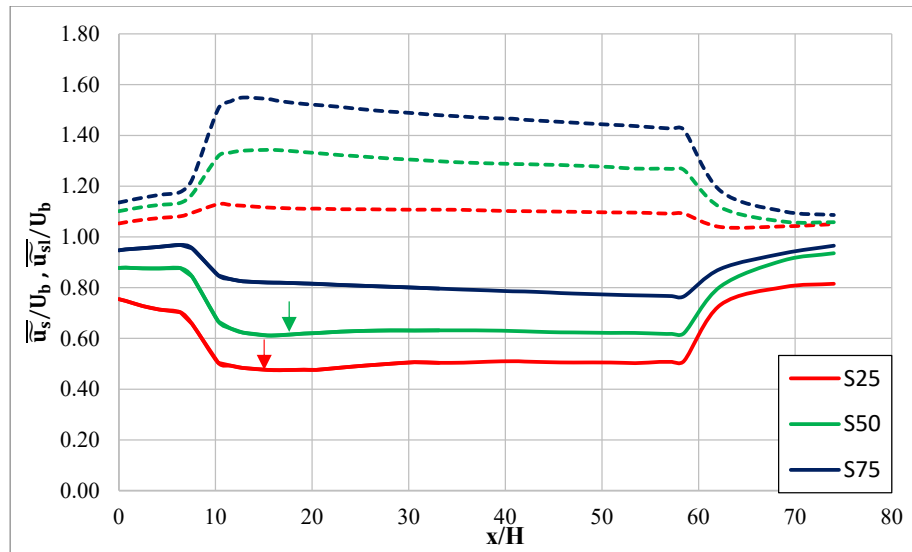
Figure 7.10. Variation of cross sectionally averaged mean streamwise velocity inside the stem layer, $\overline{\overline{u}}_s/U_b$ ($0<z<h_v$, solid lines), and the surface layer $\overline{\overline{u_{sl}}}/U_b$ ($h_v<z<H$, dashed lines)

Figure 7.10 shows that mean streamwise velocity in the stem layer increases as the submergence ratio increases, which explains the discrepancies between streamwise velocity contours of different cases in the previous figure. It was also seen from Figure 7.10 that the cross-sectionally averaged mean streamwise velocity in the stem layer, $\overline{\overline{u}}_s/U_b$, decelerates and reaches a constant level after a certain location for cases S25 and S50. Chen et al. (2013) described this quick deceleration of flow at the front

edge of the array as a balance between flow inertia, canopy drag and pressure. A region between the leading edge of the array (i.e., x/H=8.0) and that location (i.e., where $\overline{\widetilde{u}_s}/U_b$ becomes constant) is called the initial adjustment region. A certain amount of the flow rate in the stem layer passes the surface layer along the initial adjustment region, so there is a decay in the mean streamwise velocity at this region. After the initial adjustment region, the mean streamwise velocity in the surface layer also becomes nearly constant for S25 and S50 cases. Chen et al. (2013) propose the following formula to estimate the initial adjustment length (X_D) for channel-spanning submerged arrays:

$$\frac{X_D}{L_c} = \beta(1 + \alpha C_D a h_v) \tag{7.2}$$

where $\alpha=2.3\mp0.2$ and $\beta=1.5\mp0.2$ are experimentally determined scale factors, and L_c is the canopy drag length scale and defined as below (Belcher et al., 2003):

$$L_c = 2(1 - \lambda)/C_D a \tag{7.3}$$

The vertical arrows in Figure 7.10 demonstrate the end of the initial adjustment region based on Equation (7.2). It was seen from Figure 7.10 that the numerical results and the theoretical model (i.e., Equation (7.1)) are in good agreement for S25 and S50 cases. Moreover, Figure 7.10 demonstrates that the length of the initial adjustment region, X_D/H, slightly increases as the submergence ratio increases for constant vegetation density and stem Reynolds number. However, a similar conclusion can not be drawn for the S75 case. In that case, the mean streamwise velocity in the stem layer continues to decrease slightly along the vegetation array and does not approach any constant level.

The depth-averaged ($0<z<h_v$) turbulent kinetic energies of cases having different submergence ratios are given in Figure 7.11. In this figure, a part of the channel (i.e., $5<x/H<30$) was presented to represent the whole channel. As can be seen from that figure, an increase in the submergence ratio results in TKE amplification at some

168

local regions in vegetation arrays for a constant vegetation density and stem Reynolds number. An increase in TKE at these local regions points out that there is a formation of large-scale eddies or vortex shedding. Thus, these local regions are generally formed in the wake of the vegetation stems in the canopy flows as shown in Figure 7.11.
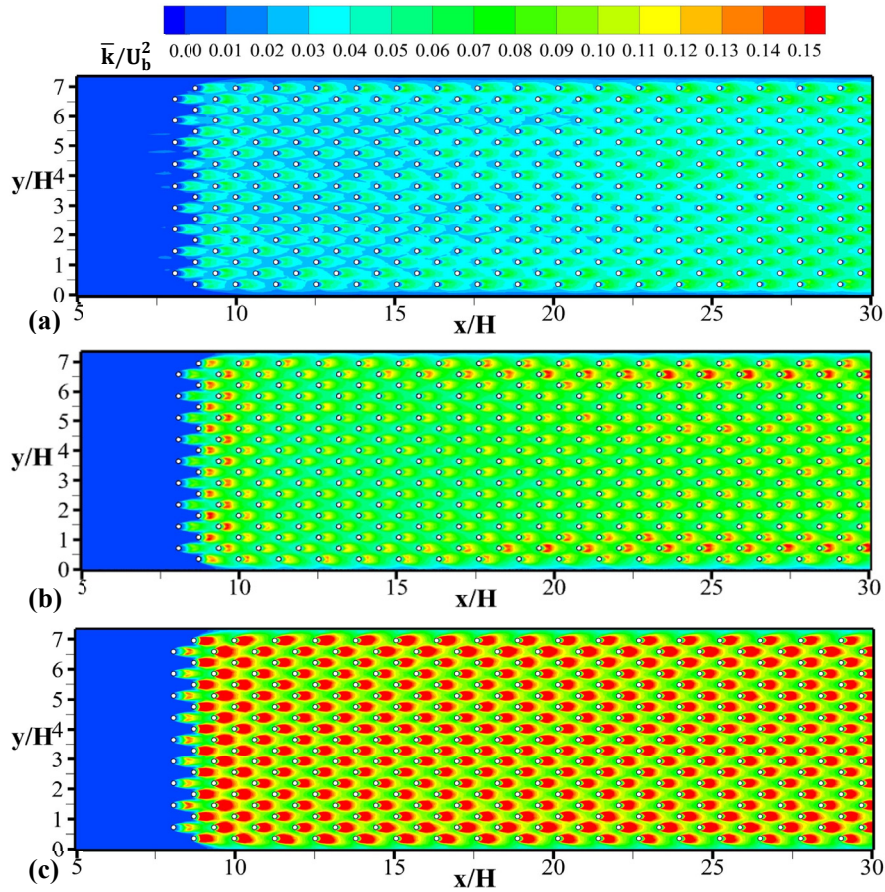
Figure 7.11. Depth-averaged turbulent kinetic energy in a horizontal plane for the upstream part of the array a) S25, b) S50 and c) S75

Furthermore, it was observed that vegetation stems at the first row of the submerged array could not generate TKE at its wake as much as other stems. This may be explained in a way that stems at the first-row experience lower impact velocity than

others, because the contraction in the flow area starts after the first vegetation row (i.e., blockage effect). Thus, the energy of vortices shed in the wake of stems at the first-row decreases. In addition, it was observed that the vegetation stems nearby the outermost and the innermost ones produce larger TKE than other stems in the same row.

Figure 7.12 demonstrates the vertical distribution of width averaged ($0<y<B$) TKE for the given cases. It can be seen that the shear layer starts to develop from the first row of the array, and the height of the shear layer grows in a streamwise direction. It was noticed that the growth rate of shear layer height increases as the submergence ratio increase. The shear layers of S50 and S75 cases reach the free surface at $x/H \approx 17.5$ and $x/H \approx 11$, respectively. After these locations, the distribution of width-averaged TKE does not vary in a streamwise direction and remains constant until the end of the array. On the other hand, the shear layer of the S25 case could not contact with the free surface. Rather, the shear layer slowly approaches its peak around $x/H \approx 26.5$ in the S25 case. Furthermore, it was observed that TKE amplification inside the array becomes more prominent with the increase in submergence ratio.
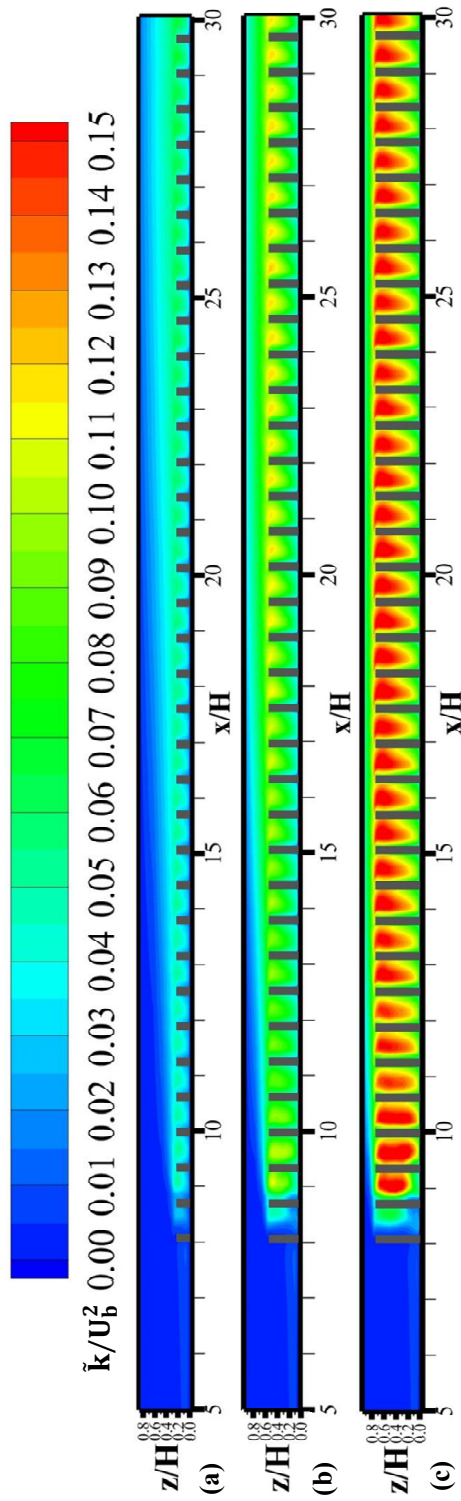
Figure 7.12. Width averaged turbulent kinetic energy in a vertical plane for the upstream part of the array a) S25, b) S50 and c) S75

171

Variation of the vertical and spanwise-averaged ($0<z<h_v$, $0<y<B$) TKE, $\bar{\bar{k}}/U_b^2$, in the flow direction is demonstrated in Figure 7.13. Similar to Figure 7.10, the mean TKE profiles in Figure 7.13 were also window averaged in the flow direction to eliminate the local effect of vegetation stems.
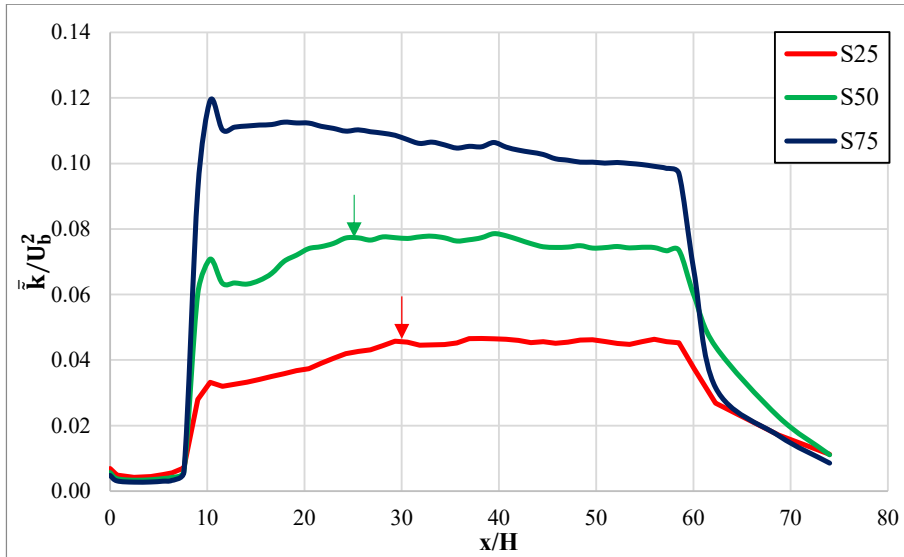
Figure 7.13. Variation of the vertical and spanwise-averaged turbulent kinetic energy inside the submerged arrays

Figure 7.13 indicates that there is a large TKE amplification around the beginning of the array, and the averaged TKE reaches its local maximum value nearly 2D inside from the front face of the array (i.e., $x/H \approx 10$). This result is also supported by TKE contours in Figure 7.11 for each case. Moreover, the averaged TKE profiles indicate that the overall TKE values reduce with a decrease in the submergence ratio. After the local maximum TKE value is reached, there is a decrease in TKE values, and this rate of decrease increases with the submergence ratio. Later, the averaged TKE values in the S25 and S50 cases rise again up to a certain location shown by vertical arrows in Figure 7.13. After these locations, the averaged TKE becomes nearly constant up to the end of the array. Contrary to these cases, the averaged TKE in the S75 case decreases continuously until the end of the array. It was also noted that the

172

decay rate of the averaged TKE after the end of the array increases with an increasing submergence ratio.

The depth-averaged ($0<z<h_v$) vertical vorticities are shown in Figure 7.14 for the upstream part of the arrays. It was observed that the wakes behind the vegetation stems were suppressed inside the array, so the wake length decreases in the streamwise direction and becomes constant. A sample of vegetation stem was taken from the mid-width of the channel (captured by the dashed red rectangle in the left figures) to compare the effect of submergence on the wake characteristics. As seen from the figures on the right-hand side, the wake length slightly increases with increasing submergence ratio. Contrary to wake lengths, the wake widths were not affected by the submergence ratio for the given vegetation density and stem Reynolds number. Moreover, Figure 7.14 demonstrates that the angle between wakes on each side of the stem slightly increases with the submergence ratio.

Furthermore, the width-averaged vorticity profiles of submerged arrays, $\widetilde{\omega_y}(H/U_b)$, (figures are not given here) reveal that there is a local region at the top of each stem where maximum vorticity develops due to the separation. However, inside the stem layer, vorticity magnitudes decrease, and negative vorticity values start to develop toward the bed.
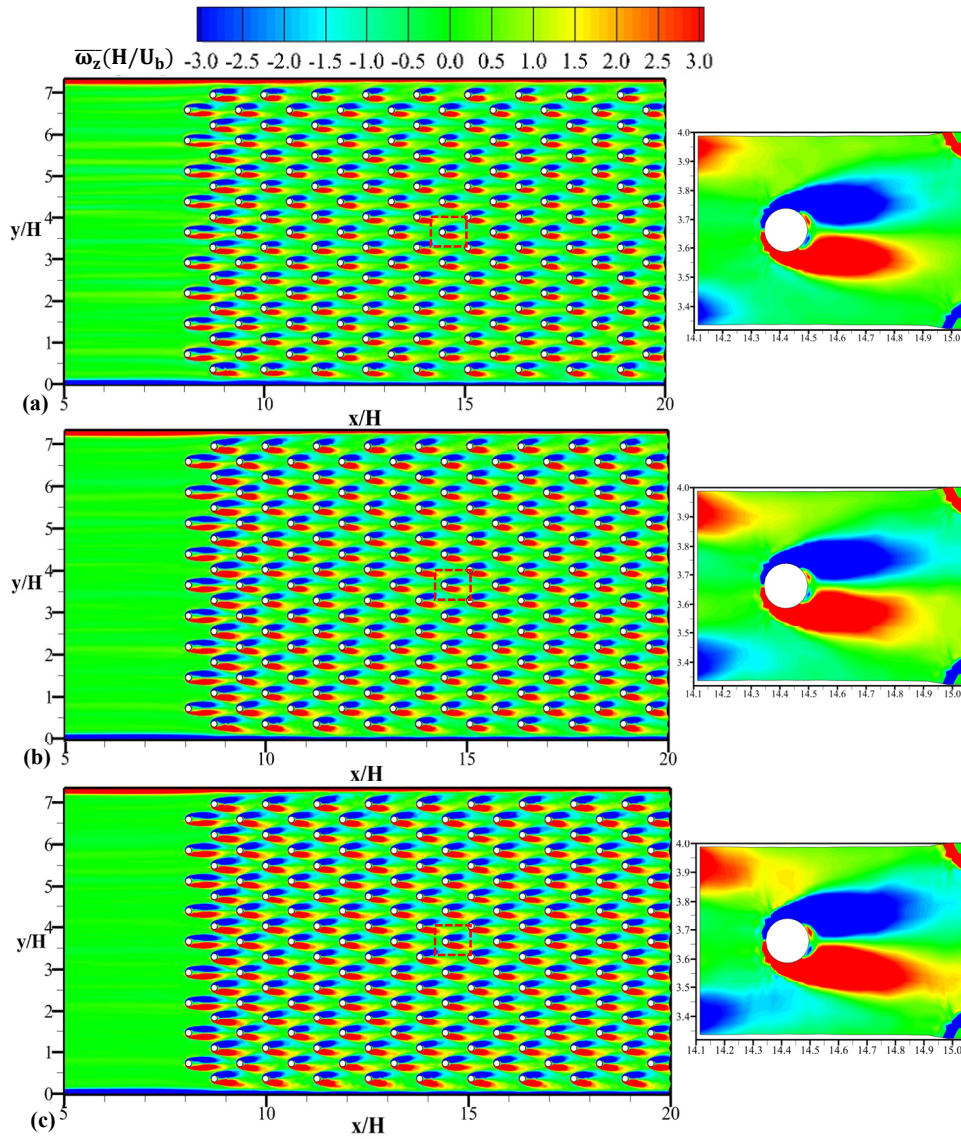
Figure 7.14. Depth-averaged vertical vorticity inside the upstream part of the array

a) S25, b) S50 and c) S75

Figure 7.15 visualize the mean flow at the upstream part of the array using the Q criterion.
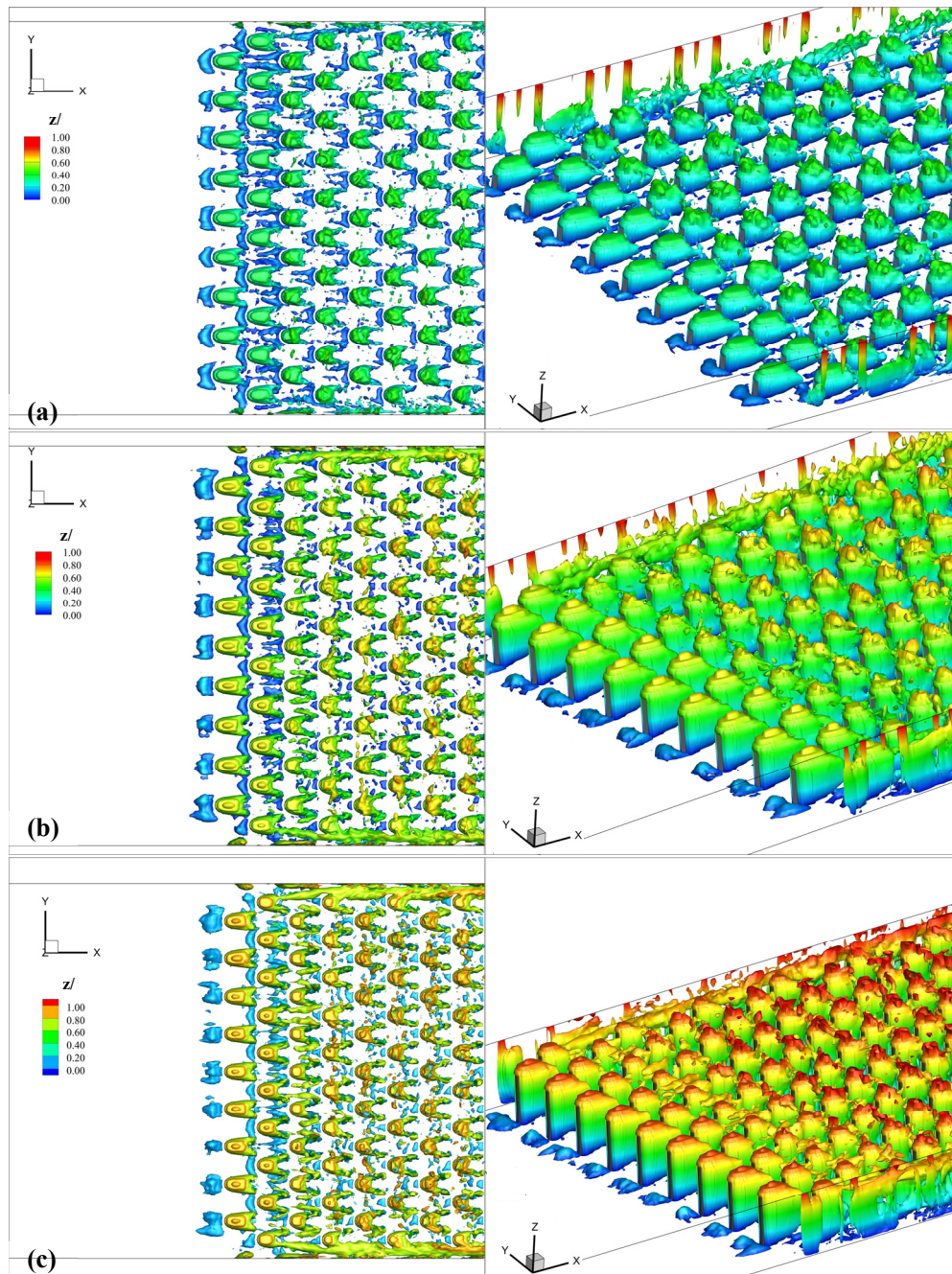
Figure 7.15. Mean flow visualization inside the upstream part of the submerged arrays with the Q criterion a) S25, b) S50 and c) S75

Although the density of the submerged vegetation array is significantly larger than that of the emergent array shown in Figure 7.1, horseshoe vortices do not develop at the base of submerged vegetation stem in any submerged cases. This can be explained by two main reasons: Firstly, the submerged vegetation cases were run for a lower stem Reynolds number (i.e., Re_{db}=6157) than that of the E30 case. Secondly, some part of the incoming flow approaching the submerged vegetation array is diverted into the surface layer. Thus, there is a decrease in downflow which is not sufficient to generate horseshoe vortices at the base of the submerged stems.

CHAPTER 8

CONCLUSIONS

8.1   Summary and Conclusion of the Study

The present study investigated the flow resistance due to the emergent and submerged vegetation array by conducting experiments and numerical analyses. Moreover, flow characteristics and structures inside the emergent and submerged vegetation array were examined. A novel experimental setup was designed and constructed to measure the total drag forces acting on emergent and submerged vegetation arrays using a drag plate. The DES model provided to evaluate bed shear stress on the drag plate and made it possible to obtain the drag coefficients from experimental measurements.

The following conclusions are drawn for the emergent vegetation cases:

In the total flow resistance analyses, it was seen that the experimental results of the present study are consistent with the data and results of the previous studies (i.e., Ishikawa et al. (2000) and Cheng & Nguyen (2011)). It was also observed that Manning's roughness coefficient increases with an increase in vegetation density and flow depth (i.e., Figure 6.2). The dimensionless parameter called roughness concentration, based on the hydraulic radius 'aR_h', includes both the effect of vegetation density and flow depth, so it was used to derive total flow resistance relationships. Instead of estimation of Manning's roughness coefficient based on qualitative evaluation (e.g., Chow, 1959), a practical equation (i.e., Equation (6.6)) was proposed to predict Manning's roughness coefficient in a more accurate way.

Similarly, Equation (6.13) was derived by performing regression analysis to estimate Darcy-Weisbach friction factor. When the estimation performances of these equations were evaluated, it was seen that Manning's roughness coefficient and Darcy-Weisbach friction factor can be predicted satisfactorily using Equations (6.6) and (6.13) having high R^2 values.

The experimental mechanism measures the total drag force acting on the drag plate, including the bed shear stresses. Thus, it was necessary to evaluate the bed shear stress contribution in the total drag to obtain the actual drag coefficient of the vegetation array. The relationship between the bed shear stress contribution and vegetation density was derived using the numerical analyses results. In the literature, Kim and Stoesser (2011) performed a similar analysis and proposed a relationship valid for relatively low stem Reynolds numbers (i.e., Re_{db} =500 and 1340) and high vegetation densities (i.e., $0.016 \leq \lambda \leq 0.25$). Although the present study was conducted with different stem Reynolds number and vegetation densities, it was observed that there is a strong consistency between the relationships of these studies (i.e., the present study and the study of Kim & Stoesser, 2011). This consistency supports the finding of Etminan et al. (2018) and reveals that the effect of stem Reynolds number on the bed friction contribution diminishes as the stem Reynolds number increases. Therefore, the data groups of Kim and Stoesser (2011) (i.e., for Re_{db}=1340) and the present study were combined to derive a new relationship (i.e., Equation (6.15)) between the bed shear contribution and vegetation density. The proposed relation, which has high R^2 value, provides to find the contribution of bed shear stress to the total resistance in a very wide range of vegetation density (i.e., $0.00436 \leq \lambda \leq 0.25$) and relatively high stem Reynolds numbers (i.e., $Re_{db} \geq 1340$).

In the experimental analyses, the effect of commonly used velocity scales (i.e., U_b, U_p and U_c) on the variation of the drag coefficient was investigated in detail. Contrary to similar studies in the literature (e.g., Etminan et al., 2017 and van Rooijen et al., 2018), it was observed from analyses that none of these velocity scales

are successful in reducing the data scattering for the given vegetation densities and stem Reynolds number in the present study. This is because the present study was performed with relatively lower vegetation densities than those of other studies. Figures 6.13-6.15 demonstrate that the spatially averaged drag coefficient is independent of stem Reynolds number, and there is not any evident effect of the vegetation density on the spatially averaged drag coefficient for the given flow conditions and vegetation characteristics. Moreover, contrary to recommendations of the past studies (e.g., Etminan et al., 2017 and van Rooijen et al., 2018), White's (1991) equation does not accurately estimate the drag coefficients based on each reference velocity scale in the present study. Therefore, new drag coefficient relations (i.e., Equations (6.21) and (6.22)), based on Sucker-Brauer's (1975) formula, were developed by considering the effect of vegetation density. Although the drag coefficient data distribution is scattered, the performance analysis shows that these equations can be used to approximately estimate the drag coefficients of emergent vegetation arrays.

In the numerical analysis, it was seen that the spanwise averaged drag coefficient decreases along the array and does not reach a constant value in the E10 case. The reason for this is that the velocity is not fully developed in the streamwise direction for the given array. Therefore, the spatially averaged drag coefficient of the numerical case is not consistent with the corresponding experimental case. The grid independency examination of this case shows that there is not any difference between the spatially averaged drag coefficients of the coarser and finer meshed cases, which means that solutions are independent of the grid. On the other hand, it was observed that the spanwise averaged drag coefficient of other numerical cases (i.e., E20 and E30) does not vary in a streamwise direction. The averaged drag coefficients of E20 and E30 cases were found to be similar to that of an isolated cylinder which reveals that the drag modifying mechanisms are not evident for the emergent vegetation cases having a density less than 0.01 for the given flow conditions. A reasonable agreement (i.e., a slight discrepancy $\approx 10\%$) was found between the spatially

averaged drag coefficients of these numerical cases and corresponding experimental runs. The potential reason for these discrepancies may be that the free surface effects were ignored in the numerical analyses (i.e., rigid lid assumption). Thus, it was proved that the novel experimental setup measures the drag forces acting on vegetation stems with pretty good accuracy. Moreover, although the E10 case was performed under the lowest stem Reynolds number compared to other cases, the largest TKE production occurred in that case. The cross-sectionally averaged TKE profiles indicate that there is a constant TKE magnitude inside the vegetation array along the streamwise direction for E20 and E30 cases; however, the TKE monotonically decreases in the E10 case. The depth-averaged vertical vorticity profiles (i.e., Figure 7.6) show that while the wake characteristics are slightly changed in the streamwise direction for E10 and E20 cases, there is not any considerable alteration in the wake characteristics for the E30 case. In addition, it was observed using the Q criterion that the horseshoe vortices develop on the front of vegetation stems located upstream of the arrays for E20 and E30 cases. However, these coherent structures do not seem in the E10 case, because the E10 case was simulated with a lower stem Reynolds number than other cases.

The following conclusions are drawn for the submerged vegetation cases:

The functional relationships, which were derived using the total flow resistance equations and the force balance equations, show that the total flow resistance parameters (i.e., Manning's roughness coefficient and Darcy-Weisbach friction factor) depend on both roughness concentration, based on the hydraulic radius, and the submergence ratio. Figure 6.31 shows that although Manning's roughness coefficient is almost independent of the submergence ratio for lower vegetation densities (i.e., $\lambda=0.00436$, 0.00981 and 0.01744), it increases with an increase in the submergence ratio for the highest density case (i.e., $\lambda=0.03924$). In addition, it was observed that Manning's roughness coefficient increases with the roughness concentration, and the rate of increase of Manning's roughness coefficient depends

on the submergence ratio (i.e., Figure 6.32). The practical relations were developed to estimate the total flow resistance parameters by performing regression analyses. Additional data groups were gathered from similar studies in the literature to extend the validity range of the proposed relationships. The performance assessments and R^2 values demonstrate that these equations can accurately predict the total flow resistance parameters.

The bed friction contribution to the total drag force was investigated by performing numerical analyses for cases having different submergence ratios. It was observed that the contribution of bed friction decreases as the submergence ratio increases (i.e., Figure 6.38). A relation (having high R^2) between the bed friction contribution and the submergence ratio was proposed by performing regression analysis, and this relation is valid for single vegetation density and stem Reynolds number (i.e., $\lambda=0.03924$ and $Re_{db}=6157$).

To calculate the actual drag coefficient in submerged arrays, it is necessary to obtain the average velocity in the stem layer. Thus, some of the previous studies, which propose a formula to derive the average stem layer velocity, were evaluated by making a comparison between the numerical results of the present study and their proposed functions. In the result of these assessments, it was found that the analytical formula proposed by the study of Klopstra et al. (1997) provides the most accurate results among these studies. Experimental analyses show that the drag coefficient of the submerged vegetation array is independent of stem Reynolds number for the submergence ratio interval $0.2<h^*<0.5$. However, it is not possible to draw an exact conclusion about the relation between the drag coefficient and stem Reynolds number for larger submergence ratios (i.e., $0.5<h^*<0.7$) due to the insufficient number of data. Moreover, it was seen that the drag coefficient exponentially decreases with an increase in the submergence ratio for the tested vegetation densities. The effect of the submergence ratio on the drag coefficient diminishes as the submergence ratio increases. Also, it was noted that the spatially averaged drag

coefficient of the submerged array reduces with an increase in vegetation density. A formula (i.e., Equation (6.46)) for the prediction of the drag coefficient was derived by performing multivariate non-linear regression analysis using the vegetation density and the submergence ratio. The performance assessment of this formula shows that Equation (6.46) can estimate the drag coefficient of the submerged vegetation array with good accuracy.

Furthermore, the numerical analyses demonstrate that the spanwise averaged drag coefficients are constant and not changed along the streamwise direction. The spatially averaged drag coefficients of submerged stems located on the drag plate were found as C_{Ds-num}= 1.84, 1.79 and 1.80 for S25, S50 and S75 cases, respectively. Therefore, the numerical analyses show that the drag coefficient does not depend on the submergence ratio for the given vegetation density and stem Reynolds number (i.e., λ=0.03924 and Re_{db}=6157). As stated previously, there is not any experimental run that directly corresponds to the numerical cases considering flow conditions and submergence ratios. Thus, the result of numerical cases was compared with experimental cases having similar flow and submergence conditions. It was evaluated from the comparison that although there is a consistency between the drag coefficients of similar experimental runs and the S25 case (i.e., a slight discrepancy $\approx$13%), the difference between the drag coefficients of experimental cases and the S50 case was found relatively high (i.e., $\approx$27%). It was considered that the deviations between the averaged stem layer velocities in the numerical analyses and those found by the analytical formula might be responsible for the discrepancies in the drag coefficients. In addition to drag coefficients, the numerical analyses show that the streamwise velocity inside the submerged vegetation array increases with the submergence ratio for the given stem Reynolds number and vegetation density. It was observed that the initial adjustment lengths of S25 and S50 cases are in good agreement with those found using the theoretical model of Chen et al. (2013). Moreover, the depth-averaged TKE profiles demonstrate that the TKE generation in

182

the wake of submerged stems increases with an increase in the submergence ratio (i.e., Figure 7.11). It was seen from the width-averaged TKE profiles that the shear layer in submerged arrays with a larger submergence ratio reaches the free surface at a shorter streamwise distance. While cross-sectionally averaged TKE profiles of S25 and S50 cases reach nearly a constant magnitude inside the vegetation array, the averaged TKE values diminish continuously along the vegetation array in the S75 case. In addition, the depth-averaged vertical vorticity profiles reveal that the wake length slightly increases as the submergence ratio increases. Finally, the Q criterion indicates that there is no horseshoe vortex development in any submerged cases due to the low stem Reynolds number.

8.2   Recommendations for Future Studies

The present study mainly focuses on the flow resistance due to rigid vegetation arrays. However, as stated previously, vegetation characteristics can vary from region to region depending on environmental conditions. There are many types of aquatic vegetation in nature such as flexible ones and ones with branches and foliage. Therefore, similar analyses can be performed with different aquatic vegetation types to investigate the vegetation characteristics on the drag coefficients. In addition to vegetation arrays, vegetation patches are frequently encountered in waterways and rivers, so the effect of vegetation patches in different shapes (e.g., circular or rectangular patches) on the flow resistance can also be investigated.

Furthermore, similar analyses can be performed on beds having different roughness characteristics to examine the effect of bed condition in vegetated channels on the total flow resistance. For experimental studies, it is strongly recommended to use non-penetrating flow measurement equipment such as laser Doppler velocimetry which provides detailed information about the flow characteristics. Experiments can

also be conducted on loose beds to evaluate the effect of vegetation on channel morphology or sediment transport capacity.

REFERENCES

Achenbach, E. (1968). Distribution of local pressure and skin friction around a circular cylinder in cross-flow up to $Re = 5 \times 10^6$. *Journal of Fluid Mechanics*, *34*(4), 625–639. https://doi.org/10.1017/S0022112068002120

Afgan, I., Kahil, Y., Benhamadouche, S., & Sagaut, P. (2011). Large eddy simulation of the flow around single and two side-by-side cylinders at subcritical Reynolds numbers. *Physics of Fluids*, *23*(7). https://doi.org/10.1063/1.3596267

Arcement, G. J., & Schneider, V. R. (1989). *Guide for Selecting Manning's Roughness Coefficients for Natural Channels and Flood Plains*. https://doi.org/10.3133/wsp2339

Armanini, A., Righetti M., & Grisenti, P. (2005). Direct measurement of vegetation resistance in prototype scale. *Journal of Hydraulic Research*, *43*(5), 481-487. https://doi.org/10.1080/00221680509500146

Auel, C., Albayrak, I., & Boes, R. M. (2014). Turbulence characteristics in supercritical open channel flows: Effects of Froude number and aspect ratio. *Journal of Hydraulic Engineering*, *140*(4), 1-16. https://doi.org/10.1061/(ASCE)HY.1943-7900.0000841

Belcher, S. E., Jerram, N., & Hunt J. C. R. (2003). Adjustment of a turbulent boundary layer to a canopy of roughness elements. *Journal of Fluid Mechanics*, *488*, 369–398. https://doi.org/10.1017/S0022112003005019

Ben Meftah, M., & Mossa, M. (2013). Prediction of channel flow characteristics through square arrays of emergent cylinders. *Physics of Fluids*, *25*(4). https://doi.org/10.1063/1.4802047

Bennett, S. J., Wu, W., Alonso, C. V., & Wang, S. S. Y. (2008). Modeling fluvial response to in-stream woody vegetation: Implications for stream corridor restoration. *Earth Surface Processes and Landforms*, *33*(6), 890–909. https://doi.org/10.1002/esp.1581

Callaghan, F. M., Cooper, G. G., Nikora, V. I., Lamouroux, N., Statzner, B., Sagnes, P., Radford, J., Malet, E., & Biggs, B. J. F. (2007). A submersible device for measuring drag forces on aquatic plants and other organisms. *New Zealand Journal of Marine and Freshwater Research*, *41*(1), 119-127. https://doi.org/10.1080/00288330709509900

Chang, K., Constantinescu, G., & Park, S. O. (2007). Assessment of Predictive Capabilities of Detached Eddy Simulation to Simulate Flow and Mass Transport Past Open Cavities. *Journal of Fluid Engineering*, *129*(11), 1372-1383. https://doi.org/10.1115/1.2786529

Chang, W. Y., Constantinescu, G. & Tsai, W. F. (2017). On the flow and coherent structures generated by a circular array of rigid emerged cylinders placed in an open channel with flat and deformed bed. *Journal of Fluid Mechanics*, *831*, 1–40. https://doi.org/10.1017/jfm.2017.558

Chang, W. Y., Constantinescu, G. & Tsai, W. F. (2020). Effect of array submergence on flow and coherent structures through and around a circular array of rigid vertical cylinders. *Physics of Fluids*, *32*(3). https://doi.org/10.1063/1.5138604

Chen, Z., Jiang, C., & Nepf, H. (2013). Flow adjustment at the leading edge of a submerged aquatic canopy. *Water Resources Research*, *49*(9), 5537– 5551. https://doi.org/10.1002/wrcr.20403

Chen, Z., Ortiz, A., Zong, L., & Nepf, H. (2012). The wake structure behind a porous obstruction and its implications for deposition near a finite patch of emergent vegetation. *Water Resources Research*, *48*(9). https://doi.org/10.1029/2012WR012224

Cheng, N. S. (2011). Representative roughness height of submerged vegetation. *Water Resources Research*, *47*(8). https://doi.org/10.1029/2011WR010590

Cheng, N. S. (2015). Single-Layer Model for Average Flow Velocity with Submerged Rigid Cylinders. *Journal of Hydraulic Engineering*, *141*(10), 6015012. https://doi.org/10.1061/(ASCE)HY.1943-7900.0001037

Cheng, N.-S., & Nguyen, H. T. (2011). Hydraulic radius for evaluating resistance induced by simulated emergent vegetation in open-channel flows. *Journal of Hydraulic Engineering*, *137*(9), 995-1004. https://doi.org/10.1061/(ASCE)HY.1943-7900.0000377

Chow, V.T. (1959). Open-channel hydraulics. McGraw-Hill

Constantinescu, G., Koken, M., & Zeng J. (2011). The structure of turbulent flow in an open channel bend of strong curvature with deformed bed: Insight provided by detached eddy simulation. *Water Resources Research*, *47*(5). https://doi.org/10.1029/2010WR010114

Constantinescu, G., & Squires, K. (2004). Numerical investigation of the flow over a sphere in the subcritical and supercritical regimes. *Physics of Fluids*, *16*(5), 1449–1466. https://doi.org/10.1063/1.1688325

Cowan, W. L. (1956). Estimating hydraulic roughness coefficients. *Agricultural Engineering*, *37*(7), 473-475.

Defina, A., & Bixio, A. C. (2005). Mean flow and turbulence in vegetated open channel flow. *Water Resources Research*, *41*(7), 1-12. https://doi.org/10.1029/2004WR003475

D'Ippolito, A., Lauria, A., Alfonsi, G., & Calomino, F. (2019)*.* Investigation of flow resistance exerted by rigid emergent vegetation in open channel. *Acta Geophysica*, *67*(3), 971–986. https://doi.org/10.1007/s11600-019-00280-8

Dubief, Y., & Delcayre, F. (2000). On coherent-vortex identification in turbulence. *Journal of Turbulence*, *1*. https://doi.org/10.1088/1468-5248/1/1/011

Dunn, C., Lopez, F., & Garcia, M. H. (1996). *Mean Flow and Turbulence in a Laboratory Channel with Simulated Vegetation* (HES 51). http://hdl.c.net/2142/12229

Etminan V., Ghisalberti, M., & Lowe, R. J. (2018). Predicting bed shear stresses in vegetated channels. *Water Resources Research*, *54*(11)*,* 9187–9206. https://doi.org/10.1029/2018WR022811

Etminan, V., Lowe, R. J. & Ghisalberti, M. (2017). A new model for predicting the drag exerted by vegetation canopies. *Water Resources Research*, *53*(4), 3179–3196. https://doi.org/10.1002/2016WR020090

Fathi-Maghadam, M., & Kouwen, N. (1997). Nonrigid, nonsubmerged, vegetative roughness on floodplains. *Journal of Hydraulic Engineering, 123* (1), 51–57. https://doi.org/10.1061/(ASCE)0733-9429(1997)123:1(51)

Fonseca, M. S., & Cahalan, J. A. (1992). A preliminary evaluation of wave attenuation by four species of seagrass*. Estuarine, Coastal and Shelf Science*, *35*(6), 565–576. https://doi.org/10.1016/S0272-7714(05)80039-3

Franke, J., Hellsten, A., Schlünzen, H. & Carissimo, B. (2007). *Best Practice Guideline for the CFD Simulation of Flows in the Urban Environment: COST Action 732 Quality Assurance and Improvement of Microscale Meteorological Models*.

Gacia, E., & Duarte, C. M. (2001). Sediment retention by a Mediterranean Posidonia oceanica meadow: The balance between deposition and resuspension. *Estuarine, Coastal and Shelf Science*, *52*(4), 505–514. https://doi.org/10.1006/ecss.2000.0753

Ghisalberti, M., & Nepf, H. (2006). The Structure of the Shear Layer in Flows over Rigid and Flexible Canopies. *Environmental Fluid Mechanics*, *6*(3), 277–301. https://doi.org/10.1007/s10652-006-0002-4

Ghisalberti, M., & Nepf, H. (2009). Shallow flows over a permeable medium: The hydrodynamics of submerged aquatic canopies. *Transport in Porous Media*, *78*(2), 309–326. https://doi.org/10.1007/s11242-008-9305-x

Gijón Mancheño, A., Jansen, W., Winterwerp, J. C., & Uijttewaal W. S. J. (2021). Predictive model of bulk drag coefficient for a nature-based structure exposed to currents. *Scientific Reports*, *11*(1). https://doi.org/10.1038/s41598-021-83035-0

Green, J. C. (2005). Modelling flow resistance in vegetated streams: review and development of new theory. *Hydrological. Processes*, *19*(6), 1245-1259. https://doi.org/10.1002/hyp.5564

Hendriks, I. E., Sintes, T., Bouma, T. J., & Duarte, C. M. (2008). Experimental assessment and modeling evaluation of the effects of the seagrass Posidonia oceanica on flow and particle trapping. *Marine Ecology Progress Series*, *356*, 163–173. https://doi.org/10.3354/meps07316

Hoerner, S. F. (1965). *Fluid-Dynamic Drag: Practical Information on Aerodynamic Drag and Hydrodynamic Resistance*. Hoerner Fluid Dynamics.

Huthoff, F., Augustijn, D. C. M., & Hulscher, S. J. M. H. (2007). Analytical solution of the depth-averaged flow velocity in case of submerged rigid cylindrical vegetation. *Water Resources. Research*, *43*(6). https://doi.org/10.1029/2006WR005625

Inoue, M., & Nakano, S. (1998). Effects of woody debris on the habitat of juvenile masu salmon (Oncorhynchus masou) in northern Japanese streams. *Freshwater Biology*, *40*(1), 1-16. https://doi.org/10.1046/j.1365-2427.1998.00346.x

Ishikawa, Y., Mizuhara, K., & Ashida, S. (2000). Effect of density of trees on drag exerted on trees in river channels. *Journal of Forest Research*, *5*, 271–279. https://doi.org/10.1007/BF02767121

Ishikawa, Y., Sakamoto, T., & Mizuhara, K. (2003). Effect of density of riparian vegetation on effective tractive force. *Journal of Forest Research*, *8*(4), 235-246. https://doi.org/10.1007/s10310-003-0032-4

James, C. S., Birkhead, A. L., Jordanova, A. A., & O'Sullivan, J. J. (2004). Flow resistance of emergent vegetation. *Journal of Hydraulic Research*, *42*(4), 390-398. https://doi.org/10.1080/00221686.2004.9641206

Jiang, H. (2020). Separation angle for flow past a circular cylinder in the subcritical regime. *Physics of Fluids, 32*(1). https://doi.org/10.1063/1.5139479

Kim, S. J., & Stoesser, T. (2011). Closure modeling and direct simulation of vegetation drag in flow through emergent vegetation. *Water Resources Research*, *47*(10). https://doi.org/10.1029/2011WR010561

Kirkil, G., & Constantinescu G. (2009). Nature of flow and turbulence structure around an in-stream vertical plate in a shallow channel and the implications for sediment erosion. *Water Resources Research*, *45*(6). https://doi.org/10.1029/2008WR007363

Klopstra, D., Barneveld, H. J., van Noortwijk, J. M., & van Velzen, E. H. (1997). Analytical model for hydraulic roughness of submerged vegetation. *Proceedings of the 27th IAHR Congress: Theme A, Managing Water: Coping with Scarcity and Abundance*, 775–780.

Koken, M., & Constantinescu G. (2008). An investigation of the flow and scour mechanisms around isolated spur dikes in a shallow open channel: 1. Conditions corresponding to the initiation of the erosion and deposition process. *Water Resources Research*, *44*(8). https://doi.org/10.1029/2007WR006489

Koken, M., & Constantinescu, G. (2009). An investigation of the dynamics of coherent structures in a turbulent channel flow with a vertical sidewall obstruction. *Physics of Fluids*, *21*(8). https://doi.org/10.1063/1.3207859

Koken, M., & Constantinescu, G. (2011). Flow and turbulence structure around a spur dike in a channel with a large scour hole. *Water Resources Research*, *47*(12). https://doi.org/10.1029/2011WR010710

Koken, M., & Constantinescu, G. (2021). Flow structure inside and around a rectangular array of rigid emerged cylinders located at the sidewall of an open channel. *Journal of Fluid Mechanics*, *910*. https://doi.org/10.1017/jfm.2020.900

Kothyari, U. C., Hayashi, K., & Hashimoto, H. (2009). Drag coefficient of unsubmerged rigid vegetation stems in open channel flows. *Journal of Hydraulic Research*, *47*(6), 691-699. https://doi.org/10.3826/jhr.2009.3283

Lee, J. K., Roig, L. C., Jenter, H. L., & Visser, H. M. (2004). Drag coefficients for modeling flow through emergent vegetation in the Florida Everglades. *Ecological Engineering*, *22*(4-5), 237–248. https://doi.org/10.1016/j.ecoleng.2004.05.001

Li, R.-M., & Shen, H. W. (1973). Effect of Tall Vegetations on Flow and Sediment. *Journal of the Hydraulics Division*, *99*(5), 793–814. https://doi.org/10.1061/JYCEAJ.0003647

Liu, C., Shan, Y., & Nepf, H. (2021). Impact of stem size on turbulence and sediment resuspension under unidirectional flow. *Water Resources Research*, *57*(3). https://doi.org/10.1029/2020WR028620

Liu, D., Diplas, P., Fairbanks, J. D., & Hodges, C. C. (2008). An experimental study of flow through rigid vegetation. *Journal of Geophysical Research: Earth Surface*, *113*(4). https://doi.org/10.1029/2008JF001042

Liu, M. Y., Huai, W. X., Yang, Z. H., & Zeng, Y. H. (2020). A genetic programming-based model for drag coefficient of emergent vegetation in open channel flows. *Advances in Water Resources*, *140*. https://doi.org/10.1016/j.advwatres.2020.103582

Liu, X., & Zeng, Y. (2017). Drag coefficient for rigid vegetation in subcritical open-channel flow. *Environmental Fluid Mechanics*, *17*(5), 1035–1050. https://doi.org/10.1007/s10652-017-9534-z

Luhar, M., Rominger, J., & Nepf, H. (2008). Interaction between flow, transport and vegetation spatial structure. *Environmental Fluid Mechanics*, *8*(5-6), 423–439. https://doi.org/10.1007/s10652-008-9080-9

Luo, S. C., Gan, T. L., & Chew, Y. T. (1996). Uniform flow past one (or two in tandem) finite length circular cylinder(s). *Journal of Wind Engineering and Industrial Aerodynamics,* *59*(1), 69–93. https://doi.org/10.1016/0167-6105(95)00036-4

Meijer, D. G., & van Velzen, E. H. (1999). Prototype-scale flume experiments on hydraulic roughness of submerged vegetation. *Proceedings of the 28th IAHR World Congress*. https://www.iahr.org/library/infor?pid=13833

Mulahasan, S., & Stoesser, T. (2017). Flow resistance of in-line vegetation in open channel flow. *International Journal of River Basin Management*, *15*(3), 329-334. https://doi.org/10.1080/15715124.2017.1307847

Nepf, H. M. (1999). Drag, turbulence, and diffusion in flow through emergent vegetation. *Water Resources Research*, *35*(2), 479-489. https://doi.org/10.1029/1998WR900069

Nepf, H. M. (2012). Hydrodynamics of vegetated channels. *Journal of Hydraulic Research*, *50*(3), 262–279. https://doi.org/10.1080/00221686.2012.696559

Nepf, H. M., & Vivoni, E. R. (2000). Flow structure in depth-limited, vegetated flow. *Journal of Geophysical Research*: *Oceans*, *105*(C12), 28547–28557. https://doi.org/10.1029/2000JC900145

Nguyen, H. T. (2012). Characteristics of hydraulic resistance and velocity profile in vegetated open-channel flows [Doctoral dissertation, Nanyang Technological University]. https://doi.org/10.32657/10356/50541

Nikora, V., Larned, S., Nikora, N., Debnath, K., Cooper, G., & Reid, M. (2008). Hydraulic resistance due to aquatic vegetation in small streams: Field study. *Journal of Hydraulic Engineering*, *134*(9), 1326–1332. https://doi.org/10.1061/(ASCE)0733-9429(2008)134:9(1326)

Petryk, S. (1969). *Drag on cylinders in open channel flow* [Doctoral dissertation]. Colorado State University.

Pollen, N., & Simon, A. (2005). Estimating the mechanical effects of riparian vegetation on stream bank stability using a fiber bundle model. *Water Resources Research*, *41*(7), 1-11. https://doi.org/10.1029/2004WR003801

Quartel, S., Kroon, A., Augustinus, P. G. E. F., van Santen, P., & Tri, N. H. (2007). Wave attenuation in coastal mangroves in the Red River Delta, Vietnam. *Journal of Asian Earth Sciences*, *29*(4), 576–584. https://doi.org/10.1016/j.jseaes.2006.05.008

Ramamurthy, A. S., & Lee, P. M. (1973). Wall effects on flow past bluff bodies. *Journal of Sound Vibration*, *31*(4), 443-448. https://doi.org/10.1016/S0022-460X(73)80259-7

Rodi, W., Constantinescu, G., & Stoesser, T. (2013). *Large-Eddy Simulation in Hydraulics*. CRC Press. https://doi.org/10.1201/b15090

Roušar, L., Zachoval, Z., & Julien, P. (2016). Incipient motion of coarse uniform gravel. *Journal of Hydraulic Research*, *54*(6), 615-630. https://doi.org/10.1080/00221686.2016.1212286

Schlichting, H. (1979). *Boundary-Layer Theory* (7th ed.). McGraw-Hill.

Schoneboom, T., Aberle, J., & Dittrich, A. (2011). Spatial Variability, Mean Drag Forces, and Drag Coefficients in an Array of Rigid Cylinders. In P. Rowinski (Ed.), *Experimental Methods in Hydraulic Research. Geoplanet: Earth and Planetary Sciences* (pp. 255-265). Springer Berlin, Heidelberg. https://doi.org/10.1007/978-3-642-17475-9_18

Shin, J. Y., Park, S. S., & An, K. G. (2004). Removal of Nitrogen and Phosphorus Using Dominant Riparian Plants in a Hydroponic Culture System. *Journal of Environmental Science and Health, Part A*, 39(3), 821-834. https://doi.org/10.1081/ESE-120027744

Simon, A., Bennett, S. J., & Neary, V. S. (2004). Riparian Vegetation and Fluvial Geomorphology: Problems and Opportunities. In S. J. Bennett & A. Simon (Eds.), *Riparian Vegetation and Fluvial Geomorphology* (pp. 1–10). American Geophysical Union (AGU). https://doi.org/https://doi.org/10.1029/008WSA01

Skłodowski, M., Kiedrzyńska, E., Kiedrzyński, M., Urbaniak, M., Zielińska, K. M., Kurowski, J. K., & Zalewski, M. (2014). The role of riparian willows in phosphorus accumulation and PCB control for lotic water quality improvement. *Ecological Engineering*, *70*, 1–10. https://doi.org/10.1016/j.ecoleng.2014.03.088

Sonnenwald, F., Stovin, V., & Guymer, I. (2019). Estimating drag coefficient for arrays of rigid cylinders representing emergent vegetation. *Journal of Hydraulic Research*, *57*(4), 591-597. https://doi.org/10.1080/00221686.2018.1494050

Spalart, P. R. (2000a). Strategies for turbulence modeling and simulations. *International Journal of Heat and Fluid Flow*, *21*(3), 252-263. https://doi.org/10.1016/S0142-727X(00)00007-2

Spalart, P. R. (2000b). Trends in turbulence treatments. In *Fluids 2000 Conference and Exhibit*. American Institute of Aeronautics and Astronautics. https://doi.org/doi:10.2514/6.2000-2306

Stewart, M. T., Cameron, S. M., Nikora V. I., Zampiron, A., & Marusic, I. (2019). Hydraulic resistance in open-channel flows over self-affine rough beds. *Journal of Hydraulic Research*, *57*(2), 183-196. https://doi.org/10.1080/00221686.2018.1473296

Stoesser, T., Kim, S. J., & Diplas, P. (2010). Turbulent flow through idealized emergent vegetation. *Journal of Hydraulic Engineering*, *136*(12), 1003–1017. https://doi.org/10.1061/(ASCE)HY.1943-7900.0000153

Stone, B. M. (1997). *Hydraulics of flow in vegetated channels* [Master's thesis]. Clarkson University.

Stone, B. M., & Shen, H. T. (2002). Hydraulic resistance of flow in channels with cylindrical roughness. *Journal of Hydraulic Engineering*, *128*(5), 500–506. https://doi.org/10.1061/(ASCE)0733-9429(2002)128:5(500)

Sucker, D., & Brauer, H. (1975). Fluiddynamik bei quer angeströmten Zylindern. *Wärme- und Stoffübertragung*, *8*, 149–158. https://doi.org/10.1007/BF01681556

Sumner, D., Heseltine, J. L., & Dansereau, O. J. P. (2004). Wake structure of a finite circular cylinder of small aspect ratio. *Experiments in Fluids*, *37*(5), 720–730. https://doi.org/10.1007/s00348-004-0862-7

Tanino, Y., & Nepf, H. M. (2008a). Laboratory investigation of mean drag in a random array of rigid, emergent cylinders. *Journal of Hydraulic Engineering*, *134*(1), 34-41. https://doi.org/10.1061/(ASCE)0733-9429(2008)134:1(34)

Tanino, Y., & Nepf, H. M. (2008b). Lateral dispersion in random cylinder arrays at high Reynolds number. *Journal of Fluid Mechanics*, *600*, 339–371. https://doi.org/10.1017/S0022112008000505

Thompson, A. M., Wilson, B. N., & Hansen, B. J. (2004). Shear stress partitioning for idealized vegetated surfaces. *Transactions of the ASAE*, *47*(3), 701–709. https://doi.org/10.13031/2013.16102

Tinoco, R. O., & Cowen, E. A. (2013). The direct and indirect measurement of boundary stress and drag on individual and complex arrays of elements. *Experiments in Fluids*, *54*(4), 1–16. https://doi.org/10.1007/s00348-013-1509-3

van Rooijen, A., Lowe, R., Ghisalberti, M., Conde-Frias, M., & Tan, L. (2018). Predicting current-induced drag in emergent and submerged aquatic vegetation canopies. *Frontiers in Marine Science*, *5*. https://doi.org/10.3389/fmars.2018.00449

Vanoni, V. A., & Brooks, N. H. (1957). *Laboratory studies of the roughness and suspended load of alluvial streams* (No. E-68). Sedimentation Laboratory, California Institute of Technology. https://resolver.caltech.edu/CaltechKHR:SedLabRpt-E-68

Wang, W. J., Peng, W. Q., Huai, W. X., Katul G. G., Liu, X. B., Qu, X. D. & Dong F. (2019). Friction factor for turbulent open channel flow covered by vegetation. *Scientific Reports*, *9*(1). https://doi.org/10.1038/s41598-019-41477-7

White, B. L., & Nepf, H. M. (2007). Shear instability and coherent structure in shallow flow adjacent to a porous layer. *Journal of Fluid Mechanics*, *593*, 1–32. https://doi.org/10.1017/S0022112007008415

White, F. M. (1991). *Viscous fluid flow* (2nd ed.). McGraw-Hill.

Wieselsberger, C. (1922). *New data on the laws of fluid resistance* (No. NACA-TN-84). https://ntrs.nasa.gov/citations/19930080855

Wilcock, R. J., Champion, P. D., Nagels, J. W., & Crocker, G. F. (1999). The influence of aquatic macrophytes on the hydraulic and physicochemical properties of a New Zealand lowland stream. *Hydrobiologia*, *416*(1), 203-214. https://doi.org/10.1023/A:1003837231848

Wilson, C. A. M. E., & Horritt, M. S. (2002). Measuring the flow resistance of submerged grass. *Hydrological. Processes*, *16*(13), 2589-2598. https://doi.org/10.1002/hyp.1049

Windham, L., Weis, J. S., & Weis, P. (2003). Uptake and distribution of metals in two dominant salt marsh macrophytes, Spartina alterniflora (cordgrass) and Phragmites australis (common reed). *Estuarine, Coastal and Shelf Science*, *56*(1), 63–72. https://doi.org/10.1016/S0272-7714(02)00121-X

Wooding, R. A., Bradley, E. F., & Marshall, J. K. (1973). Drag due to regular arrays of roughness elements of varying geometry. *Boundary-Layer Meteorology*, *5*, 285–308. https://doi.org/10.1007/BF00155238

Wu, F.-C., Shen, H. W., & Chou, Y.-J. (1999). Variation of Roughness Coefficients for Unsubmerged and Submerged Vegetation. *Journal of Hydraulic Engineering*, *125*(9), 934–942. https://doi.org/10.1061/(ASCE)0733-9429(1999)125:9(934)

Yang, J. Q., Kerger, F., & Nepf, H. M. (2015). Estimation of the bed shear stress in vegetated and bare channels with smooth beds. *Water Resources Research*, *51*(5), 3647–3663. https://doi.org/10.1002/2014WR016042

Yang, W., & Choi, S. U. (2010). A two-layer approach for depth-limited open-channel flows with submerged vegetation. *Journal of Hydraulic Research*, *48*(4), 466-475. https://doi.org/10.1080/00221686.2010.491649

Yen, B. C. (2002). Open Channel Flow Resistance. *Journal of Hydraulic Engineering*, *128*(1), 20–39. https://doi.org/10.1061/(ASCE)0733-9429(2002)128:1(20)

Zdravkovich, M. M. (1987). The effects of interference between circular cylinders in cross flow. *Journal of Fluids and Structures*, *1*(2), 239–261. https://doi.org/10.1016/S0889-9746(87)90355-0

Zdravkovich, M. M. (1997). *Flow Around Circular Cylinders, Vol. 1: Fundamentals*. Oxford University Press.

Zdravkovich, M. M. (2003). *Flow Around Circular Cylinders Vol. 2: Applications*. Oxford University Press.

Zhang, J., Zhang, S., Chen, S., Liu, M., Xu, X., Zhou, J., Wang, W., Ma, L., & Wang, C. (2021). Overland flow resistance law under sparse stem vegetation coverage. *Water*, *13*(12). https://doi.org/10.3390/w13121657

Zhang, S., Liu, Y., Zhang, J., Liu, Y., & Wang, Z. (2018). Study of the impact of vegetation direction and slope on drag coefficient. *Iranian Journal of Science and Technology*, *Transactions of Civil Engineering*, *42*(4)*, 381-390. https://doi.org/10.1007/s40996-018-0107-2

Zong, L., & Nepf, H. (2011). Spatial distribution of deposition within a patch of vegetation. *Water Resources Research*, *47*(3). https://doi.org/10.1029/2010WR009516

Žukauskas, A. (1972). Heat Transfer from Tubes in Crossflow. In J. P. Hartnett & T. F. Irvine (Eds.), *Advances in Heat Transfer* (Vol. 8, pp. 93–160). Elsevier. https://doi.org/https://doi.org/10.1016/S0065-2717(08)70038-8

APPENDICES

A. Experimental Data for Emergent Vegetation Cases

Table A.1 Emergent cases having vegetation density λ=0.03924

λ=0.03924, S=0.01							
Exp. No	**Q (lt/s)**	**H (m)**	**F_T (N)**	**Exp. No**	**Q (lt/s)**	**H (m)**	**F_T (N)**
1	19.70	0.068	6.37	7	49.80	0.172	16.85
2	20.30	0.158	3.44	8	50.50	0.142	19.93
3	29.90	0.153	8.43	9	59.10	0.183	22.67
4	30.80	0.098	10.26	10	59.90	0.163	25.23
5	40.60	0.171	11.39	11	69.60	0.183	32.19
6	40.90	0.122	14.86	12	69.60	0.196	29.32
λ=0.03924, S=0.005							
Exp. No	**Q (lt/s)**	**H (m)**	**F_T (N)**	**Exp. No**	**Q (lt/s)**	**H (m)**	**F_T (N)**
13	19.70	0.146	3.74	20	59.20	0.174	24.05
14	29.10	0.108	9.89	21	60.40	0.201	21.98
15	30.60	0.149	9.82	22	69.50	0.193	29.55
16	40.10	0.167	12.16	23	69.80	0.202	30.16
17	40.30	0.133	14.05	24	79.70	0.212	35.39
18	50.30	0.155	18.65	25	89.40	0.230	42.47
19	50.50	0.187	16.60				
λ=0.03924, S=0.0025							
Exp. No	**Q (lt/s)**	**H (m)**	**F_T (N)**	**Exp. No**	**Q (lt/s)**	**H (m)**	**F_T (N)**
26	21.20	0.138	3.53	32	49.80	0.158	18.75
27	30.80	0.116	11.04	33	59.20	0.177	23.35
28	32.20	0.143	9.73	34	60.20	0.207	25.18
29	40.30	0.136	14.15	35	69.30	0.197	30.02
30	41.40	0.165	12.41	36	70.20	0.216	30.54
31	49.10	0.182	15.57	37	79.40	0.217	37.15

Table A.2 Emergent cases having vegetation density λ=0.01744

λ=0.01744, S=0.01							
Exp. No	Q (lt/s)	H (m)	F_T (N)	Exp. No	Q (lt/s)	H (m)	F_T (N)
38	29.80	0.072	7.79	44	59.00	0.160	10.87
39	31.10	0.113	3.62	45	59.50	0.126	18.00
40	40.40	0.093	10.85	46	69.50	0.153	17.24
41	40.60	0.148	4.87	47	70.40	0.141	22.08
42	50.30	0.111	14.55	48	79.20	0.155	25.78
43	50.30	0.161	6.99	49	80.00	0.157	23.11
λ=0.01744, S=0.005							
Exp. No	Q (lt/s)	H (m)	F_T (N)	Exp. No	Q (lt/s)	H (m)	F_T (N)
50	20.50	0.065	3.20	56	50.70	0.122	11.33
51	31.10	0.177	3.05	57	61.00	0.183	9.96
52	31.80	0.087	5.91	58	61.20	0.139	14.90
53	39.10	0.104	8.13	59	69.30	0.187	13.25
54	40.00	0.165	4.81	60	70.20	0.156	18.71
55	50.50	0.213	5.74	61	79.20	0.196	17.35
λ=0.01744, S=0.0025							
Exp. No	Q (lt/s)	H (m)	F_T (N)	Exp. No	Q (lt/s)	H (m)	F_T (N)
62	20.80	0.074	3.76	68	49.70	0.160	9.77
63	30.00	0.212	2.05	69	59.90	0.147	14.67
64	30.30	0.094	5.64	70	60.90	0.188	11.70
65	40.00	0.148	7.36	71	69.10	0.201	14.72
66	40.90	0.114	8.40	72	70.20	0.163	18.68
67	49.20	0.128	10.91	73	79.40	0.229	17.13

Table A.3 Emergent cases having vegetation density λ=0.00981

λ=0.00981, S=0.01							
Exp. No	Q (lt/s)	H (m)	F_T (N)	Exp. No	Q (lt/s)	H (m)	F_T (N)
74	29.40	0.143	2.46	84	60.30	0.102	11.96
75	30.00	0.060	5.84	85	60.90	0.100	12.31
76	30.20	0.060	5.89	86	69.30	0.112	13.88
77	40.30	0.076	7.88	87	70.00	0.148	8.49
78	40.90	0.076	8.12	88	71.80	0.113	13.73
79	41.00	0.143	3.29	89	79.20	0.121	15.33
80	49.40	0.090	10.19	90	79.60	0.124	15.09
81	50.30	0.143	4.38	91	80.40	0.148	10.82
82	50.80	0.090	10.22	92	88.80	0.132	17.29
83	60.20	0.145	6.30	93	90.10	0.148	13.83
λ=0.00981, S=0.005							
Exp. No	Q (lt/s)	H (m)	F_T (N)	Exp. No	Q (lt/s)	H (m)	F_T (N)
94	29.40	0.165	1.50	100	59.70	0.116	8.70
95	31.20	0.074	3.80	101	61.30	0.167	5.74
96	40.60	0.166	2.62	102	69.80	0.129	10.78
97	41.50	0.091	5.51	103	71.10	0.170	8.11
98	50.50	0.166	3.99	104	79.50	0.171	10.60
99	50.70	0.104	7.35	105	80.40	0.141	13.11
λ=0.00981, S=0.0025							
Exp. No	Q (lt/s)	H (m)	F_T (N)	Exp. No	Q (lt/s)	H (m)	F_T (N)
106	29.40	0.167	1.65	112	59.10	0.120	8.82
107	29.80	0.077	3.42	113	60.40	0.167	6.46
108	39.00	0.095	5.40	114	69.30	0.133	10.79
109	39.50	0.163	2.91	115	70.30	0.170	8.74
110	49.60	0.168	4.43	116	79.30	0.145	12.77
111	50.30	0.108	7.11	117	79.60	0.174	11.52

Table A.4 Emergent cases having vegetation density λ=0.00436

λ=0.00436, S=0.01							
Exp. No	Q (lt/s)	H (m)	F_T (N)	Exp. No	Q (lt/s)	H (m)	F_T (N)
118	39.80	0.096	3.54	124	70.30	0.087	10.09
119	40.00	0.048	7.57	125	72.00	0.192	6.01
120	49.60	0.144	3.76	126	79.40	0.095	15.14
121	50.30	0.061	8.23	127	80.70	0.185	6.98
122	59.20	0.207	3.76	128	89.90	0.223	7.41
123	60.30	0.073	9.22				
λ=0.00436, S=0.005							
Exp. No	Q (lt/s)	H (m)	F_T (N)	Exp. No	Q (lt/s)	H (m)	F_T (N)
129	30.40	0.066	3.54	135	69.60	0.142	6.94
130	39.70	0.084	4.30	136	70.40	0.114	8.46
131	41.20	0.118	3.24	137	79.70	0.169	7.52
132	50.20	0.126	4.39	138	80.60	0.124	9.85
133	51.00	0.096	5.56	139	90.30	0.206	7.86
134	60.60	0.127	6.36				
λ=0.00436, S=0.0025							
Exp. No	Q (lt/s)	H (m)	F_T (N)	Exp. No	Q (lt/s)	H (m)	F_T (N)
140	29.40	0.071	2.28	146	59.40	0.113	6.31
141	30.30	0.106	2.25	147	60.00	0.131	6.03
142	40.20	0.125	3.19	148	69.60	0.124	7.92
143	40.40	0.088	3.76	149	69.80	0.127	8.99
144	50.00	0.128	4.38	150	80.30	0.137	9.67
145	50.50	0.103	4.97				

B. Experimental Data for Submerged Vegetation Cases

Table B.1 Submerged cases having vegetation density λ=0.03924

λ=0.03924, S=0.01							
Exp. No	Q (lt/s)	H (m)	F_T (N)	Exp. No	Q (lt/s)	H (m)	F_T (N)
1	29.90	0.129	1.22	7	61.10	0.192	2.99
2	39.00	0.089	6.74	8	69.30	0.117	10.89
3	40.60	0.157	1.63	9	69.50	0.157	5.44
4	50.00	0.100	8.16	10	79.60	0.199	5.03
5	51.30	0.165	2.31	11	80.10	0.128	12.05
6	59.90	0.110	9.46	12	89.60	0.134	13.22
λ=0.03924, S=0.005							
Exp. No	Q (lt/s)	H (m)	F_T (N)	Exp. No	Q (lt/s)	H (m)	F_T (N)
13	30.30	0.086	5.54	19	59.20	0.209	2.03
14	30.50	0.208	0.95	20	60.00	0.121	9.91
15	39.80	0.099	7.08	21	69.50	0.130	11.20
16	40.00	0.217	1.22	22	70.40	0.164	4.33
17	49.90	0.236	1.76	23	79.30	0.139	12.23
18	50.10	0.111	8.63	24	80.20	0.206	4.46
λ=0.03924, S=0.0025							
Exp. No	Q (lt/s)	H (m)	F_T (N)	Exp. No	Q (lt/s)	H (m)	F_T (N)
25	30.30	0.091	3.81	35	59.50	0.210	1.36
26	30.90	0.193	0.28	36	59.90	0.126	7.22
27	31.20	0.175	0.23	37	69.60	0.219	2.82
28	40.40	0.153	0.56	38	69.80	0.135	8.17
29	40.70	0.105	5.18	39	69.90	0.235	1.59
30	40.80	0.209	0.45	40	79.50	0.209	2.61
31	49.70	0.219	2.12	41	80.00	0.189	3.95
32	50.20	0.227	0.68	42	80.30	0.145	8.99
33	50.50	0.116	6.40	43	89.90	0.231	4.09
34	59.40	0.203	2.12				

Table B.2 Submerged cases having vegetation density λ=0.01744

							λ=0.01744, S=0.01						
Exp. No	**Q (lt/s)**	**H (m)**	**F_T (N)**		**Exp. No**	**Q (lt/s)**	**H (m)**	**F_T (N)**
44	29.70	0.065	5.55		50	61.40	0.097	7.64
45	39.90	0.077	5.92		51	68.90	0.102	8.50
46	40.70	0.201	0.73		52	69.80	0.204	1.58
47	49.80	0.201	0.97		53	79.20	0.110	9.37
48	50.30	0.087	6.90		54	79.50	0.202	1.82
49	58.00	0.202	1.21		55	90.10	0.202	2.55
				λ=0.01744, S=0.005				
Exp. No	**Q (lt/s)**	**H (m)**	**F_T (N)**		**Exp. No**	**Q (lt/s)**	**H (m)**	**F_T (N)**
56	29.50	0.232	0.36		62	59.50	0.107	4.70
57	31.20	0.076	2.61		63	59.50	0.236	0.97
58	39.90	0.086	3.27		64	69.00	0.236	1.34
59	40.10	0.235	0.49		65	69.30	0.115	5.75
60	49.60	0.236	0.73		66	78.50	0.125	6.40
61	50.90	0.098	4.05		67	80.90	0.236	1.82
				λ=0.01744, S=0.0025				
Exp. No	**Q (lt/s)**	**H (m)**	**F_T (N)**		**Exp. No**	**Q (lt/s)**	**H (m)**	**F_T (N)**
68	29.30	0.214	0.67		75	60.00	0.159	1.74
69	30.00	0.079	2.47		76	69.80	0.121	6.06
70	41.00	0.109	1.07		77	70.60	0.184	2.01
71	41.10	0.091	3.34		78	79.50	0.189	2.41
72	50.80	0.103	4.20		79	80.10	0.129	6.80
73	50.90	0.130	1.48		80	89.80	0.204	4.02
74	59.80	0.111	5.07					

Table B.3 Submerged cases having vegetation density λ=0.00981

Exp. No	Q (lt/s)	H (m)	F_T (N)	Exp. No	Q (lt/s)	H (m)	F_T (N)
λ=0.00981, S=0.01							
81	40.20	0.176	0.58	87	69.40	0.176	1.74
82	40.70	0.071	5.16	88	69.90	0.096	7.35
83	49.80	0.174	1.04	89	80.20	0.107	8.13
84	51.40	0.081	5.81	90	80.20	0.175	2.20
85	59.90	0.093	6.84	91	88.60	0.111	9.03
86	60.20	0.168	1.39	92	88.60	0.165	2.78
λ=0.00981, S=0.005							
93	28.90	0.160	0.46	100	59.90	0.099	4.41
94	30.30	0.069	1.91	101	70.30	0.107	5.36
95	40.60	0.080	2.74	102	71.50	0.160	2.85
96	41.20	0.158	0.91	103	80.90	0.158	3.30
97	49.30	0.162	1.37	104	81.20	0.115	6.31
98	50.50	0.090	3.57	105	88.70	0.120	7.03
99	59.80	0.160	2.05				
λ=0.00981, S=0.0025							
106	29.50	0.206	0.97	113	61.30	0.205	1.46
107	29.80	0.075	2.32	114	68.60	0.115	5.58
108	39.20	0.086	3.25	115	70.30	0.209	1.70
109	41.40	0.206	0.85	116	80.20	0.208	2.07
110	50.30	0.096	3.95	117	80.60	0.125	6.04
111	50.80	0.203	0.97	118	89.40	0.209	2.19
112	59.00	0.107	4.76				

Table B.4 Submerged cases having vegetation density λ=0.00436

Exp. No	Q (lt/s)	H (m)	F_T (N)
λ=0.00436, S=0.01			
119	29.10	0.118	1.34
120	41.50	0.131	1.57
121	51.40	0.123	2.13
122	60.70	0.133	2.13
123	69.10	0.173	2.24
124	79.90	0.134	3.80

λ=0.00436, S=0.005							
Exp. No	Q (lt/s)	H (m)	F_T (N)	Exp. No	Q (lt/s)	H (m)	F_T (N)
125	30.20	0.168	0.81	131	69.30	0.101	6.50
126	39.70	0.144	0.81	132	70.50	0.115	3.92
127	49.20	0.140	1.50	133	79.70	0.111	6.82
128	50.70	0.083	5.77	134	84.30	0.172	3.57
129	60.20	0.091	6.08	135	89.10	0.118	7.34
130	60.30	0.122	2.19	136	99.00	0.124	7.76

λ=0.00436, S=0.0025							
Exp. No	Q (lt/s)	H (m)	F_T (N)	Exp. No	Q (lt/s)	H (m)	F_T (N)
137	30.70	0.133	1.42	144	69.60	0.104	4.17
138	40.70	0.117	2.01	145	70.00	0.137	3.55
139	40.90	0.080	3.12	146	79.50	0.114	4.63
140	50.50	0.133	2.36	147	79.60	0.156	3.66
141	50.60	0.090	3.59	148	89.10	0.194	3.43
142	60.30	0.138	2.84	149	89.80	0.121	5.56
143	60.40	0.094	3.82				

CURRICULUM VITAE

Surname, Name: Haspolat, Emre

EDUCATION

Degree	Institution	Year of Graduation
MS	METU Civil Engineering	2015
BS	METU Civil Engineering	2013
High School	Torbalı Anadolu High School	2008

WORK EXPERIENCE

Year	Place	Enrollment
2015-Present	METU	Research Assistant
2014-2014	TED University	Research Assistant
2013-2015	TUBİTAK Project	Project Assistant

FOREIGN LANGUAGES

Advanced English

PUBLICATIONS

Gogus, M., & Haspolat, E. (2021). Effect of sediment properties on incipient motion of large solitary particles on fixed bed. *Proceedings of the Institution of Civil Engineers: Water Management*. https://doi.org/10.1680/jwama.20.00071

Haspolat, E., & Gogus, M. (2022). Estimation of Critical Submergence at Single Horizontal Intakes Under Asymmetric Flow Conditions. *Arabian Journal for Science and Engineering*, *47*, 12509-12520. https://doi.org/10.1007/s13369-021-06507-5

CONFERENCE PROCEEDINGS

Gogus, M., Koken, M., Zaloğlu, C., & Haspolat, E. (2015). Determination of Critical Submergence Depth at Horizontal Intakes under Asymmetric Flow Conditions. *36th IAHR World Congress*, 28 June – 03 July 2015, The Hague, Netherlands.

Gogus, M., Altan-Sakarya, A. B., Koken, M., Dinçer, A. E., Yavuz, C., & Haspolat, E. (2015). Yukarı Kaleköy Barajı HES Dolusavak Hidrolik Model Deneyleri. *4. Su Yapıları Sempozyumu*, November 2015, Antalya, Turkey.

Gogus, M., Koken, M., Zaloğlu, C., & Haspolat E. (2016). Determination of Critical Submergence at Horizontal Intakes under Symmetrical Flow Conditions. *12th International Congress on Advances in Civil Engineering*, 21 -23 September 2016, Istanbul, Turkey.

Koken, M., Aydın, I., Haspolat, E., & Şahin A. N. (2017). Experimental and Numerical Investigation of Piano Key Weirs. *37th IAHR World Congress*, 13 -18 August 2017, Kuala-Lumpur, Malaysia.

PROJECTS

Formation and Prevention of Vortices at Hydropower Plants which Contain Single and Multi Horizontal Intake Structures, Scholarship Student, The Scientific and Technological Research Council of Turkey (TUBITAK), Project No: 113M326, 2013-2015.

Yukarı Kaleköy Dam and Hydroelectric Power Plant Spillway Hydraulic Model Studies, Researcher, Private Institution, 2015.

Aşağı Kaleköy Dam Hydraulic Model Studies, Researcher, Private Institution, 2016-2017.